DISSERTATION

GEOLOGICAL CONTROL ON AQUIFER STORAGE AND RECOVERY (ASR) FEASIBILITY AND EFFICIENCY IN CARBONATE AQUIFERS (EDWARDS AQUIFER AND FLORIDAN AQUIFER)

Submitted by

Christophe Wakamya Simbo

Department of Geosciences

In partial fulfillment of the requirements

For the Degree of Doctor of Philosophy

Colorado State University

Fort Collins, Colorado

Summer 2024

Doctoral Committee:

Advisor: Sally Sutton

Tom Sale
Michael Ronayne
John Ridley

ABSTRACT

GEOLOGICAL CONTROL ON AQUIFER STORAGE AND RECOVERY (ASR) FEASIBILITY AND EFFICIENCY IN CARBONATE AQUIFERS (EDWARDS AQUIFER AND FLORIDAN AQUIFER)

Aquifer storage and recovery (ASR) is increasingly being used to enhance freshwater security and sustainability. Though proven technology, ASR implementation and efficiency are mainly controlled by the aquifer system's geological characteristics. Aquifer or reservoir quality, aquifer geochemistry and heterogeneity, and ASR-induced stress exerted on aquifer systems affect the operation of ASR and, hence, ASR recovery feasibility and efficiency. This dissertation evaluates the feasibility of ASR operations in two major carbonate aquifers in the USA: the brackish portion of the Edwards aquifer and the Floridan aquifer. Aquifer matrix petrology and geochemistry, groundwater geochemistry, surface water geochemistry, and time series water chemistry coupled with numerical modeling with PHAST and Geochemists' Workbench (GWB), and analytical modeling were used to understand the aquifers and evaluate ASR optimization strategies.

The Edwards Aquifer petrography provides insights into the aquifer texture, fabric, and aquifer/reservoir quality controlled by depositional and post-depositional processes. Though the development of porosity and permeability are likely controlled by the precursor texture of the aquifer matrix, diagenetic processes, mainly dolomitization together with fracturing and dissolution, may be the main agents affecting aquifer quality for ASR operation. Suitable aquifer zones for water storage are characterized by permeability likely controlled by intercrystalline, fracture, and vuggy porosity in dolomitic zones. Bulk aquifer geochemistry documents major and

trace elements, with high MgO/CaO revealing extensive dolomitization preferentially located towards the middle of the Person and Kainer Formations, aquifer units within the Edwards aquifer system. The relatively higher content of SiO_2, Al_2O_3, and, to some extent, K_2O and TiO_2 in confining layers points to a modest increase in clay minerals compared to aquifer sections. Clay minerals, together with compaction features observed in confining layer thin sections, potentially reduce confining layer permeability and porosity. However, high fracture porosity within the Regional Dense Member (RDM) confining layer separating both Edwards aquifer zones offers potential pathways connecting both zones. That these fractures may, in fact, be pathways is supported by changes in groundwater hydrochemistry in the non-targeted aquifer zone (Kainer) during the initial ASR recharge cycle.

Based on injectant and groundwater chemistry and time series water chemistry of recovered water samples during the first ASR operation cycle, initial and evolved hydrochemical facies were evaluated in the Edwards aquifer ASR operation (in New Braunfels). Forward GWB water-water and water-rock interaction modeling revealed the mixing of the injectant and the native groundwater to be the main contributing factor in the hydrochemical facies evolution of groundwater during the first ASR recharge cycle. Estimated hydraulic conductivity values using the numerical PHAST model and corroborated by the Hemker analytical model support the combined effect of lateral flow and vertically-induced flow of high total dissolved solids (TDS) groundwater from the Kainer Formation into the Person Formation via the RDM confining layer during ASR recovery. Estimated hydraulic property values (hydraulic conductivity and porosity) of these three aquifer layers aided in predicting the recovery rate to optimize ASR operations. Implementation of two ASR wells, respectively screened in the Person and Kainer Formations, presents a potential long-term ASR optimization strategy at the Edwards aquifer study site.

Induced arsenic releases to concentrations higher than their maximum contaminant level (MCL) of 10 µg/L hinder aquifer storage and recovery (ASR) operations worldwide. Statistical data and time series analyses of the recovered water hydrochemical data were used to assess the operational methodology maintaining the buffer zone for arsenic attenuation during ASR operations in the Floridan aquifer. Additionally, based on Injectant and groundwater hydrochemical data with geochemical data of the aquifer matrix , 1D GWB reactive transport model was used to assess the buffer zone operation methodology that holds promise in managing arsenic releases during ASR operations in the Floridan aquifer. Time series data from the Tampa ASR operations show a positive correlation between percent recovery and arsenic concentration in the recovered water, with high recovery percentages inducing mobilization of arsenic up to 38 µg/L, a value roughly four times the arsenic maximum contaminant level of 10 µg/L. Further, the developed 1D forward reactive transport model suggests underlying processes that control arsenic behavior upon injection of oxygenated source water into a reducing carbonate storage zone. Two model scenarios were used in this study. Model scenario 2 developed such that a larger oxygen front expanded up to 565 m away from the ASR well, three times further than in scenario 1, and promoted the production of Fe(III) oxides/oxyhydroxides with abundances up to 18,700 µg/Kg formed at 555 m away from the ASR well. These Fe(III) oxides/oxyhydroxides may provide sorbing sites that attenuate arsenic concentrations in the groundwater.

ACKNOWLEDGMENTS

First and foremost, I would like to gratefully acknowledge the help, support, and encouragement of my advisor Dr. Sally Sutton, for the effort to provide invaluable assistance and inspired ideas. Her support cannot be understated.

I would like to thank my thesis Committee, Dr. Tom Sale, Dr. Mike Ronayne, and Dr. John Ridley for accepting to be part of this academic journey. I am also grateful to Dr. Jens Blotevogel for his initial acceptance to be part of the committee before moving to Australia. His early involvement and guidance positively impacted the course of this Ph.D. project. Your collective guidance, insights, and constructive feedback have been instrumental in shaping the nascent stages of my research project.

My sincere gratitude to David Pyne for his invaluable contributions to this project. His unwavering dedication, extensive knowledge, and willingness to share his expertise were essential in the course of this Ph.D. The data provided from the ASR operations in Texas (New Braunfels) and Florida (in Tampa and Kissimmee) were significant in advancing our understanding of the extent to which geology affects ASR operations in carbonates and ways for ASR optimization. It has been an honor to work with him, and I acknowledge the positive impact he has had on this project. Further, I extend my sincere appreciation to Gregg Jones for his contribution to sharing a significant portion of the ASR data of the Tampa ASR wellfields. His support contributed to the success of the last chapter of this Ph.D. project.

To Dr. Walt McNab and Dr. Konrad, thank you for your support and contribution to the third chapter of this work. Your willingness to dedicate your time and expertise, despite your

busy schedules, to reviewing part of this work has been truly invaluable. Warmest thanks are also extended to Dr. David Budd for valuable discussions in the second chapter and to Dr. Katie Snell for the time to use cathodoluminescence microscopy at the University of Colorado Boulder Geological Sciences.

Thank you to the entities that generously supported me throughout my studies, enabling the pursuit of my degree: Colorado State University Geosciences Department, the Warner College of Natural Resources, the Geological Society of America, the Rocky Mountain Association of Geologists Foundation, the American Water Works Association (Rocky Mountain Section), the National Association of Black Geoscientists, the Colorado Scientific Society, the Colorado Groundwater Association, and the ASR Systems LLC.

I would like to thank faculty, staff in the Department of Geosciences, Colorado State University, and colleagues and friends for their support throughout my Ph.D. program.

I want to extend my deepest gratitude to my family, who, despite the physical distance between us, played an indispensable role in making my dreams a reality. To my parents, your unwavering belief in me, constant encouragement, and boundless love have been the guiding stars on my journey. Even from afar, your presence was felt in every milestone I reached. Despite the passing of my beloved mother, I firmly believe that the values of resilience and determination she instilled in me continue to guide my journey. To my siblings, your virtual companionship and genuine enthusiasm added a special spark to my journey. The support you've provided from across the miles has been nothing short of incredible, and I am forever grateful for the part you've played in this journey of accomplishment.

DEDICATION

To my mother, Beatrice Fatuma, who left too soon but whose enduring spirit continues to guide my path. Your motherly belief in my potential laid the foundation upon which I built this dissertation. Your legacy of hard work and faith in both effort and the divine and merciful God provided the strength I needed to overcome even the most daunting obstacles. This work is a tribute to your selfless support and a testament to the indelible impact you've had on my life!

TABLE OF CONTENTS

CHAPTER 1: INTRODUCTION

Excluding frozen water in glaciers, groundwater represents more than 98% of the world's fresh water. Groundwater provides nearly 50% of all the water used by the world's 8 billion people (Boswinkel, 2000; IUCN, 2016). Respectively, 36%, 42% and 27% of produced groundwater is used for irrigation, households, and manufacturing (Döll et al., 2012). Aquifers in carbonate media particularly play an important socio-economic role in providing freshwater for human consumption, agriculture, and groundwater-dependent ecosystems (Bakalowicz, 2005). Approximately 20 to 25% of the world's population is supplied by groundwater in aquifers of carbonate origin (Ford and Williams, 2007; Goldscheider et al., 2020). Notably, in the U.S. alone, an estimated total groundwater withdrawal of up to 16% (or 2,440 Mgal/day) is sourced from carbonate aquifers for public supply water use in comparison to other lithologies (Lovelace et al., 2015). However, with increasing demand for good quality water, climate variability and change, as well as growth in global population, urbanization, and the ensuing need for irrigation and food security, stress on groundwater resources has intensified (Konikow and Kendy, 2005), prompting the need to enhance freshwater security and diversification strategies. Valhondo and Carrera (2019) attribute the finite supply of water resources to a global lack of water and the spatial and temporal imbalances between water demand and supply. Therefore, balancing water demand and supply requires innovative water resources management techniques that harness the temporal (seasonal) availability of water resources and convert it into a more reliable and sustainable supply strategy.

Managed aquifer recharge (MAR) is an increasingly used tool to maintain, enhance, and secure a long-term supply of freshwater from overexploited groundwater systems (Dillon et al., 2019). MAR serves multiple purposes, such as improving seasonal and interannual drinking

water supplies, mitigating land subsidence, and restoring ecosystems. Multiple techniques can be used to deliver water to aquifers, including engineered infiltration basins, riverbank filtration, soil aquifer treatment, and injection-based methods like aquifer storage (and/or transfer) and recovery, fall under the umbrella of managed aquifer recharge. Aquifer storage and recovery is one of the MAR widely used techniques involving a single dual-purpose well for direct injection, storage, and later recovery of water supplies to overcome the gap between future water supplies and demand (Figure 1.1) (Pyne, 2005).

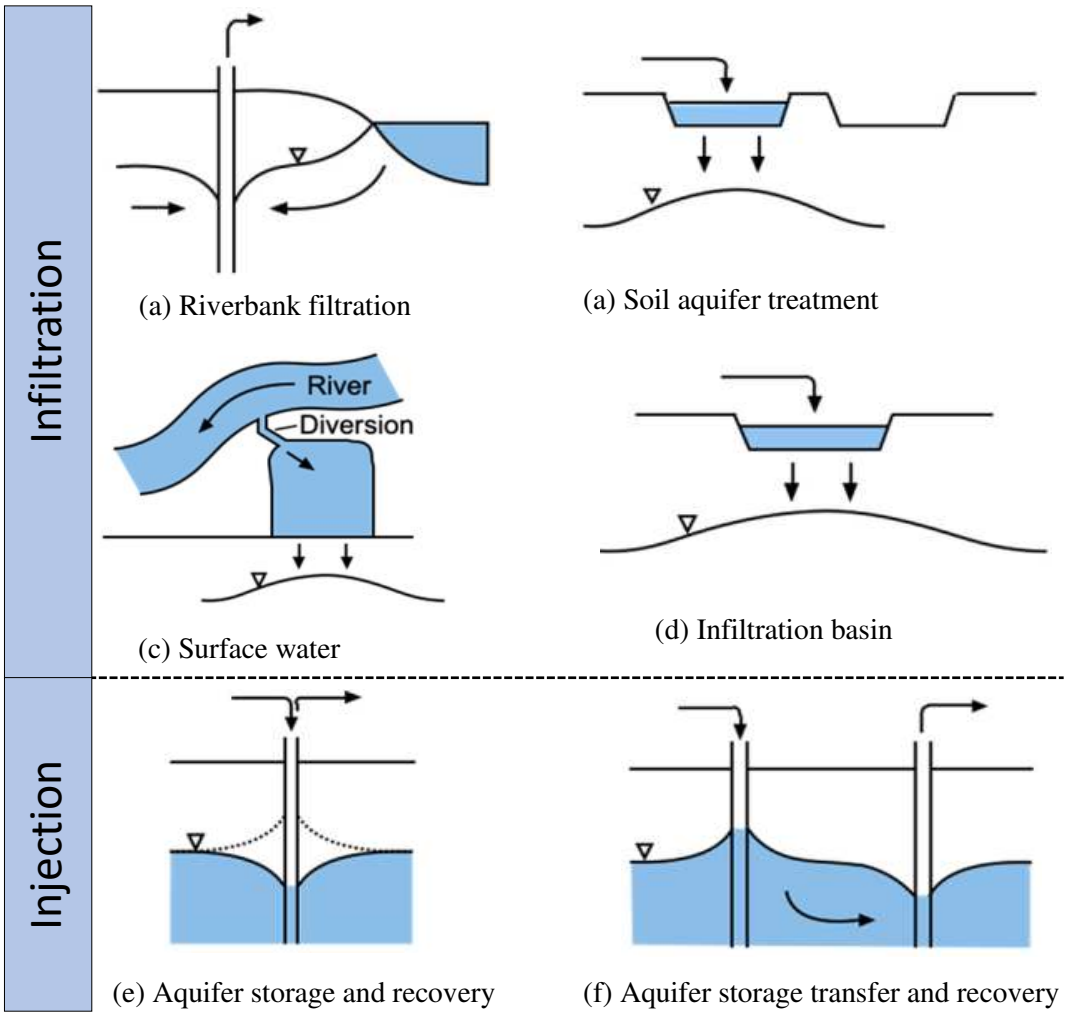

Figure 1.1. illustrates common MAR types via infiltration and injection (modified from Fakhreddine et al., 2021).

As a water resource management technique to secure and enhance water supplies for human and environmental beneficial purposes, aquifer storage and recovery (ASR) takes advantage of three main functions of the aquifer; ASR uses the storage reservoir function during wet periods to store a large volume of surface water in underground porous media, hence reducing evaporative losses and minimizing surface contamination within the required limited land area. The conduit function confers on the aquifer the ability to readily store and transmit water, a property used by a single well ASR for injection of surface water and recovery of stored water when needed. To achieve drinking water standards, ASR uses the aquifer as a filter plant for its inherent physical, chemical, and biological capabilities to purify water under certain circumstances (Bear, 1979) —without considering the ASR-induced geogenic contamination. This water-supply strategy consisting of deliberate recharge of an aquifer and subsequent recovery after a certain storage time using a single well is seeing increased use based on studies evidencing that ASR enhances the sustainability of regional water resources (Alqahtani et al., 2020). However, the effectiveness of ASR systems is dependent on site-specific geological factors. In contrast to other sedimentary rock types serving as aquifers (sandstones, conglomerates, etc.), carbonates inherit their heterogeneity and complex porosity and permeability from the diagenesis of carbonate grains and mud. Carbonate pore structure and fabric patterns can vary from submicron pores to kilometer-scale cave systems (Saller et al., 1994; Mazzullo, 2004; Moore and Wade, 2013; Head and Vanorio, 2016), with permeabilities spanning more than six orders of magnitude (Ng and Santamarina, 2023). These heterogeneities lead to complex porosity and permeability relationships that can be conducive to the development of aquifers (Hiatt and Pufahl, 2016). The resulting uncertainty in fluid flow in carbonate aquifers affects groundwater management operations such as aquifer storage and

recovery (Maliva et al., 2002). Hence, the petrological characterization of the carbonate aquifer matrix is important in understanding the aquifer and predicting its behavior during ASR operation, aiding in ASR feasibility and optimization.

Furthermore, in addition to its bulk carbonate mineralogy, possibly associated with minor evaporites and siliciclastics, carbonates host traces of mineral phases that may source geogenic trace element contamination during ASR operations. One of these elements is arsenic, typically found in (hydr)oxide minerals and commonly present in sulfides such as pyrite. The concentration of arsenic incorporated in these minerals —mineral compounds that control geogenic As contamination — tends to be high compared to other trace elements and metalloids. Studies have shown the degree of trace metal pyritization (DTMP) —a metric evaluating the degree to which reactive trace metals incorporate into pyrite — to have a decreasing order of Hg >As = Mo >Cu = Fe > Co > Ni >> Mn > Zn > Cr = Pb > Cd. This pattern indicates that sedimentary pyrite is a major sink for Hg, As, and Mo, a moderate sink for Co, Cu, Mn, and Ni, and insignificantly incorporates Cr, Pb, Zn, and Cd (Huerta-Diaz and Morse, 1992). Arsenic is a common contaminant of concern in many ASR operations due to its ubiquity in geological environments, and toxicity at trace concentrations with a federal maximum contaminant level of 10 µg/L (US EPA, 2006). Several studies have attributed arsenic contamination during ASR operations to the injection of oxidized water into the native reduced aquifer from different pathways, including (1) dissolution of arsenic-bearing mineral phases (commonly pyrite) from disturbances of redox conditions from reducing to oxidizing environments, (2) reduction of arsenate into more labile arsenite species, and (3) ligand exchange (e.g., competitive displacement of arsenate by phosphate, silicate or carbonate). Moreover, Price and Pichler (2006) demonstrated that ASR operations in aquifer lithologies with low whole-rock content in

arsenic are capable of generating relatively high As concentrations prone to As contamination in recovered water. Aquifer matrix and water geochemistry evaluation coupled with modeling tools help quantitatively predict the chemical evolution of aquifer systems, therefore providing a basis for strategies to recover a substantial quantity of groundwater meeting regulatory requirements for contaminants, such as Total Dissolved Solids (TDS) and arsenic, as examined in this study.

The above outlined geological factors present pressing issues for ASR optimization within two principal U.S. carbonate aquifers, the Edwards aquifer (in Texas) and the Floridan aquifer (in Florida). This Ph.D. research project encompasses three main topics or chapters, apart from the introduction (Chapter 1) and conclusion (Chapter 5), and whose goals are outlines below:

Chapter 2 objectives are to:

- Investigate the petrological characteristics and diagenetic processes influencing ASR feasibility.
- Analyze the porosity types and their impact on permeability within the study area.
- Examine the geochemistry of the aquifer matrix, surface water and groundwater to understand its role in ASR operations.

Chapter 3 objectives are to:

- Characterize the native groundwater and injectant in the Edwards aquifer.
- Study the evolution of hydrochemical facies and identify controlling geochemical processes.

- Estimate aquifer hydraulics to optimize ASR recovery rates in the two-layer Edwards aquifer system without inducing high Total Dissolved Solids (TDS) concentrations in the recovered water.

Chapter 4 objective is to investigate ASR operational methodologies in reducing arsenic mobilization below maximum contaminant level of 10 μg/L.

These chapters have been disseminated within the academic community. Chapter 3 has been published in Groundwater Journal. Chapters 2 and 3 have been presented at international and national conferences, respectively in the 21st International Sedimentological Congress (Theme: Resource Sedimentology, Session T9-4 Characterization of subsurface sedimentary architectures; Abstract ID: T9-41509) (presented online), and Managed Aquifer Recharge conference (Managed Aquifer Recharge: Unleashing Resiliency, Protecting Groundwater Quality) in San Antonio, Texas.

1.1 References

Alqahtani, A., Sale, T., Ronayne, M. J., & Hemenway, C., 2021. Demonstration of sustainable development of groundwater through aquifer storage and recovery (ASR). *Water Resources Management*, *35*, 429-445.

Arthur, H. S., Dickson, J. A. D., & Stacie, A. B., 1994. Cycle stratigraphy and porosity in Pennsylvanian and Lower Permian shelf limestones, eastern Central Basin Platform, Texas. *AAPG bulletin*, *78*(12), 1820-1842.

Bakalowicz, M., 2005. Karst groundwater: a challenge for new resources. *Hydrogeology Journal*, *13*, 148-160.

Bear, J., 1979. Hydraulics of groundwater. McGraw-Hill, New York.

Boswinkel, J.A., 2000. Information Note, International Groundwater Resources Assessment Centre (IGRAC), Netherlands Institute of Applied Geoscience, Netherlands. In: UNEP, 2002 Vital water graphics–an overview of the state of the world's fresh and marine waters. UNEP, Nairobi, Kenya.

Dillon, P., Stuyfzand, P., Grischek, T., Lluria, M., Pyne, R. D. G., Jain, R. C., ... & Sapiano, M., 2019. Sixty years of global progress in managed aquifer recharge. *Hydrogeology Journal*, *27*(1), 1-30.

Döll, P., Hoffmann-Dobrev, H., Portmann, F. T., Siebert, S., Eicker, A., Rodell, M., ... & Scanlon, B. R., 2012. Impact of water withdrawals from groundwater and surface water on continental water storage variations. *Journal of Geodynamics*, *59*, 143-156.

Fakhreddine, S., Prommer, H., Scanlon, B. R., Ying, S. C., & Nicot, J. P., 2021. Mobilization of arsenic and other naturally occurring contaminants during managed aquifer recharge: a critical review. *Environmental Science & Technology*, *55*(4), 2208-2223.

Ford D., Williams, P.W., 2007. Karst hydrogeology and geomorphology. Wiley, Chichester, pp 576

Goldscheider, N., Chen, Z., Auler, A. S., Bakalowicz, M., Broda, S., Drew, D., ... & Veni, G., 2020. Global distribution of carbonate rocks and karst water resources. *Hydrogeology Journal*, *28*, 1661-1677.

Head, D., & Vanorio, T., 2016. Effects of changes in rock microstructures on permeability: 3-D printing investigation. *Geophysical Research Letters*, *43*(14), 7494-7502.

Huerta-Diaz, M.A., and Morse, J.W., 1992. Pyritization of trace metals in anoxic marine sediments. *Geochimica and Cosmochimica Acta*, 56, 2681-2702.

IUCN, 2016. Managing Groundwater Sustainability, ed. M Smith, K Cross, M Paden and P Laban Vol. 11 (Switzerland: Gland).

Konikow, L. F., & Kendy, E., 2005. Groundwater depletion: A global problem. *Hydrogeology Journal*, *13*, 317-320.

Lovelace, J. K., Nielsen, M. G., Read, A. L., Murphy, C. J., & Maupin, M. A., 2020. Estimated groundwater withdrawals from principal aquifers in the United States, 2015. U.S. Geological Survey Circular 1464.

Mazzullo, S. J., 2004. Overview of porosity evolution in carbonate reservoirs. *Kansas Geological Society Bulletin*, *79*(1-2), 1-19.

Moore, C. H., & Wade, W. J., 2013. Natural fracturing in carbonate reservoirs. In *Developments in Sedimentology* (Vol. 67, pp. 285–300). Elsevier.

Ng, K., & Santamarina, J. C., 2023. Mechanical and hydraulic properties of carbonate rock: The critical role of porosity. *Journal of Rock Mechanics and Geotechnical Engineering*, *15*(4), 814-825.

Price, R.E., Pichler, T., 2006. Abundance and mineralogical association of arsenic in the Suwannee Limestone (Florida): Implications for arsenic release during water–rock interaction. *Chemical Geology*, 228(1-3), 44-56.

Pyne, R. David G., 2005. Aquifer Storage Recovery: A Guide to Groundwater Recharge Through Wells, ASR Press, 640 p.

Saller, A. H., Budd, D. A., & Harris, P. M., 1994. Unconformities and porosity development in carbonate strata: ideas from a Hedberg conference. *AAPG bulletin*, *78*(6), 857–872.

US EPA., 2019. Arsenic Rule. Retrieved from http://water.epa.gov/lawsregs/rulesregs/ sdwa/arsenic/ regulations.cfm

CHAPTER 2: PETROLOGICAL AND GEOCHEMICAL FACTORS RELATED TO AQUIFER STORAGE AND RECOVERY FEASIBILITY IN THE EDWARDS AQUIFER TRANSITION ZONE, NEW BRAUNFELS (TEXAS)

2.1. Introduction

Groundwater is a critical freshwater resource in many regions around the world facing challenges due to population growth, changing climate, and economic expansion. The demand for groundwater has significantly risen in recent decades, driven not only by municipal and agricultural needs but also by the growing industrial sector (Boretti and Rosa, 2019). The increasing trend in overexploitation of aquifers has raised concerns about the quantity and quality of groundwater supply (Gorelick and Zheng, 2015). The quality of groundwater particularly has serious consequences for water usage and human consumption (Adimalla and Taloor, 2020), making a thorough understanding of aquifer and groundwater quality assessment essential for sustainable groundwater management.

The region of South Central Texas, including the study area in New Braunfels, is no exception to these challenges. The current semiarid drought-prone climate in the region (Votteler, 2000; National Weather Service, 2022) coupled with the rising water demand and climate change, has led to notable challenges for water resource management. Studies on the consequences of these factors have projected a future annual water demand that exceeds the maximum yearly supply by 2024 in New Braunfels and many other cities along the Balcones Fault Zone of South Central Texas (Nelson, 2018). Providing more than 50% of drinking water consumed by over two million people in South Central Texas, the Edwards aquifer is disproportionately stressed with potential severe socio-economic impact (Sharp and Banner, 1997). Hence, an adequate management strategy is needed to sustain drinking water availability.

Proposed water supply strategies have pointed to an efficient and proven water management alternative, aquifer storage and recovery (ASR), in the saline portion of the Edwards aquifer. The advantages of subsurface storage in expanding water supplies have been well studied and demonstrated (Pyne, 1995; 2005; Bouwer, 2002; Dillon, 2005; Maliva and Missimer, 2010; 2012). Though a small fraction of the stored water is recovered when needed, ASR has proved successful in brackish aquifers by reducing the cost and technical resource requirements. However, the efficient conversion of a seasonally available water supply to a reliable, resilient, and sustainable water resource supply via ASR depends on system-specific hydrogeological and hydrogeochemical conditions (Maliva et al., 2020), which determine the quantity and quality of recoverable water. Hydraulic properties in carbonate aquifers are largely dependent on depositional and post-depositional processes that have operated during aquifer evolution (Hiatt and Kyser, 2000). Indeed, carbonate aquifers tend to have high degrees of heterogeneity due to their relatively high variability in depositional porosity and permeability, and their susceptibility to diagenetic alteration, which can change profoundly the aquifer behavior (Maliva et al., 2002), and affect the development of groundwater resources. Despite extensive investigation in optimization strategies of ASR operations generally using hydrogeological and hydrogeochemical models (Lowry and Anderson, 2006; Ward et al., 2009; Wallis et al., 2011; Antoniou et al., 2015), aquifer matrix petrology has received little attention in guiding the success of aquifer storage and recovery operations. Further, very few studies have focused on the saline portion of the Edwards aquifer (Figure 3.2); many of them (e.g., Lambert et al., 2010; Thomas et al., 2012) mostly investigated the freshwater-saline water transition zone for potential encroachment of saline water into the freshwater zone due to overexploitation of the Edwards freshwater zone. Typically, the saline portion of the Edwards aquifer is not extensively

exploited and studied compared to its freshwater counterparts, partly because its high TDS exceeds drinking water guidelines. Therefore, knowledge of aquifer geochemistry is crucial for the successful implementation of the first ASR pilot test in the saline groundwater portion of the Edwards aquifer. This is especially important in predicting the potential mobilization of trace elements, particularly arsenic (As), which is the most common trace element of concern posing issues in other carbonate aquifers (e.g., the Floridan aquifer, in Florida, U.S.A.; Lower Tertiary sediments of the Port Wilunga Formation, in Adelaide, Australia).

This study aims to characterize the texture and fabric of the Edwards aquifer matrix. The objective is to assess and propose suitable storage zone(s) in the Person and/or Kainer Formations (Fig. 2.1) that can yield a substantial amount of water meeting demand and achieving ASR water supply reliability. Furthermore, mineralogical and paragenetic study provides valuable insights into the main diagenetic processes leading to the development of a good quality aquifer zone (s) or potential storage zone (s), while also identifying processes that would hinder ASR success. Porosity types are assessed in terms of their potential to connect and control permeability and cathodoluminescence (CL) study provides insight into the aquifer matrix by documenting cement phases/generations in relation to porosity and permeability development. Additionally, the study conducts geochemical analyses of the aquifer matrix to enhance understanding of the aquifer mineralogy and infer the fate of geogenic solutes or contaminants during ASR operations. Groundwater geochemistry aids in inferring potential inter-aquifer exchange in the two-layer Edwards aquifer of the study area.

2.2. Study area

The Edwards aquifer is a circa 152-274 m (Hovorka et al., 1995) (Figure 2.1) thick limestone interbedded with dolostone of the Lower Cretaceous Edwards group. The aquifer thickness increases towards the west and south (Maclay, 1995). In addition to being affected by sea-level changes during deposition, the Edwards group experienced changes in large-scale tectonic and hydrodynamic processes in the ancestral Gulf of Mexico, inducing the creation of the Balcones Fault Zone (BFZ) (Sharp and Banner, 1997). The area of study, in New Braunfels, is located within the San Antonio segment of the BFZ (Figure 3.3). The city of New Braunfels straddles Comal and Guadalupe counties, with a major portion of being in Comal County where it is its largest city and county seat.

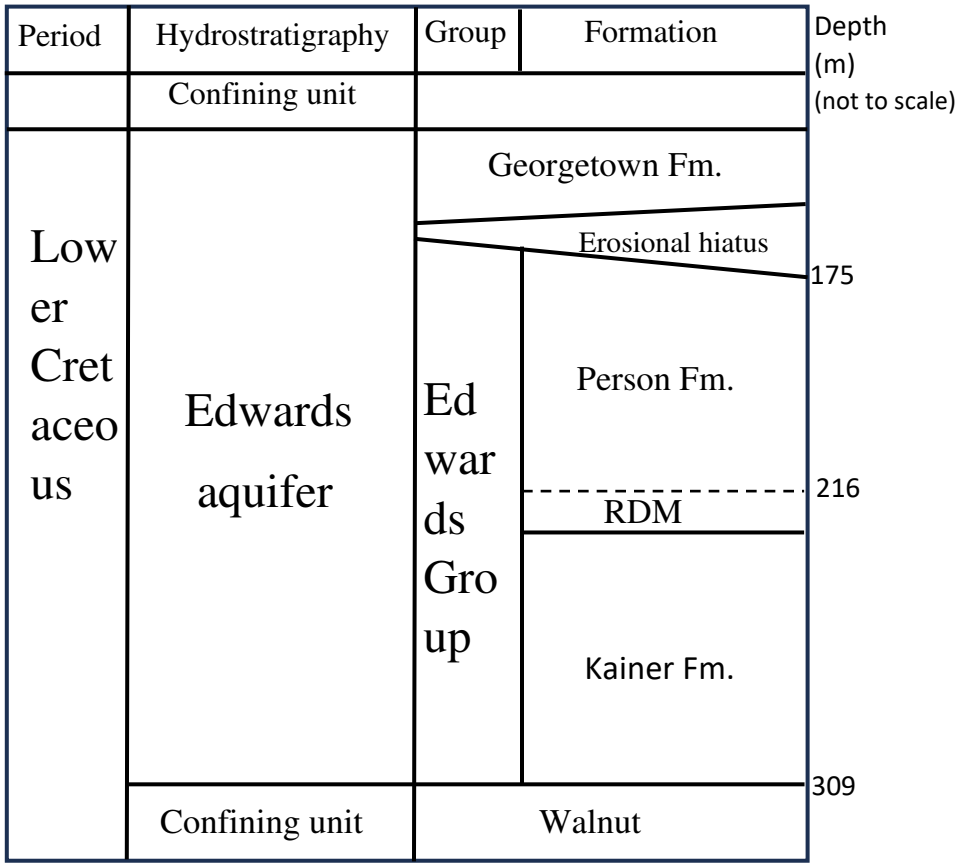

Sampling depth (m)	Sample_ID	Formation
163.5-163.9	C13	Georgetown
166.1-166.5	C11	
166.2-166.5	MI_1	
183.6-183.9	C10	Person
185-185.4	C7	
186.1-186.5	LL21	
188.6-189	C8	
190.6-190.9	C4	
205.3-205.6	MI_2	
216.5-216.7	C9	Regional Dense Member (RDM)
218.9-219.2	C12	
220.9-221.2	MI_3	
222.3-222.6	MI_4	
229.7-230	MI_5	Kainer
230.5-230.8	C2	
241.7-242.1	C3	
251.4-251.7	C1	
268.3-268.6	MI_6	
298-298.3	MI_7	
313-313.3	MI_8	Walnut

Figure 2.1. Hydrostratigraphic column of the NBU ASR well with specific depth ranges of core samples in confining units and aquifer zones in the Edwards aquifer system. Each sample was collected over a range of 0.3m. Samples collected during the first phase (prior to this study) start with initial MI while samples starting with initial "C" and "LL" were collected during the second phase (this study). The corresponding hydrogeologic cross-section is illustrated in Figure 3.1.

The Edwards aquifer was deposited during two marine transgressional events on a low-relief marine platform landward of the Stuart City Reef (Hovorka et al., 1996; Longman and Mench, 1978). Depositional fabrics show a cyclic pattern of sedimentation with dark, argillaceous wackestone to packstone beds defining the base of cycles and serving as low permeability confining units bracketing the two layers of the Edwards aquifer system. The confining layers are in descending order, the Georgetown Formation, the Regional Dense Member (RDM), and the Walnut Formation. The aquifer zones are the Kainer and the Person Formations with thicknesses estimated in the study area at ~95 m and ~46 m (Blumberg et al., 2019), respectively.

Structurally, the Edwards aquifer within the study area in New Braunfels lies within the Miocene-age Balcones Fault Zone that generally trends SW to NE with a general geometry of faults being normal throw, en echelon, and mostly downthrown to the SE with a displacement range from 30 to 244 m (Clark et al., 2016). The mechanical stratigraphy controls the fault propagation process; in less competent clay-rich limestone and dolomite, fault propagation tends to be impeded resulting in faults with shallower dips (60° degrees or less). However, faults in clay-poor, brittle, and competent carbonates are steeper (70° or more) (Young, 1972). The faults extend down into the Ouachita rocks and may transect extensionally reactivated Ouachita faults (Ferrill and Morris, 2008).

Diagenetic processes (dolomitization, calcitization, recrystallization, dedolomitization, etc.) that have overprinted and destroyed distinctive characteristics of the Edwards depositional facies (Barker et al., 1994). In early subaerial exposure of the Edwards, primary porosity was not completely destroyed, and small amounts of secondary porosity formed in the carbonate aquifer.

In the Miocene, the major faulting favored a circulating groundwater system on the upthrown side of the fault, refreshing the aquifer system, and hence creating the freshwater zone with calcite as the major aquifer mineralogy. However, on the downthrown block of the fault (south and east of BFZ), limited "oxidizing" groundwater circulation in restricted faulted blocks enhanced water-rock interaction, increasing groundwater salinity to more than 1,000 mg/l of total dissolved solids (brackish water) in the aquifer system. The badwater (or saline water) zone is characterized by reducing conditions and high TDS (sulfate, chloride, and hydrogen sulfide), and preservation of diagenetic fabrics and mineralogy associated with pre-Miocene time —calcite, dolomite, gypsum, celestite, strontianite, and fluorite (Abbott, 1973). The aquifer rock units in the badwater zone are organic-rich and have lower permeability. Between the freshwater zone and the badwater zone is the transition zone or badwater line. Both the badwater and transition zones are saline with TDS waters exceeding 1,000 mg/L. The position of the badwater zone is controlled by several factors, including the aquifer hydrodynamics and stratigraphy, the aquifer structure, and mixing of basinal brines and waters from underlying units (Sharp and Smith, 2019). The study area is located in the transition zone where structural and diagenetic studies are limited to non-existent. The ASR well, from which the core samples were retrieved during drilling, is adjacent to the New Braunfels regional airport (Figure 2.2).

Figure 2.2. Location of the ASR well in the study area, a 1.067-acre land directly adjacent to the New Braunfels (N.B.) Regional Airport. Treated surface water from the WTP (water treatment plant) is a blend of water sourced from the Guadalupe River and the groundwater from the Edwards freshwater zone. Via an extensive water transmission and distribution system, pipelines transmit water treated from the WTP to the ASR well site.

2.3. Methods

Developing an inventory of petrological, diagenetic, mineralogical, and geochemical characteristics of the aquifer host rocks is one of the critical steps in evaluating site-specific physical and chemical constraints operating during ASR. These factors control the performance of ASR systems in terms of recovery efficiency. The saline zone of the Edwards aquifer is not

extensively used or studied (Sharp and Smith, 2019), hence the paucity of well data in the study area and the need to gather information about the aquifer geology through the thin section and geochemical analyses of rock samples and groundwater during ASR operations.

2.3.1. Aquifer rock and water sampling

Both aquifer intervals (the Person and the Kainer Formations) and confining units have been sampled and characterized petrographically in relation to their potential to store and yield water during ASR operations. Shaly confining unit carbonates of the Georgetown Formation, RDM, and Walnut Formation were sampled to assess their petrographic properties, including abundance and types of porosity and prevalence of fractures.

A total of twenty rock samples were collected at distinct depth intervals and two different periods (Figure 2.1) for geochemical and petrographic analyses from cores retrieved during drilling of the ASR well at the NBU facility property. The first eight core samples were collected in May 2018 by ASR Systems and were prepared and analyzed by Mineralogy Inc. The results of the analysis can be found in Blumberg et al. (2019). The second sampling of twelve core samples was conducted in December 2020 by the author. The first eight-core sample phase will be termed “first phase sampling”, while the additional sampling period of twelve samples will be termed “second phase sampling” so as to differentiate both sample sets. The first phase of sample collection consisted of one sample from the Georgetown Formation, one sample from the Person Formation, two samples from the Regional Dense Member (RDM), three samples from the Kainer Formation, and one sample from the Walnut Formation. The second phase included collection of two additional samples from the Georgetown Formation, five samples from the Person Formation, two samples from the RDM, and three samples from the Kainer Formation.

The second phase samples were specifically collected vertically adjacent to the first phase sampling depths (Figure 2.1) to complement the aquifer characterization and better constrain the vertical heterogeneity of the aquifer textural, fabric, and diagenetic characteristics as related to the assessment of ASR feasibility. The second phase sampling did not collect in the Walnut Formation confining unit because the targeted ASR well was initially planned in the Person Formation. The petrographical and mineralogical study will hence rely on the Walnut photomicrograph from the first sampling phase retrieved from Blumberg et al. (2019).

Core samples of 6 cm in diameter and ~30 cm in length were selected during the first and second phases. While the methodology of the first-phase sampling conducted by Mineralogy Inc. was not fully detailed, the second phase consisted of a full-diameter core that was split into halves. One part served for geochemical analyses while the other part served for petrographic thin section preparation. The twelve second phase samples were sent to Actlabs (Canada) for geochemical analyses, and each had an average weight of 75 grams. Where the samples presented a homogeneous appearance, the pick of the section serving for geochemical and petrographic studies was random. However, where textures were inhomogeneous, a careful choice was made to acquire a sample that would represent the range of variation observed (biota, fractures, change in color). Figure 2.1 gives the number of samples and their depths in meters (not scaled) for the sample collection.

Water quality samples were collected by the consulting firm INTERA (Blumberg et al., 2019), and three wells were used: one ASR well and two monitoring wells (Figure 3.1). The injected water comprised a treated blend of Guadalupe River water and groundwater from wells in the freshwater zone of the Edwards aquifer. Samples of the native groundwater were obtained prior to ASR operations from two monitoring wells, with one penetrating the Person Formation,

and the other penetrating the Kainer Formation. Both monitoring wells, located 50 m apart from the ASR well, were emplaced in separate aquifer zones to investigate the potential inter-aquifer exchange within the Edwards aquifer system. Notably, this study focuses on a selected subset of time series water samples (twenty-four out of forty nine in total as indicated in Supplemental Tables 2.3 and 3.1), specifically those that demonstrate a connection between both aquifer zones during ASR recharge, using the Geochemist's Workbench ternary diagram.

2.3.2. Aquifer rock geochemistry and mineralogy

The twenty rock samples collected for petrographic analysis were also used for geochemical analyses. Analyses conducted on the eight first phase core samples by Mineralogy Inc. and used in this study include gas permeability, helium porosity, and thin section petrographic analyses. Details were not given on the first phase sample preparation or analytical conditions, and hence the results reported in Blumberg et al. (2019) will only be used qualitatively in this study.

Activation Laboratories (Ancaster, Ontario, Canada) conducted bulk geochemical analyses of the twelve samples collected during the second phase. Whole-rock geochemistry of the twelve second phase aquifer samples was analyzed by different analytical methods after fusion with $LiBO_2$ (Code 4B: Lithium Borate Fusion) and dissolution in weak HNO_3 or multiacid, depending on the element targeted for analysis. Trace elements As, Br, Cr, Sb, Sc, and Se were analyzed following multiacid digestion (with a combination of HCl, HNO_3, HF, and $HClO_4$) by instrumental neutron activation analysis (INAA), while Cu, Ni, and Zn analysis used total digestion followed by inductively coupled plasma-mass spectrometry analysis (TD-ICP-MS). Pb and U analysis was performed by fusion mass spectrometry (FUS-MS), and analysis of

S, Pb, SiO_2, Al_2O_3, Fe_2O_3, MnO, MgO, CaO, Na_2O, K_2O, TiO_2, and P_2O_5 by fusion inductively coupled plasma-optical emission spectroscopy (FUS-ICP-OES). Detailed rock preparation and analytical methods are presented on the Activation Laboratories website (*https://actlabs.com/*). Detection limits and analytical methods for the first phase samples were not provided in the Blumberg et al. (2019) report. Matrix correlation was used to infer the mineral phase containing arsenic (element of concern) and other possible trace elements that would be associated with arsenic. Trace elements having lower content than their detection limits were excluded. P values, indicating the level of statistical significance of the observed relationship between trace elements, were calculated using Python code.

2.3.3. Aquifer matrix petrography

Twelve thin sections from samples collected during the second phase were prepared to a 46x27 mm size and 30µm thickness by Spectrum Petrographics Inc. Thin sections for samples from both sampling phases were impregnated with blue-dyed epoxy, stained for calcite and ferrous iron, and polished to be suitable for microprobe, scanning electron microscopy (SEM), and Cathodoluminescence (CL). One thin section photomicrograph with initials M.I. taken from Blumberg et al. (2019) is used to demonstrate the presence of Celestine cement in the Kainer (Figure 2.7.I).

Cathodoluminescence investigation is particularly focused on aquifer zone thin sections from the second phase samples to gain further insight into the diagenetic relationship between grains, matrix cement, and porosity development.

The twelve second phase thin sections were examined to assess grain type, mineralogy, porosity type and evolution, and paragenetic sequence using optical microscopy under plane and

cross-polarized transmitted light at the Colorado State University Department of Geosciences. Cathodoluminescence microscopy was done at the University of Colorado / Boulder, Department of Geological Sciences lab using a Technosyn Luminoscope operating between 12 and 15 kV, with current ranging from 150 to 600 μA, and a vacuum pressure of 50 millitorr.

Point counting was conducted on each of the twelve second phase thin sections to estimate the modal abundance of minerals and pore types using the petrographic microscope. Additionally, porosity types were evaluated in terms of their distribution, architecture, and connectivity. Counts were done along linear transverses, minimizing sampling bias toward a particular feature on thin section samples. Supplemental Table 2.1 and Table 2.2 give the modal abundance of mineral phases and porosity types, respectively.

A range from 511 to 1643 total point counts (mineralogy and porosity types) per sample were made for the twelve thin section samples, which are statistically significant compared to the quoted number of points (250-300) suggested by Tucker (1988). The thin section characterization of carbonate rock type based on matrix content was done using the Dunham classification (Dunham, 1962). Hence, depending on the proportion of grains versus mud, carbonate samples are identified as grainstone, packstone, wackestone, and mudstone.

The modal abundance of pore types is classified according to Choquette and Pray (1970). Based on fabric selectivity, i.e. the configuration of the pore boundary and the position of the pore relative to fabric, the Choquette and Pray classification scheme is divided into fabric selective porosity (interparticle, intraparticle, growth framework, shelter, fenestral, intercrystalline, and moldic), non-fabric selective (fracture, channel, vuggy, and cavern), and fabric selective or not (breccia, boring, burrow, and shrinkage). Where there is a porosity and

fabric dependence relationship, the porosity is fabric selective. If not, the porosity is referred to as not fabric selective (Moore, 1989). Superposition (cement stratigraphy), cross-cutting and abutting relationships, and dissolution and cementation patterns observed from thin section samples are used to infer the most likely relative sequence of diagenetic events in the Edwards aquifer of the study area. Extensive observations based on all twenty first and second phase samples from confining and aquifer zone units are reported in order to yield a reliable sequence of diagenetic events that have impacted the Edwards aquifer.

2.4. Results

2.4.1. Bulk geochemistry

Results on major elements (Table 2.1) show that SiO_2, Al_2O_3, Fe_2O_3(T), and to some extent, K_2O, TiO_2, P_2O_5, and MnO are more abundant in confining units (Georgetown and RDM) than in the aquifer zone formations (Person and Kainer Formations). SiO_2 values range from 0.09 to 0.36 wt% in the aquifer zone while they vary from 3.97 to 6.67 wt% in confining units, Al_2O_3 varies from 0.03 to 0.11 % in the aquifer zone, and from 1.3 % to 1.65% in the confining units, Fe_2O_3(T) varies from 0.4 to 2.9 wt% in confining unit samples to 0.03 to 0.14 wt% in the aquifer matrix samples. CaO and MgO amounts are high in the aquifer zone samples. CaO content varies from 31.3% to 56.1% while MgO content varies from 0.19% to 19.3%. CaO and MgO show a negative correlation coefficient (Table 2.3). Samples C8 and C4 in the Person Formation have the highest % MgO/CaO, followed by sample C3 in the Kainer, sample C7 in the Person, and sample C1 in the Kainer.

The aquifer matrix contents of Se, Co, and Pb are below detection limits. As, Cr, and Sc show higher abundances in confining layers than in aquifer units. However, relatively high

content in Cu is in the RDM confining layer (C12) and the Kainer Formation (C8), U in the Kainer Formation (C1) and Mo in the Georgetown (C11), the Person Formation (C8 and C4), and Kainer Formation (C2 and C3). Bulk rock chemical analyses of arsenic show a range in arsenic concentrations from < 0.5 ppm to 30.9 ppm (Table 2.2). Taking into account only As abundance analyzed in confining unit samples, in Georgetown Formation and RDM, their mean As content is 10 ppm, with the highest As content of 31 ppm in the Georgetown Formation (C11)

Table 2.1. Composition of the Edwards aquifer in major elements.

	Sample ID	Analyte Symbol	SiO_2	Al_2O_3	$Fe_2O_3(T)$	MnO	MgO	CaO	Na_2O	K2O	TiO_2	P_2O_5	Total	Loss of Ignition (LOI)
		Unit Symbol	%	%	%	%	%	%	%	%	%	%	%	%
		Detection Limit	0.01	0.01	0.01	0.001	0.01	0.01	0.01	0.01	0.001	0.01	0.01	—
		Analysis Method	FUS-ICP	FUS-ICP	FUS-ICP	FUS-ICP	FUS-ICP	FUS ICP	FUS-ICP	FUS-ICP	FUS-ICP	FUS-ICP	FUS-ICP	GRAV
Georgetown Fm.	C13	163.5-163.9	3.97	1.39	0.62	0.05	0.41	48.9	0.07	0.16	0.05	0.05	96.2	40.6
	C11	166.1-166.5	5.90	1.56	2.90	0.05	0.42	46.8	0.05	0.20	0.08	0.03	94.0	36.0
Person Fm.	C10	183.6-183.9	0.24	0.09	0.04	0.01	0.19	54.9	0.03	< 0.01	0.00	< 0.01	99.0	43.5
	C7	185-185.4	0.26	0.11	0.14	0.01	5.80	46.9	0.05	< 0.01	0.00	< 0.01	97.2	43.9
	LL21	186.1-186.5	0.09	0.03	0.03	0.01	0.19	56.1	0.02	< 0.01	< 0.001	< 0.01	98.2	41.8
	C8	188.6-189	0.36	0.09	0.07	0.01	19.2	31.3	0.15	0.02	0.00	0.01	96.9	45.8
	C4	190.6-190.9	0.25	0.07	0.07	0.01	19.3	31.6	0.13	0.01	< 0.001	< 0.01	98.1	46.7
RDM	C9	216.5-216.7	4.24	1.30	0.40	0.01	0.75	50.4	0.03	0.22	0.04	0.01	98.3	40.9
	C12	218.9-219.2	6.67	1.65	0.47	0.01	1.66	47.4	0.06	0.17	0.05	0.01	97.9	39.8
Kainer Fm.	C2	230.5-230.8	0.15	0.04	0.04	< 0.001	0.35	54.8	0.02	< 0.01	< 0.001	< 0.01	99.0	43.5
	C3	241.7-242.1	0.09	0.03	0.03	< 0.001	6.90	47.1	0.06	< 0.01	< 0.001	< 0.01	98.6	44.5
	C1	251.4-251.7	0.15	0.06	0.04	< 0.001	4.61	49.5	0.06	< 0.01	< 0.001	< 0.01	98.7	44.3

Table 2.2. Whole-rock chemical analyses of elements (Trace element, Sr, Al, Fe, and C organic carbon) composition of the Edwards aquifer. The average composition of trace elements, Sr, Al, and Fe in sedimentary carbonates was retrieved from Principles and applications of geochemistry (Faure, 1997). Abundance values of Al and Fe are converted from their oxide amounts in Table 2.1.

	Sample_ID	Analyte Symbol	As	Cr	Sb	Sc	Sr	Cu	Zn	U	Al	Fe	S	C-Organic (HCl leach)
		Unit Symbol	ppm	ppm	ppm	ppm	ppm	ppm	ppm	ppm	ppm	ppm	ppm	%
		Detection Limit	0.5	5	0.2	0.1	610	1	1	0.1	—	—	10	0.02
		Analysis Method	INAA	INAA	INAA	INAA	FUS-ICP	TD-ICP	TD-ICP	FUS-MS	—	—	TD-ICP	IR
		Average in carbonates	1.0	11.0	0.2	1.0	610	4.0	20.0	2.2	4200	3300	1200	
Georgetown Fm.	C13	163.5-163.9	9.0	8.0	0.2	1.4	237	1.0	3.0	1.1	7360	4340	3930	0.1
	C11	166.1-166.5	30.9	14.0	0.5	1.7	248	1.0	4.0	1.6	8260	20300	22600	0.1
Person Fm.	C10	183.6-183.9	< 0.5	< 5	< 0.2	0.1	209	< 1	1.0	1.7	476	280	260	0.0
	C7	185-185.4	1.0	< 5	< 0.2	0.1	200	< 1	1.0	1.9	582	980	1350	0.0
	LL21	186.1-186.5	< 0.5	< 5	< 0.2	< 0.1	244	< 1	< 1	1.6	159	210	220	0.0
	C8	188.6-189	< 0.5	5.0	< 0.2	3.6	222	4.0	2.0	0.9	476	490	1930	0.2
	C4	190.6-190.9	0.9	< 5	< 0.2	0.1	196	1.0	2.0	2.0	370	490	1850	0.1
RDM	C9	216.5-216.7	1.3	5.0	0.3	1.0	743	< 1	5.0	1.7	6880	2800	2060	0.1
	C12	218.9-219.2	2.2	10.0	< 0.2	1.4	286	18.0	6.0	1.4	8730	3290	3810	0.1
Kainer Fm.	C2	230.5-230.8	< 0.5	< 5	< 0.2	0.1	184	2.0	1.0	2.0	212	280	610	0.1
	C3	241.7-242.1	< 0.5	< 5	< 0.2	0.1	170	< 1	< 1	2.1	159	210	970	0.1
	C1	251.4-251.7	< 0.5	< 5	< 0.2	< 0.1	175	< 1	< 1	2.5	318	280	660	0.1

From Table 2.3 (matrix correlation) and Figure 2.3, the pattern between As, Fe, and S amounts throughout the aquifer section is similar. They are all enriched in confining units relative to the low concentrations in both aquifer zones. There is a high linear correlation coefficient of As with S, and Fe with correlation coefficients (r) of 0.96 ($p<0.05$) and 0.97 ($p<0.05$), respectively. The highest correlation coefficient of 0.99 ($p <0.05$) is between Fe and S. The correlation between trace elements and Fe and S can be found in Table 2.3. Furthermore, trace elements Cr, and Ni have high correlation coefficient values with Fe, S, and As based on single sample from each sampling depth. However, when considering aquifer zones and confining units separately, it is important to note that the correlation between As, Fe, and S may be lower. Additionally, the presence of low aquifer samples may result in statistically insignificant correlations.

Table 2.3. Correlation matrix of trace elements and major oxides. Co, Se, and Pb were not considered for their content less than their respective detection limits. Correlation coefficient values more than 0.5 and 0.8 are respectively highlighted in gray to dark gray. P values, indicating the level of statistical significance of the observed relationship between Fe, As, and S, are included in the text and were calculated using Python code.

	As	*Br*	*Cr*	*Sb*	*Sc*	*Cu*	*Ni*	*Zn*	*U*	*Sr*	*Al*	*Fe*	*S*	SiO_2	Al_2O_3	Fe_2O_3(T)	*MnO*	*MgO*	*CaO*	Na_2O	K_2O	TiO_2	P_2O_5
As	1																						
Br	-0.10632	1																					
Cr	0.781609	0.111914	1																				
Sb	0.861476	-0.14193	0.747191	1																			
Sc	0.312382	0.492339	0.653214	0.319087	1																		
Cu	-0.04306	0.318341	0.464686	-0.1682	0.348934	1																	
Ni	0.898154	0.072042	0.871363	0.796793	0.473057	0.154845	1																
Zn	0.397527	0.274566	0.805057	0.552454	0.498063	0.62395	0.612017	1															
U	-0.21007	-0.24473	-0.57261	-0.22438	-0.80728	-0.34937	-0.39354	-0.48146	1														
Sr	0.000808	0.005359	0.256695	0.478305	0.160319	0.008967	0.08592	0.598505	-0.15728	1													
Al	0.612179	-0.04444	0.901969	0.722445	0.407784	0.476719	0.747924	0.899954	-0.44256	0.493861	1												
Fe	0.9883	-0.07846	0.816003	0.879426	0.333982	0.032853	0.89575	0.480727	-0.20294	0.094448	0.659812	1											
S	0.982999	-4.5E-05	0.796632	0.836825	0.357295	0.044192	0.887582	0.445708	-0.19171	0.025748	0.603504	0.993418	1										
SiO_2	0.61648	0.007293	0.915753	0.683322	0.412576	0.569439	0.743626	0.916139	-0.41503	0.451686	0.986931	0.678261	0.632787	1									
Al_2O_3	0.612169	-0.0444	0.901973	0.72243	0.407808	0.476735	0.74794	0.899971	-0.4426	0.493853	1	0.659801	0.603495	0.98693	1								
Fe_2O_3(T)	0.988302	-0.07848	0.816013	0.879422	0.333978	0.032869	0.895758	0.480735	-0.20295	0.09444	0.659829	1	0.993416	0.678276	0.659817	1							
MnO	0.836092	-0.15516	0.758941	0.775311	0.352096	-0.04899	0.854146	0.439785	-0.47963	0.051939	0.69513	0.780479	0.744443	0.632411	0.695139	0.780493	1						
MgO	-0.26165	0.870242	-0.22064	-0.34977	0.339153	-0.01785	-0.12184	-0.15665	-0.09142	-0.24286	-0.41942	-0.28019	-0.18914	-0.39507	-0.41938	-0.28021	-0.28166	1					
CaO	-0.00459	-0.91528	-0.11733	0.080356	-0.53215	-0.12744	-0.19866	-0.14431	0.260428	0.133007	0.088211	0.004526	-0.07708	0.066687	0.088164	0.004539	0.003502	-0.93682	1				
Na_2O	-0.06074	0.870399	0.093465	-0.17421	0.575208	0.143124	0.150661	0.065275	-0.33486	-0.23842	-0.1264	-0.09072	-0.01202	-0.11756	-0.12635	-0.09073	0.012172	0.921083	-0.9663	1			
K_2O	0.594052	-0.00883	0.860738	0.802006	0.42676	0.340694	0.709229	0.899275	-0.41979	0.657547	0.9712	0.651258	0.590903	0.945388	0.971197	0.651267	0.65757	-0.3801	0.061956	-0.12507	1		
TiO_2	0.807328	-0.08451	0.94543	0.846937	0.411936	0.332702	0.867921	0.807268	-0.40404	0.378513	0.960352	0.839676	0.794418	0.951576	0.960348	0.839688	0.809321	-0.41988	0.081559	-0.13229	0.935168	1	
P_2O_5	0.650179	-0.11499	0.754719	0.666472	0.494509	0.05981	0.739594	0.491313	-0.59332	0.121252	0.72977	0.593672	0.54831	0.644451	0.729778	0.593691	0.921837	-0.24597	-0.03265	0.100949	0.693208	0.770425	1

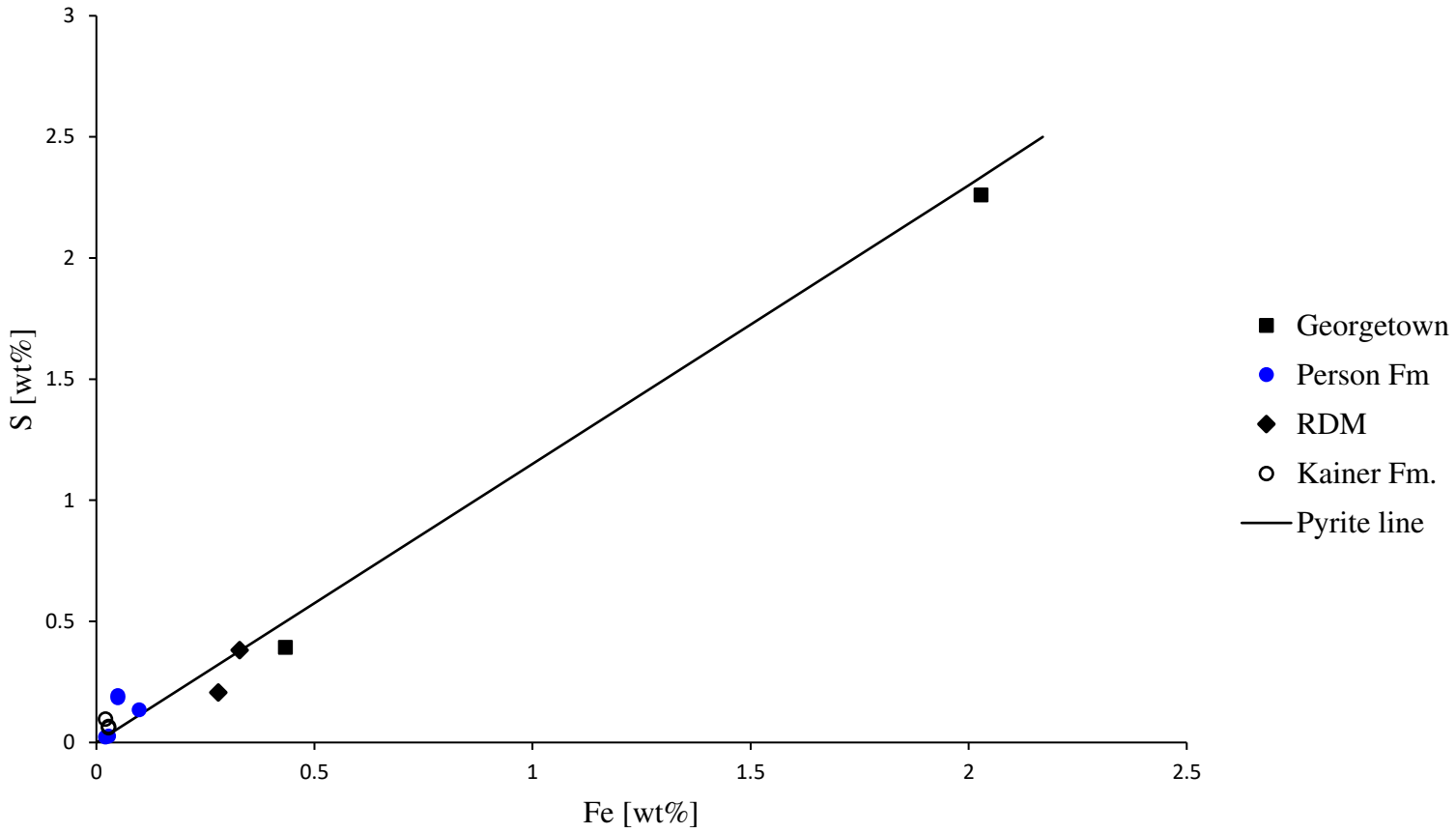

Figure 2.3 Fe versus S of the twelve samples collected during the second phase sampling. Note the good agreement of many of the samples aligning along the pyrite line.

2.4.2. Mineralogy and porosity types point counting

The point count of mineral assemblages is reported in Figure 2.4 and Supplementary Table 2.1. Overall, the mineralogy is dominated by calcite and dolomite. Calcite accounts for nearly all the carbonate in the confining units of the Georgetown Formation and RDM while dolomite occurs in the aquifer units. The accessory mineral phase of chalcedony is also preferentially found in the Georgetown and RDM Formations.

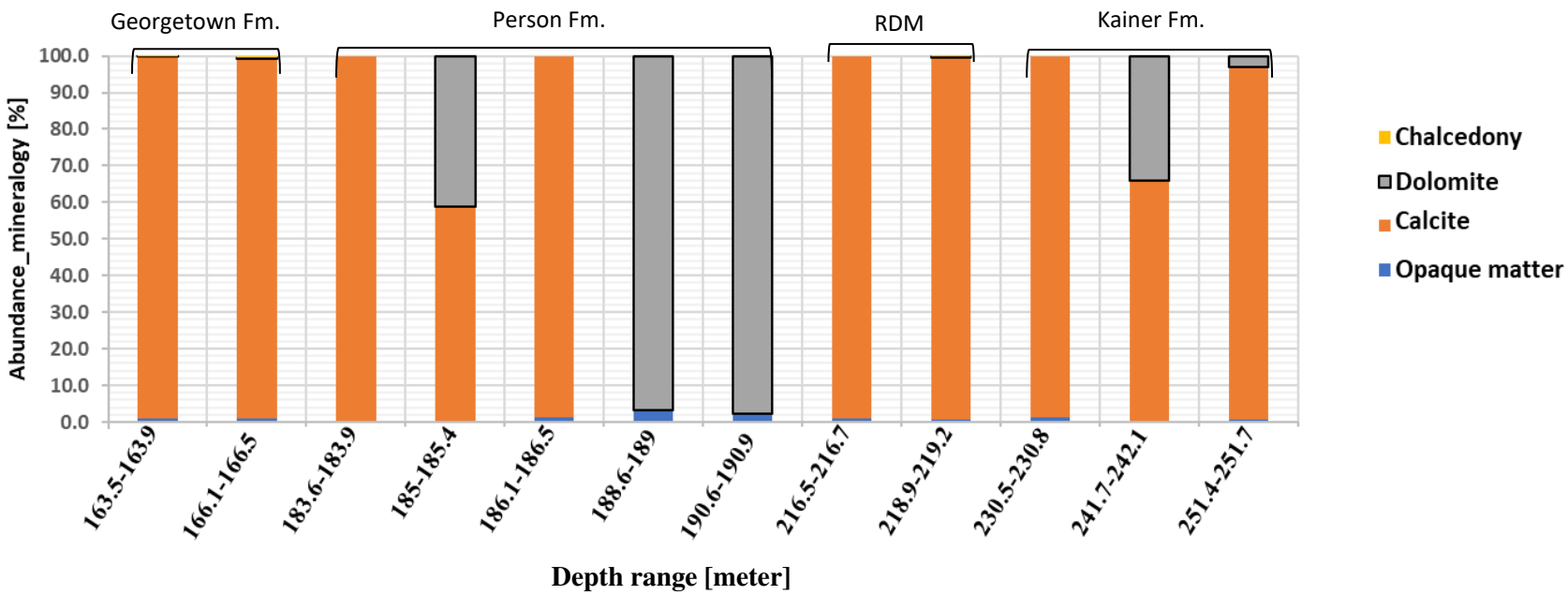

Figure 2.4 illustrates the abundance of mineralogy types in the twelve thin-section samples with calcite and dolomite being the most abundant. Minor chalcedony mineralogy was observed mostly in confining units (RDM and Georgetown Formations). Opaque matter (OM) is sparse in the confining units as well as in the aquifer zone thin-section samples.

Based on point-count analyses of porosity types of the 12 thin sections (Table 2.4), moldic, fracture, vuggy, and intercrystalline porosity types are more common in the Person Formation while interparticle, intraparticle, moldic, fracture, vuggy, and intercrystalline are observed in the Kainer Formation. From 7 to 162 point counts of porosity types were made per sample. Thin section samples dominated by dolomite present higher total porosity values while those from confining layers have fewer porosity types and, where observed, porosity is of fracture type. Figure 2.5 depicts the three main porosity types that tend to either connect to each other or to other types of porosity. The cross plot of porosity versus permeability from Blumberg et al. (2018) shows a positive correlation in the aquifer samples (Figure 2.6).

Table 2.4. Modal abundance of mineralogy and porosity types on thin sections of samples collected during the second phase sampling. Low total porosity is found in confining layer thin section samples of the RDM, and Georgetown Formations, and higher total porosity is in aquifer zones having higher proportions in dolomite and interparticle porosity type.

		sample_ ID	Mineralogy				Porosity type							Total Porosity	Total point counts	Total Porosity [%]
			OM+ opa-que	Calcite	Dolomite	Chalcedony	Interpar ticle	Intrapar tic-le	Moldic	Channel	Fract ure	Vuggy	Intercry stalline			
George-town Fm.	163.5-163.9	C13	10	1141	2	1	0	0	1	0	13	1	0	15	1184	1.27
	166.1-166.5	C11	10	1206	4	6	0	0	0	0	1	0	0	1	1228	0.08
Person Fm.	183.6-183.9	C10	3	728	0	0	0	0	5	0	3	1	4	13	757	1.72
	185-185.4	C7	1	730	302	0	0	1	0	0	0	1	67	69	1171	5.89
	186.1-186.5	LL21	7	511	0	0	0	0	25	0	0	0	1	26	570	4.56
	188.6-189	C8	19	1	555	0	0	0	0	0	20	9	133	162	899	18.02
	190.6-190.9	C4	12	612	13	0	0	0	0	0	48	8	96	152	941	16.15
RDM	216.5-216.7	C9	14	1602	0	0	0	0	0	0	27	0	0	27	1670	1.62
	218.9-219.2	C12	8	1479	5	2	0	0	0	0	5	2	0	7	1508	0.46
Kainer Fm.	230.5-230.8	C2	9	694	0	0	2	6	0	0	1	0	4	13	729	1.78
	241.7-242.1	C3		332	172	0	0	4	0	0	5	0	21	30	564	5.32
	251.4-251.7	C1	3	475	15	0	5	4	2	0	0	1	6	18	529	3.40

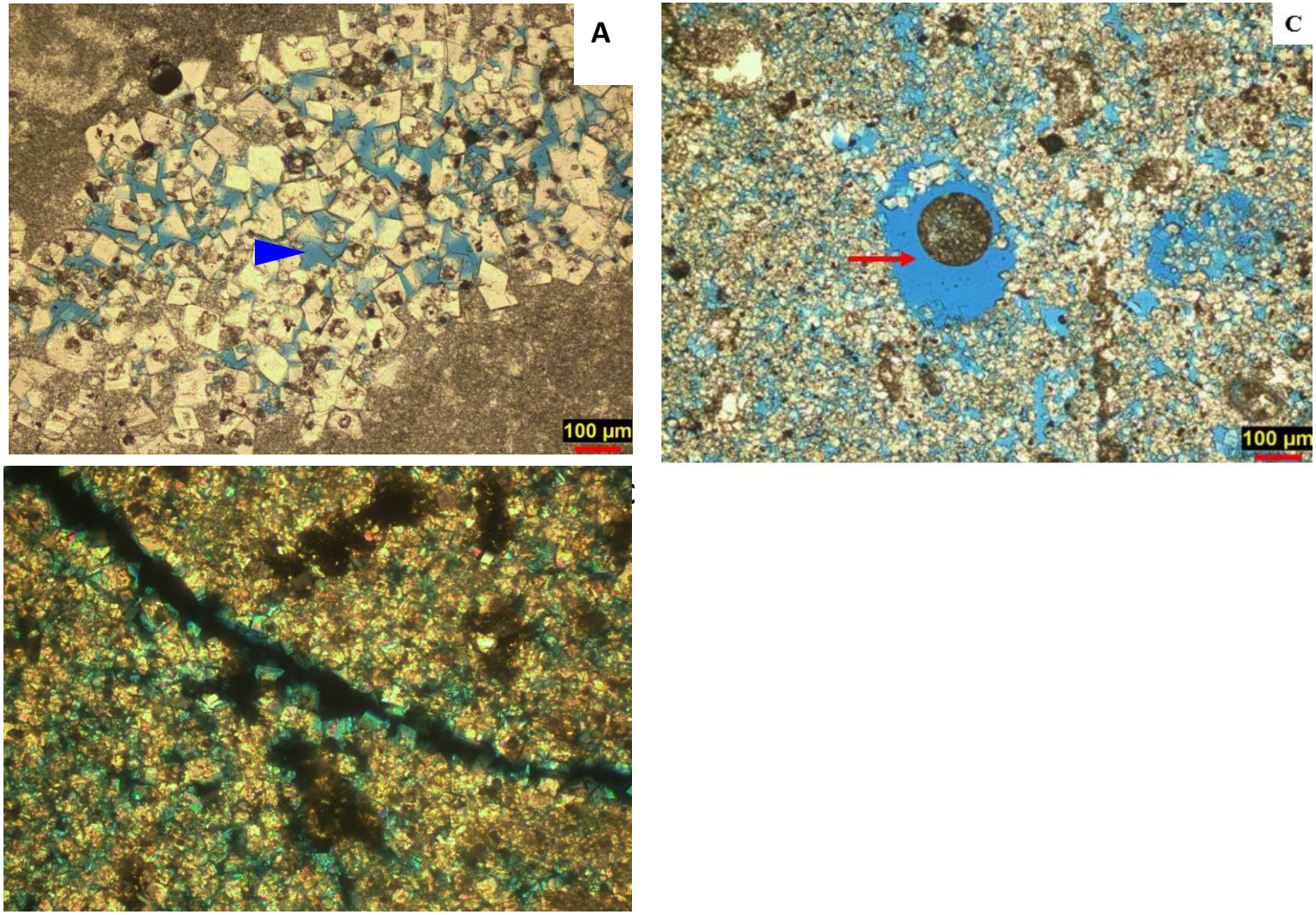

Figure 2.5 illustrates the three main types of porosity that potentially influence the hydraulic property of the Edwards aquifer zone (in some of the thin sections; intercrystalline porosity (blue arrow), vuggy porosity (red arrow), and fracture porosity (white arrows). Sample A was collected at a depth range between 185-185.4 m while samples B, and C were collected between 190.6-190.9 m. (Note that all three photomicrographs were taken with the same scale).

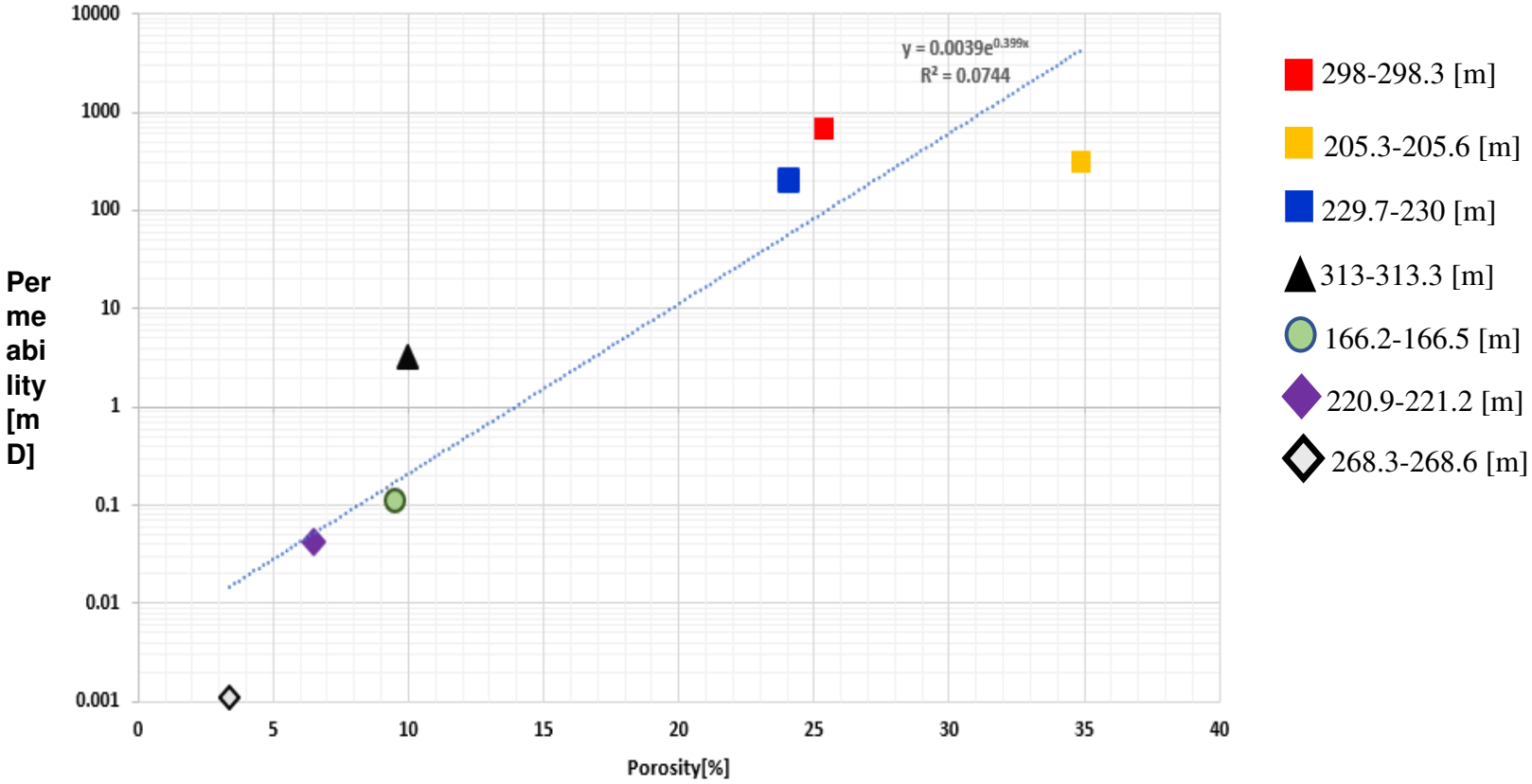

Figure 2.6. Cross plot of porosity versus permeability on seven samples collected during the first phase sampling. Note high porosity and permeability values correspond to dolomitic samples. Core lab analysis on permeability (using N_2 gas) and porosity (using helium) values were conducted by Mineralogy Inc. and reported in Blumberg et al. (2019).

2.4.3. Petrography

In terms of textural features, two confining units, the Georgetown and the RDM Formations, are mostly mud-supported, ranging from mudstone to wackestone (Figure 2.7 A, B, and C), with scarcer packstone. Thin sections in the aquifer sections of the Person and Kainer Formations show skeletal grainstone to packstone textures.

Diagenetic processes examined in twelve thin sections and observations from eight other thin section samples from Blumberg et al. (2019) are described below.

Calcite cementation is widespread and volumetrically abundant in the studied thin sections. Calcite cement fills dissolution features, both interparticle and intraparticle voids (Figure 2.7C). In Figure 2.7C calcite cement encasing the bladed chalcedony cement. Blocky cement type is common in the confining layer samples. Large blocky cement as in Figures 2.7B covers portions of the thin section is pervasively found in the confining unit of the RDM.

Dissolution features are expressed mostly as vuggy porosity (Figure 2.5B), and moldic porosity (Figure 2.7E).

Dolomitization characterizes the aquifer section of the thin section samples of the study area: Figures. 2.7 D, E, and F in the Person, and Figures 2.7 G, H and I in the Kainer. Dolomite grains fill features considered to be either dissolution or fracture-related (Figure 2.7E, Figures 2.5A, and 5B), and appear to be cut by fractures (Figure 2.5C). In one of the thin section samples from Blumberg et al. (2019), patchy replacement of dolomites by celestite is reported (Figure 2.7I) and confirmed by SEM analysis. Cathodoluminescence microscopy shows up to 3 main dolomite zonations with dolomite grain cores in Figure 2.7D having varied responses (or “mottled cores”)

typified by the dark to dark brown and bright colors. Also seen in Figures 2.7E and 2.7F is a dolomite crystal within a pore, exhibiting a perfectly sector-zoned overgrowth. Adjacent dolomite crystals partly or entirely lack the zonation pattern.

The fractures mostly cut the matrix, cement, and allochems (Figures 2.5C and 2.7B). Most fractures, if not all, are open.

Mechanical compaction, while not observed in aquifer layer samples, shows two compactional bending fabrics observed mainly in confining layer samples, especially the Georgetown Formation thin section. The fabric bends at the end of the bioclast in Figure 2.7A is likely due to clay or a micrite-rich fraction.

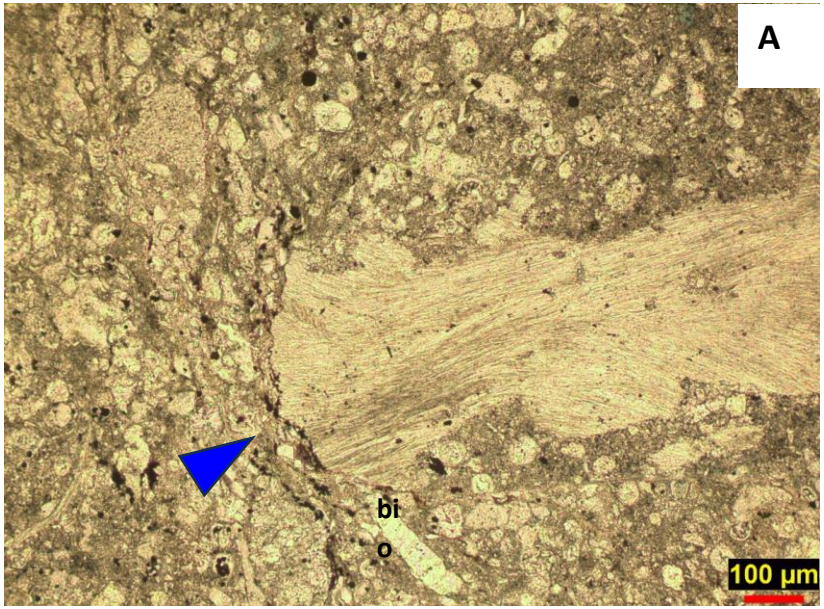
A
bi
o
100 µm

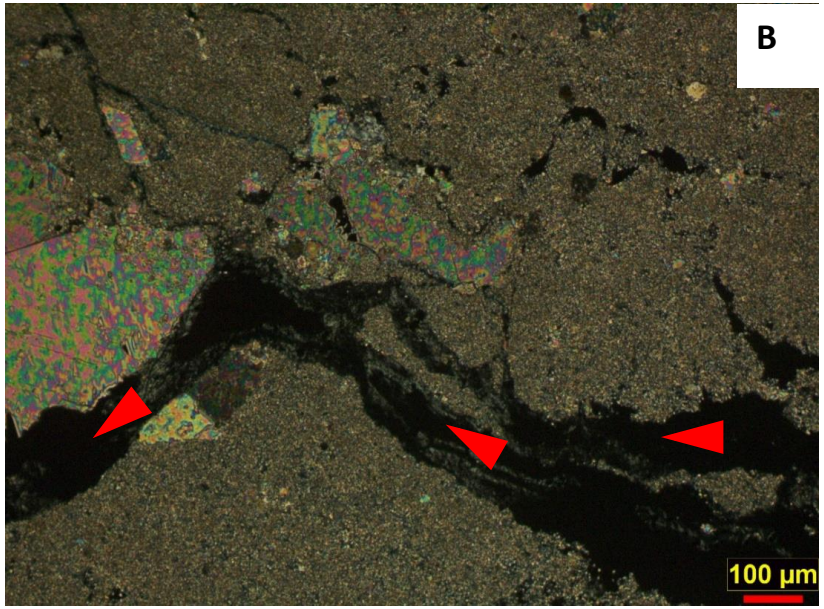
B
100 µm

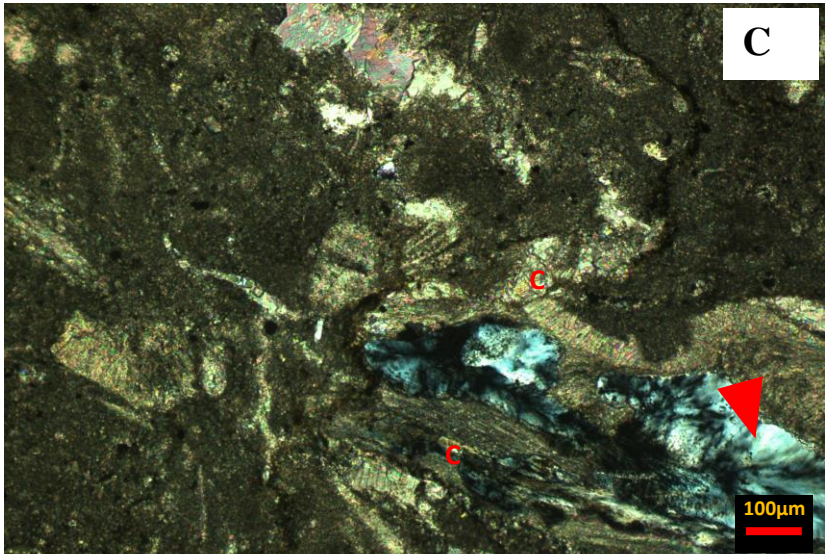
C
C
C
100µm

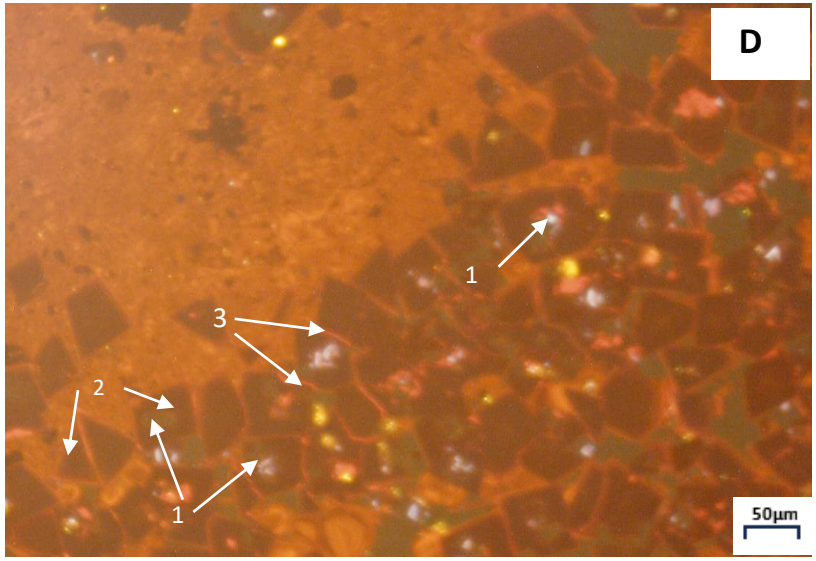
D
1
3
2
1
50µm

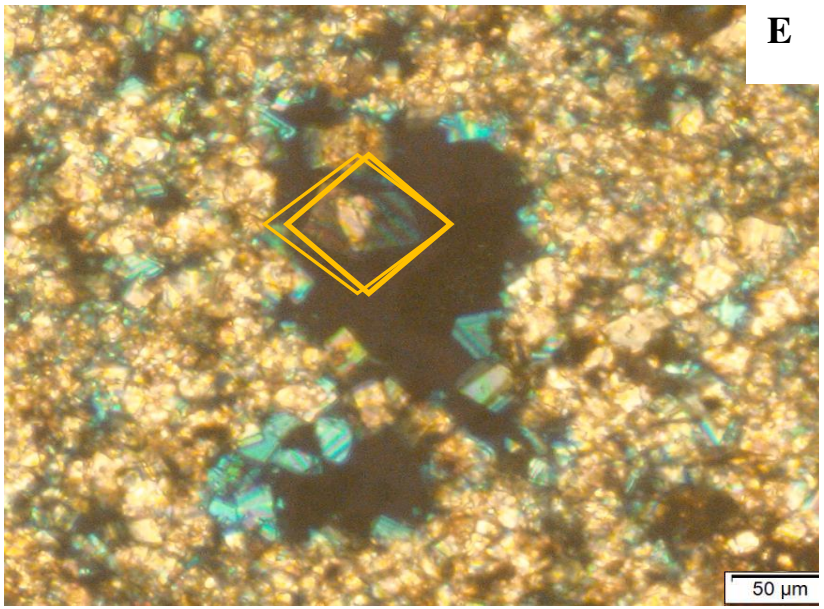
E
50 µm

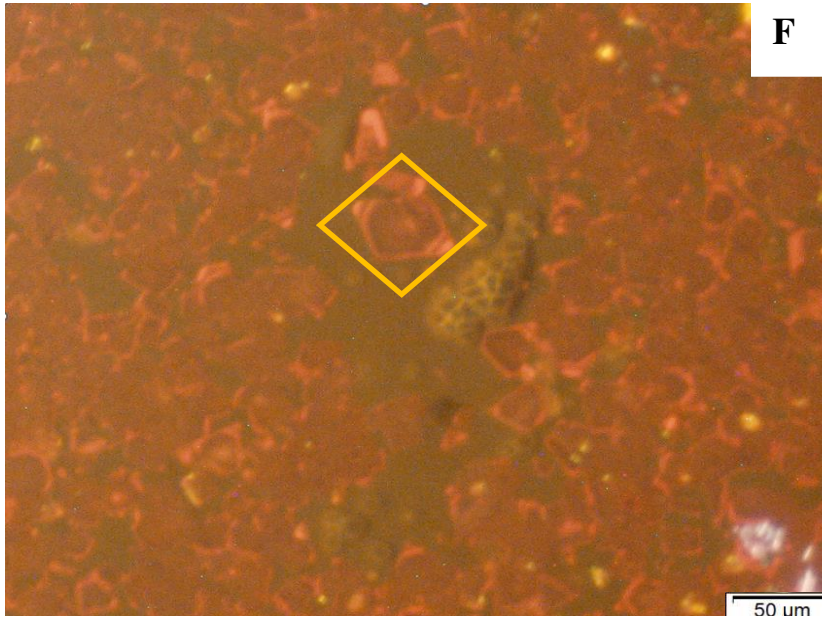
F
50 µm

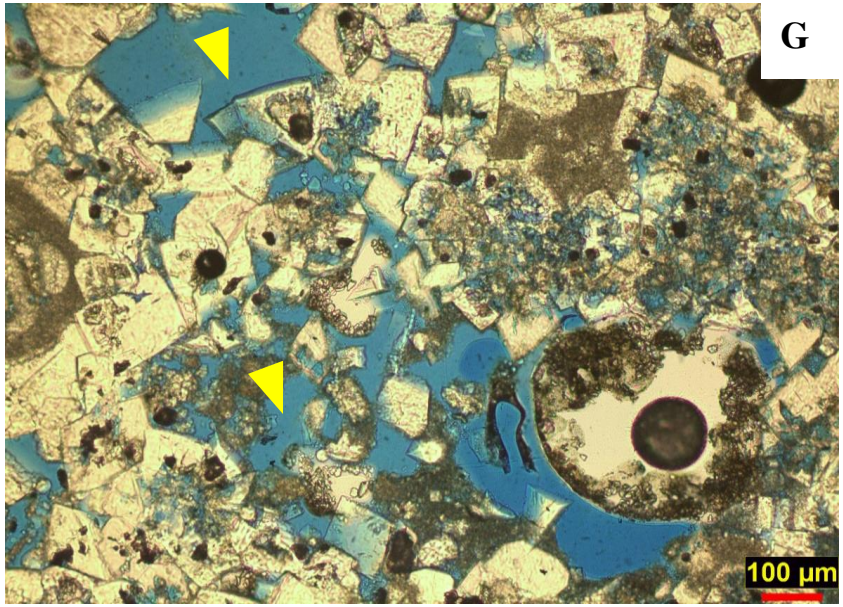
G
100 µm

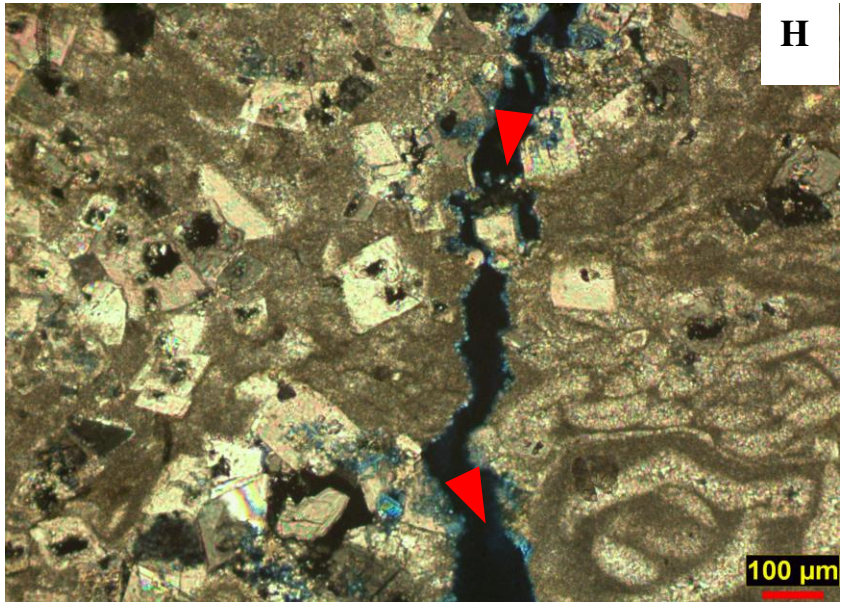
H
100 µm

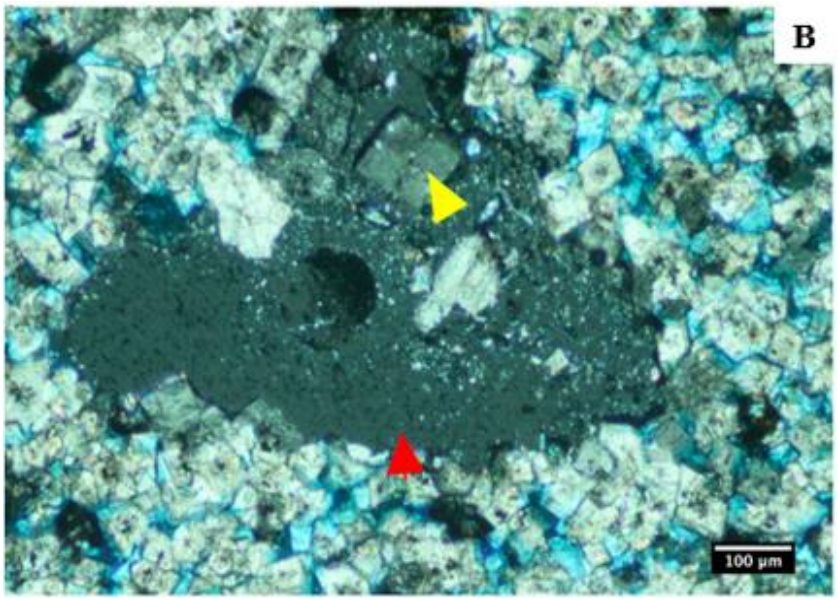

Figure 2.7. **Confining layer photomicrographs**. **A** photomicrograph is from the Georgetown Fm., **B** and **C** cross-polarized light photomicrographs are from the Regional Dense Member. **A**. Mudstone to packstone. Brachiopod shell and a concave-like fabric of matrix (blue arrow) and a partly broken bioclast (bio). The concave fabric evidences a ductile deformation during (mechanical) compaction from burial diagenesis (likely due to high matrix or clay content). Randomly scattered peloids, organic matter, and other bioclasts in the matrix (**Sample C11; depth: 166.1-166.5 m**). **B**. Mudstone with enlarged fractures cutting across the matrix, cement, and grain (red arrows). The coarse calcite crystals may have resulted from nucleation of lime mud (neomorphism). (**Sample C9; depth: 216.5-216.7 m**). **C**. Mudstone with fibrous calcite cement (C) encasing a bladed chalcedony (red arrow). Note the irregular shape of chalcedony cement. (**Sample C12; depth: 218.9-219.2 m**).

Person Formation photomicrographs: D. cathodoluminescence photomicrograph showing 3 zones: (1) mottled cores, (2) dull reddish brown replacive, and (3) pinker cement rims. The cores are inferred to have been poorly ordered dolomite susceptible to selective and varied alterations as evidenced by varied and mottle CL of cores. The final stage cement phase (the pink cement rim) further cementing dolomite grains gives an interlocking texture pattern diagnostic of pore filling dolomite cement. Zones with little (2 and 3) to none (some cores in 1) luminescence tend to have high content in Fe^{2+} (Scholle and Ulmer-Scholle, 2003). Also seen are scattered dolomite grains growing within calcite matrix (**Sample C7; depth: 185-185.4 m**). **E and F** are paired PPL and CL micrographs. The outline dolomite crystal in yellow has grown in pore with the entire CL dolo-zonation from mottled dull reddish-brown core to the late pink cement overgrowth in contrast to most crystals that either partially have the last generation cement (pink cement) or miss it (**Sample C4; depth: 190.6-190.9 m**).

Kainer Formation photomicrographs: G and H. Packstone. Intercrystalline porosity (yellow arrows) in **Figure G** and fracture porosity (red arrows) in **Figure H** with development of

interlocked euhedral to anhedral dolomite crystals in some areas. Note dolomite grains growing in calcite matrix. Fracture porosity in **Figure H** cuts bioclasts, matrix, and dolomite crystals, implying its post-deposition. (**Sample C3: depth: 241.7-242.1 m**). **I.** Dolomitic grainstone. Replacement of dolomite by celestite with preservation of characteristic rhombic dolomite outlines (pseudomorph) occluding secondary intercrystalline porosity and resulting in porosity and permeability reduction of the aquifer. Though there is preservation of intercrystalline porosity in the relict dolomitized zone, celestine replacement combined with interlocked texture would tend to reduce the porosity and permeability. Note the pore-filling celestite cement (red arrow) locally incorporating rhombs of dolomite (yellow arrows) (**Sample MI_6: depth: 268.3-268.6 m**).

2.4.4. Surface water and groundwater

The injectant water is of Ca-Mg-HCO_3 type while the native groundwaters from both the Kainer and Person Formations are of the Na-Cl type (Figure 2.8A). TDS levels in the native groundwater of the Edwards aquifer approach 10,000 mg/L, a concentration typically deemed unsuitable for domestic, agricultural, or industrial use (Warner, 2001). The Na-Cl-HCO_3 ternary diagram (Figure 2.8B) tracing the evolution of hydrochemical facies during recharge shows a) a change from Na-Cl to mixed water types of groundwater in the Kainer Formation, b) a shift from Na-Cl to mixed water types and ultimately to HCO_3 in the ASR and monitoring wells located in the Person Formation, and c) a consistently observed HCO_3 hydrochemical facies type for the injectant water from the NBU system. Chemical analyses of water samples are further described in Chapter 3.

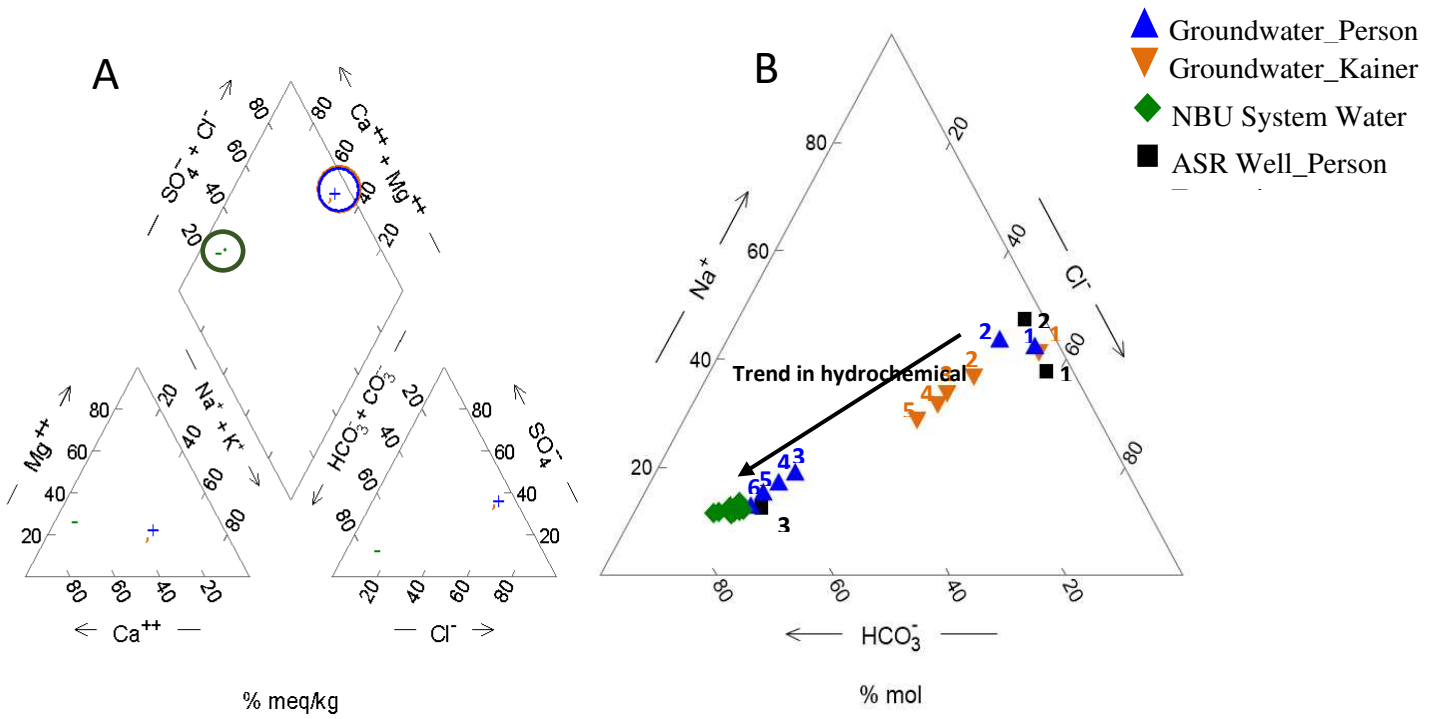

Figure 2.8. A. Piper plot of native NaCl groundwater samples (in red and blue circles) and the $CaMgHCO_3$ injectant sample (in green circle). B. Na-Cl-HCO_3 ternary diagram illustrating the evolution in hydrochemical facies of groundwater in the Person and Kainer Formations during first cycle ASR recharge. The ascending numbers are sequential samples over multiple weeks/months during the period of injection (supplemental Table 2.3) . Note that the injectant water samples maintained their hydrochemical facies field characteristic ($CaMgHCO_3$) throughout recharge time.

2.5. Discussion and interpretation

The higher abundance of dolomite (Figure 2.4) around middle Person and Kainer Formations by point counting is corroborated by increasing MgO % content in C7, C4, and C8 samples in the Person Formation, and C1 and C3 samples in the Kainer Formation. The composition of CaO and MgO specifically in samples C4 and C8 are close to the stoichiometric values of ideal dolomite estimated at 21.7% and 30.4%, respectively. A high negative correlation coefficient as shown in Table 2.3 between CaO and MgO further reflects the dolomitic nature of the carbonates, with % MgO increasing with dolomite abundance. Hovorka et al. (1995) came to the same observation that dolomitization pervades the middle Kainer and middle Person Formations. Hence, dolomitization is somewhat predictable in the Edwards aquifer.

Minor enrichment of SiO_2, Al_2O_3, and to some extent K_2O and TiO_2 in confining layers of the Georgetown Formation and the RDM suggests a modest increase in clay minerals relative to aquifer units, hence tending to possibly affect the permeability and porosity of confining layers. Additionally, the ratio of SiO_2 to Al_2O_3 is a little high in the confining RDM C12 sample for the SiO_2 to be only in clay minerals. Hence, there is likely detrital quartz silt in the RDM that is difficult to identify with optical petrography. These confining units correspond to low-energy cycles deposited in times during which carbonate accumulation rates coincident with flooding were relatively suppressed in favor of argillaceous materials rich in immobile elements (Hovorka et al., 1996).

Based on the high coefficients of correlation between Fe, As, and S (Table 2.3) and with many samples plotting along the pyrite line (Figure 2.3), it is apparent that pyrite is likely the main mineral phase hosting As in the Edwards aquifer and is mostly restricted in the Georgetown

Formation, and RDM. However, Figure 2.3 also shows some samples plotting above the pyrite line, which would suggest modest additional sulfur in the form of H_2S or sulfur in the organic matter (Price and Pichler, 2006), or from thermochemical sulfate reduction of gypsum or anhydrite minerals that are common in the Edwards aquifer. Though the badwater zone of the Edwards aquifer is known to be enriched in organic matter (Deike, 1990), bulk geochemical analyses of the samples in this study indicate limited total organic carbon (%C organic) that could be linked to sulfur availability from organic matter in the aquifer matrix. If available, H_2S would have more likely been scavenged as a result of contact with some iron occurrences in the Edwards aquifer. Furthermore, the data points falling below the pyrite line would indicate that some iron coatings in the carbonate exist and have not come in contact with available sulfide or Fe is available in the form of iron carbonate minerals (siderite). Overall, Fe and S amounts and plots closer to the pyrite line infer a possibility of pyrite as the ideal mineral phase of Fe and S. In reflected light, thin sections mostly from confining units showed scattered traces of brassy to golden yellow color grains, a common feature of pyrite. This does not preclude additional opaque minerals such as hematite, other oxide, minerals, and organic matter commonly found in carbonates. High correlation coefficient values between Cr, Sb, and Ni trace elements and As (Table 2.3) point to their association with As-bearing pyrite.

The bulk geochemistry indicates that very modest amounts of arsenic and other associated trace elements may be available for mobilization into groundwater during aquifer storage and recovery operation. However, these trace elements are most abundant in confining layers (Georgetown Fm. and RDM) which are cased, and even there show only modest concentrations. Conversely, the aquifer sections contain low concentrations in uranium, copper, and molybdenum and if mobilized into groundwater, they are unlikely to reach concentrations of

concern. What is known is that trace elements partitioning into and concentration in the groundwater depend on several factors such as redox and pH conditions, water-rock interaction and timing, the abundance of TE in the aquifer matrix, and the groundwater flow discharge. However, Price and Pichler (2006) posited that the interaction between water and the aquifer matrix containing only few parts per million As in pyrite can remobilize arsenic to concentrations higher than the As maximum contamination level (i.e., 10µg/L). Price and Pichler's hypothesis holds true when there is the possibility of dissolution of arsenic-bearing pyrite promoted by voids, fracture, and channel features rather than isolated pyrite within the limestone matrix (Florida, 2007). Pyrite oxidation and dissolution also increase the risk of groundwater quality deterioration through groundwater acidification inducing calcite dissolution enhanced by the low ionic strength of the injectant water (Descourvieres et al. 2011), and potential increase in porosity.

Understanding the timing of diagenetic processes overprinting initial depositional fabrics of the aquifer is crucial in reconstructing depositional systems and models (Harris, 2009; Hiatt and Kyser, 2000) for a better prediction of aquifer matrix (reservoir) quality and improved aquifer management. The diagenetic history in this study focuses more on the understanding the relative character and timing of diagenetic events to help guide aquifer storage and recovery operations. Unfilled fractures cutting cement and grains indicates fracturing is a late diagenetic event and possibly offered fluid pathways for further dissolution from water-rock interaction as shown by enlargement of fracture aperture (Figure 2.7B). A higher abundance of fractures in dolomitic thin sections (Figure 2.9) of the aquifer zones suggests the possibility that dolomite fractures more readily than calcite (Ahr, 2008) because of higher brittleness. Earlier workers have argued that the Edwards dolomitization is early (Longman and Mench, 1978; Choquette

and Hiatt, 2008) probably forming in the Cretaceous, thus preceding the fracture system. Calcite cementation is likely postdated by chalcedony cementation, though its texture and fabric do not provide much evidence of whether silicification proceeded by replacement or precipitation of silica-rich fluids. Compaction, mostly in confining units, affects cemented matrix and bioclasts (Figure 2.7A). Dissolution reveals a long-lived process during diagenesis of the Edwards aquifer matrix before, during, and after fracturing. Figure 2.10 illustrates and summarizes a likely relative chronology of the complex and overlapping diagenetic processes in the Edwards aquifer as follows: (1) calcite cementation, (2) chalcedony cementation restricted to confining layers, (3) mechanical compaction observed mainly in confining units, (4) dolomitization, (5) fracturing, and (6) dissolution. These paragenetic sequences result from composite observations and interpretation of relative temporal relationships of events in the diagenetic history of the Edwards aquifer in the study area.

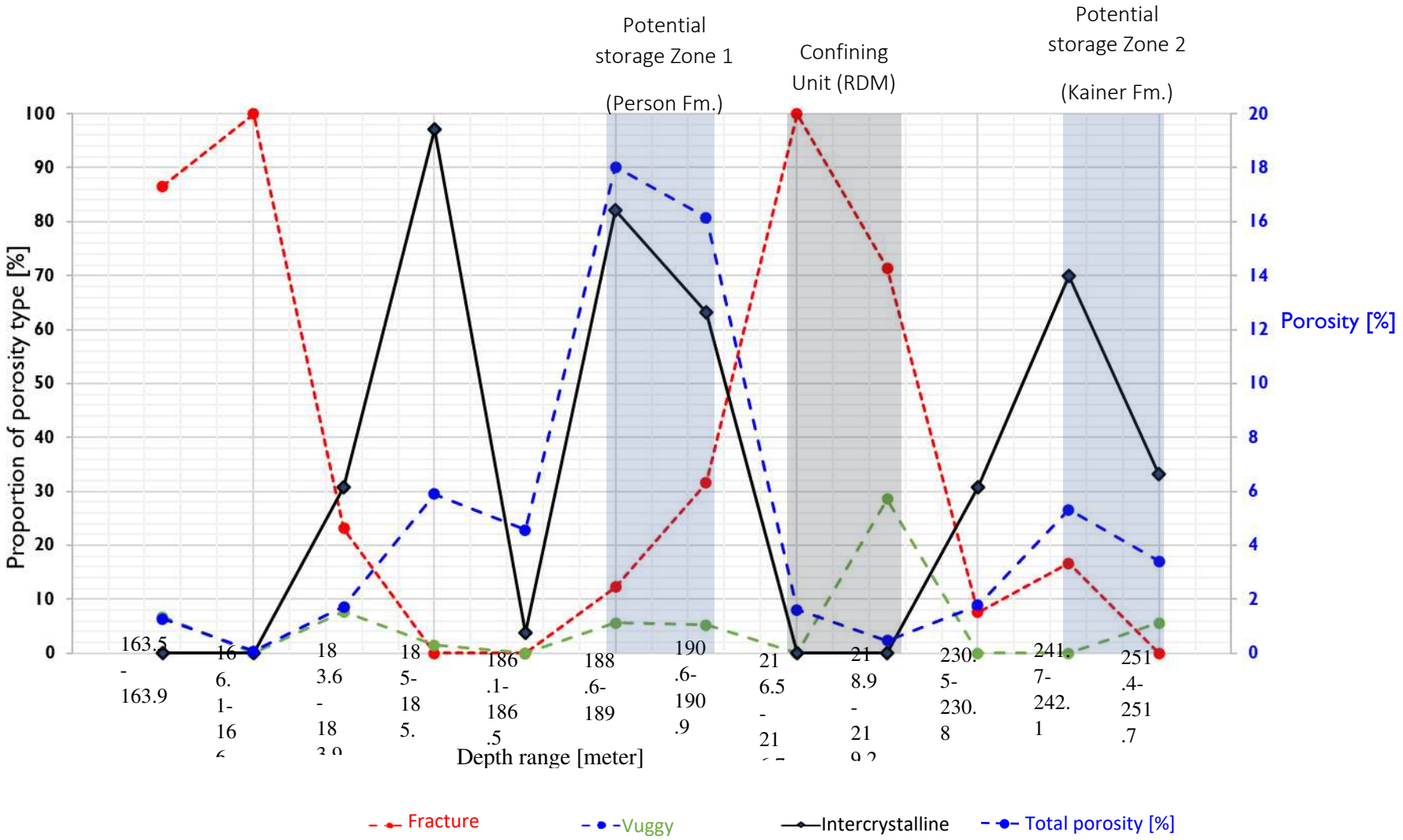

Figure 2.9 illustrates the proportion of the three main porosity types in thin section samples that are hypothesized to control the quality of the potential ASR storage zones in the Edwards aquifer.

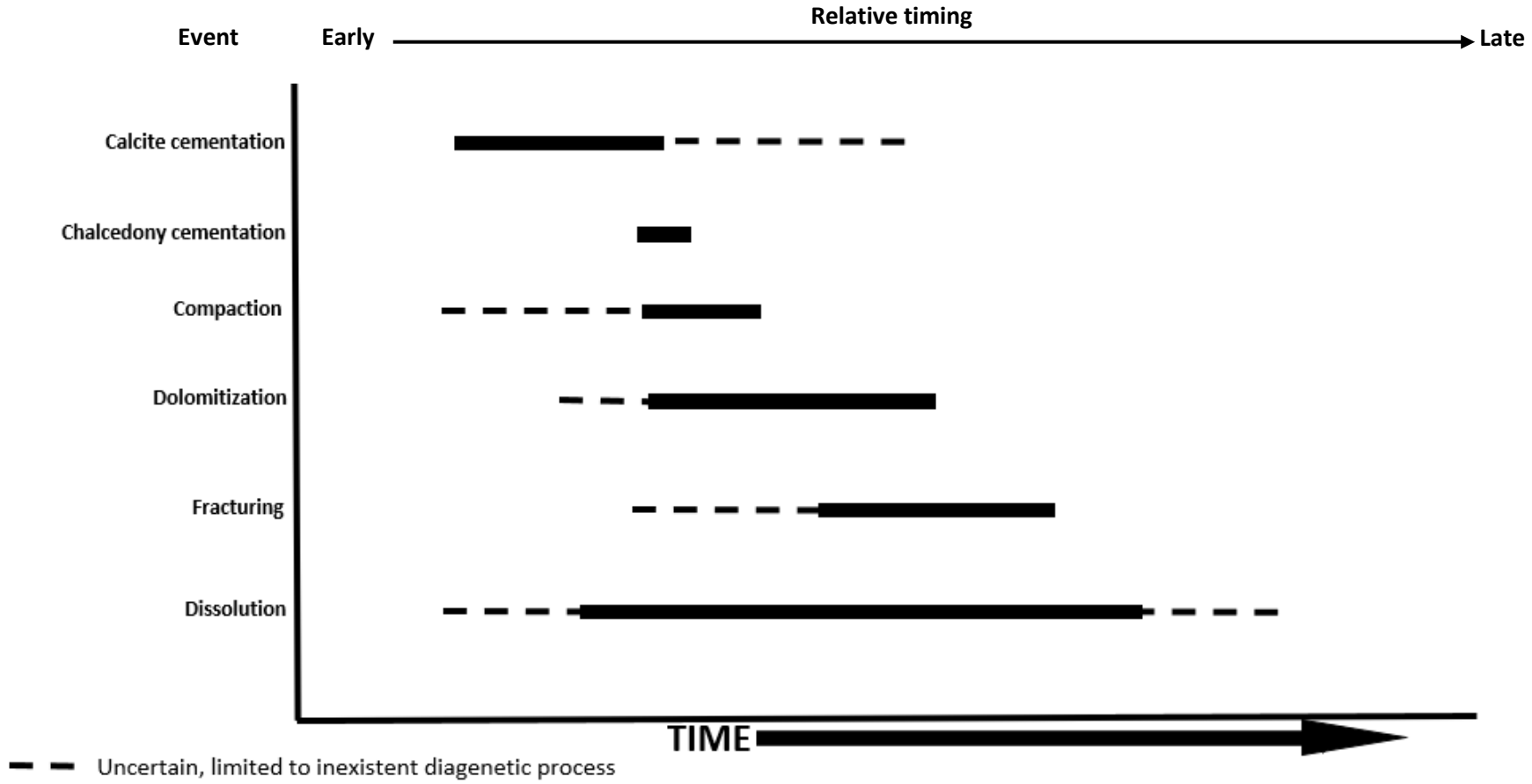

Figure 2.10. Schematic paragenesis of the Edwards aquifer in New Braunfels. Dashed lines represent limited to non-existent clues in constraining diagenetic timing.

From comparing point counting data in Table 2.4 to porosity-permeability core plug data (plotted in Figure 2.6), it can be inferred that dolomitization, fracturing, and dissolution in the Kainer and Person Formations may be the main diagenetic drivers for aquifer development resulting in pore types and networks favorable for ASR storage. The high permeability and porosity following dolomitization result from textural change by the formation of generally well-crystalline rhombohedral dolomite with intercrystalline porosity distribution favoring pore connectivity. This textural pattern is more likely linked to dolomitization in a precursor grain-supported limestone (Figures 2.7E and 2.7F). Additionally, intercrystalline porosity associated with fracture and vuggy porosity types shows a pattern in well-connected porosity distribution that would improve hydraulic property values in some intervals of both aquifer sections. This would explain the high total porosity recorded by point count in dolomitic zones (Table 2.4). In contrast, precursor lime mud likely resulted in intergrown dolomite crystals cemented by calcite or dolomite cement, as evidenced in Figure 2.7D. According to Rose (1972), this type of intergrown dolomite in the Edwards aquifer resulted from physical compaction in still-unlithified lime mud. The interlocking and dense framework of dolomite crystals as in Figure 2.7D together with replacement of dolomite by celestite (Figure 2.7I) have the potential to destroy the porosity and permeability of the aquifer/reservoir. Further, pore filling dolomite cement as in Figure 2.7E contributes to porosity and permeability destruction. The association of celestite with dolomite (Figure 2.7I) is attributed to dolomitization of aragonite or limestone in sabkha environments where Mg-enriched brines react with aragonite to form dolomite and Sr^{2+} ions. The Sr-bearing fluid released from this process would react with gypsum or anhydrite to later precipitate celestite (Wood and Shaw, 197; Illing et al., 1965; Longman and Mench, 1978; Hanor, 2000), obstructing the pore. Furthermore, Sr values (in Table 2.2) indicate that replacement of dolomite

by Celestite probably did not occur on a scale that affected the porosity and permeability of the aquifer.

The intercrystalline porosity, in addition to fracture porosity, and vuggy porosity, would allow a range of transmissivity values that a) is high enough to allow injection and recovery of water at a sufficient rate; and b) low enough to limit the seepage of injected water while maximizing its recoverability. However, the transmissivity translated to conductivity values over a thickness of the aquifer storage zone would need to lie within a range of values dictated by the pumping rate and recoverability percentage (Missimer et al., 2002). As highlighted by Budd and Vacher (2004), while flow dominantly occurs within fractures, matrix permeability mainly defined by connected intercrystalline porosity is critical to aquifer hydraulics. This matrix permeability controls leakage into and out of storage in blocks between fractures.

The confining pressure may reduce the porosity and permeability, but other studies have shown that in addition to the distribution of dolomite crystal grains, dolomitization preserves porosity by creating a rigid framework that inhibits compaction (Machel, 1999; Maliva, 2016) while offering higher connected intercrystalline porosity pattern for high storage capacity and drainage (Warren, 2000). A network of cement overgrowth with a pore water system under hydrostatic to lithostatic pressure has also been evidenced to suppress the compaction in sucrosic dolomite (Choquette and Hiatt, 2008).

While Figure 2.6 suggests a positive correlation between porosity and permeability, it is important to note that the primary and other diagenetic fabrics and textures do not support such a correlation. Porosity types in these cases, primarily moldic, inter-, and intra-particle, are less connected and are predominantly found in mud-rich facies. These facies are commonly

encountered in confining units and aquifer zones closer to confining layers. The dolomitic zone in the interval section of 268.3-268.6 m has low porosity and horizontal permeability that could be related to the interlocked texture of dolomitic crystals, calcite cement. Fracture and vuggy porosity types shown to increase total porosity and permeability in aquifer dolomitic zones are absent to rare in Figure 2.7D suggesting that intercrystalline porosity alone may not have resulted in high porosity and permeability, especially in sections presenting interlocking dolomitic texture. The RDM data point (purple diamond) in Figure 2.6 showing low porosity and permeability values supports the observation of no apparent porosity type in a skeletal wackestone as in the case of the thin section in Figure 2.7A. Nevertheless, the thin section photomicrograph in Figure 2.7B shows fracture porosity type with a large aperture (conduit) that may have been enhanced by dissolution from invasive fluids. If dolomite abundance in the aquifer zones controls fracture porosity, a high abundance of fracture porosity in the RDM thin sections results more likely from high content in mud-supported limestone and an associated minor amount of detrital quartz silt and isolated minor pockets of chalcedony cement. Via fracture pathways limiting RDM effectiveness as a barrier to flow "sealing" the storage zone, there is potential for connecting both aquifer zones of the Edwards with consequences ranging from the seepage of the ASR stored water in the Person during injection (Figure 2.8) and storage or upconing of saline/brackish water from the Kainer Formation into the fresh stored water in the Person Formation during recovery. Inter-aquifer exchange between both the Person and Kainer groundwaters during ASR recharge is suggested by the hydrochemical facies shift from NaCl to mixed type in the Kainer groundwater, the aquifer section not targeted for storage. This calls for an alternative ASR operational strategy utilizing two ASR wells separately implemented in the Kainer and the Person Formations. This option would limit the injection and pumping-induced

gradient, thereby suppressing flow along whatever hydraulic connection exists between ASR storage zones in the Kainer and Person Formations. Additionally, an increase in the ASR water storage capacity can be achieved.

Based on preliminary geological assessments of core supplemented by geophysical log data (Blumberg et al., 2019), a depth interval from 186 to 216 m (in the Person Formation) was chosen to host surface water for the initial ASR operation on which this research project is based. The selection of the target storage zone is supported by the graph of permeability versus porosity of the eight samples from the first phase sampling revealing a high porosity and permeability of the sample collected within that interval, from 205.3 to 205.6 m (Figure 2.6). Point counting of additional samples within the storage zone shows high total porosity of samples from 188.6 m to 190.9 m resulting from intercrystalline, fracture, and vuggy porosity types that would potentially be conducive to high permeability in dolomitic aquifer zones. In addition to the high permeability zone revealed in the Kainer Formation by Blumberg et al. (2019) in the sample collected between 298 m to 298.3 m (Figure 2.6), the point counting of the second phase samples (Table 2.4, Figure 2.6) indicates potential additional dolomitic zones, from circa 241.7 m to 251.7 m that would be proper for ASR storage target. These interval zones show the highest potential as targets for a successful ASR operation based on porosity types and abundance that would yield an acceptable range in hydraulic property values allowing substantial storage and recovery during ASR. Both interval zones assessed from the second phase samples may be extended depending on further characterization of unselected rock samples above and below the sections collected in the Person and Kainer Formations.

Though offering critical insights into aquifer hydraulics and geochemistry, petrological investigation of a limited set of samples and record of effective and non-effective porosities are

likely not adequate for a definitive analysis. Additionally, difference in depositional processes in confining units versus aquifer zones would need to be considered to yield sound petrological interpretations affecting aquifer hydraulics and geochemistry.

2.6. Conclusion

Bulk rock geochemistry supports petrographic observations of dolomite-rich sections preferentially located in aquifer sections of the Person and Kainer Formations. The Georgetown and RDM confining layers are calcite-rich with small amounts of clay minerals. Though arsenic, chromium, antimony, nickel, copper, uranium, and molybdenum do not show substantial enrichment in the Edwards aquifer zones, the confining layers show modestly higher amounts of these elements probably due to their association with shaly facies and organic matter. Being an element of concern in many ASR operations, arsenic was found to be primarily concentrated in pyrite based on the positive correlation between Fe and S and high correlation coefficients between As, Fe, and S. Arsenic is also likely associated with Cr, Sb, and Ni, but their mobilization into the groundwater during ASR activities is minimal because they are present only at very modest concentrations and are largely restricted to the cased sections of confining layers.

Depositional fabric and mainly post-depositional processes are the controlling factors in the final aquifer texture, fabrics, and quality. Permeability, porosity development, and control of the Edwards aquifer quality likely resulted from precursor textural characteristics of the aquifer matrix (grain-supported and mud-supported), which were later overprinted by diagenetic processes. Though subjected to chronologically complex and overlapping diagenetic phases, it appears that dolomitization, together with fracturing and dissolution are the key diagenetic processes favoring aquifer quality for ASR operations.

Thin section observations show that certain porosity types (intercrystalline, fracture, and vuggy) tend to control the final permeability of potentially suitable ASR aquifer zones. However, fractures within the RDM confining layer impede its barrier to flow, connecting both aquifer zones. This is evidenced by the hydrochemical facies shift from NaCl to mixed type in the Kainer groundwater, the aquifer zone not intended for ASR storage. Ultimately, this undermines the feasibility of the ASR single-well operation. Two ASR wells respectively screened in the assessed dolomitic zones of the Person and Kainer Formations would allow improvement of ASR recovery efficiency with water quantity and quality meeting minimum requirements. These findings emphasize the need for a multidisciplinary approach that considers not only hydrogeological and hydrogeochemical investigations but also petrology and geochemistry of the aquifer, to gain comprehensive insights into the aquifer behavior for better management of groundwater resources. Understanding the nature and magnitude of aquifer matrix heterogeneity and geochemistry can help minimize uncertainties and limitations associated with aquifer hydraulics and geochemistry and improve the efficiency and effectiveness of ASR operations.

2.7. References

Abbott, O.L., 1973. The Edwards Limestone in the Balcones fault zone, south-central Texas. Ph.D. Thesis, University of Texas at Austin, Texas, USA.

Adimalla, N.; Taloor, A. K., 2020. Introductory editorial for 'Applied Water Science' special issue: "Groundwater contamination and risk assessment with an application of GIS." *Applied Water Science Journal,* 10, 1-2.

Antoniou, E.A., Van Breukelen, B.M., Stuyfzand, P.J., 2015. Optimizing aquifer storage and recovery performance through reactive transport modeling. *Applied Geochemistry*., 61, 29-40.

Ahr, W.M., 2008. Geology of Carbonate Reservoirs: The Identification Descriptions and Characterization of Hydrocarbon Reservoirs in Carbonate Rocks. John Wiley and Sons, Inc., Hoboken, NJ, USA; pp. 296.

Barker, R.A., Bush, P.W., Baker, E.T., 1994. Geologic history and hydrogeologic setting of the Edwards-Trinity aquifer system, West-central Texas (No.94). *U.S. Geological Survey*: Austin, TX, USA; p.51.

Blumberg, F.M., Deeds, N.E., Pyne, R.D.G., 2019. New Braunfels Utilities: Aquifer Storage and Recovery Demonstration Project. Report prepared for the Texas Water Development Board Contract No. 1600011957; Austin, TX, USA, pp. 362.

Boretti, A., Rosa, L., 2019. Reassessing the projections of the world water development report. NPJ Clean Water, 2(1), 15.

Bouwer, H., 2002. Artificial recharge of groundwater: Hydrogeology and engineering. *Hydrogeology Journal*, 10, 121–142.

Budd, D.A., Vacher, H.L., 2004. Matrix permeability of the confined Floridan Aquifer, Florida, USA. *Hydrogeology Journal*, *12*, 531-549.

Choquette, P.W., Hiatt, E.E., 2008. Shallow-burial dolomite cement: a major component of many ancient sucrosic dolomites. *Sedimentology Journal*, 55, 423-460.

Choquette, P.W., Pray, L.C., 1970. Geological nomenclature and classification of porosity in sedimentary carbonates. *AAPG Bulletin*, 54, 207–250.

Clark, A.K., Golab, J.A., Morris, R., 2016. Geologic framework and hydrostratigraphy of the Edwards and Trinity aquifers within northern Bexar and Comal Counties, Texas: USGS Scientific Investigations Map 3366, 1 sheet, scale 1:24,000, pamphlet, pp. 28.

Deike, R.G., 1990. Dolomite dissolution rates and possible Holocene dedolomitization of water-bearing units in the Edwards aquifer, south-central Texas. *Hydrogeology Journal*, 112(3-4), 335-373.

Descourvieres, C., Prommer, H., Oldham, C., Greskowiak, J., 2011. Water quality changes during aquifer storage and recovery: Quantification of water-sediment interactions and reactive transport modeling. In Proceedings of International Conference on Environmental Science and Development (ICESD 2011).

Dillon, P., 2005. Future management of aquifer recharge. *Hydrogeology Journal*, 13, 313–316.

Dunham, R.J., 1962. Classification of carbonate rocks according to depositional texture. In: Ham, W.E. (ed.), Classification of carbonate rocks. *AAPG Memoir* 1, pp. 108–121.

Ewing, T.E., 1991. The tectonic framework of Texas, with accompanying tectonic map of Texas: Austin. University of Texas, Bureau of Economic Geology, Austin, TX, USA, pp. 36.

Faure, G., 1997. Principles and applications of geochemistry, 2nd edition, Upper Saddle River, NJ, USA, pp. 624.

Ferrill, D.A., Morris, A.P., 2008. Fault zone deformation controlled by carbonate mechanical stratigraphy, Balcones fault system, Texas; *AAPG Bulletin*, 92, 359-380.

Florida, S., 2007. Arsenic Mobilization in Two Suwannee Limestone Aquifer Storage Recovery Systems; Report prepared for the Southwest Florida Water Management District, FL, USA, pp. 120.

Gorelick, S. M., Zheng, C., 2015. Global change and the groundwater management challenge. *Water Resources Research*, 51(5), 3031-3051.

Hanor, J.S., 2000. Barite–celestine geochemistry and environments of formation. Reviews in Mineralogy and Geochemistry, 40(1), 193-275.

Harris, P.M., 2009. Depositional environments of carbonate platforms. AAPG Search and Discovery Article, 60032, 31-60.

Hiatt, E., Kyser, K., 2000. Links between depositional and diagenetic processes in basin analysis: porosity and permeability evolution in sedimentary rocks. In Kyser, K. (ed.), Fluids, and Basin Evolution: Short Course Series Volume 28, Mineral. Ass. of Canada, pp. 63-92.

Hovorka, S.D. Dutton, A.R., Ruppel, S.C., Yeh, J., 1996. Edwards aquifer ground-water resources: Geologic controls on porosity development in platform carbonates, South Texas: Texas Bureau of Economic Geology Report of Investigations 238, Austin, TX, USA, pp. 75.

Hovorka, S.D., Mace, R.E., Collins, E.W., 1995. Regional distribution of permeability in the Edwards aquifer, Report 95-02; Edwards Underground Water District, San Antonio, TX, USA, pp. 128.

Illing, L.V., Wells, A.J., and Taylor, J.C.M., 1965. Penecontemporary dolomite in the Persian Gulf. Soc. Econ. Paleontol. Mineral. Spec. Publ., 13, 89-111.

Lambert, R.B., Hunt, A.G., Stanton, G.P., Nyman, M.B., 2010. Lithologic and physicochemical properties and hydraulics of flow in and near the freshwater/saline-water transition zone, San Antonio segment of the Edwards aquifer, south-central Texas, Based on water-level and borehole geophysical log data, 1999–2007: U.S. Geol. Surv. Scientific Investigations Report 2010–5122, Austin, TX, USA, pp. 69.

Longman, M.W., Mench, P.A., 1978. Diagenesis of Cretaceous limestones in the Edwards aquifer system of south-central Texas: a scanning electron microscope study. *Sedimentary Geology*, 21(4), 241-276.

Lowry, C.S., Anderson, M.P., 2006. An assessment of aquifer storage recovery using groundwater flow models. *Groundwater Journal*, 44(5), 661-667.

Maclay, R.W., 1995. Geology and hydrology of the Edwards Aquifer in the San Antonio area, Texas (Vol. 95, No. 4186). *U.S. Geological Survey*; Austin, TX, U.S.A., pp. 64.

Maliva, R.G., Kennedy, G.P., Martin, W.K., Missimer, T.M., Owosina, E.S., Dickson, J.A.D., 2002. Dolomitization-induced aquifer heterogeneity: Evidence from the upper Floridan aquifer, southwest Florida. *Geological Society of America Bulletin*, 114(4), 419-427.

Maliva, R.G., Manahan, W.H, Missimer, T.M., 2020. Aquifer Storage and Recovery Using Saline Aquifers: Hydrogeological Controls and Opportunities. *Groundwater Journal*, 58, 9–18.

Maliva, R.G., Missimer, T.M., 2010. Aquifer Storage and Recovery and Managed Aquifer Recharge Using Wells: Planning, Hydrogeology, Design, and Operation. Houston, Texas: Schlumberger Corporation. Methods in Water Resources Evaluation; Schlumberger Water Services: Houston, TX, USA, p. 578.

Maliva, R.G., Missimer. T.M., 2012. Arid Lands Water Evaluation and Management. Springer-Verlag Berlin/Heidelberg, Germany, pp. 1076.

Moore, C.H., 1989. Carbonate Diagenesis and Porosity. Elsevier, Amsterdam, pp. 338.

National Weather Service. Drought Information statement South Central Texas. [Online]. Available: https://www.weather.gov/media/ewx/ewx-drought.pdf (Accessed on 15 May 2022).

Nelson, R., 2018. NBU examines the future of water in New Braunfels, releases 20-year plan. Community Impact Newspaper. 17 July 2018. [Online]. Available: https://communityimpact.com/environment/2018/07/17/nbu-examines-the-future-of-water-in-new-braunfels/ (Accessed on 20 July 2021).

Price, R.E., Pichler, T., 2006. Abundance and mineralogical association of arsenic in the Suwannee Limestone (Florida): Implications for arsenic release during water–rock interaction. *Chemical Geology*, 228(1-3), 44-56.

Pyne, R.D.G., 1995. Groundwater Recharge and Wells: A Guide to Aquifer Storage Recovery, 1st ed. CRS Press. Boca Raton, FL, USA, pp. 400.

Pyne, R.D.G., 2005. Aquifer Storage Recovery: A Guide to Groundwater Recharge Through Wells, 2nd ed. ASR Systems, Gainesville, FL, USA, pp. 640.

Rose, P.R., 1972. Edwards Group, surface, and subsurface, central Texas: University of Texas at Austin, Bureau of Economic Geology Report of Investigations, 74.

Scholle, P.A., Ulmer-Scholle, D.S., 2003. A color guide to the petrography of carbonate rocks: grains, textures, porosity, diagenesis, AAPG Memoir 77, Tulsa, Oklahoma, USA, pp. 474.

Sharp, J.M. Jr., Banner, J.L., 1997. The Edwards aquifer: A resource in conflict. *Geological Society of America*, 7, 1-9.

Sharp, J.M., Smith, B.A., 2019. Water quality and the bad-water (saline-water) zone of the Edwards (Balcones Fault Zone) Aquifer. In Sharp, J.M., Jr., Green, R.T., and Schindel, G.M. (eds.), The Edwards Aquifer: The Past, Present, and Future of a Vital Water Resource. *Geological Society of America*, Memoir 215, pp. 149–158.

Thomas, J.V., Stanton, G.P., Lambert, R.B., 2012. Borehole Geophysical, Fluid, and Hydraulic Properties Within and Surrounding the Freshwater/saline-water Transition Zone, San Antonio Segment of the Edwards Aquifer, South-central Texas, 2010-2011. *U.S. Geological Survey Scientific Investigations Report* 2012–5285, Austin, TX, USA, pp. 65.

Tucker, M.E., 1988. Techniques in sedimentology. Blackwell Scientific, Oxford, USA, pp. 482.

Votteler, T.H., 2000. Drought: Drought Is a Normal Condition in Texas. The Great Drought of the 1950s May Have Been Just a Taste of What's to Come. Texas Parks & Wildlife, Austin, Texas, USA, 58, pp. 16- 25.

Wallis, I., Prommer, H., Pichler, T., Post, V., B., Norton, S., Annable, M.D., Simmons, C.T., 2011. Process-based reactive transport model to quantify arsenic mobility during aquifer storage and recovery of potable water. *Environmental Science & Technology Journal*, 45(16), 6924-6931.

Ward, J.D., Simmons, C.T., Dillon, P.J., Pavelic, P., 2009. Integrated assessment of lateral flow, density effects, and dispersion in aquifer storage and recovery. *Journal of Hydrology*, 370(1-4), 83-99.

Warner, D.L., 2001. Technical and Economic Evaluation of the Protection of Saline Groundwater Under the Safe Drinking Water Act and the UIC Regulations. Report prepared for Groundwater Protection Council.

Young, K., 1972. Mesozoic history, Llano region. In Barnes, V.E., Bell, W.C., Clabaugh, S.E., Cloud, P.E., Jr., McGehee, R.V., Rodda, P.U., and Young, K. (eds.), Geology of the Llano region and Austin area, field excursion: Austin, University of Texas, Bureau of Economic Geology Guidebook 13, Texas, USA, pp. 154.

Ward, J.D., Simmons, C.T., Dillon, P.J., Pavelic, P. 2009. Integrated assessment of lateral flow, density effects, and dispersion in aquifer storage and recovery. *Journal of Hydrology*, 370(1-4), 83-99.

Warner, D.L. (2001). Technical and Economic Evaluation of the Protection of Saline Groundwater under the Safe Drinking Water Act and the UIC Regulations. Report prepared for Groundwater Protection Council. Google Scholar

Wood, M.W., Shaw, H.F. 1976. The geochemistry of celestites from the Yate area near Bristol (U.K.). *Chemical Geology*, 17, 179-193.

Young, K., 1972. Mesozoic history, Llano region. In Barnes, V.E., Bell, W.C., Clabaugh, S.E., Cloud, P.E., Jr., McGehee, R.V., Rodda, P.U., and Young, K. (eds.), Geology of the Llano region and Austin area, field excursion: Austin, University of Texas, Bureau of Economic Geology Guidebook 13, Texas, USA, pp. 154.

CHAPTER 3: HYDROGEOCHEMICAL EVALUATION OF AQUIFER STORAGE AND RECOVERY IN EDWARDS AQUIFER, NEW BRAUNFELS, TEXAS

3.1. Introduction

Aquifer Storage and Recovery (ASR) involves the recharge of freshwater into suitable aquifer section(s) during times when freshwater is in excess and later recovery of the injected freshwater via the same well during times of peak demand or emergency need (Pyne, 1995). Three phases form each ASR cycle: (a) the recharge phase corresponding to excess freshwater availability, (b) the storage phase covering periods of sufficient freshwater availability, and (c) the recovery phase initiated during a decrease in freshwater supply relative to water demand (Li et al., 2022). Water stored in a targeted aquifer zone during ASR can be sourced from several types of water bodies such as rivers, lakes, reclaimed water, or even water from an adjoining aquifer (Lowry and Anderson, 2006). Water stored in aquifers, in contrast to surface water reservoirs, is safe from evaporation over a larger storage reservoir with greater storage capacity (Kocis et al., 2017; Scanlon et al., 2016). With the advantages offered by ASR, it is increasingly being regarded as a reliable technology providing sufficient storage capacity for freshwater to meet increasing water demand (Maliva and Missimer, 2010). For drinking water supplies, ASR has seen increased use in the USA, Europe, the Middle East, and Australia (Gerges et al., 2020; Maliva et al. 2005; Pyne 2005; Kresic, 2006; Maliva and Missimer, 2010; Miotlinski et al., 2014) to maintain, enhance and secure seasonally or intermittently excess water for a sustainable supply of freshwater (Dillon et al., 2019). An estimated 30% of ASR systems are located in brackish to saline aquifers (Pyne, 2005), providing improved sustainability of water management strategies in areas having seasonally available excess water even in high total dissolved solids (TDS) groundwater systems. However, in all managed aquifer recharge (MAR) techniques, two key

factors are considered: *recovery efficiency*, which assesses the water volume recovered relative to the stored amount, and *the quality of the recovered water compared to the recharged water* (Miotlinski et al., 2014). Both quality and quantity parameters significantly influence water resource availability (Evenson et al., 2013). While it is difficult to maximize the quantity and quality of groundwater recovered in brackish aquifers (Culkin et al., 2008), ASR technology offers operational benefits in improving recovery efficiency (Maliva et al., 2020). One operational methodology consists of creating a zone of stored water of substantial volume in ASR wells early in the cycle testing process and maintaining it through each subsequent cycle. According to this ASR operational strategy, the excess "injected" water mixes with native groundwater to act as a buffer (buffer zone). Hence, knowledge of the geochemistry of the injectant, geochemistry of the native groundwater, aquifer hydraulic properties, and heterogeneity is critical in assessing the extent to which hydrogeochemistry controls ASR operational feasibility.

With increasing water demand and increasing trend in hydrologic extremes in Texas (U.S.), the Texas Water Development Board (TWDB) conducted feasibility studies to find new water supplies or enhance water availability via new storage methods. In terms of hydrogeological suitability for ASR, the Edwards aquifer is one of the four major Texas aquifers that indicated high suitability for ASR operation (Shaw et al., 2020; Smith et al., 2017). ASR project is being implemented in the Edwards aquifer in New Braunfels (Figure 3.1), one of the fastest-growing U.S. cities, for additional and sustainable sources of water. New Braunfels sits above the portion of the Edwards aquifer called the badwater zone due to its elevated salinity of over 1,000 mg/L total dissolved solids (TDS) (Sharp and Smith, 2019). This research is based on an ASR project aimed at diverting and injecting freshwater (river water and groundwater from the freshwater

zone of the Edwards aquifer) into the badwater zone of the Edwards aquifer in New Braunfels. The ASR project is being implemented in three phases: the first phase targets recovery of 6,819 m^3/day for 70 days. The second phase targets recovery of an estimated 15,911 m^3/s, and the third phase targets 40,915 m^3/s. The third phase target of 40,915 m^3/s for 210 days is based on a possible repeat of the 1950s drought of record during which the longest period of virtually no rainfall was seven months. This study documents the feasibility of ASR operations in the brackish portion of the Edwards aquifer based on the hydrogeochemical characteristics of the groundwater system and its evolution. The study is based on data from the first ASR phase targeting a recovery volume of 1.5 million gallons per day (MGD) for 70 days. However, the 1.5 MGD targeted recovery volume and the length of recovery time were not met upfront because of limited hydrogeological knowledge of the ASR site. Additionally, this study explores the geochemical processes (mixing, water-water, and water-rock interaction) that might have affected the groundwater geochemistry during the first cycle recharge and storage time. Simulation of water-water and water-rock interactions further helps estimate the extent to which the aquifer hydraulic properties might be impacted during ASR operations. Additionally, transport modeling is used to estimate the hydraulic properties of the Edwards aquifer and ultimately assess the optimum ASR recovery rate. This study is of significant importance because this part of the Edwards aquifer has a paucity of hydrogeological data and limited usage due to the brackish/saline nature of the aquifer.

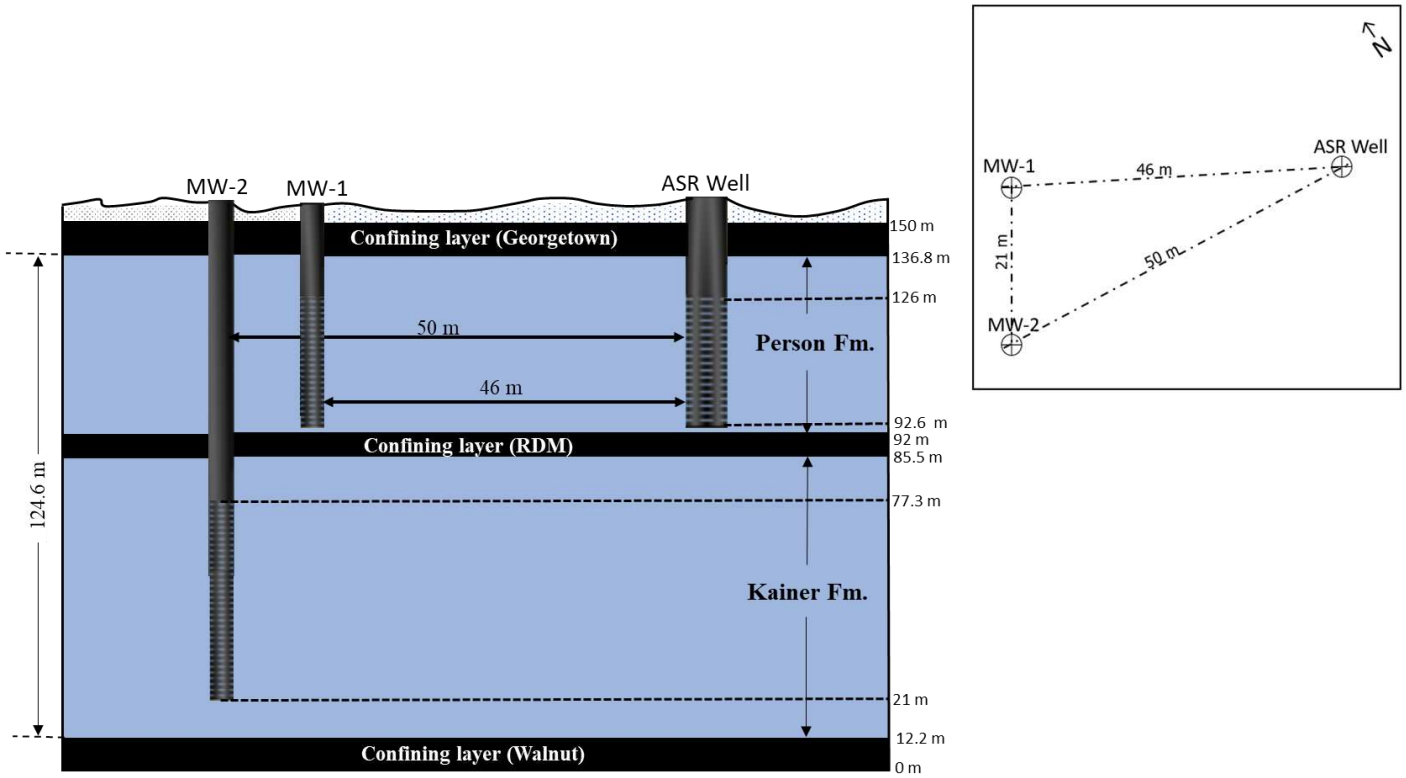

Figure 3.1. Hydrogeologic cross-section and plan view of the New Braunfels ASR project, illustrating the cased and open interval sections of the ASR and monitoring wells. ASR Well latitude/longitude: 29°42'17.10"N/ 98° 3'12.20"W.

3.2. Hydrogeologic setting

The Edwards aquifer is the sole source aquifer for two million people in South-central Texas, including the city of New Braunfels (Sharp and Banner, 1997; Hovorka et al., 1998; Smith et al., 2005; Wong et al., 2014). Water from the Edwards aquifer is used in agriculture, industry, recreation, municipal purposes, and in sustaining rare and endangered species that depend on spring flows at San Marcos Springs and Comal Springs (in New Braunfels) (Edwards aquifer authority, 2012b; Schindel, 2019).

Carbonate rocks of the Edwards aquifer in the vicinity New Braunfels were deposited in Early Cretaceous time in the shallow subtidal to tidal flat marine San Marcos platform developed behind the shelf-edge Stuart City reef (Rose, 1972; Sharp, 1997). Cretaceous depositional processes resulted in variable rock fabrics with a stacked pattern of beds of distinctive properties mapped as formations and hydrostratigraphic zones (Lindgren et al., 2004). The Edwards aquifer comprises the Kainer Formation, the Person Formation, and the overlying Georgetown Formation (Maclay and Small, 1983; Barker et al., 1994; Maclay, 1995). Hydrostratigraphically, the Edwards Group is subdivided into eight informal hydrogeologic subdivisions comprising the four members of the Kainer Formation, the three members in the Person Formation, and the Georgetown Formation (Hanson and Small, 1995). Both the Kainer and Person Formations have estimated thicknesses of 73.3 m and 51.3 m, respectively, with a 6.5 m thick Regional Dense member (RDM) confining layer separating the two aquifer zones (Figure 3.2). The Edwards aquifer lies within and is associated with the Balcones Fault Zone, a major structural system of predominantly down-to-the-southeast normal faults with a net displacement of 610 m (Maclay and Small, 1986).

The petrography of the Edwards aquifer reveals high dolomitic sections predominantly situated within the aquifer sections of the Person and Kainer Formations, supported by bulk rock geochemistry. Confining layers, such as the Georgetown and RDM formations, exhibit a calcite-rich composition with traces of clay minerals. Depositional fabric and subsequent diagenetic processes, including dolomitization, fracturing, and dissolution, significantly influence the aquifer's texture and quality, making it favorable for Aquifer Storage and Recovery (ASR) operations (see Chapter 2 for detailed analysis).

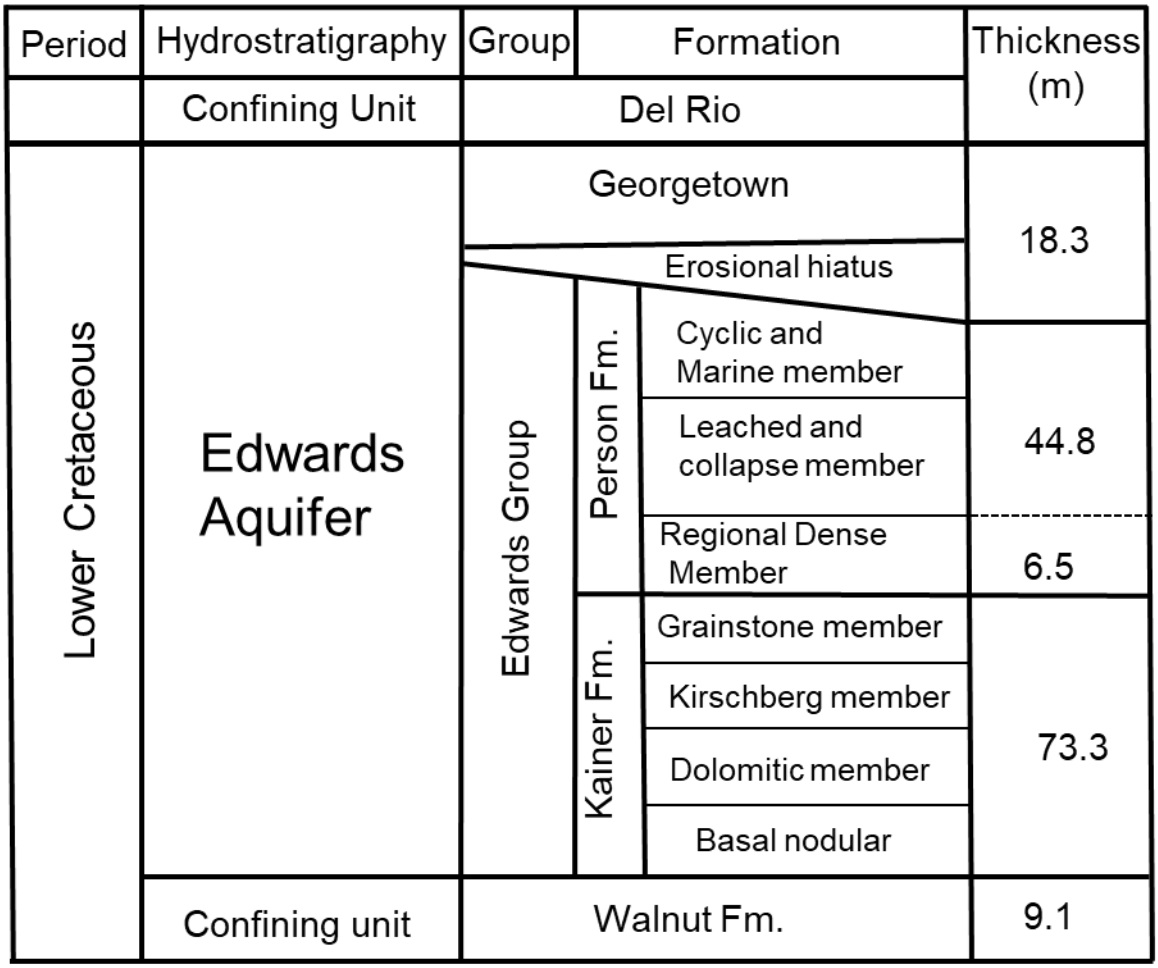

Figure 3.2. Schematic hydrostratigraphic column of the Edwards aquifer in the study area with thickness values of the Kainer and Person Formations and the semi-confining RDM member separating them. Above the Person Formation is an indication of several episodes of erosion and karstification following tectonic uplift and prolonged subaerial exposure and the ensuing

removal of much of the cyclic and marine member before Georgetown Formation deposition. Thickness values are based on the core collected from the ASR well and retrieved in Blumberg et al. (2019) report.

The 25-30 km wide Balcones Fault Zone (Figure 3.3) —separating the Edwards Plateau from the Gulf Coastal Plain in South Texas— controls the hydrogeology and geochemistry of the Edwards aquifer by (1) thinning or offsetting aquifer strata, thus disrupting fault block communication (Allan, 1989; Maclay, 1989), and (2) creating barriers and/or pathways for fluid flows (Maclay, 1995; Caine et al., 1996). While the juxtaposition of less permeable zones impedes flow across faults, flow across faulted blocks is favored by the juxtaposition of permeable beds (Sharp, 1990). The Edwards aquifer water quality is dictated by aquifer stratigraphy, structure, lithology, geomorphology, cross-formational flow, mixing with saline formation waters, and water-rock interactions (Sharp, 1990). A combination of these factors makes the Edwards aquifer an anisotropic medium (e.g., Maclay, 1995; Lindgren et al., 2004).

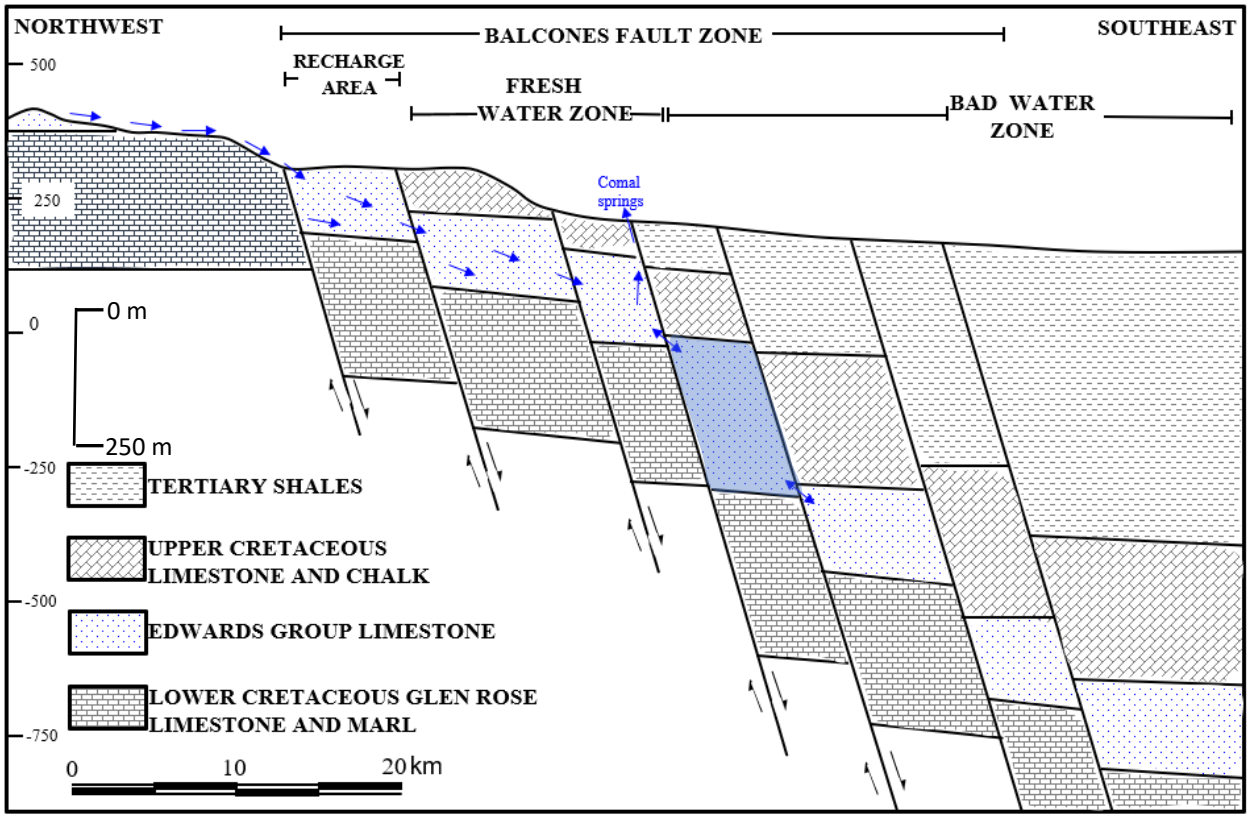

Figure 3.3. illustrates the Balcones Fault Zone (BFZ) and the two main zones (freshwater, and badwater zones) of the Edwards aquifer through NW-SE Cross-section (Modified from Longman and Mech,1978). The downdip limit of the freshwater zone is represented by a 1,000 mg/L total dissolved solids (TDS) contour, perpendicular to the plane of the page. The plausible location of the ASR site is within the aquifer block highlighted in blue color. The salinity in the badwater zone goes up to 250,000 mg/L towards the Gulf Coast. Note that the aquifer thickness changes spatially, hence this figure gives a general NW-SE structural pattern of the Edwards aquifer. Blue arrows show the direction of surface water (in the drainage area), and groundwater flow. *The barrier to flow is shown by the double-sided arrows within the first faulted block of the badwater zone.*

The study area is located in the badwater zone of the Edwards aquifer. The badwater zone is defined by an isoconcentration line commonly known as the "badwater line", which separates fresh-water from water exceeding 1,000 mg/L TDS (Figure 3.3). The badwater line demarcates the updip and rapidly circulating (90 to 900 cm/day) freshwater portion of the Edwards from the downdip slowly migrating (1-2 cm/day) basinal fluid, hence marking a significant decline in

permeability (Maclay and Small, 1986; Maclay and Land, 1988; Clement, 1989; Sharp, 1990). The permeability in the badwater zone is estimated to be 2 to 3 orders of magnitude less than the permeability in the freshwater zone (Maclay and Land, 1988). Within the badwater zone, the salinity grades up to 250,000 mg/L TDS (Maclay and Land, 1988). Petrologic study conducted in the second chapter indicates that dolomitization, fracturing and dissolution are the major diagenetic processes controlling the effective permeability.

Previous studies include numerical models of groundwater flow (Maclay and Land, 1988; Scanlon et al., 2003; Lindgren et al., 2004; Green et al., 2019), Edwards aquifer hydrogeology and management (Maclay, 1989; McKinney and Watkins, 1993), aquifer sedimentology, stratigraphy, aquifer matrix permeability, and porosity, karst and fracture porosity (Maclay and Small, 1983; Hovorka et al., 1994, 1995 and 1998), diagenetic studies (Hovorka et al., 1994; Ellis, 1985; Choquette and Hiatt, 2008), and the hydrochemistry of the Edwards (Person and Rettman, 1976; Maclay et al., 1980; Clement and Sharp, 1987; Oetting et al., 1992; Oetting et al., 1996; Sharp and Smith, 2019). Integration of the results of these studies conducted mostly in the freshwater zone improved hydrogeological and hydrogeochemical models of the Edwards aquifer. With the current stress on the Edwards aquifer due to the increasing trend in the population (Sandoval, 2021), these models are an important guide for ASR operations. Due to the complexity of the aquifer, including depositional environments and diagenetic processes, results from previous large-scale studies may not accurately represent the more restricted, small-scale, and relatively poorly studied zone of the Edwards aquifer — the bad water zone, where the current study area (New Braunfels) is located (Figure 3.1 and Figure 3.3).

3.2.1 Previous work

3.2.1.1 Groundwater sampling

Water quality samples collected by consulting firm INTERA (Blumberg et al., 2019) encompass a) the injected water from the New Braunfels Utility (NBU) system, which is a treated blend of Guadalupe River water and groundwater from wells in the freshwater zone of the Edwards; b) the native groundwater from the Person and Kainer Formations aquifers before ASR operations (or recharge of water); and c) the mixed injected water-native groundwater recovered from the monitoring and ASR wells during ASR operations. There are three wells, one ASR well and two monitoring wells (MW), through which time-series groundwater (mixed injectant-native groundwater) samples were collected during ASR operations. Native groundwater from the Person Formation was collected 46 m west of the ASR well via monitoring well labelled MW-1, while groundwater from the Kainer Formation was sampled from monitoring well labelled MW-2 at ~50 m southwest of the ASR well (Figure 3.1). Both monitoring well groundwaters were sampled after field measurements of water quality parameters (pH, temperature, and specific conductance) had stabilized. The second monitoring well was installed in the Kainer Formation to determine if there is a vertical hydraulic gradient between the Person and Kainer Formations, allowing for possible inter-aquifer water exchange between both portions of the Edwards aquifer system. A total of 56 time-series samples (injected water, native groundwater, and mixed-surface water and groundwater) were collected from the NBU system, the ASR well, and the monitoring wells from October 2019 to April 2022 (Table 3.1). One month separated most dates of water sampling from the monitoring wells and NBU system water. Sampling in the ASR well was conducted at the end of a 48-hour pump test from March 2020 to January 2022 mainly for regulatory requirement purposes. Water samples during

recharge and storage (from October 2019 to November 2021) are used here to trace the evolution of hydrochemical facies of groundwater around the ASR well and evaluate to what extent the water type in the vicinity of the ASR well varied and evolved compared to those from the monitoring wells.

Table 3.1. Composition of major elements in the injectant water (NBU System Water), mixed surface water-groundwater in the Person Formation in ASR well (ASR D1), mixed surface water-groundwater in the Person Formation in monitoring well (MW-1), mixed surface water-groundwater in the Kainer Formation in monitoring well (MW-2). The first groundwater sampling data in monitoring wells is native groundwater. Dates having missing data of one or more analytes on the Person and Kainer groundwaters are not represented in this table and were not included in the geochemical model. Supplemental Table 3.1 includes all dates having partial to all data and information on the ASR operational mode.

Lab Number	Sampling Date	Sample ID	Calcium [mg/L]	Magnesium [mg/L]	Sodium [mg/L]	Potassium [mg/L]	Total Alkalinity [mg/L]	Chloride [mg/L]	Sulfate [mg/L]	TDS [mg/kg]
Detection limit [mg/L]			2.5	0.5	5	1	5	200	200	[none]
589487	3/16/2020	ASR D1	2,000	700	2000	100	600	5000	2000	10,000
589800	3/18/2020	ASR D1	900	400	2,000	100	400	3,000	3,000	9,000
658355	11/30/2021	ASR D1	80	20	10	2	200	40	40	400
659495	12/8/2021	ASR D1	100	40	70	5	200	100	200	700
663912	1/18/2022	ASR D1	100	50	100	8	200	200	200	1,000
HS19101085	10/17/2019	MW-2	800	400	1,000	70	400	3,000	3,000	9,000
633434	4/21/2021	MW-2	200	70	200	10	200	700	300	1,000
637631	6/03/2021	MW-2	100	60	200	10	200	700	300	1,000
641571	7/08/2021	MW-2	100	50	100	10	200	600	200	1,000
646331	8/17/2021	MW-2	100	50	100	9	200	600	300	1,000
647997	9/1/2021	MW-2	100	60	200	10	200	700	300	1,000
649683	9/17/2021	MW-2	100	70	200	10	200	700	400	1,000
652721	10/12/2021	MW-2	100	50	100	7	200	200	200	900

Lab Number	Sampling Date	Sample ID	Calcium [mg/L]	Magnesium [mg/L]	Sodium [mg/L]	Potassium [mg/L]	Total Alkalinity [mg/L]	Chloride [mg/L]	Sulfate [mg/L]	TDS [mg/kg]
656100	11/9/2021	MW-2	100	40	70	5	20	200	200	800
656930	11/16/2021	MW-2	100	50	100	7	200	200	200	900
658353	11/30/2021	MW-2	100	50	100	8	200	200	200	1,000
659493	12/8/2021	MW-2	300	200	500	30	300	1,000	900	3,000
664821	1/25/2022	MW-2	400	200	700	50.0	300	1,000	1,000	4,000
667384	2/15/2022	MW-2	100	60	100	10	200	300	300	1,000
671506	3/22/2022	MW-2	100	40	90	7	200	200	50	700
675356	4/26/2022	MW-2	90	30	40	4	200	90	100	600
590823	3/25/2020	MW-1	800	400	2,000	100	300	3,000	3,000	9,000
591199	3/31/2020	MW-1	200	90	400	20	200	600	500	2,000
621883	1/12/2021	MW-1	80	30	30	2	200	50	70	500
630366	3/31/2021	MW-1	80	20	20	2	200	50	60	500
633435	4/21/2021	MW-1	80	20	20	2	200	300	40	700
637630	6/03/2021	MW-1	70	20	20	2	200	300	40	700
641570	7/08/2021	MW-1	70	20	10	3	200	300	30	700
647996	9/1/2021	MW-1	70	20	20	2	200	300	40	700
649684	9/17/2021	MW-1	70	20	20	2	200	300	40	700
651722	10/12/2021	MW-1	70	20	20	2	200	40	50	400
656101	11/9/2021	MW-1	80	20	20	2	200	40	50	400
656931	11/16/2021	MW-1	70	20	20	2	200	40	60	400

Lab Number	Sampling Date	Sample ID	Calcium [mg/L]	Magnesium [mg/L]	Sodium [mg/L]	Potassium [mg/L]	Total Alkalinity [mg/L]	Chloride [mg/L]	Sulfate [mg/L]	TDS [mg/kg]
658354	11/30/2021	MW-1	80	20	20	2	200	40	60	400
659494	12/8/2021	MW-1	100	50	100	8	200	200	200	900
664822	1/25/2022	MW-1	100	60	200	10	200	300	300	1,000
667385	2/15/2022	MW-1	80	20	30	3	20	60	80	500
671507	3/22/2022	MW-1	80	20	20	2	200	40	30	400
675357	4/26/2022	MW-1	70	20	20	2	200	40	50	400
590822	3/25/2020	NBU System Water	60	20	10	2	200	30	30	300
613964	10/22/2020	NBU System Water	80	20	10	2	200	30	30	400
619958	12/17/2020	NBU System Water	70	20	10	2	200	20	30	400
621882	1/12/2021	NBU System Water	70	20	10	2	200	20	30	400
630368	3/31/2021	NBU System Water	70	20	10	2	200	30	30	300
633436	4/21/2021	NBU System Water	70	20	10	2	200	30	30	300
637632	6/03/2021	NBU System	70	20	10	2	200	20	30	300

Lab Number	Sampling Date	Sample ID	Calcium [mg/L]	Magnesium [mg/L]	Sodium [mg/L]	Potassium [mg/L]	Total Alkalinity [mg/L]	Chloride [mg/L]	Sulfate [mg/L]	TDS [mg/kg]
		Water								
641572	7/08/2021	NBU System Water	70	20	10	3	200	30	30	300
646333	8/17/2021	NBU System Water	60	20	10	2	200	30	30	300
656102	11/9/2021	NBU System Water	70	20	10	2	200	30	30	400

3.2.1.2. Groundwater analysis

Water quality samples were analyzed by ALS Environmental (Houston, Texas and Fort Collins, Colorado, USA) from 2018 to 2019 and subsequently from 2020 by PCS Laboratories (University City, Texas, USA). SO_4^{2-}. NO_3^- (as N), Cl^-, Br^-, and F^- were determined by ion chromatography according to EPA method 300. Alkalinity was titrated by colorimetry using EPA method SM232OB, P was determined by colorimetry according to EPA method E365.3, and TDS was calculated using EPA method SM2540C by filtration and evaporation to dryness at 180°C. The detection limits of major dissolved constituents can be found in Table 3.1.

3.3. Methodology

3.3.1. Water chemical characterization, evolution, and simulation

The development of geochemical models in this study employed two main software packages, the Geochemist's Workbench (GWB) program, version 17.0 (Bethke et al., 2023), and the PHAST code (Parkhurst et al., 2004). The GWB program is an integrated software suite designed to address a wide range of geochemical challenges in aqueous systems. Within this suite, two key programs, GSS and React, utilize the GWB thermo.tdat database for the purpose of this study. GSS functions as a spreadsheet program that facilitates the manipulation and visualization of geochemical datasets. In this particular context, GSS employs the Piper diagram to characterize the water types involved in the ASR operation in New Braunfels. The trilinear diagram is also used to show major trends in the evolution of water types of the native groundwater during recharge and storage in the first cycle of ASR operation. On the other hand, React is employed to trace the reaction processes (or reaction path) during the first cycle of recharge and storage. Two reaction modeling scenarios are considered. First, the scenario within

which the injectant (freshwater) is titrating into the native groundwater and the result of mixing both fluids in all possible mixing ratios is evaluated in terms of chemical components in fluids. This "water-water" model configuration helps in capturing the hydrochemical facies evolution during ASR operation. Ratios of injectant to groundwater from 0 to 5 and from 0 to 20 parts are used to capture the spatial and temporal dynamics of hydrochemical facies evolution with successive recharges of freshwater into the aquifer. Mixing is thus being modeled in ratios from zero to as high as 5 and 20 parts injectant to one part native groundwater, respectively. The second model scenario will track the evolution of the aquifer system (aquifer matrix and pore fluid) through which the injectant fluid migrates. The reaction of the injectant with native groundwater and the aquifer materials results in a possible change of porosity and permeability via mineral precipitation and/or dissolution relative to key mineral phases of the aquifer (calcite and dolomite with minor anhydrite and gypsum). As the model continuously displaces the native groundwater, a mixing ratio from 0 to 5 parts injectant to one part native groundwater is set to span 500 days, covering the approximate time of recharge and storage. In this way, within 500 days, the native groundwater is being continuously displaced a total of 5 times over the course of the simulation. The length of time and the volume of water injected are largely arbitrarily chosen to just give a calculation endpoint with a high ratio of injectant within a substantial time, and more importantly, capture reaction processes controlling mineral stability. Furthermore, this model will substantiate the contribution the aquifer mineral dissolution or precipitation (if any) might have in controlling the evolution of groundwater geochemistry during recharge and storage. Based on Blumberg et al. (2019) report, the mineralogical composition of the aquifer storage zone, as determined by XRD analysis, is 0.5 % calcite and 99.5% dolomite. The porosity value of 0.35 of the aquifer matrix is based on helium gas porosimetry in one rock sample,

though this value may not define the porosity of the entire aquifer media of interest for water storage. Further, considering the high porosity media is the prime storage zone during ASR operation (Price and Pichler, 2006), this relatively high bulk porosity value (35%) aids to infer whether precipitation and/or dissolution occurred. 2,900 cm^3 is considered the initial bulk volume of the aquifer material. Assuming the initial porosity of the storage section of the aquifer matrix is 0.35 and the amount of bulk volume of 2,900 cm^3, the native groundwater volume that could occupy the porous media is estimated to be 1,015 cm^3. The calculated mineral volume is estimated to be 1,885 cm^3. Model parameters are quite simplistic but useful from a conceptual point of view to account for both mass-transfer configurations revealing whether the groundwater hydrochemical facies evolution results from the simple mixing of both water types (injectant and native groundwater), from the interaction of both water types and aquifer matrix, or a combination of both factors. Reaction path modeling is based on the native Person Formation groundwater and the first injectant water (NBU System water) data found in Table 3.2.

Table 3.2. Native groundwater quality data of the Edwards Kainer (MW-2 in Figure 3.1) and Person Formations (MW-1 in Figure 3.1) from monitoring wells and water quality from the NBU System water before ASR operation. Data from monitoring well in the Person and Kainer Formations is taken from their respective first sampling in **Table 3.1**. Water from the NBU system water TDS, charge imbalance, water types, saturation index of main mineral phases of the aquifer of these three different water types were characterized by the GSS program. Note the difference in density of 0.58% between the native groundwater and the injectant (NBU System).

Sample ID	Unit	Native Person Formation	Native Kainer Formation	NBU System water
Ca++	mg/l	800	800	60
Mg++	mg/l	400	400	20
Na+	mg/l	2,000	1,000	10
K+	mg/l	100	70	2
HCO3-	mg/l	300	400	200
SO4--	mg/l	3,000	3,000	30
Cl-	mg/l	3,000	3,000	30
pH	pH	7.4	7.2	7.9
Total Dissolved Solids	mg/kg	9,000	9,000	300
Charge imbalance	eq/kg	0.02	-8×10^{-3}	8×10^{-4}
Water type		Na-Cl	Na-Cl	Ca-Mg-HCO3
Calcite	log Q/K	0.9	0.7	0.6
Anhydrite	log Q/K	-0.4	-0.3445	-2
Dolomite	log Q/K	2.6	2.307	2
Gypsum	log Q/K	-0.2	-0.2	-2
Halite	log Q/K	-4	-4	-8.081
Density	g/cm^3	1.002	1.002	0.9962

The TDS is defined here based on major ions (Ca^{2+}, Mg^{2+}, Na^{+}, K^{+}, SO_4^{2-}, CO_3^{2-}, HCO_3^{-}, Cl^{-}); additional minor inorganic and organic substances contributing to TDS are ignored.

In conjunction with the GWB, the geochemical software model PHAST was utilized to simultaneously capture the major physical and chemical processes governing the fate and transport of major ions during ASR. PHAST is a three-dimensional, multicomponent, reactive transport simulator coupling PHREEQC (geochemical model) and HST3D (solute transport

model) with constant density and temperature of the flow and transport model in saturated groundwater media (Parkhurst et al., 2004; Parkhurst et al., 2004). For a reasonably accurate description of solute transport in subsurface media, multicomponent solute transport, and chemical reactions are simultaneously coupled, a method referred to as the "one-step method" (Barry et al., 2000). However, PHAST uses a two-step (or operator splitting) method wherein solute transport and chemical reaction calculations are solved sequentially without iteration (Parkhurst et al., 2010). Where chemical reactions are neglected, the governing transport equation of chemical constituents in groundwater considering advection, dispersion, and fluid sinks/sources is defined as:

$$\frac{\partial(\theta C)}{\partial t} = \frac{\partial}{\partial x_i}\left(\theta\, D_{ij}\frac{\partial C}{\partial x_j}\right) - \frac{\partial}{\partial x_i}\,(qiC) + q_s C_s$$

Where θ is porosity (dimensionless), C is component's dissolved concentrations, D_{ij} is the hydrodynamic dispersion (L^2T^{-1}), qi is the Darcy velocity(LT^{-1}), q_s is the flow rate of a fluid source or sink per unit aquifer volume (T^{-1}), and Cs is the concentration of the fluid source or sink flux (ML^{-3}).

Though PHAST does not account for density-driven flow, the estimated 0.58% density contrast between the Person Formation native groundwater and the injectant water can be dismissed given the high flow rate induced by ASR operations (Wallis et al., 2011). For an idealized constant and uniform density groundwater, coupling groundwater flow, and ionic transport allows for the control of fluid velocity distribution in the solute transport while ionic transport minimally affects the fluid velocity field (Parkhurst et al., 2010).

3.3.3.1 Flow and transport modeling

PHAST was initially selected as a flow and transport model for this study because of its reactive transport modeling capability. However, because (1) subsequent analyses indicate major cation and anion species in this portion of the Edwards Aquifer behave conservatively, and (2) the two monitoring wells – one each in the lower and upper portions of the aquifer – offer extremely limited spatial resolution of water chemistry changes during injection, PHAST was used primarily as a screening model to help constrain aquifer hydraulic parameters based on chloride breakthrough curves. Separately, a multi-aquifer analytical groundwater flow model – free from grid constraints and imposed lateral boundary conditions – was used as a second, fully independent means with which to constrain the aquifer hydraulic conductivity structure.

3.3.3.1.1. PHAST Model

Simulation of the measured breakthrough of chloride (a conservative chemical constituent) at two observation wells separately penetrating the Person Formation and the Kainer Formation can be used to estimate the hydraulic property values of both aquifer zones and of the Regional Dense Member semi-confining unit. In the case of the Person Formation targeted for ASR storage, knowledge of the extent to which the intervening leaky confining unit allows for communication between aquifer zones is critical in ASR recovery optimization. Chloride is widely used as a conservative tracer to evaluate solute origin and transport processes (Fabryka-Martin et al., 1987). For the latter, the Cl^- ion is used because it has a low abundance in most common rock-forming minerals, does not partition into the gas phase (excluding high-temperature hydrothermal systems), has a high solubility in natural waters, and has low adsorption capacity (Feth, 1981). Chloride is also commonly used as an internal tracer for evaluating geochemical processes involved in transport. The concentration of chloride can

change in response to external factors (recharge in this case), hence helping to better understand and parameterize the geological formation (Blackmore et al., 2018; Pedretti et al., 2022). Due to the fact that both the Person and Kainer Formations have similar chemistries and chloride abundance, especially when compared to the injectant water, spatial and temporal variability in Cl^- in both storage zones before ASR operations recharge will be ignored. The large contrast in chloride concentrations between injected water and native brackish groundwaters provides a useful tracer of movement of surface water in the aquifer (Petkewitch et al., 2004).

The pre-pumping flow direction was neglected because the brackish portion of the Edwards is considered stagnant (Sharp and Banner, 1997). Studies in the Edwards badwater zone have indicated that the zone is hydrologically isolated partly by faults functioning as barriers to flow (Groschen and Buszka, 1997). If there is a background hydraulic flow gradient in the study area, it is likely too small to affect the model outcome, and hence was not considered in the model. Constant head boundary conditions are set at the right and left ends of the model to set up the direction and magnitude of flow during the recharge. Grid boundaries along fixed head conditions were expanded outwards from the ASR well to allow expression of the groundwater mound induced by the recharge.

Since the Georgetown and the Walnut Formations function as good confining units impeding vertical flow, they are here modeled as no-flow, and hence for simplification purposes, they are not represented in the model domain. A-124.6 m thick semi-confined aquifer is thus considered an idealized system emulating the Edwards aquifer in the study area. The 124.6 m for the initial head assumes hydrostatic conditions across the system to reproduce the static no-flow recharge, pre-pumping groundwater condition.

The bottom layer is the Kainer Formation with a thickness of 73.3 m extending from 0 m (i.e., defined as datum) to 73.3 m. A-6.5 m thick RDM leaky confining layer extends from 73.3 m to 79.8 m. The Person Formation stretches from 79.8 m to 124.6 m. The model domain is ~2,000 m in length and 940 m in width. All three layers of the aquifer model domain geometry were ideally considered constant and flat. The model grid was discretized with 61 nodes at 32.8 m spacing in the X direction, 31 nodes at 30 m spacing in the Y direction, and 7 nodes at 18 m spacing in the Z direction. There is some grid refinement near the recharge wells down to circa 10 meters horizontally. Further, vertical spacing within the aquitard layer is refined to 2 meters (Supplemental Figure 3.1).

The ASR and monitoring wells are completed as open holes in the storage zones, and are not screened. The ASR well (Person Formation) is an open hole from 10.8 m to 44.2 m. The Person Formation monitoring well (MW-1) is an open hole from 10 m to 44 m. The Kainer Formation monitoring well (MW-2) is an open hole from 59.5 m to 115.8 m. The recharge rate was discontinuous with estimated values of 0.025 m^3/s for 105 days, 0.0029 m^3/s for 102 days, and 0.019 m^3/s for 387 days. While the first recharge rate was known, the rest of the variable recharge rate values were roughly estimated in accordance with the evolution of head values recorded in monitoring wells. There were also brief periods of no recharge. Limitations in historical data of recharge rates can eventually lead to errors in head calibration and the solute transport model. However, the ultimate aim of the model is to reproduce major trends in observed and simulated chloride concentrations.

After conceptualization of the model domain in the transport file, the chemistry input file and geochemical processes occurring during the ASR project were defined. Native groundwater in the Person and Kainer Formations, and subsequent injectant time series water composition,

were defined. The use of the equilibrium approach of salt species transport in this model is justified because they would tend to reach equilibrium faster than the time allowed to move the fluid from one cell to another (Bahr and Rubin, 1987; Knapp, 1989; Miotliński, 2008). Since all solutes behave conservatively, the PHAST model is a coupled flow and transport without reactions.

Calibration first proceeded with the flow-only model scenario to approximately match the major trend in the observed temporal head changes in the Person and Kainer Formations (Supplemental Table 3.2) during the ASR injection period. ASR injection rates were used in the head calibration process. However, because the ASR injection rates were not well recorded and there were limited monitoring wells in the study area, the difference between the calibrated and measured heads of up to several meters was tolerated. The temporal head distribution in the model domain was transferred into Surfer (version 25.0), leveraging its contouring capabilities, to approximate only the simulated and interpolated maximum head changes data close to the monitoring wells (Supplemental Figure 3.2). Model sensitivity was performed based on three main hydraulic parameters: specific storage (Ss), conductivity (K), and effective porosity (Φ).

Similar to the PHAST groundwater flow model, the PHAST solute transport and chemistry are also modeled as transient, and based on the use of chloride as a conservative tracer, hydraulic properties of the three layers of the Edwards aquifer were estimated. This entailed applying a least-squares optimization scheme, implemented with Python, to minimize differences between the observed and simulated chloride concentration trends by adjusting hydraulic conductivity (K) and effective porosity (Φ). Because of the anisotropic nature of the Edwards aquifer, conductivity values in the Person and Kainer Formations were allowed to vary in all three directions. The K values in each of the three layers were set to vary within three orders of

magnitude, while the effective porosity variation was limited to within one order of magnitude during the estimation process. These assumptions are reasonable considering the Edwards aquifer anisotropy and heterogeneity and the size of interconnected pores effective for groundwater transmission range by four to five orders of magnitude (Maclay, 1995). Furthermore, the longitudinal, horizontal and vertical dispersivity were set arbitrarily to 30 m, 3 m, and 3 m respectively. Given the fracture nature of the Edwards aquifer, the chosen dispersivity values reflect the dominant transport processes and were set to capture solute dispersion and mixing within the aquifer system. Gelhar et al. (1992) estimated values of the longitudinal dispersivity to range up to two to three orders of magnitude in fractured aquifers, and the ratio of longitudinal to horizontal dispersivity and vertical dispersivity up to three orders of magnitude. Due to the fact that the contribution of molecular diffusion is likely to be smaller than hydrodynamic dispersion in fractured carbonate aquifers, its value was set to 10^{-9} m^2/s .

3.3.3.1.2. Analytical flow model

With chloride time series data available from only two extraction wells in different vertical positions within the Edwards Aquifer, the system is underdetermined with optimization of a full set of hydraulic parameters (i.e., PHAST model). Under this condition, parameter optimization yields a plausible but non-unique combination of values. An independent means for estimating aquifer hydraulic properties is an analytical solution for steady-state radial flow in a multi-layer aquifer setting in response to pumping developed by Hemker (1984). This solution posits a series of aquifers (i.e., horizontal flow regime), separated by aquitards (i.e., vertical flow regime), with the hydraulic properties (thickness and hydraulic conductivity) specified independently.

The Hemker model was used to constrain scalar hydraulic conductivity values for the Person Formation, the Kainer Formation, and the RDM portions of the Edwards Aquifer through a trial-and-error approach that attempted to match modeled recharge mounds at the radial distances of the two monitoring wells with respect to the ASR well against observed mounds (on the order of 20 to 40 meters in both wells). The hydraulic conductivities of the underlying and overlying aquitard layers required by the Hemker model were set to vanishingly small values. Further detailed discussion on the Hemker analytical solution can be found in the supplementary documentation. Supplemental Figures 3.3, 3.4, and 3.5, and Supplemental Tables 3.3 and 3.4 provide relevant insights to this discussion.

3.3.3.2. Optimum recovery rate

After approximation of the hydraulic properties of the three layers, optimum recovery rate estimation was done by trial and error methodology using the computer program Model Viewer 1.6 (Hsieh and Winston, 2002). Considering 40 days of storage, a recovery rate that would not induce high TDS levels exceeding 1,000 mg/L was estimated for a 60-day recovery period. Model viewer capabilities to display scalar data such as TDS for 60 days of recovery aided in defining spatial and temporal transport of the bulk solute ions plume expressed as TDS.

3.4. Results

3.4.1. Injectate water and native groundwater chemistry characterization

Major element chemical data for the injectant water and native groundwater in the Kainer and Person Formations are represented in Table 3.1. More comprehensive physical and chemical data of injectant water (NBU system water) and native groundwater in the Kainer and Person

Formations are represented in Supplemental Table 3.1. The field pH value of 7.9 defines the initial injectant water sample, while values of 6.4 and 7.2 are the initial native groundwater pH values of the Person and Kainer Formations, respectively (Table 3.3.). The injectant water is of Ca-Mg-HCO3 type with the Edwards aquifer freshwater zone having a slightly higher value in TDS, alkalinity, and hardness than the Guadalupe River water (Table 3.2). The native groundwaters from both the Kainer and Person Formations are of Na-Cl water type (Table 3.3). TDS values in the Edwards native groundwater approach 10,000 mg/L, a level commonly considered unusable for domestic, agricultural or industrial purposes (Warner, 2001; IOGCC, 2006). The NBU system water has TDS values lower than the recommended Texas Commission on Environmental Quality (TCEQ) standard TDS level (1,000 mg/L), ranging from 300 mg/L to 400 mg/L (Table 3.1).

Table 3.3. Water quality data of the Edwards aquifer freshwater zone and the Guadalupe River, the mix of which is the injectant. TDS and water type were evaluated by the GSS program/ Geochemist's workbench. Samples were collected on June 6, 2018 (retrieved from Blumberg et al. report, 2019).

Sample ID	Unit	Guadalupe River water (Treated)	Edwards Aquifer Freshwater zone
Ca++	mg/l	60	80
Mg++	mg/l	20	20
Na+	mg/l	8	9
K+	mg/l	2	1
HCO3-	mg/l	200	200
SO4--	mg/l	30	50
Cl-	mg/l	30	20
pH	pH	7.9	7.6
Water type		Ca-Mg-HCO3	Ca-Mg-HCO3
TDS	mg/kg	300	400

TDS in the Kainer Formation decreased from 9,000 mg/L to 1,000 mg/L during recharge (recharge) while the TDS in the Person Formation declined from 9,000 mg/L to 400 mg/L

(Figure 3.4), based on data from monitoring wells. At the ASR well, the TDS decreased to 400 mg/L from 10,000 mg/L during recharge. An increasing TDS trend is hence observed from the ASR well to the monitoring well (MW-1), both wells being screened in the Person Formation (Table 3.1). By the end of the first cycle recharge, at the end of November 2021, TDS was measured at 400 mg/L in the ASR, and the monitoring wells, TDS values within the acceptable limit for drinking water in Texas. Rapid TDS increase was observed during recovery in both monitoring wells in the Person and the Kainer. From December 8, 2021, a decrease in pumping rate from 0.0630 m^3/s to 0.0440 m^3/s induced a decreased gradient in the TDS trend in both monitoring wells. From January 25, 2022, with a recharge rate of ~ 0.03 m^3/s, the TDS decreased substantially in both monitoring wells to values lower than the Secondary Maximum Contaminant Level (SMCL) of 1,000 mg/L (Table 3.1).

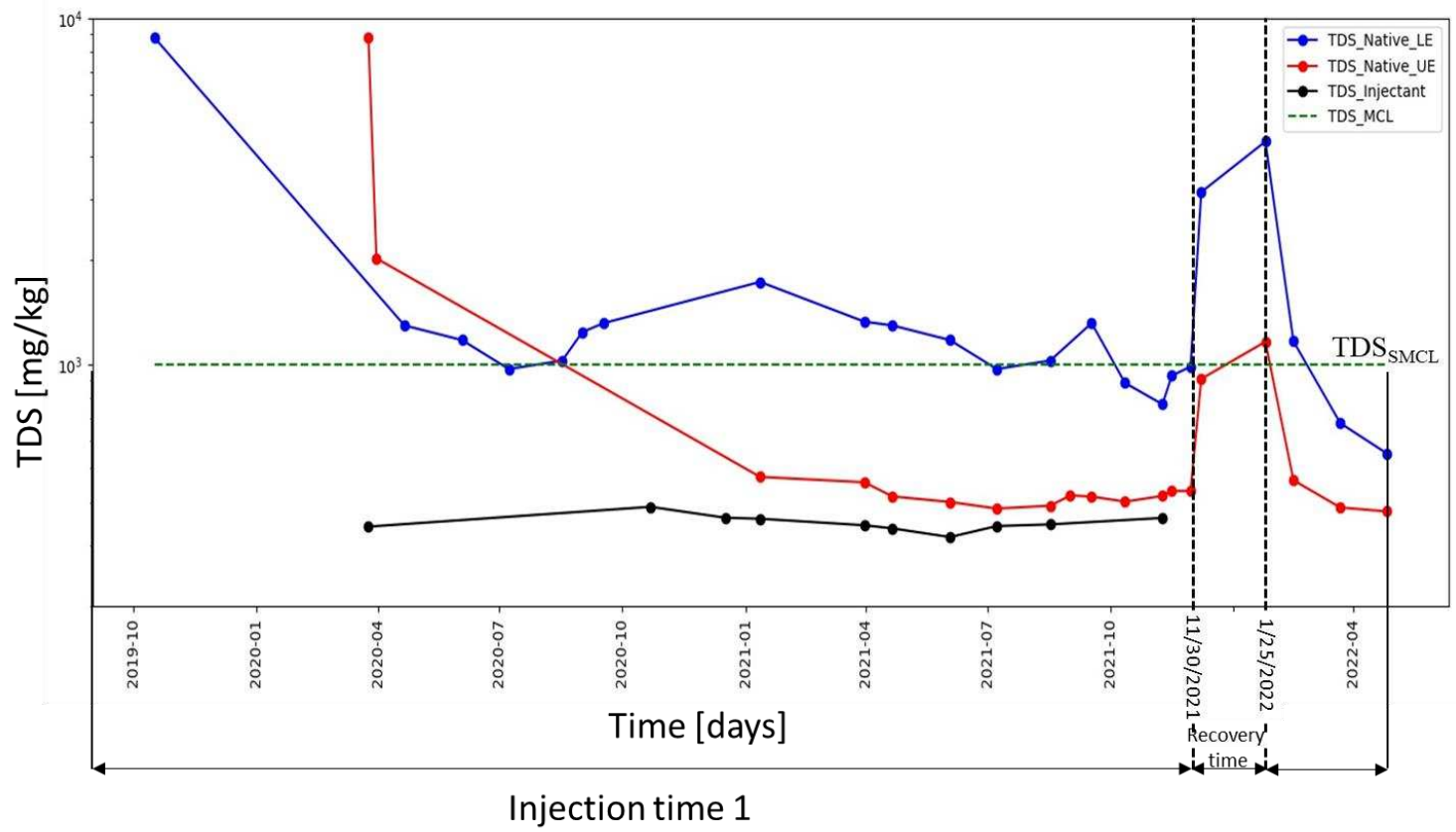

Figure 3.4. TDS evolution of native groundwater during recharge and storage of the first cycle ASR operation until November 30, 2021(TDS values were obtained from dissolved major element values in Supplementary table 3.1). From the end of November 2021 to December 8, 2021 (black circle), the recovery rate of 0.06 m^3/s induced a high TDS increase. From December 8, 2021, a decreased recovery rate to 0.03 m^3/s was followed by a degreased TDS gradient trend. The TDS values from native Person groundwater (TDS_Person Fm.) and native Kainer Formation groundwater (TDS_Kainer Fm.) were collected from monitoring wells. TDS of the injectant (NBU System water) varies from 316.8 to 387.4 mg/L. TDS values of the groundwater in the Person Formation decreased to values lower than their secondary maximum contaminant level (SMCL) of 1,000 mg/L. The targeted storage zone of the first cycle ASR operation is in the Person Formation.

Native groundwater from the Person and Kainer Formations has a similar ionic abundance. Anion components are dominated by Cl^- with the following order in their anionic abundance, $Cl^- > SO_4^{2-} > HCO_3^-$ (mg/L). The dominant cation is Na^+ with decreasing abundance from Na^+ to Ca^{2+}, Mg^{2+}, and K^+ (mg/L) in the native groundwater of both storage zones. In the injectant, the anionic composition is dominated by HCO_3^-, followed by SO_4^{2-} and Cl^- (mg/L); while a decreasing trend in the abundance of cationic components is from Ca^{2+} to Mg^{2+}, Na^+, and K^+ (mg/L) (Table 3).

The piper diagram (Figure 3.5) tracing the evolution of hydrochemical facies during recharge and storage shows a) a change from Na-Cl to mixed water types of groundwater in the Kainer Formation, b) a change from Na-Cl to mixed water type to Ca-Mg-HCO_3 in the ASR and monitoring wells screened in the Person Formation, and (c) a consistent Ca-Mg-HCO_3 water type for NBU system water (injectant).

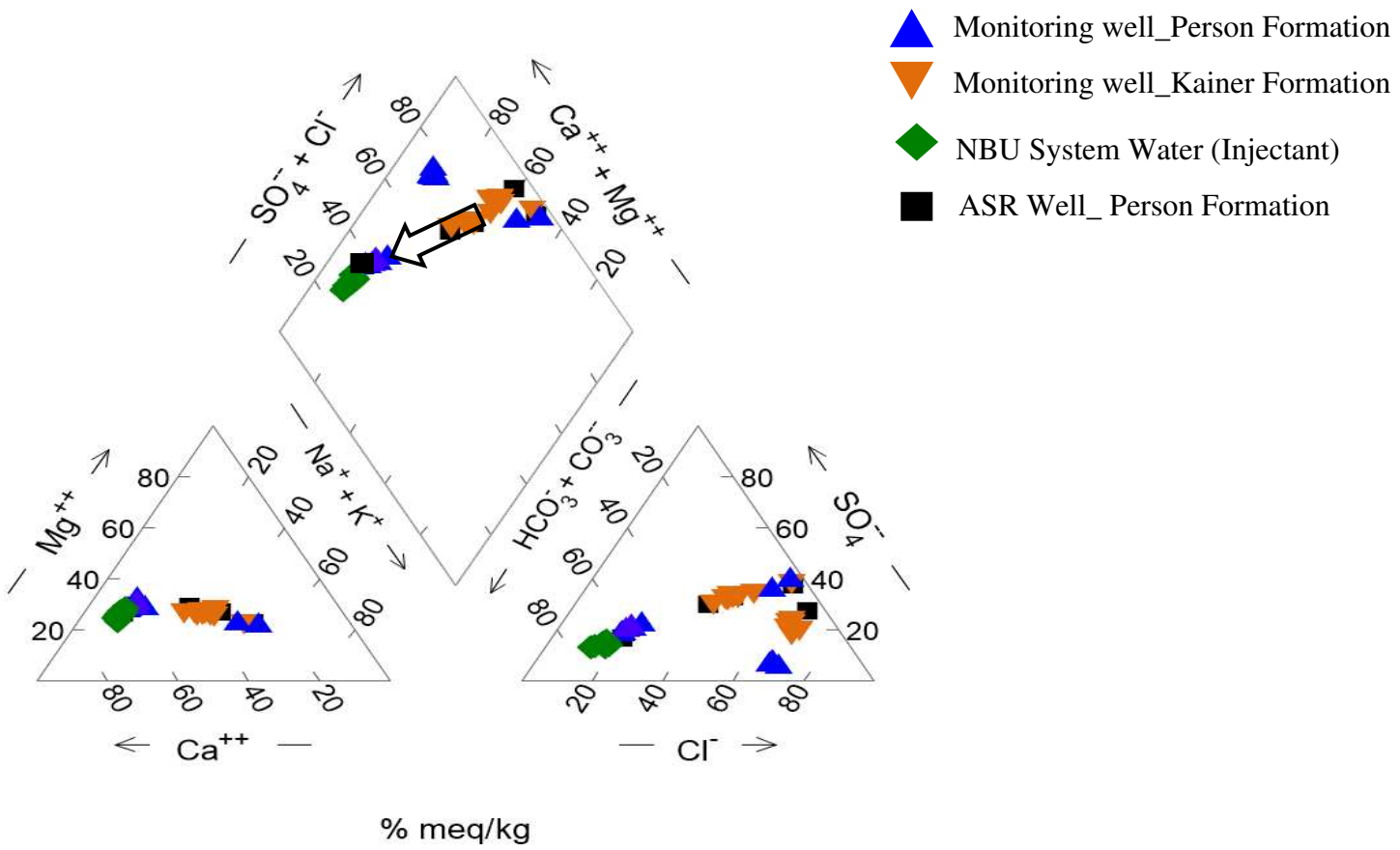

Figure 3.5. Piper diagram of water types involved during recharge and storage of the first ASR cycle (see Supplementary table 3.1). Note that the recharge and storage period ended on November 30th, 2021, i.e., data collected after that date were not considered. Arrows show the general trend in the evolution of water facies from the Person and Kainer Formations towards the Ca-Mg-HCO3 water facies type. The hydrochemical water facies from the monitoring well in the targeted storage zone (Person Formation) evolves up to the injectant water type field via an intermediate mixed type. However, the evolution of the groundwater facies type from the Kainer Formation terminates halfway in the mixed water facies type toward the injectant hydrochemical facies field

Consideration of reaction path modeling based on the water-water interaction configuration shows that the increased injectant ratios from 5 to 20 parts injectant to one part native groundwater promotes a hydrochemical facies change toward a more Ca-Mg-HCO3 water type (Figure 3.6.1 and Figure 3.6.2).

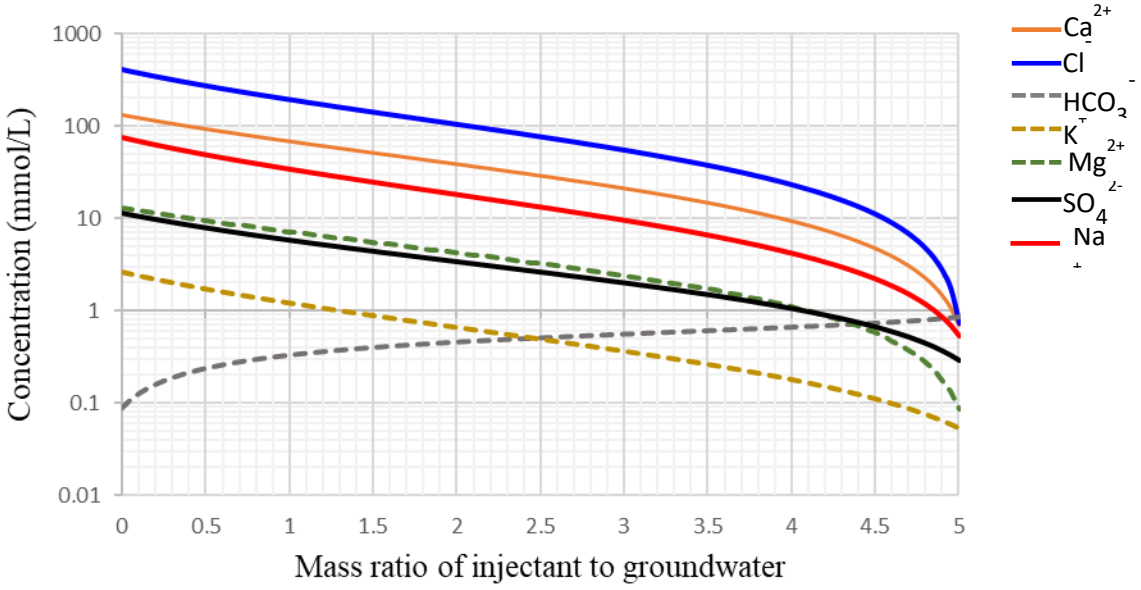

Figure 3.6.1. Species' concentrations when reacting 5 Kg of injectant water in 1 Kg of native groundwater of the Person Formation.

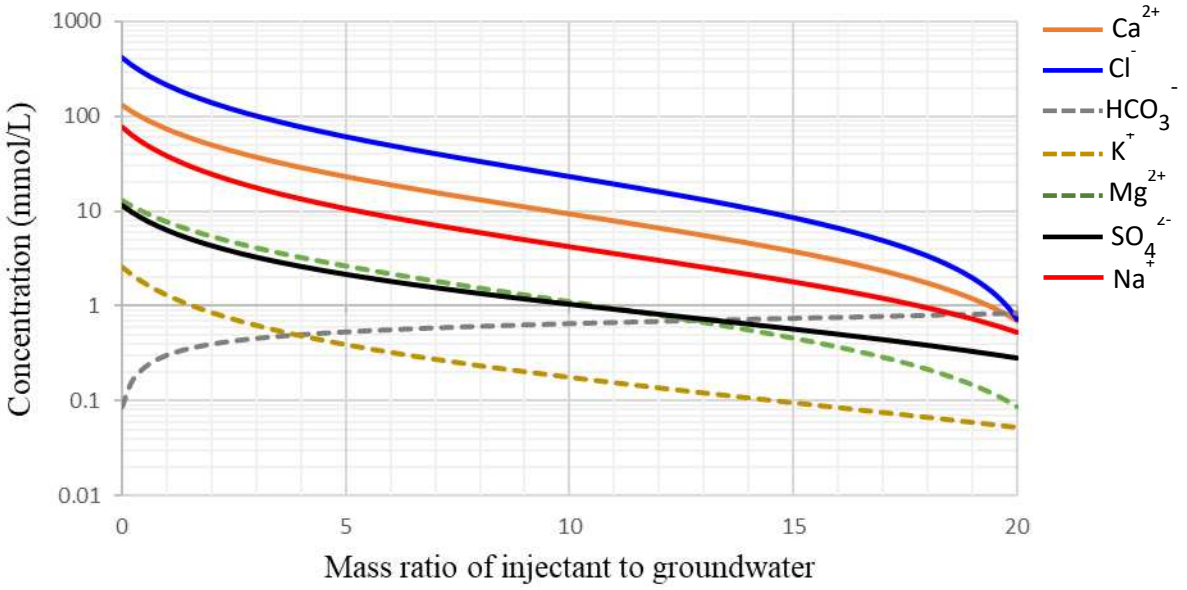

Figure 3.6.2. Species' concentrations when reacting 20 Kg of injectant water in 1 Kg of native groundwater of the Person Formation. Note the hydrochemical facies evolves towards HCO3-*water type, reflecting the injectant NBU system water. The ASR well is located towards a higher mixing fraction.*

Baseline native groundwaters (prior to ASR operations) in the Kainer and Person Formations are supersaturated with respect to dolomite and calcite. They are undersaturated with respect to anhydrite, gypsum, and halite. These mineral phases were chosen based on an idealized mineralogy of the brackish portion of the Edwards aquifer. NBU system water (injectant) is saturated with respect to dolomite and calcite but undersaturated with respect to anhydrite, gypsum, and halite. Saturation index values of calcite and dolomite in native groundwater of the Person and Kainer Formations are higher than those in the injectant water (NBU System water) (Table 3.2). The water-water interaction model substantiates the pattern in major chemical components in groundwater evolving towards the injectant water type (Ca-Mg-HCO3) with an increasing injectant-to-native groundwater mixing ratio (Figure 3.6.1 and Figure 3.6.2). However, the water-rock model simulation predicts a relatively small volume change for calcite in the aquifer when reacting 5 kg of injectant within 500 days. After 500 days of flushing

the aquifer storage system with 5 kg of injectant, the estimated change in the calcite mineral volume yielded is 0.88 cm^3 per 2,900 cm^3 aquifer bulk volume considered in the simulation. The dolomite volume change is very minimal. Though small, the volume of aquifer mineral dissolved leads to a net increase in porosity estimated at 0.095%. The pH is seen decreasing during the simulation run from 7.4 to 6.53 (Figure 3.7).

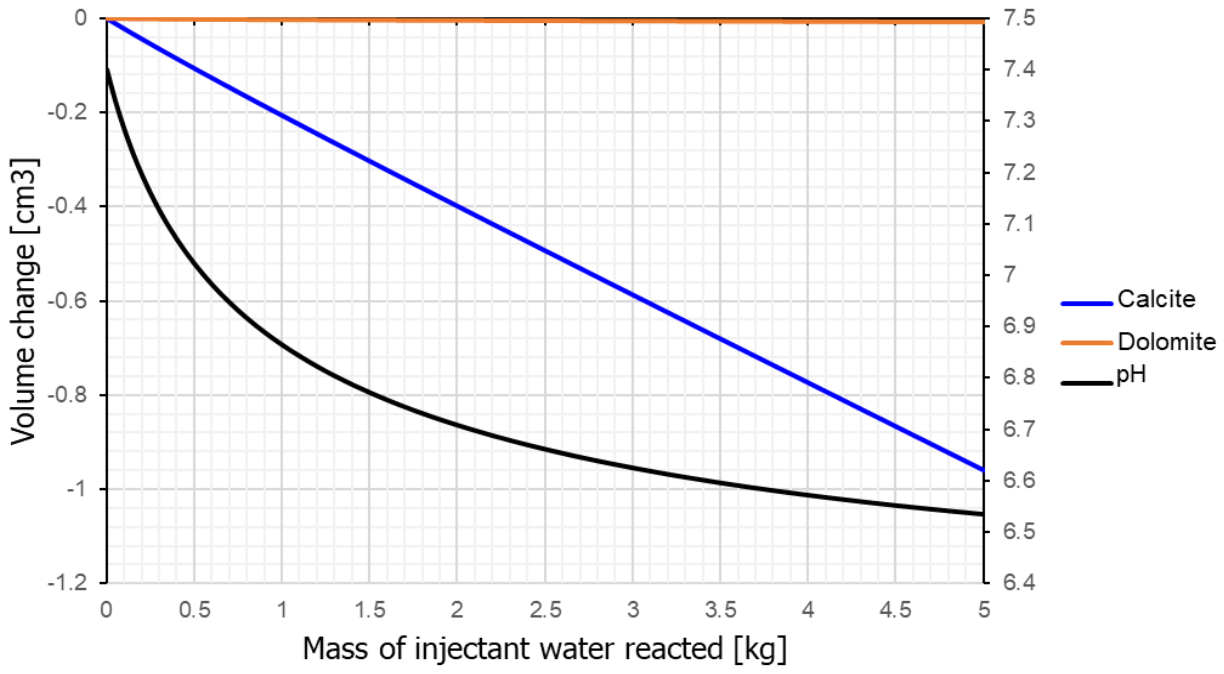

Figure 3.7. Predicted mineral volume change in the Edwards aquifer when reacting 5 kg of injectant water with pH decrease resulting from calcite dissolution.

3.4.2. Hydraulic properties, and recovery rate estimation

Results of hydraulic properties (K and Φ) in Table 3.4 were assessed based on the transport model calibration using chloride (Figure 3.8). The estimated hydraulic conductivity Kx, Ky, and Kz values in the Person Formation are 3.7 10^{-6} m/s, 3.0 10^{-6} m/s, and 4.9 10^{-7} m/s, respectively. The Kainer Formation conductivity Kx, Ky and Kz values are 7.3 10^{-5} m/s, 7.1 10^{-5} m/s, and 8.9 10^{-6} m/s, respectively. The semi-confining RDM Kx, Ky and Kz values are 4.1 10^{-7} m/s, 4.1 10^{-7} m/s, and 6.0 10^{-7} m/s, respectively. These results are crudely in agreement with the conductivity values yielded by the analytical solution (Supplemental Table 3.3). Simulated effective porosity values are estimated to be 1.5 10^{-2}, 4.9 10^{-2}, and 8.4 10^{-2} respectively for the Person Formation, Kainer Formation, and confining layers. Based on these estimated hydraulic property values of the three layers, the freshened groundwater in the Person Formation, exhibiting a TDS less than 450 mg/L, extends up to 150 m away from the ASR well by the end of the injection period. The estimated optimum recovery rate that would not induce high TDS at the ASR well is 0.03 m^3/s (or 476 gpm) for 60 days of recovery (Figure 3.9). Figure 3.10 illustrates how the simulated Cl^- concentration is sensitive to the specific storage, conductivity, and porosity. In the Kainer Formation observation well (MW-2), when the effective porosity value increases by a factor of 10, the simulated chloride concentration is 5.2 10^{-2} (mol/kgw). In contrast, it levels off to 8.1 10^{-4} (mol/kgw) when the effective porosity value decreases by a factor of 10 through 600 days of simulated time. With a 10-fold increase or decrease in hydraulic conductivity values, the simulated chloride reached 2.9 10^{-2} (mol/kgw) and 0.2 10^{-2} (mol/kgw), respectively, by the end of the recharge period. In the Person Formation observation well (MW-1), the simulated chloride concentration is more sensitive to the effective porosity than to conductivity and specific storage parameters. However, the simulated chloride concentration

does not show a significant change when the Ss value is decreased and increased by a factor of 10 in both observation wells.

Table 3.4. Calibrated values of hydraulic conductivity (K) (m/s) and effective porosity (Φ) in all three layers of the Edwards aquifer considered in the model.

Edwards_Layers	Kx	Ky	Kz	Φ
Person Formation	$3.7x10^{-6}$	$3.0x10^{-6}$	$4.9x10^{-7}$	$1.5x10^{-2}$
Kainer Formation	$7.3x10^{-5}$	$7.1x10^{-5}$	$8.9x10^{-6}$	$4.9\ x10^{-2}$
Confining layer (RDM)	$4.1x10^{-7}$	$4.1x10^{-7}$	$6.0x10^{-7}$	$8.4\ x10^{-2}$

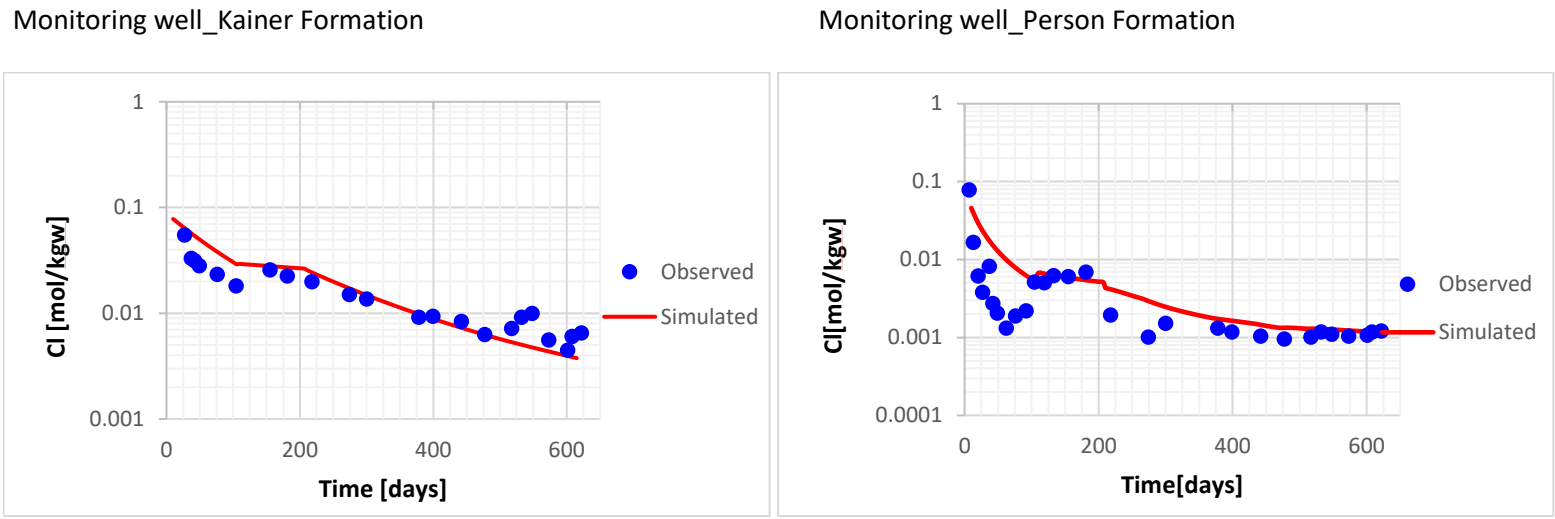

Figure 3.8. Observed and simulated chloride concentrations in monitoring wells.

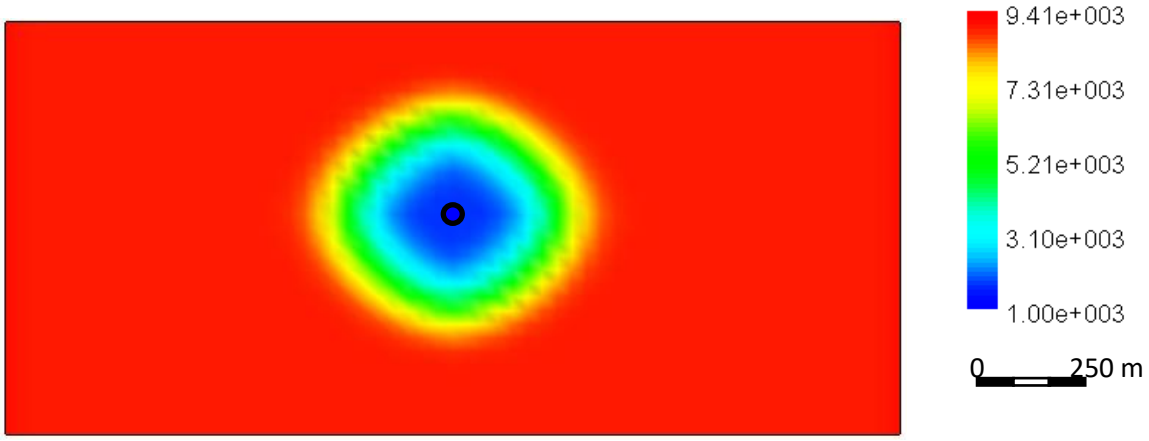

Figure 3.9. Distribution of TDS values in mg/L around the ASR well (black circle) after 60 days of recovery following 40-day storage.

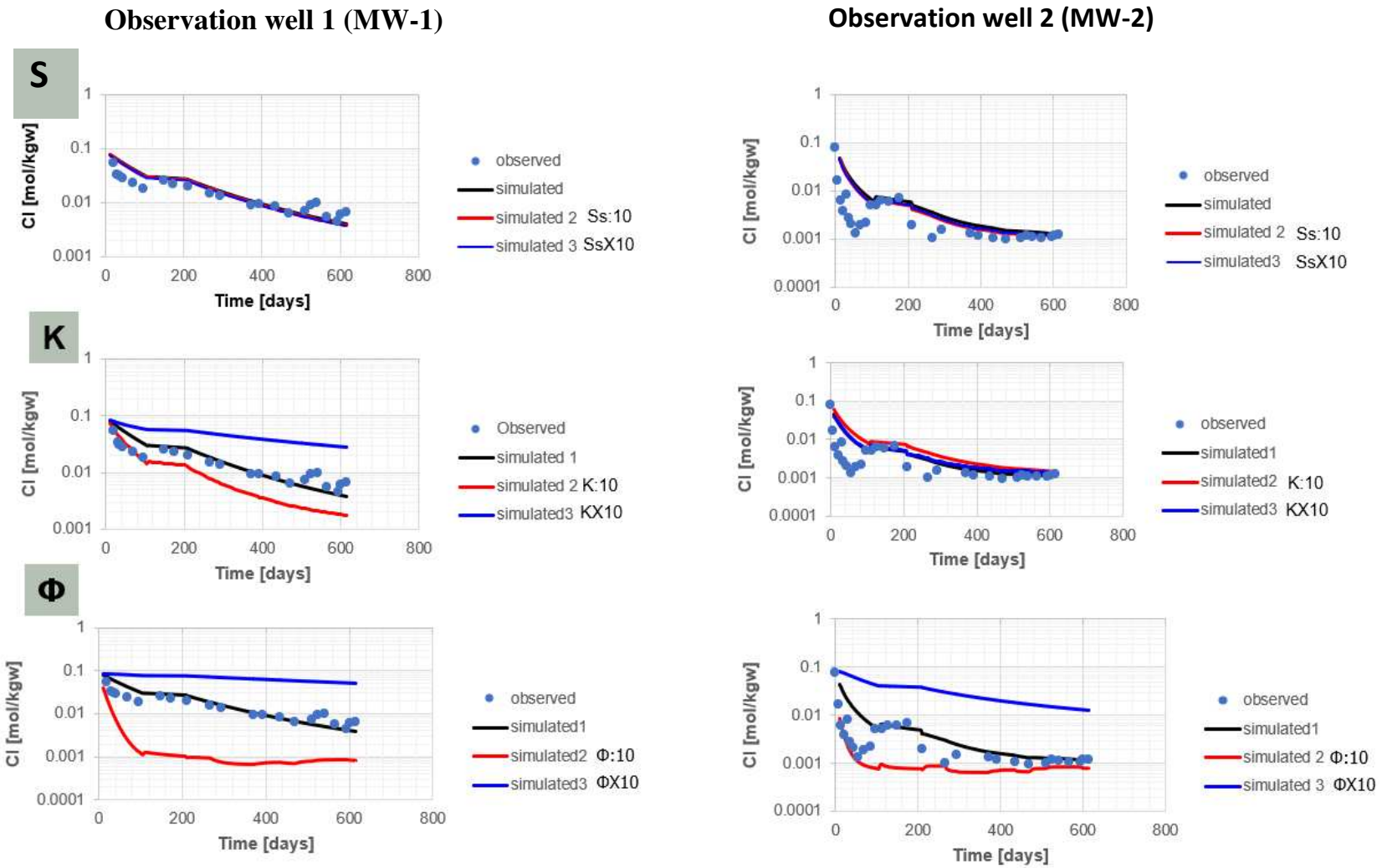

Figure 3.10. Sensitivity of chloride concentrations to specific storage (Ss), hydraulic conductivity (K) and porosity (Φ).

3.5. Discussion and interpretation

3.5.1. Characterization of the chemical composition of waters and groundwater evolution

Injectant water and native groundwater exhibit compositional differences based on their sources of origin. While the injectant water is a blend of Guadalupe River water and groundwater from the freshwater zone of the Edwards, both water types appear to reflect the composition of the rocks they interact with. The Guadalupe River flows from its headwaters in the Edwards Plateau region where predominantly Cretaceous limestone (Edwards aquifer outcrops) riverbed is intercalated with thinly bedded layers of shale and sandstone (Ashworth, 1983; Keen-Zebert and Curran, 2009). The carbonate riverbed along the course of the Guadalupe River likely sources a substantial amount of Ca^{2+} and HCO_3^- when interacting with river water in equilibrium with CO_2. Additionally, a portion of the Guadalupe River water represents drainage from the Unconfined Edwards aquifer. Likewise, the chemistry of the freshwater zone of the Edwards is sourced from water-rock interaction in the carbonate-dominated Edwards aquifer. The Na-Cl hydrochemical facies of the native groundwater of the Edwards badwater zone may have resulted from several processes wherein, among others, halite dissolution, and Na/Ca exchange with clays are invoked (Clement, 1989; Oettings et al., 1996). Furthermore, the sodium and chloride-rich water type of the native groundwater likely resulted from evolved basinal brines that have migrated up-dip or by the cross-formational flow through fractures and/or faults (Land and Prezbindowski, 1981). This is supported by the fact that areas of faults with the highest offsets in the New Braunfels area of the badwater zone of the Edwards have recorded the largest concentrations of sodium and chloride (Sharp and Smith, 2019). Other studies support the upward and landward flow of saline water migration from the gulfward units (Dutton et al., 2006; Hoff and Dutton, 2017). High sulfate concentrations in native Person and Kainer

groundwaters in the saline zone are hypothesized to be sourced from the dissolution of gypsum and other sulfate-bearing minerals (Maclay, Rettman, and Small, 1980), anhydrite (Schultz and Halty, 1997), and from a deep-seated origin (Banner, 1996).

The Piper diagram in Figure 3.5 shows a trend of native groundwater in the Person and Kainer Formations during the first ASR cycle recharge. The native groundwater from the Kainer Formation does not show a large range in hydrochemical facies, evolving from Na-Cl to mixed type (Ca-Mg-Cl). The Kainer Formation was not the storage zone targeted for ASR, so this shift in hydrochemical facies suggests a possible connection between both storage zones. On the other hand, the Person Formation hydrochemical groundwater facies progressed further towards the injectant chemical facies type (Ca-Mg-HCO3) with a TDS value decreasing below the TDS value limit of 1,000 mg/ L. In Figure 3.4, however, the trend in TDS values decreases with increasing recharge, implying a progressive freshening of the native groundwater in both storage zones. Furthermore, Kainer Formation shows a greater TDS increase than Person Formation at a high recovery rate of 0.06 m^3/s, from 900 to 3,000 (mg/kg) in the Kainer Formation and from 400 to 900 (mg/Kg) in the Person Formation. Since the two storage zones are separated by the Regional Dense Member (RDM) semi-confining unit, it is likely that the RDM leakage induced a downward intrusion of freshwater stored in the Person into the Kainer, resulting in a progressive TDS decrease therein. During recovery, however, the initial high recovery rate likely induced a high hydraulic gradient resulting in the upconing of brackish groundwater from the Kainer Formation. Reduction of the recovery rate resulted in a drop in the TDS gradient in the groundwater of both storage zones. This further supports the possibility of a hydraulic connection between the Kainer and Person Formations. Moreover, partial penetration of the ASR well within a high hydraulic conductivity zone, along with preferential flow via fractures within

the aquifer storage zone, could have resulted in excessive mixing between the injectant and the brackish native groundwater. Halihan et al. (2000) reported that fractures (and not channels) are the main control of flow in the San Antonio segment of the Edwards aquifer where the study area is located. Therefore, it is critically important to gain a further understanding of the heterogeneity and hydraulic properties of the RDM semi-confining layer and both storage zones in the study area for improved ASR recovery efficiency.

High flow rates induced by recovery pumping may promote enhanced chemical and physical processes (dispersive mixing, dilution, and advection) in areas surrounding the ASR well, resulting in a decrease in TDS values towards the ASR well. With increasing recharge time, the ratio of injectant/native groundwater increases, leading to a transition from the Cl^- water type to the HCO_3^- water type. This transition is accompanied by a decline in the total dissolved solids (TDS) characteristic of the injectant water. Moreover, solute or TDS transport during ASR operations depends on various factors, including aquifer heterogeneity, density contrast, dispersivity (Maliva et al., 2020; Maliva et al., 2020; Miotlinski et al., 2014), molecular diffusion, and advection (Ward et al., 2009). More importantly, the relatively large value set for longitudinal dispersivity is believed to considerably disperse solute plume hence mixing of dissolved components. The collective influence of these factors controls the feasibility of ASR operations. For example, some authors have shown that recovery efficiency tends to decrease with increasing storage zone salinity due to a combination of mixing with native groundwater and buoyancy stratification (or free convection) (Reese and Alvarez-Zarikian, 2007; Maliva et al., 2020).

Due to spatial and temporal complexities (Ward et al., 2009), the mixing ratio would be difficult to locate and delineate in the storage zone from the ASR well location. However, in

injectant-to-native groundwater ratio due to longer recharge times results in decreased TDS values at the ASR well and monitoring wells.

Water-rock interaction resulting in minimal calcite dissolution and an estimated 0.095% increase in the pore volume of the aquifer storage zone implies a potential increase in permeability of the aquifer system. Though minimal, calcite dissolution is expected since Ca^{2+} concentration increases with the cube root of the CO_2 when mixing two waters with different CO_2 pressures (Appelo and Postma, 2005), and the injectant being CO_2-rich. Furthermore, since dolomite is thermodynamically more stable than calcite within a wide range of temperatures and pressures (Althoff, 1977), calcite is more prone to dissolve in the mixed system. Calcite dissolution is followed by a pH decrease from 7.4 to 6.5 due to H^+ released into groundwater following the reaction. Figure 3.7 displays the predicted mineral volume change in the Edwards Aquifer resulting from the following reaction:

$CaCO_3 + HCO_3^- + 3H^+ = Ca^{2+} + 2H_2CO_3 = Ca^{2+} + 2HCO_3^{2-} + 2H^+$. However, the amount of dissolved calcite estimated to be 0.88 cm^3 is de minimus compared to the aquifer mineral volume (2,900 cm^3) set in the model. Therefore, calcite dissolution is likely a minimal contributing factor to the hydrochemical facies evolution of groundwater during recharge as shown in Figure 3.5. Mixing reflected in the water-water interaction model is more likely the main controlling pathway influencing the evolution of hydrochemical facies from Na-Cl water type towards Ca-Mg-HCO3.

3.5.2. Estimated hydraulic model parameters and recovery rate

Based on simulated chloride concentrations (Figure 3.8), conductivity and effective porosity values in the Kainer, Person, and RDM layers resemble a heterogeneous multilayer carbonate aquifer. Higher Kx and Ky values than Kz in aquifer zones indicate a dominant horizontal flow. Dominant horizontal flow implies high horizontal mixing (and limited vertical mixing) as also substantiated by a faster TDS drop in the Person Formation than in the Kainer Formation. As also observed by Parkhurst and Petkewich (2002), a large portion of the injectant moving through hydraulically conductive zones and the rest via the aquifer matrix causes TDS in the monitoring wells to be greater than the injectant TDS. However, the installation of multiple piezometers in the study area would enhance the estimation of Kx and Ky values.

The estimated RDM semi-confining layer Kz of 6.0 10^{-7} m/s is a reasonable value that would enable a hydraulic connection between both aquifer zones, especially if there is an induced hydraulic gradient between both zones during ASR operation. Fracture porosity recorded in the RDM thin sections (not shown here) is likely a contributing factor to the high Kz favoring leakage and connection of both storage zones. Furthermore, the variable thickness of the RDM with a very thin layer in some portions of the aquifer system could also promote the hydraulic connection between both aquifer zones. The modeled effective porosity depicts an ideal value of the bulk aquifer mass, though the Edwards aquifer system is defined by a triple porosity (matrix, fracture, and channel) pattern (Halihan et al., 2000; Budd and Vacher, 2004). The modeled Cl^- concentration is most sensitive to conductivity and effective porosity because these two parameters accurately predict groundwater flow and solute transport in the subsurface environment (Zheng and Bennett, 2002). In particular, higher sensitivity of chloride concentrations to vertical hydraulic conductivity highlights the impact a leaky confining layer

can have on flow pathways and solute transport. However, the lack of model sensitivity to storage could account for fractures within the aquifer system suppressing the control the storage parameter might otherwise exert in the overall flow pattern and chloride concentrations.

The simulated recovery rate of 0.03 m^3/s for 60 days that would not induce high TDS surpassing the secondary MCL represents 41 MG of water recovered, or 16 % of the total 253 MG of water injected during the first recharge cycle. The low recovery rate limits TDS increase up to the desired length of recovery time (60 days) upon which the threshold of 1,000 mg/L TDS is attained. The remaining 212 MG would be left in the aquifer and serve as a TDS buffer for subsequent recharge cycles, hence promoting increased recovery efficiency. Additionally, the implementation of two ASR wells separately targeting the Person and Kainer Formations holds promise in limiting induced hydraulic connection between both aquifer zones during recharge and recovery. This dual-well configuration represents a potential ASR optimization strategy to maximize efficiency of ASR operations while ensuring the recovered water meets acceptable TDS thresholds.

3.6. Conclusion

Characterization of injectant water and native groundwater chemistries, hydrochemical facies evolution, and aquifer hydraulic parameters is critical in evaluating the efficiency of aquifer storage and recovery (ASR) and optimizing ASR operations. While the NaCl facies type of the Edwards aquifer native groundwater likely results from halite dissolution and updip migration of brines, the Ca-Mg-HCO_3 type of the injectant reflects the Edwards aquifer matrix and riverbed geochemical composition. Though small amounts of calcite from the aquifer matrix are predicted to dissolve, mixing appears to adequately account for the hydrochemical facies evolution of groundwater during ASR operations. The lines of evidence pointing to a leaky confining RDM layer are: (a) hydrochemical facies evolution of the native Kainer groundwater from Na-Cl to mixed type, and (b) declining TDS values of the non-targeted ASR storage zone of the Kainer groundwater during recharge. This study suggests that further refined estimation of the hydraulic properties of the three layers, particularly the intervening semi-confining RDM layer, is critical for optimizing ASR operations. A substantial record in pumping/injectant rate history, sufficient monitoring data points, and geophysical logging would reduce uncertainty in the model parameterization and optimum ASR recovery rate.

3.7. References

Allan, U.S. 1989. Model for hydrocarbon migration and entrapment within faulted structures. *Bulletin of the American Association of Petroleum Geologists* 73, no. 7: 803–811.

Althoff, P.L. 1977. Structural refinements of dolomite and magnesian calcite and implications for dolomite formation in the marine environment. *American Mineralogist* 62, no.7-8: 772-783.

Appelo, C.A.J. and Postma D., 2005. *Geochemistry, groundwater, and pollution*. 2nd Ed. Leiden: Balkema, 649 p.

Ashworth, J.B., 1983. Groundwater availability of the lower Cretaceous formations in the hill country of south-central Texas. Texas Water Development Board, Report no. 273, Austin, TX.

Bahr, J.M. and Rubin, J., 1987. Direct comparison of kinetic and local equilibrium formulations for solute transport affected by surface reactions. *Water Resources Research* 23, no. 3: 438–452.

Banner, J.L., 1996. Seminar on Edwards aquifer saline-zone monitoring, SCTX Liaison Committee Meeting, November 20, 1996, San Antonio, Texas: Oral presentation.

Barker, R.A., Bush, P.W. and Baker, E.T., 1994. Geologic history and hydrogeologic setting of the Edwards-Trinity aquifer system, West-central Texas. U.S. Geological Survey Water-Resources Investigations Report 94-4039, 51 p.

Barry, D. A., Bajracharya, K., Crapper, M., Prommer, H., and Cunningham, C. J., 2000. Comparison of split-operator methods for solving coupled chemical non-equilibrium

reaction/groundwater transport models. *Mathematics and Computers in Simulation* 53, no. 1-2: 113-127.

Bethke, C.M., B. Farrell, M. Shafifi., 2023. The Geochemist's Workbench®, Release 17. GWB Reaction Modeling Guide. Aqueous Solutions, LLC, Champaign, IL, 209 p.

Blackmore, S., D., Pedretti, Mayer, K.U., Smith, L., and Beckie, R.D., 2018. Evaluation of single-and dual-porosity models for reproducing the release of external and internal tracers from heterogeneous waste-rock piles. *Journal of Contaminant Hydrology* 214: 65-74.

Blumberg, F.M., Deeds, N.E., and Pyne, R.D.G., 2019. New Braunfels Utilities: Aquifer Storage and Recovery Demonstration Project. TWDB Contract No. 1600011957. https://www.twdb.texas.gov/innovativewater/asr/projects/EAA/index.asp. Accessed June 2022.

Caine, J.S., J.P. Evans, and C.B. Forster. 1996. Fault zone architecture and permeability structure. *Geology* 24: 1,025–1,028.

Choquette, P.W. and Hiatt. E.E., 2008. Shallow-burial dolomite cement: a major component of many ancient sucrosic dolomites. *Sedimentology Journal* 55: 423-460.

Clement, T.J. and Sharp, J.M. Jr., 1987. Hydrochemical facies of the Edwards aquifer, Williamson and Bell Counties, Texas. In: J.C. Yelderman Jr., R.M. Slade Jr., J.M. Sharp Jr., and C.M. Woodruff Jr. (Editors), Hydrogeology of the Edwards Aquifer in the Northern Balcones and Washita Prairie Segments. *Geological Society of America (South-*

Central Section) Guidebook, reprinted in Austin *Geological Society Guidebook 10*, Earth Enterprises, Austin, TX, 61-70.

Clement, T.J., 1989. Hydrochemical facies in the badwater zone of the Edwards aquifer, central Texas. Doctoral dissertation, University of Texas at Austin.

Culkin, S.L., Singha, K. and Day-Lewis, F.D., 2008. Implications of rate-limited mass transfer for aquifer storage and recovery. *Groundwater Journal* 46, no. 4: 591-605.

Dillon P, and 30 others, 2019. Sixty years of global progress in managed aquifer recharge. *Hydrogeology Journal* 27, no. 1: 1–30. https://doi.org/10.1007/s10040-018-1841-z

Dutton, A.R., Nicot, J.P., and Kier, K.S., 2006. Hydrodynamic convergence of hydropressured and geopressured zones, Central Texas, Gulf of Mexico Basin, USA. *Hydrogeology Journal* 14: 859-867.

Edwards Aquifer Authority (EAA). 2012. Recovery Implementation Program—Habitat Conservation Plan (November). San Antonio, Texas, Edwards Aquifer Authority, 414 p.

Ellis, P.M., 1985. Diagenesis of the Lower Cretaceous Edwards Group in the Balcones Fault zone area, south-central Texas. Ph.D. Dissertation., University of Texas, Austin, Tex., p. 290.

Evenson, E.J., Orndorff, R.C., Blome, C.D., Böhlke, J.K., Hershberger, P.K., Langenheim, V.E., and Wood, T.M., 2013. US Geological Survey Water Science Strategy—observing, Understanding, Predicting, and Delivering Water Science to the Nation. U.S. Department of the Interior, U.S. Geological Survey Circular 1383–G, 49 p.

Fabryka-Martin, J., Davis, S.N. and Elmore, D., 1987. Applications of 129I and 36Cl in hydrology. Nuclear Instruments and Methods in Physics Research Section B: Beam Interactions with Materials and Atoms 29, no. 1-2: 361-371.

Feth, J.H., 1981. Chloride in natural continental water; a review. U.S. Geological Survey Water-Supply Paper 2176, 30 p.

Gelhar, L. W., Welty, C., & Rehfeldt, K. R. 1992. A critical review of data on field-scale dispersion in aquifers. Water resources research, 28(7), 1955-1974.

Gerges, N.Z., Dillon, P.J., Sibenaler, X.P., Martin, R.R., Pavelic, P., Howies, S.R. and Dennis, K., 2020. South Australian experience in aquifer storage and recovery. In Management of aquifer recharge for sustainability, 453-458. Adelaide, Australia: Balkema.

Green, R.T., Winterle, J., and Fratesi, B., 2019. Numerical groundwater models for Edwards Aquifer systems. In: Sharp JM Jr, Green RT, Schindel GM (eds) The Edwards aquifer: the past, present, and future of a vital water resource. *Geological Society of America Memoirs* 215:19–28.

Groschen, G.E., and Buszka, P.M., 1997. Hydrogeologic framework and geochemistry of the Edwards Aquifer saline-water zone, South-Central Texas. U.S. Geological Survey Water-Resources Investigations 97-4133.

Halihan, T., Mace, R.E., and Sharp, J.M. Jr., 2000. Flow in the San Antonio segment of the Edwards Aquifer: matrix, fractures, or conduits? *In: Groundwater flow and contaminant transport in carbonate aquifers*, Eds. C.M. Wicks and I.D. Sasowsky, Balkema, Rotterdam, 129-146.

Hanson, J.A., and Small, T.A., 1995. Geologic Framework and Hydrogeologic Characteristics of the Edwards Aquifer Outcrop, Hays County, Texas. U.S. Geological Survey Water-Resources Investigations Report 95-4265.

Hemker, C. J., 1984. Steady groundwater flow in leaky multiple-aquifer systems. *Journal of Hydrology*, 72, no. 3-4: 355-374.

Hoff Jr, S.Z., and Dutton, A.R., 2017. Beyond the Bad-Water Line—A Model for the Occurrence of Brackish Water in Upper Coastal Plain Aquifers in Texas. Gulf Coast Association of Geological Societies Journal 6: 135-149.

Hovorka, S.D., Dutton, A.R., Ruppel, S.C., and Yeh, J., 1994. Sedimentologic and diagenetic controls on aquifer properties, Lower Cretaceous Edwards carbonate aquifer, Texas: Implications for aquifer management. *Gulf Coast Association of Geological Societies* 44: 277-284.

Hovorka, S.D., Mace, R.E., and Collins, E.W., 1995. Regional distribution of permeability in the Edwards aquifer. Report 95-02. San Antonio, Texas, Edwards Underground Water District, 128 p.

Hovorka, S.D., Mace, R.E., and Collins, E.W., 1998. Permeability structure of the Edwards aquifer, South Texas—Implications for aquifer management. Texas Bureau of Economic Geology Report of Investigations 250, Austin, 55 p.

Hsieh, P.A. and Winston, R.B., 2002. User's Guide to Model Viewer, a Program for Three-Dimensional Visualization of Ground-water Model Results. U.S. Geological Survey Open-File Report 02-106, 18 p.

IOGCC. 2006. A Guide to Practical Management of Produced Water from Onshore Oil and Gas Operations in the United States. Interstate Oil and Gas Compact Commission and ALL Consulting. Oklahoma City, Oklahoma. https://iogcc.ok.gov/sites/g/files/gmc836/f/produced_water_guidebook2-2006_0.pdf. Accessed March 2022.

Keen-Zebert, A., and Curran, J.C., 2009. Regional and local controls on the spatial distribution of bedrock reaches in the Upper Guadalupe River, Texas. *Geomorphology* 112, no. 3-4: 295-305.

Knapp, R.B., 1989. Spatial and temporal scales of local equilibrium in dynamic fluid-rock systems. *Geochimica et Cosmochimica Acta* 53, no. 8: 1955-1964.

Kocis, T.N., and Dahlke, H.E., 2017. Availability of high-magnitude streamflow for groundwater banking in the Central Valley, California. *Environmental Research Letters* 12, no.8, 084009.

Kresic, N., 2006. *Hydrogeology and groundwater modeling*, 2nd ed. Boca Raton, Florida: CRC Press.

Land, L.S., and Prezbindowski, D.R., 1981. The origin and evolution of saline formation water, Lower Cretaceous carbonates, south-central Texas, USA. *Journal of Hydrology 54*, no. 1-3: 51-74.

Li, H., Lu, C., Werner, A.D., Irvine, D.J., and Luo, J., 2022. Impacts of Heterogeneity on Aquifer Storage and Recovery in Saline Aquifers. *Water Resources Research* 58, no. 5: e2021WR031306.

Lindgren, R.J., Dutton, A.R., Hovorka, S.D., Worthington, S.R.H., and Painter, S., 2004. Conceptualization and simulation of the Edwards aquifer, San Antonio region, Texas. U.S. Geological Survey Scientific Investigations Report 2004–5277, 143 p.

Lowry, C.S., and Anderson, M.P., 2006. An assessment of aquifer storage recovery using ground water flow models. *Groundwater Journal* 44, no. 5: 661 – 667.

Maclay, R. W., Rettman, P. L., and Small, T. A., 1980. Hydrochemical data for the Edwards aquifer in the San Antonio area, Texas (No. LP-131). Texas Department of Water Resources.

Maclay, R. W., and Small, T. A., 1983. Hydrostratigraphic subdivisions and fault barriers of the Edwards Aquifer, south-central Texas, U.S.A. *Journal of Hydrology* 61: 127–146.

Maclay, R. W., and Small, T. A., 1986. Carbonate Geology and Hydrology of the Edwards Aquifer in the San Antonio Area, Texas. Texas Water Development Board Report 296. https://www.twdb.texas.gov/publications/reports/numbered_reports/doc/R296/R296.pdf (Accessed May 2022).

Maclay, R. W., and Land, L. F., 1988. Simulation of flow in the Edwards Aquifer, San Antonio region, Texas, and refinement of storage and flow concepts. U.S. Geological Survey Water Supply Paper 2336-A, U.S. Geological Survey, Reston, VA., 48 p.

Maclay, R. W., 1989. Edwards Aquifer in San Antonio: Its hydrogeology and management: *South Texas Geological Society Bulletin* 30: 11–28.

Maclay, R. W., 1995. Geology and Hydrology of the Edwards Aquifer in the San Antonio Area, Texas: U.S. Geological Survey Water-Resources Investigations Report 95-4186, 64 p.

Maliva, R.G., Guo, W., and Missimer, T.M., 2005. Hydrogeology of Aquifer Storage and Recovery System Performance. Gulf Coast Association of Geological Societies Transactions 55:474–485.

Maliva, R. G., and Missimer, T. M., 2010. Aquifer storage and recovery: developing sustainable water supplies. *IDA Journal of Desalination and Water Reuse* 2, no. 2: 74-80.

Maliva, R. G., Manahan, W. S., and Missimer, T. M., 2020. Aquifer storage and recovery using saline aquifers: hydrogeological controls and opportunities. *Groundwater Journal* 58, no. 1: 9-18.

McKinney, D. C., and Watkins, D. W., 1993. Management of the Edwards aquifer: a critical assessment. Technical report CRWR 244. Center for Research in Water Resources, Bureau of Engineering
Research. University of Texas, Austin.

Miotliński, K. 2008. Coupled reactive transport modeling of redox processes in a nitrate-polluted sandy aquifer. *Aquatic Geochemistry* 14, no. 2: 117-131.

Miotliński, K., Dillon, P. J., Pavelic, P., Barry, K., and Kremer, S., 2014. Recovery of injected freshwater from a brackish aquifer with a multiwell system. *Groundwater Journal* 52, no. 4: 495-502.

Muehlberger, W. R., Galloway, W. E., Land, L. S., Sharp, J. M. Jr., Sawyer, D. S., and Light, M. P. R., 1987. Deep crustal drilling, Texas Gulf Coast, United States of America, in Boden, A., and Eriksson, K. G., eds., Deep Drilling in Crystalline Bedrock, Volume 2: Berlin, Springer-Verlag, p. 155–171.

Oetting, G. C., Banner, J. L., and Sharp, J. M. Jr. 1992. Geochemical and Sr isotopic variations in groundwaters of the Edwards aquifer, central Texas. *Geological Society of America*, Abstracts with Programs;(United States), 24 (CONF-921058).

Oetting, G.C., Banner, J.L., and Sharp, J.M. Jr., 1996. Regional controls on the geochemical evolution of saline groundwaters in the Edwards aquifer, central Texas. *Journal of Hydrology* 181, no. 1-4: 251-283.

Parkhurst, D.L., and Petkewich, M.D., 2002. Geochemical modeling of an aquifer storage recovery experiment. Charleston, South Carolina. In: Aiken GR, Kuniansky EL (eds) U.S. Geological Survey Artificial Recharge Workshop Proceedings, Sacramento, California: U.S. Geological Survey Open-File Rep 02-89: 37–40

Parkhurst, D.L., Kipp, K.L., Engesgaard, P., and Charlton, S.R., 2004. PHAST—A program for simulating groundwater flow, solute transport, and multicomponent geochemical reactions. U.S. Geological Survey Techniques and Methods 6: A8, 154 p.

Parkhurst, D.L., Kipp, K.L., and Charlton, S.R., 2010. PHAST Version 2—A program for simulating groundwater flow, solute transport, and multicomponent geochemical reactions. U.S. Geological Survey Techniques and Methods 6: A35.

Pearson Jr., F.J., and Rettman, P.L., 1976. Geochemical and isotopic analyses of waters associated with the Edwards limestone aquifer, central Texas. U.S. Geological Survey Report, Edwards Underground Water District, 35 p.

Pedretti, D., Vriens, B., Skierszkan, E.K., Baják, P., Mayer, K.U., and Beckie, R.D., 2022. Evaluating dual-domain models for upscaling multicomponent reactive transport in mine waste rock. *Journal of Contaminant Hydrology*, 244:103931.

Petkewich, M.D., Parkhurst, D.L., Conlon, K.J., Campbell, B.G., and Mirecki, J.E., 2004. Hydrologic and geochemical evaluation of aquifer storage recovery in the Santee Limestone/Black Mingo Aquifer, Charleston, South Carolina, 1998–2002. U.S. Geological Survey Scientific Investigations Report 5046: 81.

Price, R. E., & Pichler, T., 2006. Abundance and mineralogical association of arsenic in the Suwannee Limestone (Florida): Implications for arsenic release during water–rock interaction. *Chemical Geology*, *228*(1-3), 44-56.

Pyne, R.D.G., 1995. Groundwater Recharge and Wells, a guide to Aquifer Storage and Recovery. Boca Raton, Florida: Lewis. **Google Scholar**

Pyne, R.D.G., 2005. Aquifer storage recovery: a guide to groundwater recharge through wells, 608. Gainesville, Florida: ASR Systems LLC. **Google Scholar**

Reese, R.S., and Alvarez-Zarikian, C.A., 2007. Hydrogeology and aquifer storage and recovery performance in the Upper Floridan Aquifer, Southern Florida. U.S. Geological Survey Scientific Investigations Report 2006-5239. https://doi.org/10.3133/sir20065239.

Rose, P.R., 1972. Edwards Group, Surface and Subsurface, Central Texas: The University of Texas at Austin, Bureau of Economic Geology Report of Investigations 74, 198 p.

Sandoval, E., 2021. How this Texas town became one of America's fastest growing cities. The New York Times. https://www.nytimes.com/2021/08/19/us/new-braunfels-texas-growth-census.html. Accessed June 2022.

Scanlon, B.R., Mace, R.E., Barrett, M.E., and Smith, B., 2003. Can we simulate regional groundwater flow in a karst system using equivalent porous media models? Case study, Barton Springs Edwards aquifer, USA. *Journal of Hydrology* 276, no.1-4: 137-158.

Scanlon, B. R., Reedy, R. C., Faunt, C. C., Pool, D., and Uhlman, K., 2016. Enhancing drought resilience with conjunctive use and managed aquifer recharge in California and Arizona. *Environmental Research Letters* 11, no. 3: 035013.

Schindel, G.M., 2019. Genesis of the Edwards (Balcones Fault Zone) Aquifer, in Sharp, J.M., Jr., Green, R.T., and Schindel, G.M., eds., *The Edwards Aquifer: The Past, Present, and Future of a Vital Water Resource*: Geological Society of America Memoir 215, https://doi.org/ 10.1130/2019.1215(02).

Schultz, A. L., and Halty, S. R., 1997. Anhydrite: source of high sulfate concentration near Edwards aquifer "bad-water" line. *Bulletin South Texas Geological Society* 37:11–16.

Sharp, J. M., 1990. Stratigraphic, geomorphic and structural controls of the Edwards aquifer, Texas, U. S. A. In Selected Papers on Hydrogeology from the 28th International Geologic Congress, Vol.1 (eds. E. S. Simpson and J. M. Sharp, Jr.), p. 67– 82. International Association of Hydrogeologists, Heise, Hannover, Germany.

Sharp, J. M., and Banner, J. L., 1997. The Edwards Aquifer: A resource in conflict. Geological Society of America Today 7, no. 8: 1-9.

Sharp, J.M., Jr., and Smith, B.A., 2019. Water quality and the bad-water (saline-water) zone of the Edwards (Balcones Fault Zone) Aquifer, in Sharp, J.M., Jr., Green, R.T., and Schindel, G.M., eds., The Edwards Aquifer: The Past, Present, and Future of a Vital Water Resource 215, https://doi.org/ 10.1130/2019.1215(01).

Shaw, K., Stein, Z., Deeds, N., George, P., Milczarek, M., and Yan, Q., 2020. Statewide survey of aquifer suitability for aquifer storage and recovery projects or aquifer recharge projects [abridged]: Report to the 87th Texas Legislature. **Google Scholar**

Smith, B. A., Hunt, B. B., and Schindel, G. M., 2005. Groundwater flow in the Edwards Aquifer: Comparison of groundwater modeling and dye trace results. In *Sinkholes and the Engineering and Environmental Impacts of Karst*, ed. B.F. Beck, 131– 141. Reston, Virginia: American Society of Civil Engineers Geotechnical Special Publication No. 144.

Smith, B. A., Hunt, B. B., and Darling, B. K., 2017. Hydrogeology of the Saline Edwards Zone. Southeast Travis County, Central Texas: Barton Springs/Edwards Aquifer Conservation District Report of Investigations, 1015, 66 p.

Wallis, I., Prommer, H., Pichler, T., Post, V., Norton, S.B., Annable, M.D., and Simmons, C.T., 2011. Process-based reactive transport model to quantify arsenic mobility during aquifer storage and recovery of potable water. *Environmental Science & Technology* 45, no. 16: 6924–6931.

Ward, J. D., Simmons, C. T., Dillon, P. J., and Pavelic, P., 2009. Integrated assessment of lateral flow, density effects, and dispersion in aquifer storage and recovery. *Journal of Hydrology* 370, no. 1-4: 83-99.

Warner, D.L. 2001. Technical and Economic Evaluation of the Protection of Saline Ground Water Under the Safe Drinking Water Act and the UIC Regulations. Report prepared for Groundwater Protection Council. **Google Scholar.**

Wong, C. I., Kromann, J. S., Hunt, B. B., Smith, B. A., and Banner, J. L., 2014. Investigating groundwater flow between Edwards and Trinity Aquifers in central Texas. *Groundwater* 52, no. 4: 624-639.

Zheng, C., and Bennett, G.D., 2002. *Applied Contaminant Transport Modeling*, 2nd ed. New York: Wiley. **Google Scholar.**

CHAPTER 4: MANAGING ARSENIC MOBILIZATION DURING AQUIFER STORAGE AND RECOVERY IN CARBONATE AQUIFERS (FLORIDAN AQUIFER, FLORIDA, USA)

4.1. Introduction

Amidst climate stress and overpopulation, freshwater availability and quality are becoming a global concern (Maliva and Missimer, 2010; Koutroulis et al., 2019). These issues are widely recognized as the most critical challenges of the 21st century, with projections indicating a staggering global population increase of over three billion within the next 50-75 years, accompanied by a twofold increase in urban inhabitants (Jury and Vaux, 2005).

Managed aquifer recharge (MAR) is one of the strategies available to maintain, enhance and secure the quantity, reliability, and quality of water supplies (Dillon et al., 2019). MAR has seen increased interest in supplying drinking water, and current predictions indicate that MAR applications will soon provide ~ 10% of the world's drinking water (Dillon et al., 2012). One of the MAR technologies is aquifer storage and recovery (ASR) consisting of injecting treated surface water into aquifer zone(s) for later recovery when needed (Pyne, 2005) for drinking, industrial or irrigation purposes (Maliva and Missimer, 2006). Each ASR cycle is comprised of three phases: (a) the injection phase, occurring when there is an excess of freshwater availability, (b) the storage phase, taking place when there is adequate freshwater to meet demand, and (c) the recovery phase, initiated when there is a decrease in freshwater supply relative to the demand for water (Li et al., 2022). ASR systems are utilized for the storage of distinct types of water, including treated drinking water, reclaimed water, partially treated surface water, and water obtained from adjoining aquifers (Lowry and Anderson, 2006). ASR operation is attractive due

to its capacity to offer extensive storage volumes, potentially surpassing alternative options (e.g., surface water reservoirs) while maintaining a comparatively smaller surface footprint, offering lower costs, and reducing evaporative losses and vulnerability to contamination (Kocis et al., 2017; Scanlon et al., 2016). ASR systems are often able to meet water management needs with a capital cost that is typically less than half that of other water supply and storage options (Pyne, 2005).

However, two associated factors are considered in ASR operations: (1) recovery efficiency, the proportion of water recovered from the recharged water, and (2) the quality of recovered water compared to the recharged water (Miotlinski et al., 2014). Water quality can have an impact on the quantity of water recovered during ASR operations, as it may impose limitations when the recovered water fails to meet regulatory constraints for drinking purposes. For example, out of 26% of abandoned ASR operations in the U.S, circa 11% of abandonment of ASR wells is attributed to recovered water that exceeded the arsenic (As) standard levels (Bloetscher et al. 2014; Fakhreddine et al., 2021). Water resource availability indeed depends on both quality and quantity metrics (Everson et al., 2013). A disadvantage of ASR can be the need for post-recovery treatment of water resulting from induced remobilization and increased concentrations of trace elements (Fe, Mn, As, Ni, Mo, Co) when oxygenated water is injected into a reduced aquifer media (Antoniou et al., 2012). Release of these trace elements has been shown to result from the oxidation and dissolution of mineral phases (e.g., pyrite, siderite), and sedimentary organic material (SOM) contained in the aquifer matrix (Stuyfzand, 1998; Appelo et al., 1999; Fakhreddine et al., 2021). In particular, arsenic mobilization during ASR has been reported as the chief qualitative challenge in ASR operations in Florida (Mirecki, 2004; Pyne et al., 2004; Price and Pichler, 2006; Arthur et al., 2007; Jones and Pichler, 2007; Stuyfzand and

Pyne, 2010; Wallis et al., 2011), Australia (Vanderzalm et al., 2007 and 2011; Prommer et al., 2018), and the Netherlands (Stuyfzand, 2001; Stuyfzand et al., 2005; Antoniou et al., 2015). In general, pathways of arsenic mobilization during ASR include (1) oxidation of sulfide minerals (Stuyfzand, 1998; Arthur et al., 2001; Stuyfzand et al. 2002; Price and Pichler, 2006), (2) dissolution of carbonate minerals (Sø et al., 2008), (3) desorption from Fe oxyhydroxide/oxide surfaces from highly alkaline groundwater (Vanderzalm et al., 2011), reduction dissolution of Fe oxyhydroxides or reduction of As species from As(V) to As(III) or competitive displacement of As from sorption sites by other inorganic solutes (phosphates, etc.) (Wallis et al. 2011). Despite this extensive investigation on the fate and transport of arsenic during ASR operation, few studies (e.g., Antoniou et al., 2015) have examined operational methodologies aimed at improving recovered water quality and recovery efficiency and hence optimizing ASR performance. However, despite an extensive database on arsenic in ASR operations in the Upper Floridan aquifer, published geochemical studies have not addressed possible methodologies to counter arsenic mobilization during ASR. The Upper Floridan aquifer offers a unique laboratory for ASR operations with a history of both successes and failures. While some operations encountered arsenic-related challenges resulting in failures, others have been successful and continue to operate.

The geogenic origin of As during ASR operations in southern Florida is supported by the fact that neither the injectant nor the native groundwater has any appreciable As concentrations while elevated As concentrations are reported in recovered water to levels above the U.S Environmental Protection Agency (EPA) drinking water standards of 10 µg/L (Wallis et al., 2011). Arsenic as high as 11,200 mg/kg is reported to be incorporated structurally into pyrite in the Upper Floridan aquifer (Lazareva and Pichler, 2007; Price and Pichler, 2006; Pichler et al.,

2011). Oxidation dissolution of pyrite following recharge of oxygenated surface water into reducing native groundwater releases As into the stored water to levels surpassing 10 μg/L (Arthur et al., 2002). Arsenic mobilized into groundwater is subsequently oxidized from As^{3+} to As^{5+} which later sorbs on the newly formed ferrihydrite (HFO) sorption sites. Decreasing pH following pyrite dissolution and microbial activity enhances the sorption of arsenic on ferric hydroxide (Pyne et al., 2007). These oxidation and sorption processes leading to reduced arsenic concentration in groundwater take place as long as a sustained oxidizing environment is maintained in the vicinity of the ASR well. While several studies (Pyne et al., 2007; Fakhreddine et al., 2021; Wallis et al., 2011) have developed a process-based understanding of physical and geochemical factors controlling As mobilization and subsequent attenuation, operational methodologies built upon this understanding are yet to be extensively explored. Current practices in Florida consist of arsenic post-treatment of recovered water, increasing the cost of the ASR operation, and posing concerns about ASR as a reliable and sustainable water supply technology. However, to counter the mobilization of arsenic into recovered groundwater, operational methodologies have been employed, two of which are (a) low recovery rate and increasing cumulative storage volume, and (b) maintenance of a buffer zone (Figure 4.1.b) during ASR operation cycles. The first methodology (a) is employed on the premise of an incremental build-up to attain the estimated buffer zone volume in case the buffer zone volume cannot be achieved right away because of several constraints (e.g., availability of injectant water). Both the (a) and (b) methodologies have proved to promote arsenic attenuation around an ASR well based on field data in the Upper Floridan Aquifer ASR operations. Ideally, the buffer zone is formed prior to starting ASR operational cycles, and together with the stored water forms the target storage volume (TSV). The TSV comprises the stored water volume to be recovered and the buffer zone

volume (Figure 4.1.b) with both volumes being generally equal. The buffer zone volume is formed and maintained throughout the ASR cycles to counter As mobilization in water to be recovered. The buffer zone volume is adjusted based on operating performance and aquifer hydrogeochemistry; a high TDS groundwater, for example, would theoretically necessitate setting the buffer zone volume to 100% of the volume to recover (Pyne, 2005). While building a buffer zone and maintaining it throughout ASR cycles, as opposed to other methodologies, has been shown to attenuate arsenic concentration, it is, however, not well known to what extent arsenic is mobilized and distributed within the aquifer based on this method.

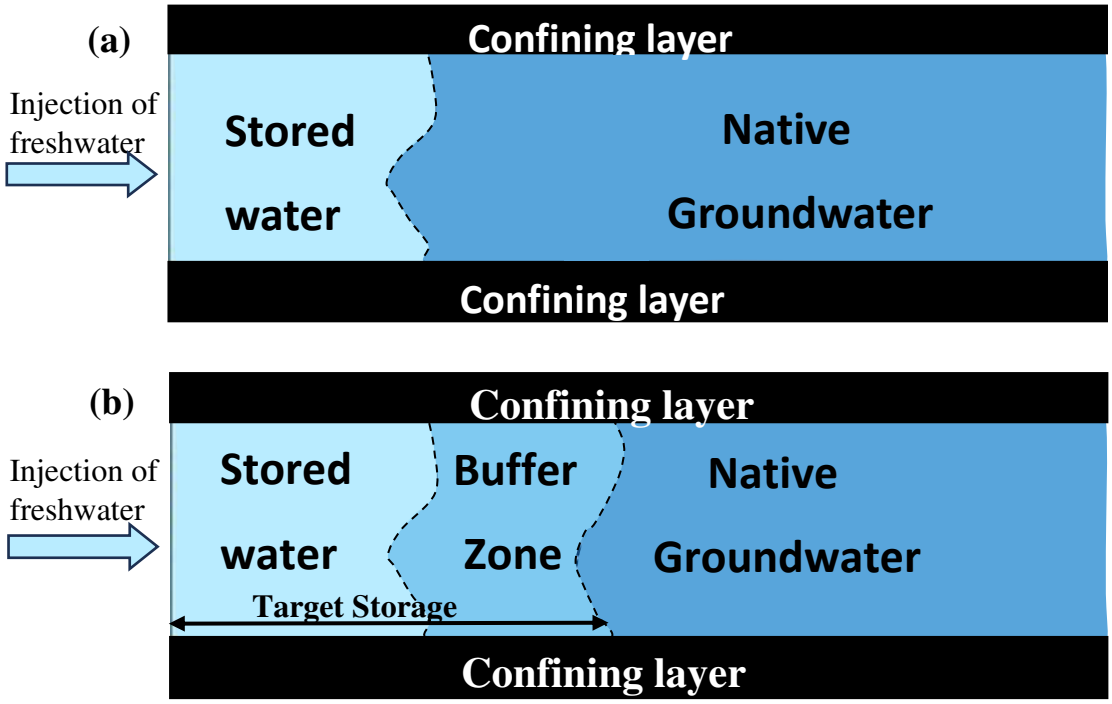

Figure 4.1. Simplified 1-D ASR conceptual models with development of stored water and native groundwater in Figure 4.1.a, and a buffer zone methodology with the buffer zone separating both the stored water and the native groundwater zones in Figure 4.1.b (Pyne, 2005). The stored zone is proximal to the ASR well and hosts significant physical and geochemical processes; the buffer zone separates the stored water from the native groundwater. The target storage volume comprises the buffer zone and the stored water zone. While the first scenario can also develop these three zones, due to its operational methodology, the stored and buffer zone are considered to be recoverable. The second scenario, however, maintains part or all of the buffer zone, and only recovers the stored water.

Based on extensive data from ASR wellfields targeting the Upper Floridan aquifer (UFA) in the Suwannee and Ocala Formations (Fig. 4.2), this study investigates arsenic mobilization and attenuation using statistical data analysis (linear regression, boxplots) coupled with the Geochemist's Workbench (GWB) 1D reactive transport model (RTM) to hypothesize possible processes controlling arsenic fate during ASR operation, the distribution and patterns of arsenic concentrations, and the extent to which operational methodologies impact arsenic fate. Data analysis is carried out on a historical data set from the City of Tampa ASR wellfields and the reactive transport model of the ongoing Kissimmee River ASR (KRASR) project. Mineralogical and geochemical data of the targeted storage zone in the Ocala are used to build an idealized 1D RTM to substantiate the pattern observed in arsenic fate using two operational methodologies (the buffer zone and the storage zone depletion) applied to the ongoing Kissimmee River ASR. The geochemical model aims to simply set fundamentals (aquifer mineral composition, redox conditions, aqueous phase chemistry, and ASR operational stresses) and validate predicted trends from historical ASR operations and determine the extent to which arsenic is mobilized and distributed temporally and spatially within the storage zone during the first injection using two ASR operational methodologies. Understanding As mobilization and fate are particularly crucial as the concentration of arsenic in the recovered water is contingent upon the temporal and spatial distribution pattern of the mobilized arsenic during the injection, formation of HFO, and sorbed As, and the geochemical processes ensuing during the ASR recovery.

Selection of these ASR operations in the Tampa and Ocala ASR wellfields (Figure 4.3A) is based on the major importance of ASR in Florida for (1) the Comprehensive Everglades Restoration Plan (CERP) for ecosystem restoration in Southern Florida; (2) continued extension of ASR well fields in all aquifer zones in the Upper Floridan aquifer and to other aquifer zones

of the Floridan aquifer system to meet ecosystem and drinking water demands; and (3) available extensive geological and time series hydrochemical datasets for ASR operations in Florida.

4.2. Hydrogeology

The ASR wells are drilled in the Floridan aquifer system (FAS), specifically in the Upper Floridan aquifer, for freshwater storage. Geologically, the multilayer FAS comprises a thick sequence of Tertiary carbonate rocks hydraulically connected to varying degrees and with permeability several orders of magnitude greater than the confining layers bounding its upper and lower surfaces (Miller, 1986).

Hydrostratigraphically (Fig. 4.2), the FAS is made of the Upper Floridan Aquifer (UFA), the Middle Confining Unit (MCU), the Lower Floridan Aquifer (LFA), and the Sub-Floridan Confining Unit. Among them, the UFA is a highly permeable carbonate aquifer ~ 300-m thick and an important source of water. The aquifer zone targeted for the studied ASR storage is in the Upper Floridan Aquifer (UFA). The other aquifer zone and units are not discussed here because they are currently not part of the ASR-targeted storage zones. Carbonate units of the Upper Floridan Aquifer (UFA) System are, in ascending order, the upper portion of the middle Eocene Avon Park Formation, the late Eocene Ocala limestone, and the early Oligocene Suwannee limestone (Figure 4.2). The Eocene Avon Park Formation and Ocala limestone are the thickest and most productive formations of the FAS (Miller, 1990).

Hydrostratigraphic unit		Series		Formation		Lithology
Surficial Aquifer System (SAS)		Holocene to Pliocene		Various		Sand, Silt, Clay, shell, peat, carbonate
Intermediate Aquifer System (IAS)/ Intermediate Confining Unit (ICU)				Hawthorn Group	Peace River Formation	Interbedded sand, silt, gravel, clay, Limestone, dolostone, phosphatic sand
					Arcadian Formation	Sandy limestone, shale beds dolostone, phosphatic sand, silt, clay
Florida Aquifer System (FAS)	Upper Floridan Aquifer (UFA)	Oligocene		Suwannee Limestone		Limestone
		Eocene	Late	Ocala Limestone		Limestone
	Middle Confining Unit (MCU)		Middle	Avon Park Formation		Limestone, dolostone, gypsum/anhydrite
	Lower Floridan Aquifer (LFA)		Early	Oldsmar Formation		Dolostone, gypsum/anhydrite
	Sub-Floridan Confining Unit	Paleocene		Cedar Keys Formation		Dolostone, dolomitic limestone, anhydrite

Figure 4.2. Hydrostratigraphic column of the Upper Floridan aquifer system (modified from Koopman, 2022; Hughes et al., 2009; Johnston and Bush 1988; Upchurch et al., 2019).

Deposited on the Florida platform in very shallow subtidal to supratidal settings (Cander, 1991), the Avon Park Formation rocks are the oldest exposed rocks in Florida (Randazzo, 1980). The lower Avon Park Formation is pervasively dolomitized with >95% dolomite, whereas the upper part is commonly undolomitized (Budd, 2001). Interstitial void spaces filled with evaporites, mainly gypsum and anhydrite, are common in deeper sections of the Avon Park Formation, resulting in reduced porosity of the formation (Tihansky, 2005). The Avon Park Formation has high total dissolved solids (TDS) of ~ 30,000 mg/L in many areas of the Lower Kissimmee basin where the study area is located (Geddes et al., 2018). It is composed of a mixture of skeletal and peloidal grains dominated by benthic foraminifera deposited in shallow water (Melzer and Budd, 2008). If present, sedimentary structures are burrows and cross-bedding (Budd 2001). Low foraminifera Sr isotope ratios and heavy oxygen isotopes suggest the diagenetic process was dominated by shallow marine burial diagenesis (Cander, 1991).

The Ocala limestone was deposited in the inner to the middle part of the distally steepened carbonate platform (Loizeaux, 1995; Budd, 2001) during late Early Cretaceous time in a shallow subtidal to tidal flat setting. It is dominated by a cyclic stacking pattern of shallowing upward skeletal peloidal wackestone, packstone, and grainstone with each sequence made of two to three depositional cycles. Each sequence is also bound by a transgressive surface showing no evidence of subaerial exposure. Intense bioturbation in the Ocala limestone has masked sedimentary structures. Though diverse, the fauna is dominated by foraminifera indicative of open marine conditions (Loizeaux, 1995).

The Oligocene Suwannee limestone shows a complex interplay essentially of subtidal facies formed on a shallow water carbonate ramp (Hammes, 1992). It is dominated by grainstone bodies up to 30 m thick exhibiting a shallowing upward cyclic pattern. The Suwannee limestone

is dominated by skeletal limestone intercalated with minor dolomite mostly occurring in the lowermost portion of the Suwannee (Gaswirth et al., 2006). The upper part of the Suwannee is abundant in mollusk molds and casts (Miller, 1986) with high moldic porosity (Price and Pichler, 2006) providing potential zones for ASR. It also may contain minor amounts of phosphatic quartz- and clay-rich limestone near the top of the formation, and a 3-6 m small layer of dolostone in the lower third. Additional minor amounts of chert nodules, organic matter, and pyrite have also been reported (Miller, 1986; Green et al., 1995).

Because the Cenozoic aquifers, and in particular the UFA, are young and thus have not been deeply buried and subjected to intense diagenetic overprints, they tend to retain much of their original matrix porosity (Budd, 2002; Budd and Vacher, 2004). With higher matrix porosity observed in the Ocala limestone, Suwannee limestone, and Avon Park Formation, comes higher matrix permeability in the range of $<10^{-14.4}$ to $10^{-11.1}$ m^2, values strongly correlated with depositional facies (Budd and Vacher, 2004). In general, the Upper Floridan aquifer comprises several thin high-flow zones (of high permeabilities) interlayered with thick zones of low permeabilities. One or two major flow zones provide the bulk of the aquifer productivity (Reese et al., 2007).

Most ASR operations target the Avon Park permeable zone (AAPZ) followed by the Suwannee limestone and to a lesser extent the Ocala limestone (Fischler et al., 2015). In all three, arsenic was found to be sequestered in pyrite and hence pyrite oxidation and dissolution is the main process of arsenic release into groundwater upon ASR injections (Lazareva et al., 2015; Arthur et al., 2005, 2007; Wallis et al., 2011).

The Kissimmee ASR project targets the storage zone in the Ocala. Native groundwater in this area has a low total dissolved solids (TDS) content and as water moves deeper into the

aquifer, TDS increases, and sulfate tends to become the dominant species due to gypsum and anhydrite minerals in the Avon Park Formation. Preferential flow zones of high permeability corresponding to unconformable formation contacts and to a lesser extent bedding planes are commonly revealed in the Ocala Formation by geophysical flow logs (Mirecki et al. 2013). In Tampa, however, the Suwannee storage zone targeted comprises wackestone to pelletal and foraminiferal grainstone (Gilboy, 1985; Hammes, 1992; Williams et al., 2002; Green et al., 1995).

4.2. 1. Previous work

In the city of Tampa, five ASR wellfields were investigated for water recovery rate and arsenic concentrations in the recovered water. Overall, there are 141 recovered water data samples distributed among each ASR field (ASR- #) considered as follows: 27 samples for ASR-4, 29 samples for ASR-5, 28 samples for ASR-6, 29 samples for ASR-7, 28 samples for ASR-8. These water data inputs are derived from the recovery periods of the fifth cycle of all five ASR well fields. These inputs will aid in understanding the relationship between percent recovery (ratio of volume recovered with volume injected) and the arsenic mobilization and attenuation. Recharge volumes range from 79.86 million gallons (MG) (minimum in ASR-5) to 155.46 MG (maximum in ASR-8) with the same storage period of 63 days in all ASR fields (see Supplementary File). The range in percent recovery is from 80% to 158.6%. The volume of water recharged and recovered, and time series water data chemistry were retrieved from the Florida Department of Environmental Protection (FDEP) Oculus Electronic Document Management System.

4.3. Methodology

Two sites (Fig. 4.3) are being investigated for arsenic mobilization and attenuation during aquifer storage and recovery. The first site is the Tampa ASR wellfield which supplied data used for statistical analysis to investigate changes in arsenic concentration patterns with time during ASR cycles with different recovery rates (or operational methodologies). This helps to make inferences on how As behaves in response to different recovery rates resulting in changes of (physico-) chemical conditions impacting arsenic behavior in aquifer media. The second site, the Kissimmee River ASR (KRASR) wellfield, is located to the North of Lake Okeechobee, and West of the Kissimmee River at circa 2,000 m away (27° 8'57.84"N, 80°52'27.00"W) from the 2013 KRASR. Based on injectant and groundwater chemistry from the KRASR site, the forward 1D reactive transport model presented here is used to predict As mobilization using two operational scenarios.

4.3.1 Recovered water data (Tampa ASR wellfields)

To easily interpret and infer processes mobilizing arsenic during ASR operations, the lower and higher % recoveries of 80% and 158.6% were compared to the temporal evolution of pH, As and ORP. However, due to the inherent interferences and limitations of standard methods for measuring oxidation-reduction potentials (ORP) (Sale et al., 2021), the accuracy and reliability of ORP measurement data are likely to have been compromised. While acknowledging this potential limitation, the available ORP data are used to provide a rough estimation of the aquifer redox dynamics during ASR operation.

The selection of the fifth ASR cycle in all 5 ASR fields is based on the availability of sufficient data and the same time frame of each ASR cycle (injection, storage, and recovery

times) easing data analysis and interpretation. Arsenic concentrations less than 0.001 µg/L (analytical limit of detection) are considered zero for convenience to facilitate the interpretation.

4.3.2 Petrography and mineralogy (KRASR wellfield)

The storage zone at the KRASR site is targeted in the Ocala limestone at depths between 166 m to 261m. The mineralogy of the Ocala limestone at this site is based on data retrieved from the 2022 ASR wellfield (Figure 4.3). X-ray diffraction (XRD) analysis done by Mineralogy Inc. (Murphy, 2022) identified calcite as the dominant mineral phase with relative modal abundance (%) ranging from 91.5 to 100 %, followed by fluoroapatite (<0.5 to 5 %), quartz (<0.5 to 3%), and dolomite (<0.5 to 1%) (Table 4.1). Trace framboidal pyrite is reported to contain arsenic in the Ocala up to 1.66% (Fischler and Arthur, 2010). Photomicrograph examination (Figure 4.4) further reveals two main mineral phases, calcite associated with minor dolomite. Point counted mineralogical abundance yields a rough estimate of 98% calcite and minor dolomite associated with sulfide mineral, likely an arsenian pyrite. For simplification purposes, the mineralogical abundance of the aquifer matrix considered in this model is as follows: calcite (98% or 800 g), and dolomite (1% or 15 g); the rest of the mineral assemblage to be considered is pyrite and arsenopyrite having a combined abundance of 1%. To maintain the model simplicity, the estimated amount of 0.2 g of pyrite (FeS_2) and 0.002 g of arsenopyrite ($FeAsS_2$) in 815.202 g of rock is set according to the mass ratio of 0.01 As/FeS_2 reported by Price and Pichler (2006).

Table 4.1. Mineralogical and chemical composition of samples from the Ocala limestone. Note that pyrite and arsenopyrite were not included as they were not identified by the XRD analysis

		Sample depth (m)			
		166.1-166.4	180.4-180.7	193.3-193.6	239.6-239.8
		Relative abundance (%)			
Mineralogical composition	Quartz	3	<0.5	<0.5	0.5
	Calcite	91.5	100	100	97
	Aragonite	(no data)	(no data)	(no data)	0.5
	Dolomite	<0.5	(no data)	<0.5	1
	Fluoroapatite	5	(no data)	<0.5	0.5
	Illite/mica	0.5	(no data)	<0.5	0.5

(retrieved from Murphy, 2022)

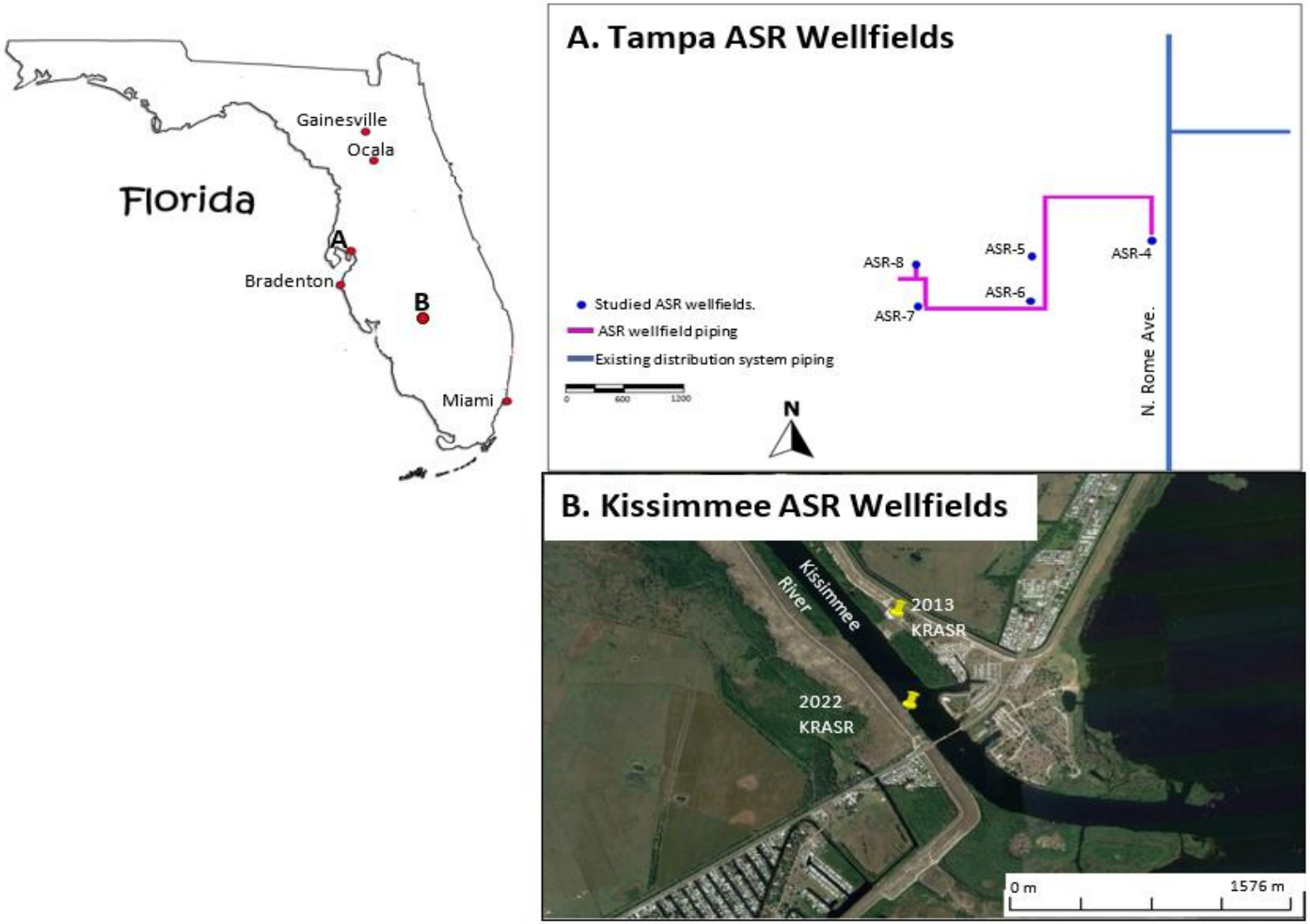

Figure 4.3. Study area maps. **a** Location of ASR wellfields in Tampa (modified from Pyne et al. 2007); **b** Kissimmee ASR wellfields.

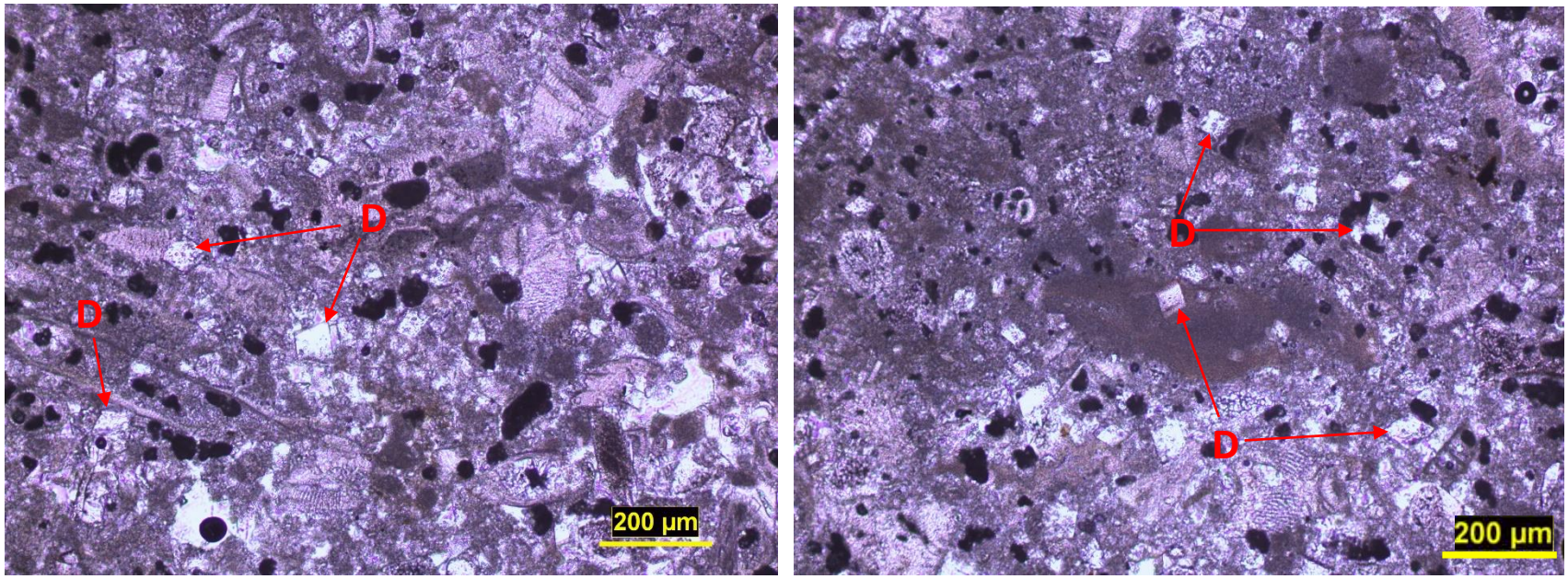

Figure 4.4. Thin section photomicrographs of the Ocala (dolomitic) limestone samples from the ASR well drill at the 2022 KRASR site (depth ranges from 199.9 – 200 m). Skeletal grains and matrix are filled (or replaced) to varying degrees by dolomite cement (D showing conspicuous dolomite grains). Black dots scattered within carbonate matrix and skeletal grains would possibly be an association of organic matter and pyrite. Note the samples were not impregnated with blue died epoxy to highlight porosity in blue color.

4.3.3 Hydrogeochemical characteristics, conceptual model, and selected reaction network (KRASR wellfield)

The reactive transport model is applied to the current Kissimmee ASR operation, specifically the 2022 KRASR wellfield (Figure 4.3). The injectant and native groundwater data (Table 4.2) used in this simulation are retrieved from the 2013 final technical data report of the 2013 KRASR wellfield (Mirecki, 2013). The 2013 ASR water data is being utilized due to the unavailability of the 2022 KRASR water data. However, it is assumed that the water composition used in both ASR operations is similar. In the 2022 KRASR wellfield operation, the injectant water consists of treated Kissimmee River water, undergoing a comparable treatment process to ensure a similar injectant water composition as in the 2013 ASR operation. Additionally, the native groundwater in both ASR wells, despite being separated by the Kissimmee River, is expected to exhibit similar geochemical characteristics.

Table 4.2. Chemistry of recharge and native groundwater.

		Recharge water quality	Native UFA water quality
Temp	°C	25.3	25.5
pH		6.7	7.8
ORP	mV	130	-283
Dissolved oxygen	mg/L	4.5	0.3
Ca	mg/L	19.2	51.5
Mg	mg/L	4.8	38.7
Na	mg/L	16.1	152
K	mg/L	4	8.3
SO_4^{2-}	mg/L	15.6	198
Cl-	mg/L	31.1	242
Total alkalinity as CaCO3	mg/L	50	91
Calcite	Log Q/K	-1.7	0.0
Dolomite	Log Q/K	-2.9	1.1
As	µg/L	0.9	<2.6
Fe	µg/L	226	28

The 2013 ASR operation involved injection of oxygenated and treated freshwater into the reduced Ocala Limestone aquifer. Though the arsenic concentration in the native groundwater is small (<2.6 µg/L), its value is set to 10 e-10 µg/L to allow calculations.

To investigate the arsenic fate, two operational methodologies for the first ASR injection cycle are tested using the modified model of Lazareva et al. (2015) in a 1D-reactive transport model of the Geochemist's workbench® 2023 software package (version 17.0.0; Bethke et al., 2022a). Specifically, the fourth model scenario in Lazareva et al. (2015) investigates mobilization of geogenic arsenic (As) using bench-scale leaching experiments from arsenic-rich rock cuttings of the Avon Park Formation (Upper Floridan Aquifer) to simulate key reactions controlling As behavior in time (and space) as water flows through it. Therefore, part of the conceptual models developed in this fourth model were included to infer the validity of the conceptual model for As attenuation using the first injection volume, the value of which depends on two scenarios involved in this study. For transport in single direction x, the equation is expressed as follows (Bethke, 2022):

$$\frac{\partial(\theta C_i)}{\partial t} = \frac{\partial}{\partial x}\left(\theta\, D_x \frac{\partial C_i}{\partial x}\right) - \frac{\partial}{\partial x}\left(\theta v_x C_i\right) + \theta R_i$$

Where θ is the porosity, C is the component's dissolved concentrations (including arsenic species), D is the dispersive coefficient tensor (L^2T^{-1}), V_x is the velocity in x direction, and Ri is the reaction rate (mol $L^{-3}T^{-1}$) comprising chemical and physical processes by which a component can be added or removed from solution in a geochemical model.

The 1-D reactive transport model simulates (1) (As-bearing) pyrite and arsenopyrite oxidation following injection of oxygen-rich injectant; (2) replacement of these two main iron sulfides by neo-formed Fe(III) oxides/oxyhydroxides (or Hydrous Ferric Oxides, HFO); and (3)

sorption of arsenic in the HFO sorption sites in aquifer matrix around the ASR well, and desorption of arsenic far away from the ASR well. Enhanced production of HFO dependent on the oxygen front development in both operations is compared and arsenic mobilization and attenuation deduced. Both model scenarios were solely based on thermodynamics and kinetic reaction rates were not included. Dissolved oxygen concentrations of recharge water and native groundwater were used in the calculation of mineral stability.

The observed arsenic mobilization and/or attenuation is hypothesized to be controlled by dynamic changes in the sorption capacity of the system resulting from precipitation followed by dissolution of HFO during simulated time. Sorption of mobilized arsenic species is achieved by coupling the reactive transport model with the generalized two-layer surface complexation model for HFO (FeOH+.sdat) developed by Dzombak and Morel (1990). In addition to consideration of the system to be in redox equilibrium, most thermodynamically stable iron mineral phases (goethite, hematite, magnetite, arsenopyrite, etc.) were suppressed to allow precipitation of iron ferric oxyhydroxide.

The aquifer is assumed to be homogeneous and the extension in the X direction is set to 1,000 m in the lateral direction such that the boundary is sufficiently far from the ASR well (here injection point) to not impact solute concentration fronts during the injection cycle. The flow model domain is discretized into 100 nodal blocks. Based on transmissivity and storativity values of 0.043 m2/s, and 0.003 respectively, from Kuniansky and Bellino (2016), and hydraulic conductivity of 0.00013 m/s reported by Lukasiewicz et al. (2001), the Theis equation was used to calculate the specific discharge rate. With a projected average injection rate of ~ 0.2 m^3/s (or 5 million gallon a day), the specific discharge rate was computed at 17 m/day using a Python code, considering a cross-sectional area of 100 m x 1m at time t = 50 days. The native groundwater

flow velocities are also considered negligible compared to those induced by the ASR well injection (Wallis et al., 2011). Values for the diffusion coefficient of 10^{-6} cm^2/s and dispersivity of 10 (calculated as the domain length divided by 100) were adopted from Lazareva et al. (2015). Their study involved column experiments conducted on cuttings from the Avon Park Formation within the Floridan aquifer, providing relevant transport parameter data for this model. Though the Floridan aquifer displays triple porosity characteristics with matrix, fracture and conduit porosity systems (Budd and Vacher, 2004; Kuniansky et al., 2012), the porosity value is reported to range from 20% to 30% (Gaswirth et al., 2006). The average porosity of 25% was used in the reactive model, porosity value reported in Mirecki (2013). Though simplistic, this approach provides valuable insights into distribution patterns of species of concern, including arsenic speciation and concentrations away from the ASR well.

To assess the degree to which this operational methodology enhances attenuation of arsenic during ASR operations, I consider two hypothetical model scenarios using a 1D GWB reactive transport model replicating injection of oxygenated water during the first ASR cycle :

(1) The first scenario corresponds to the injection of the treated surface freshwater volume corresponding to the storage volume only (Figure 4.1). Based on current practices, this volume of water is expected to be fully recovered (scenario 1).

(2) The second scenario consists of injecting the target storage volume equaling the sum of the buffer and storage zone volumes (scenario 1). In other words, instead of incrementally building a buffer zone by successive percent recovery lower than 100% in each cycle, here I consider forming the buffer zone right at the beginning of the ASR operation with an estimated volume corresponding to 70 days capacity of the ASR well. The number of days is chosen based on empirically proven arsenic attenuation efficiency and provision of operational flexibility in the

event that a greater volume of water needs to be recovered such as during severe drought (Pyne et al., 2007). The target storage volume (TSV) would hence equal a volume built for 100 days (or additional 70 days to the 30 day-recovery).

Since the 1D GWB reactive transport model is limited to accounting for storage and recovery, these two model scenarios will be based on a single injection while considering differences in their respective operations. such as their contrast in injection volume. Ultimately this approach allows inference of the fate of arsenic during recovery. Considering previous understanding of key geochemical processes affecting arsenic mobilization and fate (e.g., Wallis et al., 2011; Lazareva et al., 2015), the ultimate goal of this simplified 1D model is to elucidate the rates and mechanisms by which arsenic is mobilized and attenuated during ASR operations based on both scenarios.

4.4. Results

Figure 4.5 reveals variations in the range, median, and outliers in arsenic concentration across Tampa ASR datasets. With maximum and minimum values in arsenic concentrations of 5 and 38 µg/L, respectively, recovery rates of 158.6% and 116% show the widest ranges. The recovery rate of 80% has the smallest range of 10 to 17 µg/L arsenic. The recovery rates of 116 and 106.3% have the highest median arsenic concentrations, with values of 31 µg/L and 26 µg/L, respectively. The 158.6% recovery rate shows the widest spread with a larger interquartile range of 15 µg/L while low recovery rates of 80 and 90% show the narrowest spread with interquartile ranges of 3 µg/L and 9 µg/L. Low recovery rates show lower median values in arsenic i.e., they record lower concentrations in arsenic than high recovery rates. It is also observed that all of

these recovery rates show higher arsenic concentrations than the maximum arsenic level for drinking purposes (10 µg/L).

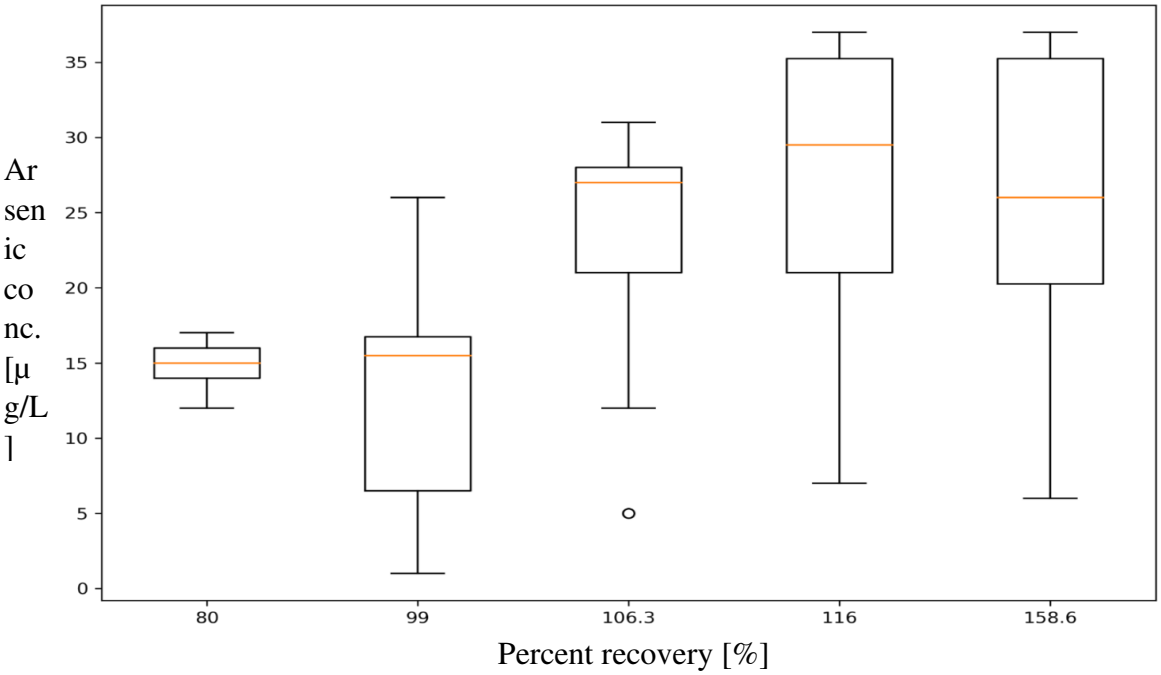

Figure 4.5. Box plot of arsenic concentration data in the recovered water for each recovery rate, indicating the range, median, and spread of the arsenic data. Note that as the percent recovered volume decreases, mobilization of arsenic also decreases. This suggest that when the injected volume exceeds the recovered, the arsenic concentrations exhibit a decreasing trend. Tampa ASR wellfields 80%, 99%, 106.3%, 116%, and 158.6% recoveries at their fifth ASR cycle and corresponding respectively to ASR-8, ASR-6, ASR-4, ASR-7 and ASR-5 wellfields (see **Figure 4.3** for their location).

Figure 4.6a and Figure 4. 6b show the temporal evolution of arsenic, pH, and ORP at both higher and lower recovery rates in wellfields ASR-5 and ASR-8, respectively. The As concentrations in ASR wells in both wellfields do not show high concentrations until February 2006, six months after initial injection. During recovery, arsenic concentration increases in both scenarios, though showing a higher increase in the scenario with the higher % recovery. With the higher recovery percentage, concentration shows an upward trend increasing 3-fold from ~10 µg/L to ~37 µg/L. However, the lower recovery of 80%, which shows a jump in As

concentration upon recovery, has high fluctuations in As concentration with no trend after the initial increase. While the pH shows a moderate fluctuation at both recovery rates, the ORP displays a fluctuation of up to 460 mV during injection and from around half of storage time the ORP shows a dramatic decreasing trend from ~ 400 mV to ~ -30 mV for 158% recovery (Figure 4.6a) and from ~400 mV to ~ -80 mV for 80% percent recovery (Figure 4.6b). Furthermore, the gap in data collection between 02/07/2006 and 03/21/2006, accompanied by a significant increase in arsenic concentration by more than three orders of magnitude, suggests that ASR recovery may have started during that period (see also Supplemental Table 4.1).

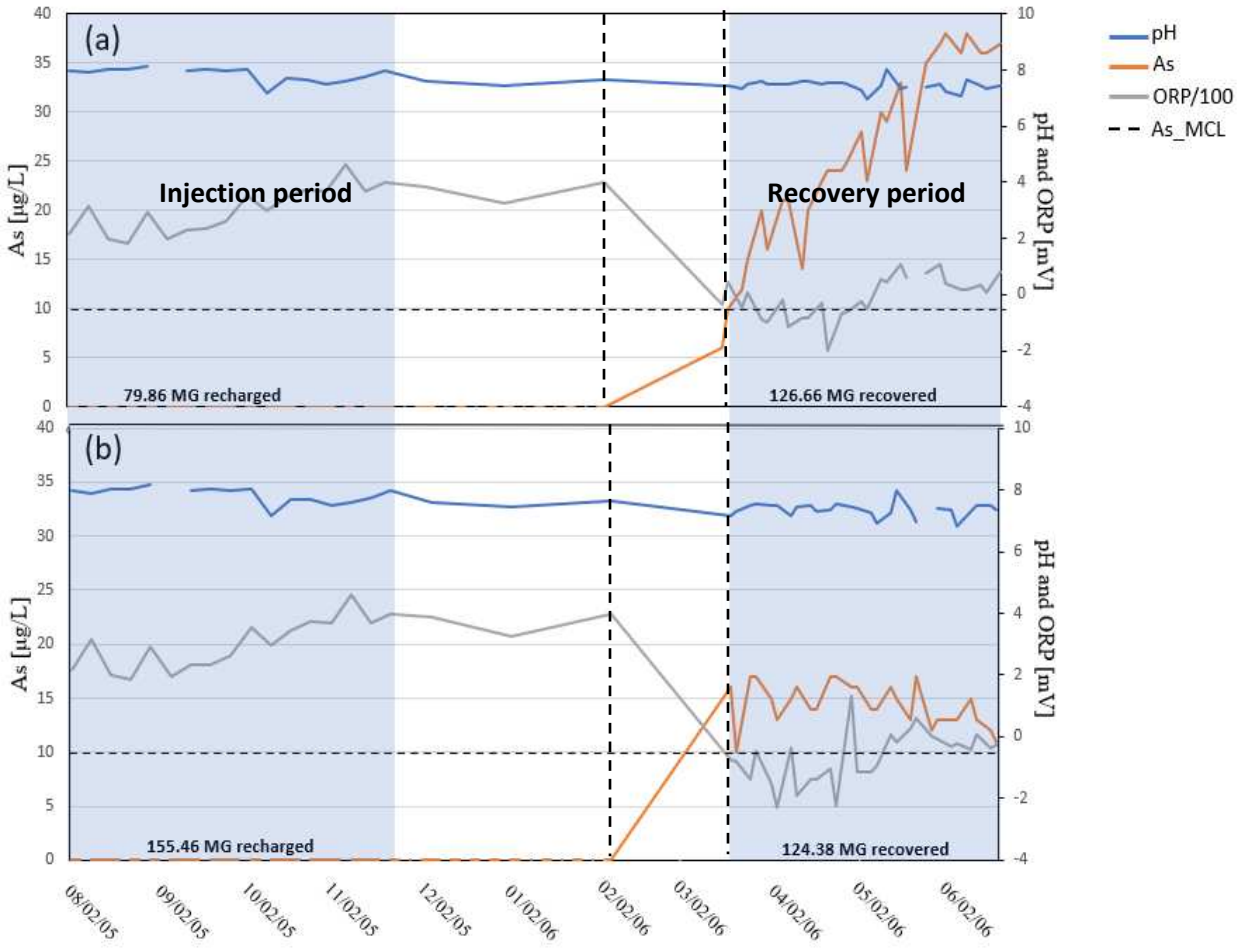

Figure 4.6. Temporal evolution of arsenic (As), pH, and oxidation-reduction potential (ORP or Eh) for the highest recovery rate (158.6%) in (a) and the lowest recovery rate (80%) in (b) at

their respective fifth cycle in ASR-5 and ASR-8 wellfields. In (a), the highest concentration of arsenic reaches up to 38 µg/L, approximately 2.2 times higher than the highest arsenic concentration in the recovered water in (b). The injection period spans from 08/02/2005 to 11/12/2005, and the storage time lasted 63 days from 12/06/2005 to 03/20/2006. Recovery period extended from 03/21/2006 to 06/27/2006 in both ASR fields. Dashed vertical lines on the figure mark the period between 02/07/2006 and 03/21/2006 where arsenic concentration and ORP data is unavailable. This data gap during this period leaves a significant interval, during which arsenic concentration appears to increase from below detection (<0.001 µg/L) to 6 µg/L.

In the Kissimmee ASR project, total arsenic concentrations in the native groundwater (<2.6 µg/L) and in the injectant (0.9 µg/L) are below the maximum contaminant level (MCL) of 10 µg/L. The native groundwater is supersaturated with dolomite and in equilibrium with calcite as indicated by their respective saturation index (SI) values of 1.1 and 0.0. The injectant water is undersaturated in both of these mineral phases with SI of -2.9 for dolomite and -1.7 for calcite. The pH values of the native groundwater and injectant are 7.8 and 6.7, respectively. The recharged water is oxic with dissolved oxygen concentrations of 4.5 mg/L, while the native groundwater is reduced with oxygen concentration of 0.3 mg/L. The hydrochemical facies of water samples in the piper diagram (Figure 4.7) reveals a NaCl water type for the native groundwater and CaMgCl for the recharged water.

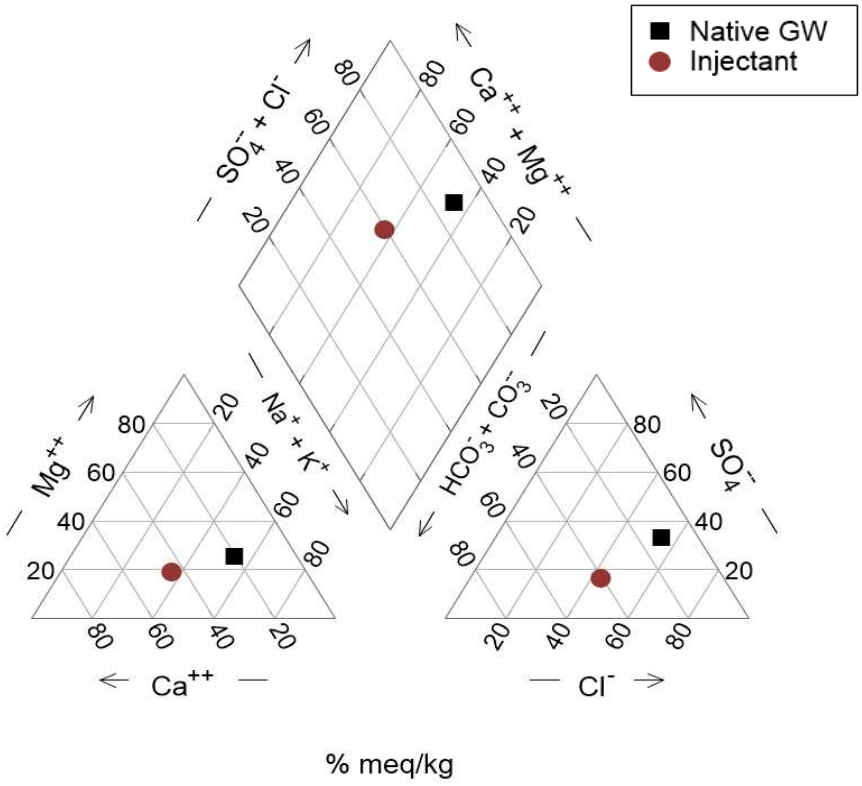

Figure 4.7. Piper diagram of the recharged water (injectant) and the native groundwater with their respective mixed type and NaCl hydrochemical facies characteristics.

Figure 4.8. shows results of the forward reactive transport model for the KRASR wellfield. The model reveals a difference in the injection front between both scenarios illustrated by the large oxygen front in scenario 2 compared to scenario 1. By the time oxygen is totally consumed, the oxygen front in scenario 2 is expanded up to 95 m, circa 3 times further than in scenario 1. This front is followed by oxidation of pyrite and formation of Fe(III) oxyhydroxide in both operations (Figure 4.9). However, scenario 2 forms a large oxygen front coincident to a large expansion front in Fe(III) oxyhydroxide with abundances up to 14,700 µg/Kg formed at 95 m away from the ASR well. At the end of the flow path, the model predicts As mobilization with As(III) being the major arsenic species in solution (97%) in both scenarios. Spatially, scenario 2

reaches 10 μg/L between 115 m and 125 m while the scenario 1 model simulation predicts the As MCL to be attained between 35 m and 45 m.

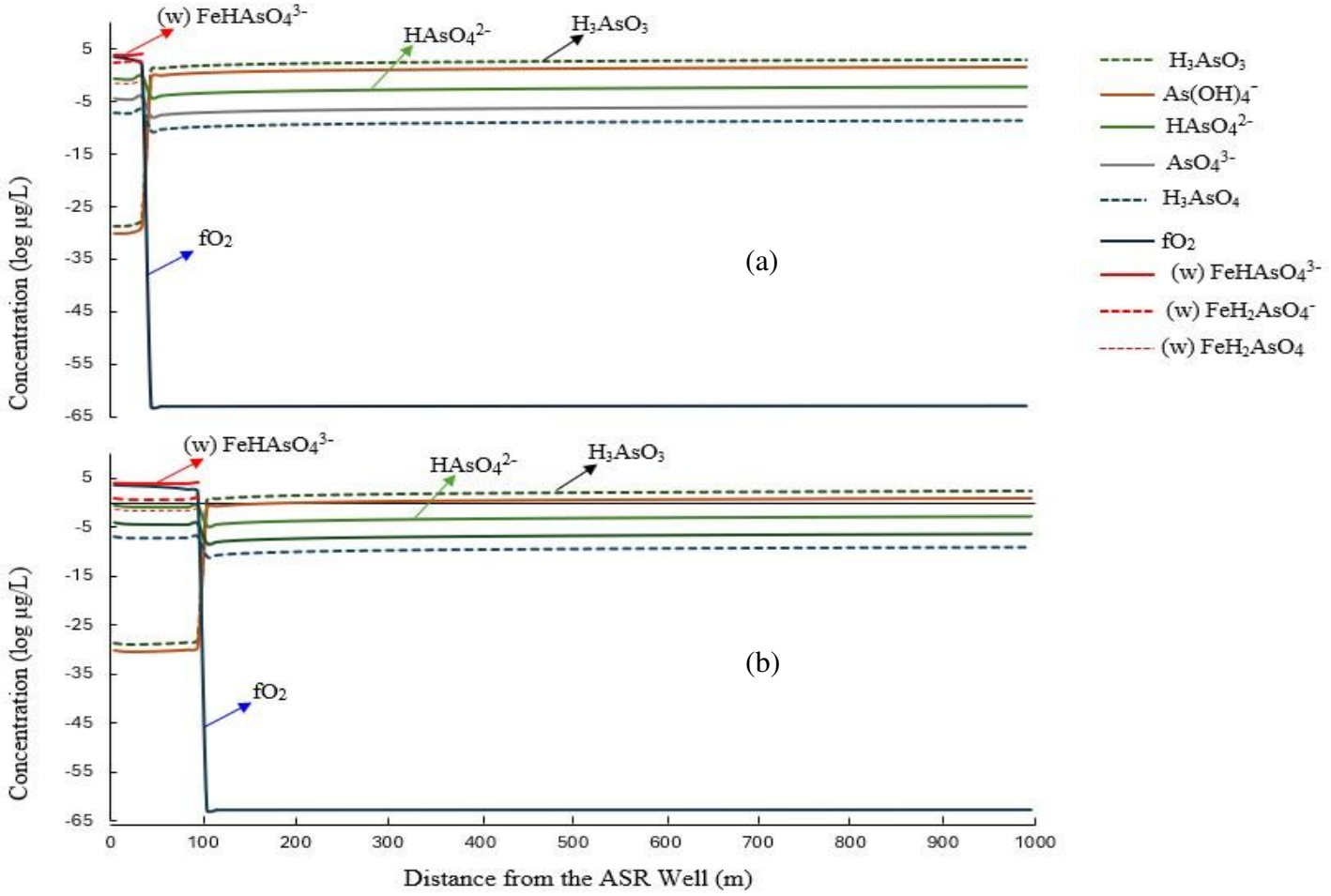

Figure 4.8. Reactive transport model showing distribution of arsenic species and O_2(aq) in both operational methodology scenarios. **a** considers the storage zone scenario only, with a 30-day injection time, while **b** shows the results considering the target storage volume (buffer zone and storage volume) for 100 days injection. Attenuation of arsenic is shown by formation of As(V) species on weak sites of hydrous ferric oxides. Species concentrations in Figures 4.8. (a) and (b) are detailed in Supplemental Tables 4.2 and 4.3.

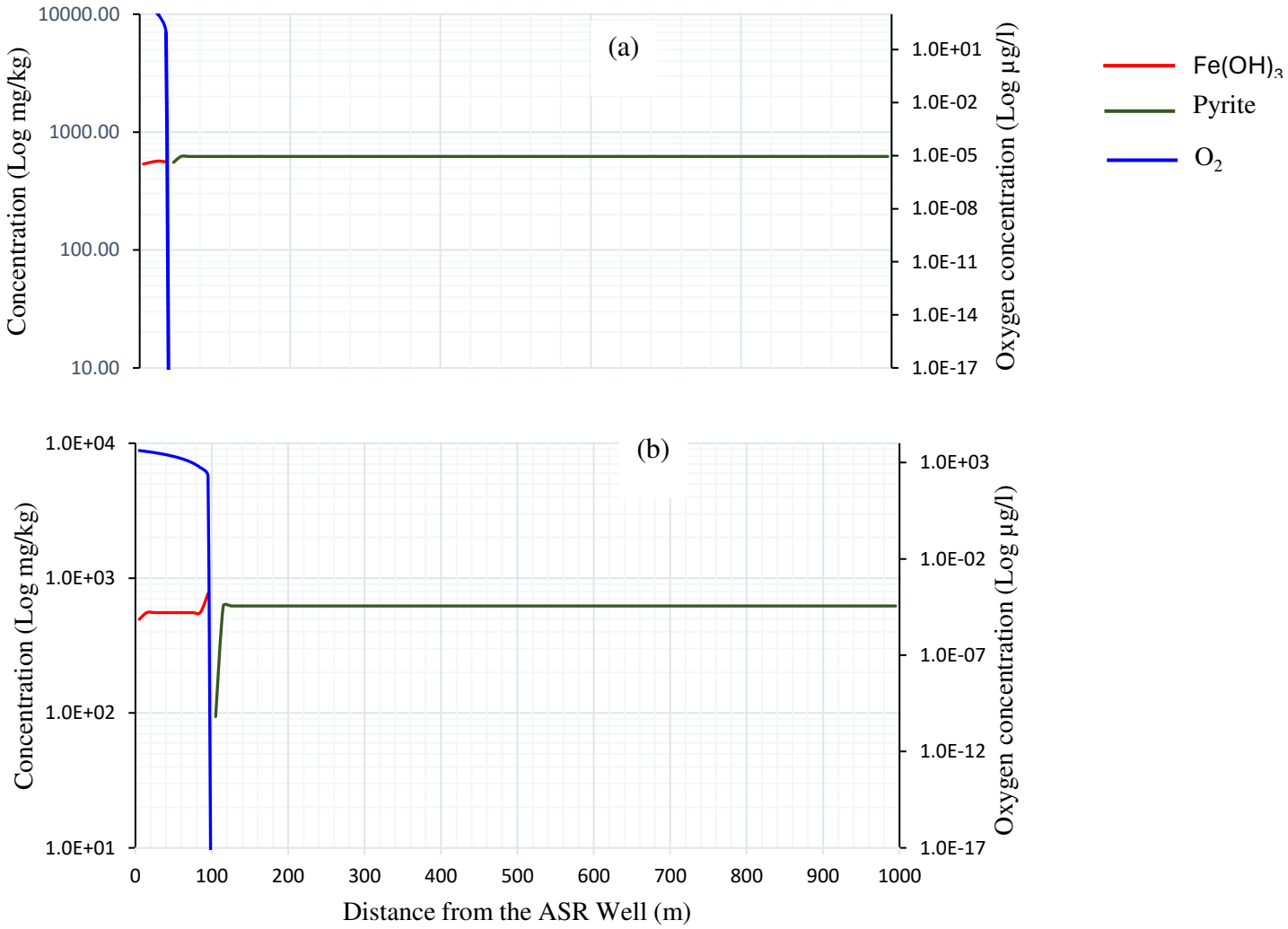

Figure 4.9. Spatial distribution of pyrite, iron hydroxide, and oxygen concentrations with storage zone scenario in (a) and target storage zone formation in (b).

An abrupt decrease in oxygen and Fe(III) oxyhydroxide concentration in both scenarios is followed by formation of reducing species like dissolved sulfide. In scenario 2, in the oxygenated zone around the ASR well, As concentrations up to ~14,689 μg/L are predicted to be adsorbed onto Fe(III) oxyhydroxide as a weak surface complex >(w) $FeOHAsO_4^{3-}$ (Figure 4.8b). However, in scenario 1, arsenic concentrations up to 14,433 μg/L are predicted to sorb onto >(w) $FeOHAsO_4^{3-}$ (Figure 4.8a). In a reducing environment, Fe(III) oxyhydroxides undergo reductive dissolution, releasing As(V), most of which is subsequently reduced to As(III). Scenario 1 shows mobilization of As(III) to a concentration of ~1,000 μg/L, over three times higher than the As (III) concentration (~300 μg/L) mobilized in scenario 2.

4.5. Discussion and interpretation

Based on arsenic concentration data in the Tampa ASR recovered water , higher recovery rates show higher ranges and to some extent have high median arsenic concentrations, indicating temporal variability in arsenic concentrations and an enhanced environment promoting arsenic partitioning into groundwater. This time-dependent arsenic mobilization associated with high recovery rates can be explained by several factors, including: (a) spatial variability of arsenic mobilized during injection due to heterogeneity in the lateral and vertical distribution of arsenic (Smedley and Kinniburgh, 2002) away from the ASR well; (b) a heterogeneous distribution of an initial host of arsenic (framboidal pyrite or to some extent Fe oxyhydroxide) within the aquifer matrix (Price and Pichler, 2006; Lazareva and Pichler, 2007) coupled to variable distribution of pyrite-rich porosity and fracture zones facilitating contact between groundwater and arsenious pyrite (Pichler et al., 2011). Most importantly, high arsenic remobilization in these high recovery rate scenarios more likely results from iron oxyhydroxide reduction and dissolution due to an

induced reverse high flow of reducing native groundwater towards the ASR (Wallis et al., 2011). Further, there are spans of time when there is no recovery during ASR recovery periods that would to some extent impact the arsenic behavior and its temporal and spatial concentration variability in the storage zone influenced by ASR operations.

In Figure 4.6a and 4.6b, the buffering capacity of carbonates maintains the pH range at 7-8. Carbonate buffered pyrite oxidation has been shown to result from dissolution of highly reactive carbonates (calcite, ankerite) following HFO precipitation, proton generation and identified by a strong molal correlation of Ca^{2+} and Mg^{2+} with HCO_3^-. Dissolution of these carbonate minerals is enhanced by the low ionic strength of the injectant water (Descourvieres et al., 2011). The fact that arsenic concentration is lower during injection reveals its potential attenuation from the strong sorption affinity of As for iron oxyhydroxide (e.g., Stollenwerk, 2003), causing partition of arsenic from the groundwater. The large decrease in ORP followed by an abrupt increase in arsenic concentration during recovery, point to a possible inverse correlation of these two parameters. In fact, as shown in other ASR operations, reversal of flow during recovery results in reversal into anoxic conditions responsible for observed arsenic remobilization (Wallis et al., 2011). However, over-recovery (158.3%) results in a higher increase in arsenic concentration up to three times the standard 10 µg/L, implying recovery induced enhanced invasion of a reducing environment in the ASR well vicinity. Though showing an increase in As concentration upon start of recovery, the scenario with a low recovery rate of 80% displays a decrease in arsenic concentration with time during recovery towards the As MCL, pointing to its possible long-term attenuation during recovery. ASR operations in Tampa and Peace River have shown that a positive cumulative storage volume through subsequent cycles enhanced arsenic attenuation to levels lower than ten µg/L while those with negative

cumulative storage volume (or recovery volume higher than injection volume) had the highest As concentration (Pyne et al., 2007; Jones, 2015). In fact, the incremental formation of a buffer zone (Figure 4.1) is built from cumulative storage volumes where constraints on water availability to build the buffer zone early in cycle testing is limited. If availability of recharge water is not limited, it is customary to build and maintain the buffer zone from the beginning of the ASR cycle (Pyne et al., 2007).

Arsenic concentrations lower than the MCL (10 µg/L) are reported during recharge and, more notably, conspicuously appear in the vicinity of the ASR well, where oxygen concentrations are higher as corroborated in the model results in Figure 4.8a and 4.8b. This is shown to have resulted from sorption sites provided by Fe(III) oxyhydroxides formed in the oxygenated part of the flow path during injection. Arsenious pyrite oxidation and dissolution have resulted in arsenic re-adsorption onto or co-precipitation with the neo-formed Fe(III) oxyhydroxides, mainly occurring as a weak surface site complex $>(w)FeOHAsO_4^{3-}$. Several authors have reported sorption of Arsenic onto Fe(III) oxyhydroxides upon injection of oxidizing recharged waters during ASR cycles (Wallis et al., 2012; Antoniou et al., 2015; Fakhreddine et al., 2021). Furthermore, scenario 2 taking into account the buffer zone and the storage zone volumes resulted in formation of more substantial amounts of Fe(III) oxyhydroxides than scenario 1, and that is shown to have resulted in major attenuation of arsenic at the end of the reaction path simulation. Having an arsenic concentration of ~300 µg/L at 995 m , scenario 2 shows promise as a methodology to counter high arsenic mobilization compared to scenario 1 that remobilizes arsenic up to 1,000 µg/L at 995 m. Upon recovery, It is hence inferred that scenario 2 would more likely yield less As concentration in the recovered water than scenario 1. As reported by Price and Pichler (2006), an aquifer matrix low in As can generate high As

concentration of several orders of magnitude above the As MCL due to an induced high water-rock interaction during ASR operations.

Furthermore, scenario 2 having produced considerable amounts of Fe(III) oxyhydroxides over a larger area from the ASR well would obviously promote arsenic partition or co-precipitation onto Fe(III) oxyhydroxides formed. Wallis et al. (2011) concluded that not all precipitated HFO that form during injection phases dissolve during recovery when the extraction volume is less than injected volume. Scenario 2, with a buffer zone equal in volume to the storage zone, would hence tend to decrease the recovery ratio resulting in decreasing amounts of HFO that would be reduced and dissolved, releasing arsenic that had been sorbed. This also suggest that attenuation of As concentration to drinking standards can be achieved and improved more quickly with subsequent ASR cycles in scenario 2 when % recovery volume is lower than 100%.

While this simplified 1D forward model supports the conceptual model for the mobilization and attenuation of arsenic during ASR using the operational methodology scenario 2, complexity of the actual subsurface system would point to the non-linearity and nonuniqueness of the controlling factors in arsenic fate (redox, pH, arsenopyrite and HFO dissolution, mineral kinetics) due to, 1/incomplete measurement of groundwater parameters (Wallis et al. 2011); 2/ other phases (minerals and organic matter) potential to source and sorb arsenic were not included in the model; 3/ microbial metabolic processes whereby microbial respiring organism harness energy by electron transfer from reduced to oxidized species (Bethke et al., 2008) impacting dissolved oxygen concentration, oxidation-reduction potential, groundwater geochemical speciation including arsenic behavior and fate. The organic matter would likely enhance microbial reduction of HFO, followed by arsenic releases (Wallis et al.,

2011) during the ASR recovery phase. 4/In terms of operational methodology, there is uncertainty in the choice of the number of days (here 70 days) at the design ASR recovery capacity to build an effective buffer zone that contribute to preserving arsenic attenuation during recovery period. All these limiting factors would need further assessment relying on consistent time series data from the ASR well and monitoring wells enabling understanding of the extent to which arsenic can be attenuated via enhancement of the oxygenated front and development of a "buffer zone."

4.6. Conclusion and limitations

The magnitude of arsenic release into groundwater in the Upper Floridan carbonate aquifer is herein modeled and the model indicates that it may be controlled by the recovery percentage during aquifer storage and recovery. While a low % recovery tends to induce low arsenic concentration mobilized into groundwater, a high % recovery remobilizes arsenic to concentrations up to three orders of magnitudes. The 1D reactive transport model using an injection cycle based on two scenarios corroborates qualitative understanding of the underlying processes that control arsenic fate upon injection of oxygenated source water into a reducing carbonate storage zone aquifer by 1/ oxidation dissolution of arsenious pyrite by oxygenated source water injected into a reducing carbonate aquifer; 2/ formation of neo-formed Fe(III) oxyhydroxides providing sorbing sites that attenuate arsenic concentrations into groundwater. The development of an oxygen front around the ASR well promotes formation of HFO, leading to the As partition into the mineral phase mainly as weak sites complexes of $>(w)FeOHAsO_4^{3-}$. Depending on the operational methodology employed to enhance or decrease oxygenation around the ASR well, arsenic concentrations is shown to respectively increase or decrease accordingly. Furthermore, at the redox transition towards reducing environments, reduction

dissolution of neo-formed Fe(III) oxyhydroxides results in high remobilization of arsenic (As III) into groundwater. However, compared to scenario 1, the model scenario 2 shows a much lower concentration of remobilized As(III). Therefore, the operational methodology that promotes an increased oxygen front shows promising results that need further investigation. It is, however, uncertain to what extent the oxygen front can be depleted leading to further remobilization of arsenic to possible high concentrations in subsequent ASR cycles in the promising model scenario 2. More robust inverse geochemical modeling based on extensive data is hence needed to examine this operational methodology in ASR field sites where an initial buffer volume has been injected and followed by successive ASR cycles generating a consistent record of physico-chemical and microbiological time series data in ASR and monitoring wells. Effective implementation of this operational methodology offers potential to limit high arsenic concentration while reducing the need for costly arsenic removal treatment in the recovered water.

4.7. References

Antoniou, E.A., Van Breukelen, B.M., Putters, B., Stuyfzand, P.J., 2012. Hydrogeochemical patterns, processes and mass transfers during aquifer storage and recovery (ASR) in an anoxic sandy aquifer. *Appl. Geochem.*, *27*(12), 2435-2452.

Antoniou EA, van Breukelen BM, Stuyfzand, P.J., 2015. Optimizing aquifer storage and recovery performance through reactive transport modeling. *Appl. Geochem.*, *61*, 29-40.

Appelo, C.A.J., Drijver, B., Hekkenberg, R., De Jonge, M., 1999. Modeling in situ iron removal from ground water. *Groundwater Journal*, *37*(6), 811-817.

Arthur, J.D., Dabous, A.A., Cowart, J.B., 2002. Mobilization of arsenic and other trace elements during aquifer storage and recovery, southwest Florida. In U.S. Geological Survey artificial recharge workshop proceedings (pp. 47-50) Denver, Colorado.

Arthur, J.D., Dabous, A.A., Cowart, J.B., 2005. Water–rock geochemical considerations for aquifer storage and recovery: Florida case studies. *Developments in Water Sc.*, *52*, 327-339.

Arthur, J.D., Dabous, A.A., Fischler, C., 2007. Aquifer storage and recovery in Florida: geochemical assessment of potential storage zones. In: Fox P (ed) Management of aquifer recharge for sustainability. Proc. 6th Int. Symp. on managed aquifer recharge of groundwater. Acacia, Phoenix, AZ, pp 185–197.

Bethke, C.M., Farrell, B., Shafifi, M., 2022a. The Geochemist's Workbench®, Release 17. GWB Reactive Transport Modeling Guide. Aqueous Solutions, LLC, Champaign, IL, p. 181.

Bethke, C.M., Ding, D., Jun, Q., Sanford, R.A., 2008. Origin of microbiological zoning in groundwater flows. *Geol. J. 36, 739–742.*

Bethke, C.M., Farrell, B., Shafifi, M., 2020b. The Geochemist's Workbench®, Release 14. GWB Reaction Modeling Guide. Aqueous Solutions, LLC, Champaign, IL, p. 209.

Bloetscher, F., Sham, C.H., Danko, III, J. J., Ratick, S., 2014. Lessons learned from aquifer storage and recovery (ASR) systems in the United States. *Journal of Water Resource and Protection*, *6*(17), 1603.

Budd, D.A., 2001. Permeability loss with depth in the Cenozoic carbonate platform of west-central Florida. *AAPG bulletin*, *85*(7), 1253-1272.

Budd, D.A., 2002. The relative roles of compaction and early cementation in the destruction of permeability in carbonate grainstones: a case study from the Paleogene of west-central Florida, USA. *Journal of Sedimentary Research*, *72*(1), 116-128.

Budd, D.A., Vacher, H.L., 2004. Matrix permeability of the confined Floridan Aquifer, Florida, USA. *Hydrogeology Journal*, *12*, 531-549.

Cander, H.S., 1991 Dolomitization and water-rock interaction in the middle Eocene Avon Park Formation, Floridan aquifer. Jackson School of Geosciences, University of Texas at Austin, PhD Thesis.

Descourvieres, C., Prommer, H., Oldham, C., Greskowiak, J., 2011. Water quality changes during aquifer storage and recovery: Quantification of water-sediment interactions and reactive transport modeling. In Proceedings of International Conference on Environmental Science and Development (ICESD 2011).

Dillon, P., Fernandez, E.E., Tuinhof, A., 2012. Management of aquifer recharge and discharge processes and aquifer storage equilibrium. IAH contribution to GEF-FAO Groundwater Governance Thematic Paper 4.

Dillon, P., Stuyfzand, P., Grischek, T., Lluria, M., Pyne, R.D.G., Jain, R.C., ... Sapiano, M., 2019. Sixty years of global progress in managed aquifer recharge. *Hydrogeology Journal, 27(1), 1-30.*

Dzombak, D.A., Morel, F.M.M., 1990. Surface Complexation Modeling: Hydrous Ferric Oxide. John Wiley and Sons, New York.

Eisenlohr, L., Bouzelboudjen, M., Király, L., Rossier, Y., 1997. Numerical versus statistical modelling of natural response of a karst hydrogeological system. *Journal of hydrology*, *202*(1-4), 244-262.

Evenson, E.J., Orndorff, R.C., Blome, C.D., Böhlke, J.K., Hershberger, P.K., Langenheim, V.E., Wood, T.M., 2013. US Geol. Surv. Water Science Strategy—observing, Understanding, Predicting, and Delivering Water Science to the Nation. U.S. Department of the Interior, U.S. Geological Survey Circular 1383–G, 49 p.

Fakhreddine, S., Prommer, H., Scanlon, B.R., Ying, S.C., Nicot, J.P., 2021. Mobilization of arsenic and other naturally occurring contaminants during managed aquifer recharge: a critical review. *Environmental Science & Technology, 55(4), 2208-2223*.

Fischler, C., Arthur, J. D., 2010. Geochemical, mineralogical and petrographic characterization of rocks comprising the upper Floridan Aquifer in south Florida. *Florida Geological Survey FDEP-FC389, Tallahassee Florida*.

Fischler, C., Hansard, P., Ladle, M., Burdette, C., .2015. A Review of Selected Florida Aquifer Storage and Recovery (ASR) Sites and Their Geochemical Characteristics. Report of Investigation, Florida Geol. Surv., Florida. Google scholar

Gaswirth, S.B., Budd, D.A., Crawford, B.R., 2006. Textural and stratigraphic controls on fractured dolomite in a carbonate aquifer system, Ocala limestone, west-central Florida. *Sedimentary Geology Journal, 184(3-4), 241-254*.

Geddes, E., Coonts, S., Collins, B., 2018. Geochemistry of the Upper Floridan Aquifer and Avon Park Permeable Zone Within the South Florida Water Management District. Technical Publication WS-47, South Florida Water Management District.

Gilboy, A.E., 1985. Hydrogeology of the Southwest Florida Water Management District, SWFWMD Regional Analysis Section. Technical Report 85-01, 18p.

Green, R.C., Arthur, J.D., DeWitt, D.W., 1995. Lithostratigraphic and hydrostratigraphic cross sections through Pinellas and Hillsborough counties, southwest Florida (No. 61). Florida Geological Survey.

Hammes, U., 1992. Sedimentation patterns, sequence stratigraphy, cyclicity, and diagenesis of early Oligocene carbonate ramp deposits, Suwannee Formation, southwest Florida, U.S.A. Department of Geological Sciences, University of Colorado, PhD Thesis.

Hughes, J.D., Vacher, H.L., Sanford, W.E., 2009. Temporal response of hydraulic head, temperature, and chloride concentrations to sea-level changes, Floridan aquifer system, USA. *Hydrogeology Journal*, 17: 793-815.

Jones, G.W., Pichler, T., 2007. Relationship between pyrite stability and arsenic mobility during aquifer storage and recovery in southwest central Florida. *Environmental Science & Technology*, 41 (3), p.723–730.

Jones, G.W., 2015. Investigation of the Mechanisms for Mobilization of Arsenic in Two ASR Systems in Southwest Central Florida. School of Geosciences, University of South Florida, PhD Thesis.

Johnston, R.H., Bush, P.W., 1988. Summary of the Hydrology of the Floridan Aquifer System in Florida and in Parts of Georgia, South Carolina, and Alabama. U.S. Geol. Surv. Professional Paper 1403-A, United States Government Printing Office, Washington.

Jury, W.A., Vaux, Jr.H., 2005. The role of science in solving the world's emerging water problems. *Proceedings of the National Academy of Sci.*, *102*(44), 15715-15720.

Kocis, T.N., Dahlke, H.E., 2017. Availability of high-magnitude streamflow for groundwater banking in the Central Valley, California. *Environ. Res. Lett.* 12, no.8, 084009.

Koopman, S., 2022. Occurrence and mobility of molybdenum during managed aquifer recharge in carbonate aquifers. Department of Geosciences, University of Bremen, PhD Thesis.

Koutroulis, A.G., Papadimitriou, L.V., Grillakis, M.G., Tsanis, I.K., Warren, R., Betts, R.A., 2019. Global water availability under high-end climate change: A vulnerability based assessment. *Global and Planetary Change*, *175*, 52-63.

Kuniansky, E.L., Bellino, J.C., Dixon, J., 2012. Transmissivity of the upper Floridan aquifer in Florida and parts of Georgia, South Carolina, and Alabama. U.S. Department of the Interior, U.S. Geological Survey.

Lazareva, O., Druschel, G., Pichler, T., 2015. Understanding arsenic behavior in carbonate aquifers: Implications for aquifer storage and recovery (ASR). *Applied Geochemistry*, *52*, 57-66.

Li, H., Lu, C., Werner, A.D., Irvine, D.J., Luo, J., 2022. Impacts of heterogeneity on aquifer storage and recovery in saline aquifers. *Water Resources Research*, *58*(5), e2021WR031306.

Loizeaux, N.T., 1995. Lithologic and hydrogeologic frameworks for a carbonate aquifer: evidence for facies-controlled hydraulic conductivity in the Ocala Formation, West-Central Florida. Department of Geological Sciences, University of Colorado, Boulder, MS Thesis.

Lowry, C.S., Anderson, M.P., 2006. An assessment of aquifer storage recovery using ground water flow models. *Groundwater Journal*, *44*(5), 661-667.

Lukasiewicz, John, 2001, Floridan aquifer system test well program City of South Bay, Florida, South Florida Water Management District Technical Publication WS-2, 90 p.

Maliva, R.G., Missimer, T.M., Clayton, E.A., Dickson, J.A.D., 2009. Diagenesis and porosity preservation in Eocene microporous limestones, South Florida, USA. *Sedimentary Geology Journal, 217(1-4), 85-94*.

Maliva, R.G., Manahan, W.S., Missimer, T.M., 2020. Aquifer storage and recovery using saline aquifers: Hydrogeological controls and opportunities. *Groundwater Journal*, *58*(1), 9-18.

Maliva, R.G., Missimer, T.M., 2010. Aquifer storage and recovery: developing sustainable water supplies. *IDA J. of Desalination and Water Reuse*, *2*(2), 74-80.

Melzer, S.E., Budd, D.A., 2008. Retention of high permeability during shallow burial (300 to 500 m) of carbonate grainstones. *Journal of Sedimentary Research*, *78*(8), 548-561.

Miller, J.A., 1990. Ground water atlas of the United States Alabama, Florida, Georgia, and South Carolina (HA 730-G). U.S. Geological Survey.

Miotliński, K., Dillon, P.J., Pavelic, P., Barry, K., Kremer, S., 2014. Recovery of injected freshwater from a brackish aquifer with a multiwell system. *Groundwater Journal* 52, no. 4: 495-502.

Miller, J.A., 1986. Hydrogeologic framework of the Floridan aquifer system in Florida and parts of Georgia, Alabama, and South Carolina (Vol. 1). Department of the Interior, U.S. Geological Survey.

Mirecki, J.E., 2004. Water-quality Changes During Cycle Tests at Aquifer Storage Recovery (ASR) Systems in South Florida. U.S. Army Corps of Engineers, Engineer Res. and Development Center, TR-04-8.

Mirecki, J., 2013. Comprehensive Everglades Restoration Plan aquifer storage and recovery pilot project: Final technical data report for the Kissimmee River and Hillsboro ASR systems. South Florida Water Management District and US Army Corps of Engineers. Jacksonville, FL: US Army Corps of Engineers.

Murphy, T.B., 2022. SFWMD C-38S Continuous Corehole Boring: M01C38SL (non-published). Accessed 25 May 2023.

Othman, D.B., Luck, J.M., Tournoud, M.G., 1997. Geochemistry and water dynamics: application to short time-scale flood phenomena in a small Mediterranean catchment: I. Alkalis, alkali-earths, and Sr isotopes. *Chemical Geology*, *140*(1-2), 9-28.

Pichler, T., Price, R., Lazareva, O., Dippold, A., 2011. Determination of arsenic concentration and distribution in the Floridan Aquifer System. *Journal of Geochemical Exploration*, *111*(3), 84-96.

Price, R.E., Pichler, T., 2006. Abundance and mineralogical association of arsenic in the Suwannee Limestone (Florida): Implications for arsenic release during water–rock interaction. *Chemical Geology*, *228*(1-3), 44-56.

Prommer, H., Sun, J., Helm, L., Rathi, B., Siade, A.J., Morris, R., 2018. Deoxygenation Prevents Arsenic Mobilization during Deepwell Injection into Sulfide-Bearing Aquifers. *Environmental Science & Technology*, *52*, 13801-13810.

Pyne, R.D.G., 2004. Aquifer Storage and Recovery (ASR) Issues and Concepts: St. Johns River Water Management District.

Pyne, R.D.G., 2005. Aquifer Storage Recovery: A Guide to Groundwater Recharge Through Wells. Gainesville, Florida: ASR Systems. Google Scholar

Pyne, R.D.G., Brown, J.C., Pichler, T., Vanderzalm, J., Stuyfzand, P.J., Lisle, J.T., ... Stolz, J., 2007. Evaluation of arsenic mobilization processes occurring during aquifer storage recovery activities. Final report prepared for Southwest Florida Water Management District.https://www.swfwmd.state.fl.us/sites/default/files/medias/documents/asr_systems_arsenic.pdf (accessed on 14 February 2023).

Randazzo, A.F., 1980. Geohydrologic model of the Floridan aquifer in Southwest Florida Water Management District: Gainesville, University of Florida, Florida Water Resources Res. Center Publication 46, 79 p.

Reese, R.S., Alvarez-Zarikian, C.A., 2007. Hydrogeology and aquifer storage and recovery performance in the Upper Floridan aquifer, southern Florida, U.S. Geological Survey Scientific Investigations Report 2006-5239, 110 p.

Reisenhofer, E., Adami, G., Barbieri, P., 1998. Using chemical and physical parameters to define the quality of karstic freshwaters (Timavo River, North-eastern Italy): a chemometric approach. *Water research*, *32*(4), 1193-1203.

Scanlon, B.R., Reedy, R.C., Faunt, C.C., Pool, D., Uhlman, K., 2016. Enhancing drought resilience with conjunctive use and managed aquifer recharge in California and Arizona. *Environmental Res. Letters* 11, no. 3: 035013.

Smedley, P.L., Kinniburgh, D.G., 2002. A review of the source, behaviour and distribution of arsenic in natural waters. *Applied Geochemistry*, *17*(5), 517-568.

Sø, H.U., Postma, D., Jakobsen, R., Larsen, F., 2008. Sorption and desorption of arsenate and arsenite on calcite. *Geochimica et Cosmochimica Acta*, *72*(24), 5871-5884.

Stollenwerk, K.G., 2003. Geochemical processes controlling transport of arsenic in groundwater: a review of adsorption. *Arsenic in ground water: Geochemistry and occurrence*, 67-100.

Stuyfzand, P.J., 1998. Quality changes upon injection into anoxic aquifers in the Netherlands: evaluation of 11 experiments. In: Peter, J.H. (Ed.), Arti*fi*cial Recharge of Groundwater, Proc. 3rd Intern. Symp. On Arti*fi*cial Recharge. Balkema, Amsterdam, pp 283-291.

Stuyfzand, P.J., 2001. Pyrite oxidation and side reactions upon deep well injection. Proceedings of the WRI-1010th International Symposium on Water-Rock Interaction, Villasimius, Italy, 10-15.

Stuyfzand, P.J., Vogelaar, A.J., Wakker, J., 2002. Hydrogeochemistry of prolonged deep well injection and subsequent aquifer storage in pyritiferous sands; DIZON pilot, Netherlands. In: Dillon, P.J. (Ed.), Management of Aquifer Recharge for Sustainability, Proc. 4th Internat. Symp. on Artificial Recharge of Groundwater, Adelaide, South Australia, 22–26 September 2002. Swets & Zeitlinger, Lisse, 107–110.

Stuyfzand, P.J., Wakker, J.C., Putters, B., 2005, Water quality changes during Aquifer Storage and Recovery (ASR): results from pilot Herten (Netherlands), and their implications for modeling. In Recharge Systems for Protecting and Enhancing Groundwater Resources, Proceedings of the 5th International Symposium on Management of Aquifer Recharge, ISMAR5, Berlin, pp 11-16.

Stuyfzand, P.J., Pyne, R.D.G., 2010. Arsenic behavior in SW Florida ASR systems and its expert modeling. In Achieving Groundwater Supply Sustainability & Reliability through Managed Aquifer Recharge, Proceedings of the 7th International Symposium on Managed Aquifer Recharge, ISMAR7, Abu Dhabi, pp 9-13.

Tihansky, A.B., 2005. Effects of aquifer heterogeneity on groundwater flow and chloride concentrations in the upper Floridan aquifer near and within an active pumping well field, west-central Florida. United States Geol. Surv. Scientific Investigations Report, U.S. Geological Survey.

Upchurch, S., Scott, T.M., Alfieri, M.C., Fratesi, B., Dobecki, T.L., 2019. The Karst Systems of Florida -Understanding Karst in a Geologically Young Terrain. Springer International Publishing, Cham, Switzerland, 450 pp.

Vanderzalm, J.L., Dillon, P.J., Le Gal La Salle, C., 2007. Arsenic mobility under variable redox conditions induced during ASR. In P. Fox (Ed.), *Management of aquifer recharge for sustainability*, *Proceedings of the 6th International Symposium on Managed Aquifer Recharge of Groundwater* (pp. 209–219). Phoenix: Acacia Publishing.

Vanderzalm, J.L., Dillon, P.J., Barry, K.E., Miotlinski, K., Kirby, J.K., Le Gal La Salle, C., 2011. Arsenic mobility and impact on recovered water quality during aquifer storage and recovery using reclaimed water in a carbonate aquifer. *Applied Geochemistry*, *26*, 1946-1955.

Williams, H., Cowart, J.B., Arthur, J.D., 2002. Florida Aquifer Storage and Recovery Geochemical Study, Southwest Florida: Year One & Year Two Progress Report (No. 100). Florida Geological Survey.

Wallis, I., Prommer, H., Pichler, T., Post, V.B., Norton. S., Annable, M.D., Simmons, C.T., 2011. Process-based reactive transport model to quantify arsenic mobility during aquifer storage and recovery of potable water. *Environmental Science & technology, 45(16), 6924-6931.*

Wang, Y., Ma, T., Luo, Z., 2001. Geostatistical and geochemical analysis of surface water leakage into groundwater on a regional scale: a case study in the Liulin karst system, northwestern China. *Journal of Hydrology 246 (1-4), 223-234.*

CHAPTER 5. CONCLUSIONS

This dissertation investigates optimization of Aquifer Storage and Recovery (ASR) operations for sustainable water supply on the Edwards and Floridan aquifers as case studies. Through a multidisciplinary approach encompassing petrology, geochemistry, hydrogeology, and reactive transport modeling, this research aims to enhance understanding of the complex interactions of geological factors within these aquifer systems for enhanced efficiency in ASR operations.

The second chapter examines the neglected yet critical control petrology and geochemistry of aquifer matrix and surface and groundwater chemistry in guiding optimization of ASR operations for sustainable water supply in the poorly known saline portion of the two-layer Edwards aquifer in one of the fastest-growing U.S. cities. The Edwards aquifer petrography and geochemistry shed light on the aquifer's petrology and trace element compositions, with dolomitization, fracturing, and dissolution found to be key factors likely affecting hydraulic properties. While the RDM confining unit's low permeability likely derives from well-preserved compaction features and the modest presence of clay minerals, high fracture porosity may connect both aquifer zones during ASR operations, as also suggested by the Piper plot water facies evolution. Geochemical investigations reveal minimal mobilization of trace elements into groundwater during ASR. However, Arsenic's presence, which is relatively higher in the confining layers and primarily associated with pyrite, raises concern.

From a different perspective, chapter 3 uses water geochemistry, PHAST, and Geochemist’s Workbench software to investigate the feasibility and optimization of ASR in the Edwards aquifer study site. Hydraulic conductivity assessment highlights horizontal and vertical flow, suggesting fractures play a significant role in achieving ASR efficiency. Based on

petrological, geochemical, and hydrogeological lines of evidence, the proposed implementation of two ASR wells operating separately in the dolomitic aquifer portions of the Kainer and Person Formations represents a potential ASR optimization strategy.

Nevertheless, the observed inconsistency in the estimated values of porosity and permeability, derived from both thin section analysis (in chapter 2) and numerical modeling (in Chapter 3), can be attributed to the scale dependence of these hydraulic parameters. This arises from the three distinct scales of carbonate pore systems: the matrix scale (as evaluated in thin sections), the fracture scale, and the karst scale. Essentially, smaller scale thin section measures all matrix porosity (effective and not effective) whereas the larger scale just captures effective matrix porosity that feeds into fractures or karst conduits. These two chapters emphasizes the need for a multidisciplinary approach to optimize groundwater management and enhance ASR operations.

Chapter 4 tests the long-standing ASR operational methodology aiming at substantially decreasing arsenic concentration to acceptable arsenic drinking water thresholds in the Floridan aquifer. Using boxplot and linear regression statistical analysis coupled with a 1D reactive transport model, this chapter demonstrates a connection between arsenic concentrations and the percentage of recovery, showing a relationship between recovery rate and arsenic mobility. Based on two ASR scenarios, the GWB forward reactive transport model highlights mechanisms driving arsenic fate. These mechanisms encompass the oxidation of arsenic-bearing pyrite, the adsorption of mobilized arsenic onto neo-formed Fe(III) oxides/oxyhydroxides, and the consequential reductive dissolution of Fe(III) oxides/oxyhydroxides following recovery, culminating in the remobilization of arsenic. Of significant note is the operational methodology involving a sustained temporal and spatial oxidizing environment around the ASR well, offering

a pathway to attenuate elevated arsenic concentrations during the ASR recovery process. This strategic insight bears the potential to not only enhance ASR efficiency but also alleviate the need for resource-intensive arsenic removal interventions, thereby charting a course toward sustainable, reliable, and high-quality freshwater supply strategies.

APPENDICES

Appendix A: Supplemental information for Chapter 2: Petrological and geochemical factors related to aquifer storage and recovery feasibility in the Edwards aquifer transition zone, New Braunfels (Texas)

Supplemental Table 2.1. Mineralogy point count of the 12 thin section samples. Note that confining layers are highlighted in yellow and the aquifer formations in blue.

	Depth range [m]	**Sample_ID**	**Total counts**	**OM [%]**	**Calcite [%]**	**Dolomite [%]**	**Chalcedony [%]**
Confining Unit (Georgetown)	163.5-163.9	C13	1154	0.9	98.9	0.2	0.1
	166.1-166.5	C11	1226	0.8	98.4	0.3	0.5
Person Formation	183.6-183.9	C10	731	0.4	99.6	0.0	0.0
	185-185.4	C7	731	0.1	58.5	41.3	0.0
	186.1-186.5	LL21	518	1.4	98.6	0.0	0.0
	188.6-189	C8	575	3.3	0.0	96.7	0.0
	190.6-190.9	C4	637	1.9	0.3	97.8	0.0
Confining Unit (RDM)	216.5-216.7	C9	1616	0.9	99.1	0.0	0.0
	218.9-219.2	C12	1494	0.5	99.0	0.3	0.1
Kainer Formation	230.5-230.8	C2	703	1.3	98.7	0.0	0.0
	241.7-242.1	C3	504	0.0	65.9	34.1	0.0
	251.4-251.7	C1	493	0.6	96.3	3.0	0.0

Supplemental Table 2.2. Modal abundance of pore types on the thin sections of samples collected during the second phase sampling.

	Depth range	sample_ID	Total Porosity	Interparticle [%]	Intraparticle [%]	Moldic [%]	Fracture [%]	Vuggy [%]	Intercrystalline [%]	Total Porosity [%]	Total Porosity	Total point counts
Georgetown Confining Unit	163.5-163.9	C13	15	0	0	6.7	86.6	6.7	0	1.3	15	1184
	166.1-166.5	C11	1	0	0	0	100	0	0	0.1	1	1228
Person Formation	183.6-183.9	C10	13	0	0	38.4	23.1	7.7	30.8	1.7	13	757
	185-185.4	C7	69	0	1.4	0	0	1.5	97.1	5.9	69	1171
	186.1-186.5	LL21	26	0	0	96.2	0	0	3.8	4.6	26	570
	188.6-189	C8	162	0	0	0	12.3	5.6	82.1	18.0	162	899
	190.6-190.9	C4	152	0	0	0	31.6	5.2	63.2	16.2	152	941
RDM confining unit	216.5-216.7	C9	27	0	0	0	100	0	0	1.6	27	1670
	218.9-219.2	C12	7	0	0	0	71.4	28.6	0	0.5	7	1508
Kainer Formation	230.5-230.8	C2	13	15.4	46.2	0	7.6	0	30.8	1.8	13	729
	241.7-242.1	C3	30	0	13.3	0	16.7	0	70	5.3	30	564
	251.4-251.7	C1	18	27.8	22.2	11.1	0	5.6	33.3	3.4	18	529

Supplemental Table 2.3. Major element data in injectant water, groundwater, and mixed groundwater and injectant in ASR well (ASR_Well), in monitoring well open in the Kainer Formation (MW_Kainer Fm.) and monitoring well open in the Person Fm. (MW_Person Fm.).

Water sample	Ca^{2+}	Mg^{2+}	Na^{+}	K^{+}	HCO_3^{-}	SO_4^{2-}	Cl^{-}	pH	Date
-	mg/l	mg/l	mg/l	mg/l	mg/l	mg/l	mg/l	-	-
ASR Well	1508	713	1903	107	610	2459	4512	6.2	3/16/2020
ASR Well	882	445	1812	105	350	2532	2915	6.2	3/18/2020
ASR Well	75.4	19.3	14.6	1.98	206	42	39	8.1	11/30/2021
MW_Kainer Fm.	821	381	1470	68.3	369	2720	2980	7.2	10/17/2019
MW_Kainer Fm.	156	66.1	175	11.8	216	338	333	7.3	4/21/2021
MW_Kainer Fm.	123	50.9	115	9.68	212	240	223	7.1	7/8/2021
MW_Kainer Fm.	117	46.3	96.9	7.03	210	209	198	7.4	10/12/2021
MW_Kainer Fm.	107	39.8	74.8	5.52	212	169	159	7.5	11/9/2021
MW_Person Fm.	808	405	1778	104	324	2658	2780	6.6	3/25/2020
MW_Person Fm.	222	94.4	353	19	212	539	592	6.8	3/31/2020
MW_Person Fm.	82.2	26	26.9	2.41	218	70	54	7.1	1/12/2021
MW_Person Fm.	81.3	24.5	23.1	2.33	220	60	47	7.5	3/31/2021
MW_Person Fm.	72.6	22.4	17.5	2.44	200	50	37	7.5	6/3/2021
MW_Person Fm.	69.3	19.6	14.1	2.86	202	45	34	7.3	7/8/2021
Injectant	63.5	17.9	12.2	2.04	188	30	26	7.9	3/25/2020
Injectant	80.6	17.2	14.9	1.81	212	30	31	7.9	10/22/2020
Injectant	72.3	17.4	12.4	1.55	208	30	24	7.2	12/17/2020
Injectant	69.1	17.8	12.3	1.61	214	29	23	7	1/12/2020
Injectant	66.4	17.7	12.7	1.83	190	31	25	7.5	3/31/2021
Injectant	65.7	17	13.1	2.04	180	31	26	8.4	4/21/2021
Injectant	67	15	10.5	1.99	170	30	24	7.5	6/3/2021
Injectant	68.6	15.5	11.8	2.74	186	31	28	7.4	7/8/2021
Injectant	64.7	15.6	12.4	1.98	192	30	30	7.5	8/17/2021
Injectant	68.6	16.6	12	1.84	204	31	28	7.5	11/9/2021

Appendix B: Supplemental information for Chapter 3: Hydrogeochemical evaluation of aquifer storage and recovery in Edwards aquifer, New Braunfels, Texas.

Supplemental Table 3.1. Record of physical and chemical Water Quality Parameters collected at the NBU ASR Demonstration Project. Blank cells within the physical and chemical parameter columns represent specific values that were not measured or recorded during data collection.

Lab Nbr	*Sample ID*	*Date Taken*	*Field pH*	*Field ORP [mV]*	*Field Dissolved Oxygen [mg/L]*	*Field Conductivity, Specific at 25° C [µS/ cm]*	*Total Alc. [mg/L]*	*Cl^- [mg/L]*	*SO_4^{2-} [mg/L]*	*Ca^{2+} [mg/L]*	*Mg^{2+} [mg/L]*	*K^+ [mg/L*	*Na^+ [mg/L]*	**Operating Mode: Recharge Storage Recovery/Pumping/ Flush/ Maintenance**
Detection Limit [mg/L]			***-***	***-***	***-***	***-***	***5***	***200***	***200***	***2.5***	***0.5***	***1***	***5***	
589487	ASR Well	3/16/2020	6.2	-320	0.43	21,200	610	4,512	2,459	1,508	713	107	1,903	Flush/Pumping
589800	ASR Well	3/18/2020	6.2	-259	0.42	16,980	350	2,915	2,532	882	445	105	1,812	Flush/Pumping
623683	ASR Well	1/12/2021	7.9	-168	0.06	1,376	260	135	148	105			69.1	Flush/Pumping
658355	ASR Well	11/30/2021	8.1	277	0.8	438	206	39	42	75.4	19.3	1.98	14.6	Recovery/Pumping
659495	ASR Well	12/8/2021	6.7	-248	0.39	1,441	212	147	155	97.2	40.3	5.28	72.9	Recovery/Pumping
663912	ASR Well	1/18/2022	7.0	-221	0.4	1,593	210	226	230	119	50.5	7.5	116	Flush/Pumping
HS19101085	MW-2	10/17/2019	7.2			11,890	369	2980	2720	821	381	68.3	1,470	
592883	MW-2	4/14/2020	6.9			8,570	286	1,954	1,928	602				

Lab Nbr	*Sample ID*	*Date Taken*	*Field pH*	*Field ORP [mV]*	*Field Dissolved Oxygen [mg/L]*	*Field Conductivity, Specific at 25° C [µS/ cm]*	*Total Alc. [mg/L]*	*Cl^- [mg/L]*	*SO_4^{2-} [mg/L]*	*Ca^{2+} [mg/L]*	*Mg^{2+} [mg/L]*	*K^+ [mg/L*	*Na^+ [mg/L]*	**Operating Mode: Recharge Storage Recovery/Pumping/ Flush/ Maintenance**
594185	MW-2	4/24/2020	6.9			6,050	266	1,172	1,117	367				
594616	MW-2	4/29/2020	6.9			5,400	242	1,116	995	355				
595454	MW-2	5/6/2020	6.9			5,330	240	1,001	902	332				
598093	MW-2	6/2/2020	6.8	-291	0.35	5,387	244	828	751	285				
	MW-2	6/18/2020	6.8	-243	0.36	3,769								
601044	MW-2	6/30/2020	7.0	-315	0.34	5,403	210	643	610	225				
606895	MW-2	8/20/2020	6.9	-360	0.35	5,508	258	913	807	292				
609449	MW-2	9/15/2020	6.8	-357	0.15	4,107	258	802	775	287				
613965	MW-2	10/22/2020	7.3	-353	0.24	3,565	230	704	663	248				
619960	MW-2	12/17/2020	6.9	-344	0.31	2,978	240	535	508	207				
621884	MW-2	1/12/2021	6.6	-310	0.23	2,937	220	486	469	205	91	17.1	256	
630367	MW-2	3/31/2021	7.3	-235	0.17	1,958	212	325	390	155	65.9	11.5	170	
633434	MW-2	4/21/2021	7.3	-379	0.37	2,130	216	333	338	156	66.1	11.8	175	
637631	MW-2	6/03/2021	7.2	-172	0.1	1,914	202	298	296	149	63.5	11.0	158	
641571	MW-2	7/08/2021	7.1	-22	0.12	1,233	212	223	240	123	50.9	9.68	115	
646331	MW-2	8/17/2021	7.4	-199	1.93	1,649	214	255	254	123	52.6	8.77	119	
647997	MW-2	9/1/2021	7.3		1.68	2,430	218	326	323	143	63.8	11.2	155	
649683	MW-2	9/17/2021	7.4		1.93	1,994	210	355	346	149	72.5	12.1	170	
652721	MW-2	10/12/2021	7.4		1.66	1,702	210	198	209	117	46.3	7.03	96.9	
656100	MW-2	11/9/2021	7.5		1.07	1,489	212	159	169	107	39.8	5.52	74.8	
656930	MW-2	11/16/2021	7.4	-214	2.2	1,860	220	215	220	119	46	7.34	102	

Lab Nbr	*Sample ID*	*Date Taken*	*Field pH*	*Field ORP [mV]*	*Field Dissolved Oxygen [mg/L]*	*Field Conductivity, Specific at 25° C [µS/ cm]*	*Total Alc. [mg/L]*	*Cl^- [mg/L]*	*SO_4^{2-} [mg/L]*	*Ca^{2+} [mg/L]*	*Mg^{2+} [mg/L]*	*K^+ [mg/L*	*Na^+ [mg/L]*	**Operating Mode: Recharge Storage Recovery/Pumping/ Flush/ Maintenance**
658353	MW-2	11/30/2021	7.7	-241	0.47	1,614	216	232	240	123	52.0	7.76	112	
659493	MW-2	12/8/2021	7.0	-285	0.6	5,945	258	985	933	308	154	33.3	478	
664821	MW-2	1/25/2022	6.9	-382	1.62	6,860	264	1415	1314	441	215	50.0	711	
667384	MW-2	2/15/2022	7.0	-250	0.37	1,926	206	298	302	144	61.8	10.1	149	
671506	MW-2	3/22/2022	7.2	-221	0.34	1,308	202	171	54	113	44.5	6.67	88.6	
675356	MW-2	4/26/2022	7.2	-182	0.27	895	204	90	101	85.3	30.3	3.66	42.4	
	MW-2	4/29/2022	7.3	-211	0.42	1,114								
	MW-2	5/2/2022	7.4	-216	0.34	1,219								
	MW-2	5/5/2022	7.2	-230	0.33	1,322								
	MW-2	5/9/2022	7.4	-221	0.4	1,458								
HS18090667	MW-1	9/13/2018					376	2780	2460	769	378	66.2	1,410	
590823	MW-1	3/25/2020	6.4	-324	0.41	17,900	324	2,790	2,658	808	405	104	1,778	
591199	MW-1	3/31/2020	6.8	-327	0.3	3,780	212	592	539	222	94.4	19	353	
592032	MW-1	4/7/2020	7	-212	0.34	1,430	208	218	210	125				
592882	MW-1	4/14/2020	*6.3			1,130	204	135	144	106				
594184	MW-1	4/24/2020	*6.1			1,860	218	292	288	143				
594615	MW-1	4/29/2020	*6.1			812	208	97	106	97.9				

Lab Nbr	*Sample ID*	*Date Taken*	*Field pH*	*Field ORP [mV]*	*Field Dissolved Oxygen [mg/L]*	*Field Conductivity, Specific at 25° C [µS/ cm]*	*Total Alc. [mg/L]*	*Cl^- [mg/L]*	*SO_4^{2-} [mg/L]*	*Ca^{2+} [mg/L]*	*Mg^{2+} [mg/L]*	*K^+ [mg/L*	*Na^+ [mg/L]*	**Operating Mode: Recharge Storage Recovery/Pumping/ Flush/ Maintenance**
595453	MW-1	5/6/2020	*6.1			764	192	73	79	80.5				
596745	MW-1	5/19/2020	7.0	73.3	1.01	670	210	47	56	85.9				
598094	MW-1	6/2/2020	7.1	222	0.36	784	208	67	76	89.5				
599953	MW-1	6/18/2020	7.1	135	0.35	853	208	78	86	90.6				
601043	MW-1	6/30/2020	7.2	-253	0.34	1,243	206	182	184	110				
602603	MW-1	7/15/2020	6.8	-359	0.18	1,051	218	179	186	124				
604277	MW-1	7/29/2020	7.0	-367	0.02	1,574	220	220	234	126				
606896	MW-1	8/20/2020	7.1	-376	0.35	1,954	232	214	230	131				
609448	MW-1	9/15/2020	7.0	-355	0.13	1,665	232	244	259	137				
613966	MW-1	10/22/2020	7.6	-317	0.22	1,050	210	69	85	89.5				
619959	MW-1	12/17/2020	7.1	4.1	1.06	647	210	36	51	77.8				
621883	MW-1	1/12/2021	7.1	47.2	2.3	742	218	54	70	82.2	26	2.41	26.9	
630366	MW-1	3/31/2021	7.5	-120	1	389	220	47	60	81.3	24.5	2.33	23.1	
633435	MW-1	4/21/2021	8.2	-312	0.71	669	194	42	55	76.5	23.3	2.42	21.2	
637630	MW-1	6/03/2021	7.5	-73.2	0.66	609	200	37	50	72.6	22.4	2.44	17.5	
641570	MW-1	7/08/2021	7.3	129	0.86	521	202	34	45	69.3	19.6	2.86	14.1	
646332	MW-1	8/17/2021	7.4	7.25	3.23	602	202	36	46	70.6	20.8	2.10	15.6	
647996	MW-1	9/1/2021	7.4		2.47	784	204	42	60	70.5	23.6	2.24	18.2	
649684	MW-1	9/17/2021	7.4		3.23	730	210	39	52	72.1	24.9	2.17	17.6	
652722	MW-1	10/12/2021	7.6		2.92	752	202	37	48	74.1	22.2	2.24	16.7	

Lab Nbr	*Sample ID*	*Date Taken*	*Field pH*	*Field ORP [mV]*	*Field Dissolved Oxygen [mg/L]*	*Field Conductivity, Specific at 25° C [µS/ cm]*	*Total Alc. [mg/L]*	*Cl^- [mg/L]*	*SO_4^{2-} [mg/L]*	*Ca^{2+} [mg/L]*	*Mg^{2+} [mg/L]*	*K^+ [mg/L*	*Na^+ [mg/L]*	**Operating Mode: Recharge Storage Recovery/Pumping/ Flush/ Maintenance**
656101	MW-1	11/9/2021	7.6		2.76	839	212	38	48	79.6	22.1	2.1	16.2	
656931	MW-1	11/16/2021	7.5	-98.6	2.09	845	220	42	57	72	21.9	2.21	17.6	
658354	MW-1	11/30/2021	7.5	-147	0.44	793	208	43	59	75.6	24.9	2.31	19.5	
659494	MW-1	12/8/2021	7.1	-205	1.42	1,765	216	208	215	113	49.6	7.94	103	
664822	MW-1	1/25/2022	7.2	-201	3.52	1,954	214	291	292	143	64.5	10.3	150	
667385	MW-1	2/15/2022	7.1	-152	0.56	744	198	61	76	77.3	25.3	2.53	28.2	
671507	MW-1	3/22/2022	7.3	-133	1.22	620	194	43	29	75.3	24.3	2.43	21.3	
675357	MW-1	4/26/2022	7.4	-108	2.54	630	194	40	47	74.1	22.1	2.3	18.7	
	MW-1	4/29/2022	7.4	-91.5	0.33	685								
	MW-1	5/2/2022	7.5	-61.2	0.84	698								
	MW-1	5/5/2022	7.5	-71.7	0.35	705								
	MW-1	5/9/2022	7.5	-64.2	0.41	710								
590822	NBU System Water	3/25/2020					188	26	30	63.5	17.9	2.04	12.2	Recharge from 3/25 2020 to 7/8/2020
594186	NBU System Water	4/24/2020					198	27	30	67.1				
	NBU System Water	5/19/2020	7.2	340	8	536								

Lab Nbr	*Sample ID*	*Date Taken*	*Field pH*	*Field ORP [mV]*	*Field Dissolved Oxygen [mg/L]*	*Field Conductivity, Specific at 25° C [µS/ cm]*	*Total Alc. [mg/L]*	*Cl^- [mg/L]*	*SO_4^{2-} [mg/L]*	*Ca^{2+} [mg/L]*	*Mg^{2+} [mg/L]*	*K^+ [mg/L*	*Na^+ [mg/L]*	**Operating Mode: Recharge Storage Recovery/Pumping/ Flush/ Maintenance**
599952	NBU System Water	6/18/2020	7.1	340	8.00	656	210	25	30	74.3				
601045	NBU System Water	6/30/2020	7.0	430	3.47	942	216	24	30	78.6				
613964	NBU System Water	10/22/2020	7.9	412	14.90	581	212	31	30	80.6	17.2	1.81	14.9	Recharge from 7/9/2020 to 10/18/2020
619958	NBU System Water	12/17/2020	7.2	405	8.46	540	208	24	30	72.3	17.4	1.55	12.4	Recharge from 10/18/2020 to 11/9/2021
621882	NBU System Water	1/12/2021	7.0	405	8.19	539	214	23	29	69.1	17.8	1.61	12.3	
630368	NBU System Water	3/31/2021	7.5	431	8.43	498	190	25	31	66.4	17.7	1.83	12.7	
633436	NBU System Water	4/21/2021	8.4	361	6.94	531	180	26	31	65.7	17	2.04	13.1	
637632	NBU System Water	6/03/2021	7.5	403	9.09	511	170	24	30	67	15.0	1.99	10.5	
641572	NBU System Water	7/08/2021	7.4	549	9.28	460	186	28	31	68.6	15.5	2.74	11.8	
646333	NBU System Water	8/17/2021	7.5	448	8.30	554	192	30	30	64.7	15.6	1.98	12.4	

Lab Nbr	*Sample ID*	*Date Taken*	*Field pH*	*Field ORP [mV]*	*Field Dissolved Oxygen [mg/L]*	*Field Conductivity, Specific at 25° C [µS/ cm]*	*Total Alc. [mg/L]*	*Cl^- [mg/L]*	*SO_4^{2-} [mg/L]*	*Ca^{2+} [mg/L]*	*Mg^{2+} [mg/L]*	*K^+ [mg/L*	*Na^+ [mg/L]*	**Operating Mode: Recharge Storage Recovery/Pumping/ Flush/ Maintenance**
656102	NBU System Water	11/9/2021					204	28	31	68.6	16.6	1.84	12	

Supplemental Table 3.2. Record of water levels in monitoring wells open in the Person Formation (MW-1), and the Kainer Formation (MW-2). Highlighted in blue are initial heads before the first recharge cycle.

Person Formation			**Kainer Formation**		
Date	Water level	Water level	Date	Water level	Water

Person Formation			Kainer Formation		
	[ft]	[m]		[ft]	level [m]
3/24/2020	617.9009901	188.3362218	3/17/2020	616.2078961	187.8202
3/26/2020	691.0891089	210.6439604	3/29/2020	676.6402584	206.24
3/27/2020	708.5544554	215.967398	4/6/2020	688.2101651	209.7665
3/30/2020	728.5148515	222.0513267	4/14/2020	693.1528759	211.273
4/10/2020	731.009901	222.8118178	4/20/2020	699.7611287	213.2872
4/20/2020	743.4851485	226.6142733	4/25/2020	699.7421855	213.2814
5/2/2020	746.8118812	227.6282614	4/30/2020	704.6936393	214.7906
5/12/2020	745.980198	227.3747644	5/5/2020	712.9601482	217.3103
5/24/2020	751.8019802	229.1492436	5/10/2020	717.9130592	218.8199
6/5/2020	755.960396	230.4167287	5/14/2020	724.5285978	220.8363
6/12/2020	751.8019802	229.1492436	5/21/2020	734.446077	223.8592
6/21/2020	750.970297	228.8957465	5/25/2020	743.5424426	226.6317
7/1/2020	744.3168317	226.8677703	6/1/2020	741.0339294	225.8671
7/2/2020	706.8910891	215.460404	6/5/2020	738.5356165	225.1057
7/2/2020	671.960396	204.8135287	6/12/2020	741.8229854	226.1076
7/2/2020	690.2574257	210.3904634	6/19/2020	741.7996707	226.1005
7/2/2020	728.5148515	222.0513267	6/25/2020	735.980474	224.3268
7/12/2020	647.8415842	197.4621149	6/25/2020	717.754228	218.7715
7/22/2020	642.8514851	195.9411327	6/26/2020	702.0117233	213.9732

Person Formation			Kainer Formation		
7/30/2020	640.3564356	195.1806416	6/26/2020	682.9570778	208.1653
8/9/2020	636.1980198	193.9131564	6/28/2020	662.2398046	201.8507
8/18/2020	633.7029703	193.1526653	7/6/2020	648.129327	197.5498
8/25/2020	634.5346535	193.4061624	7/13/2020	642.3072159	195.7752
9/9/2020	632.8712871	192.8991683	7/20/2020	639.7972456	195.0102
9/24/2020	629.5445545	191.8851802	7/27/2020	637.2887325	194.2456
10/9/2020	629.5445545	191.8851802	8/3/2020	634.777305	193.4801
10/15/2020	644.5148515	196.4481267	8/15/2020	633.909562	193.2156
10/16/2020	656.1584158	199.9970851	8/28/2020	632.621062	192.8229
10/16/2020	686.9306931	209.3764752	9/9/2020	629.6801345	191.9265
10/16/2020	675.2871287	205.8275168	9/18/2020	628.8211345	191.6647
10/17/2020	701.0693069	213.6859248	9/26/2020	628.7919911	191.6558
10/23/2020	706.8910891	215.460404	10/2/2020	627.9431913	191.3971
10/24/2020	686.0990099	209.1229782	10/11/2020	631.2232744	192.3969
10/25/2020	658.6534653	200.7575762	10/12/2020	656.0723449	199.9709
10/28/2020	641.1881188	195.4341386	10/13/2020	678.437674	206.7878
10/29/2020	666.1386139	203.0390495	10/14/2020	690.8578377	210.5735
10/28/2020	687.7623762	209.6299723	10/19/2020	697.4690048	212.5886
10/29/2020	703.5643564	214.4464158	10/20/2020	677.5845027	206.5278
11/3/2020	715.2079208	217.9953743	10/20/2020	660.1881133	201.2253

Person Formation			Kainer Formation		
11/17/2020	714.3762376	217.7418772	10/22/2020	645.2681795	196.6777
11/29/2020	715.2079208	217.9953743	10/24/2020	656.8584865	200.2105
12/13/2020	715.2079208	217.9953743	10/24/2020	686.6808683	209.3003
12/23/2020	713.5445545	217.4883802	10/28/2020	702.4088013	214.0942
1/1/2021	715.2079208	217.9953743	11/5/2020	708.1784544	215.8528
1/11/2021	715.2079208	217.9953743	11/15/2020	709.8017385	216.3476
			11/24/2020	708.9412814	216.0853
			11/30/2020	711.4060795	216.8366

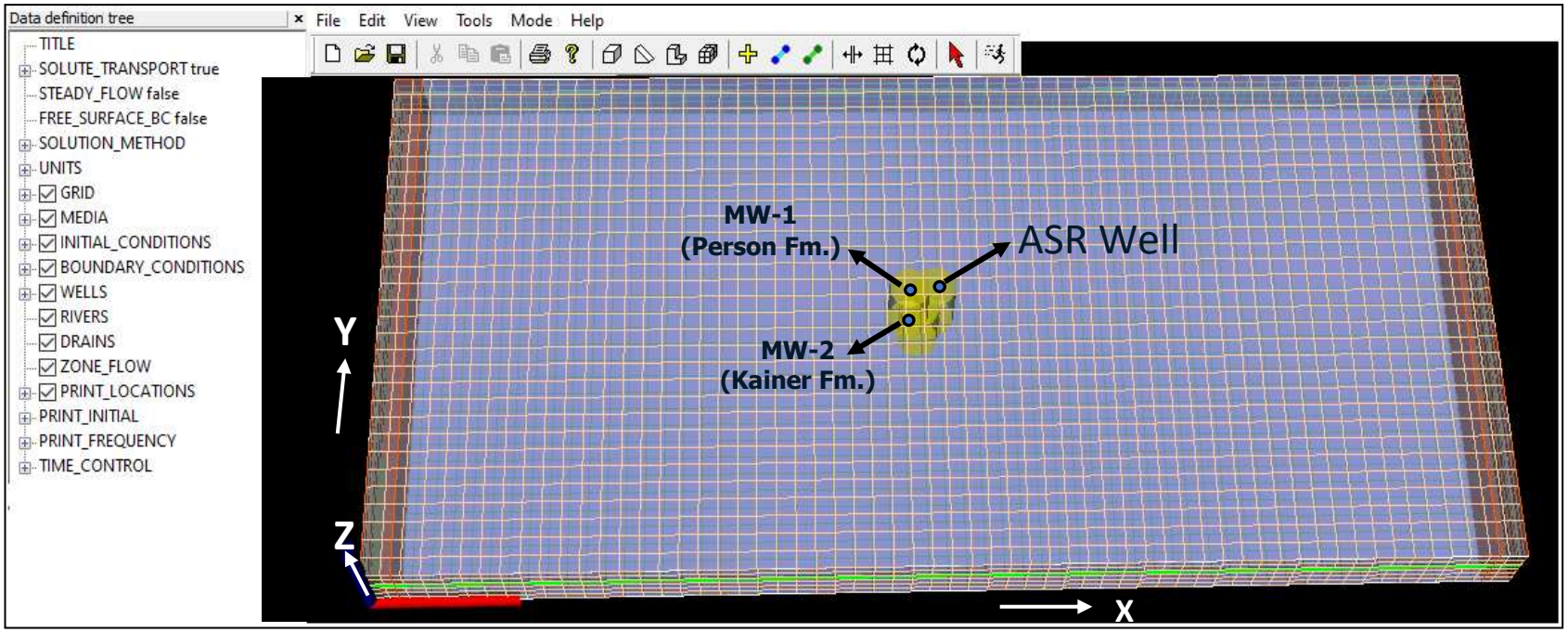

Supplemental Figure 3.1. PHAST model grid of the study area. The simulation region was discretized in the X, Y, and Z directions with uniform spacing of nodes in each direction. 2,000 m in length with 61 nodes, 940 m in width with 31 nodes, and 124.6 m thick with 7 nodes. Grid refinement was done in the vicinity of the injection (ASR) well and the confining layer (RDM).

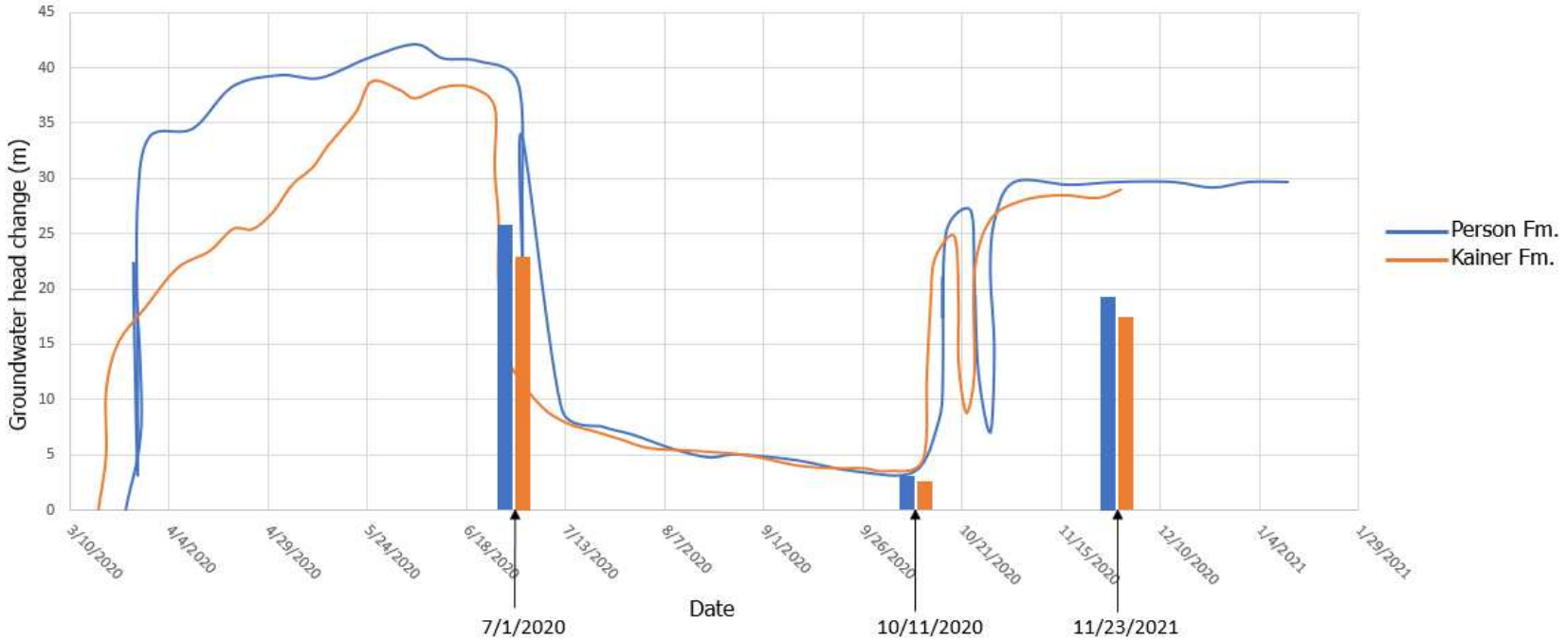

Supplemental Figure 3.2. Observed and simulated groundwater head changes associated with each recharge period. Note that the simulated groundwater head changes are the maximum head changes at the end of each recharge period in both monitoring wells.

Analytic flow modeling

Considering that (1) the average groundwater elevation changes over the recharge period (Supplemental Figure 3.2.), where both head change curves track each other to a large extent; (2) the chloride signature of the recharge water arrives at the monitoring well open in the Person Formation earlier than at the monitoring well open in the Kainer Formation (Supplemental Figure 3.3); the two-layer aquifer is hypothesized to behave like a multilayered leaky aquifer system.

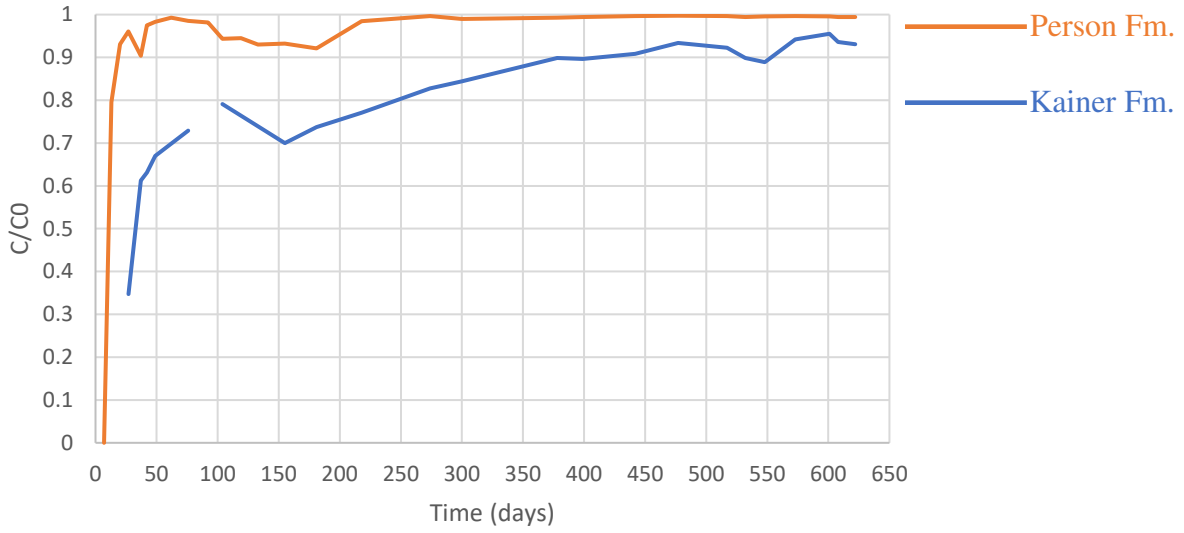

Supplemental Figure 3.3. Time series evolution of chloride concentrations in both aquifer zones. C0 is the injectant chloride concentration, and C is the time series chloride concentration recorded in each monitoring well.

Hemker's (1984) analytical solution for a steady groundwater flow in leaky multiaquifer systems is developed to evaluate the numerical PHAST model results. While the analytical model dispenses from boundary condition effects and gridding issues, etc., its simplifying assumptions give important insights critical to the model (Haitjema, 2006) for a quick screening model purpose. The fundamental assumption in the theory of steady groundwater flow model in leaky

aquifer systems is that the under- and/or overlying aquifers supply or discharge the entire leakage while maintaining an unchanged hydraulic head within these two layers (Hemker, 1984). However, within 50 meters distant from the ASR well over months of injection, herein, the analytical solution simulates the head change, the gradient, the flux, and the horizontal travel time in both monitoring wells.

Herein, two aquifer layers, the Person and Kainer Formations, are separated and enclosed by confining layers. RDM semi-confining layer separates both aquifer layers. A schematic illustrating the model domain of interest is depicted in supplemental Figure 3.4 below:

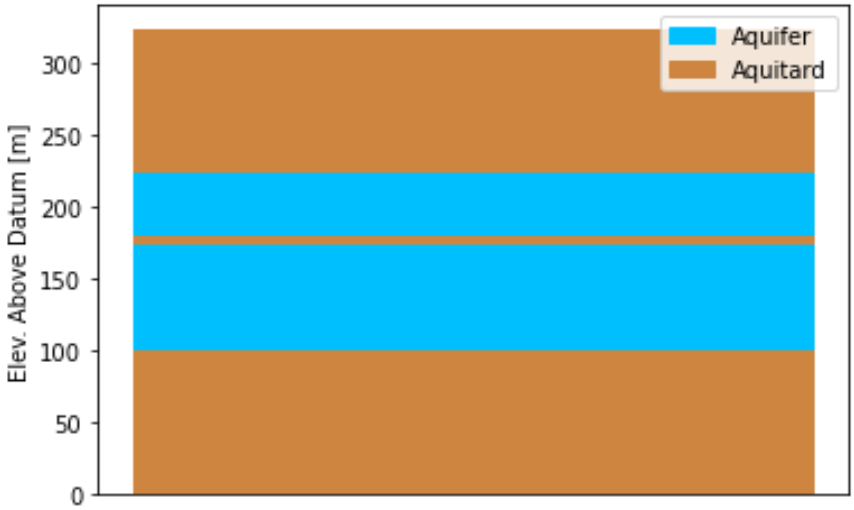

Supplemental Figure 3.4. A 2D conceptual model of the study site.

Vertical extents are taken from the PHAST model setup. The two thick aquitards above and below the two aquifer layers are dummy units with vanishingly small hydraulic conductivities. This forces the overall model to behave as a semi-confined system; the analytical solution insists that every aquifer unit is surrounded on both top and bottom by an aquitard.

By assigning property values to this analytical model (arrived at by trial and error using python codes), below ***Supplemental Table 3.3*** gives the estimated conductivity values roughly similar to the PHAST calibrated numbers:

	"Calibrated" PHAST model	Analytical Model
Person Formation	Kx = 3.6e-6 Ky = 3.0e-6 Kz = 4.9e-7	K = 3.3e-6
Confining layer	Kx = 4.1e-7 Ky = 4.1e-7 Kz = 6.0e-7	K = 8.2e-7
Kainer Formation	Kx = 7.3e-5 Ky = 7.1e-5 Kz = 8.9e-6	K = 1.4e-5

With this parameterization, supplemental Figure 3.5 below presents profiles of groundwater head changes in aquifer layers of the Person and Kainer Formations.

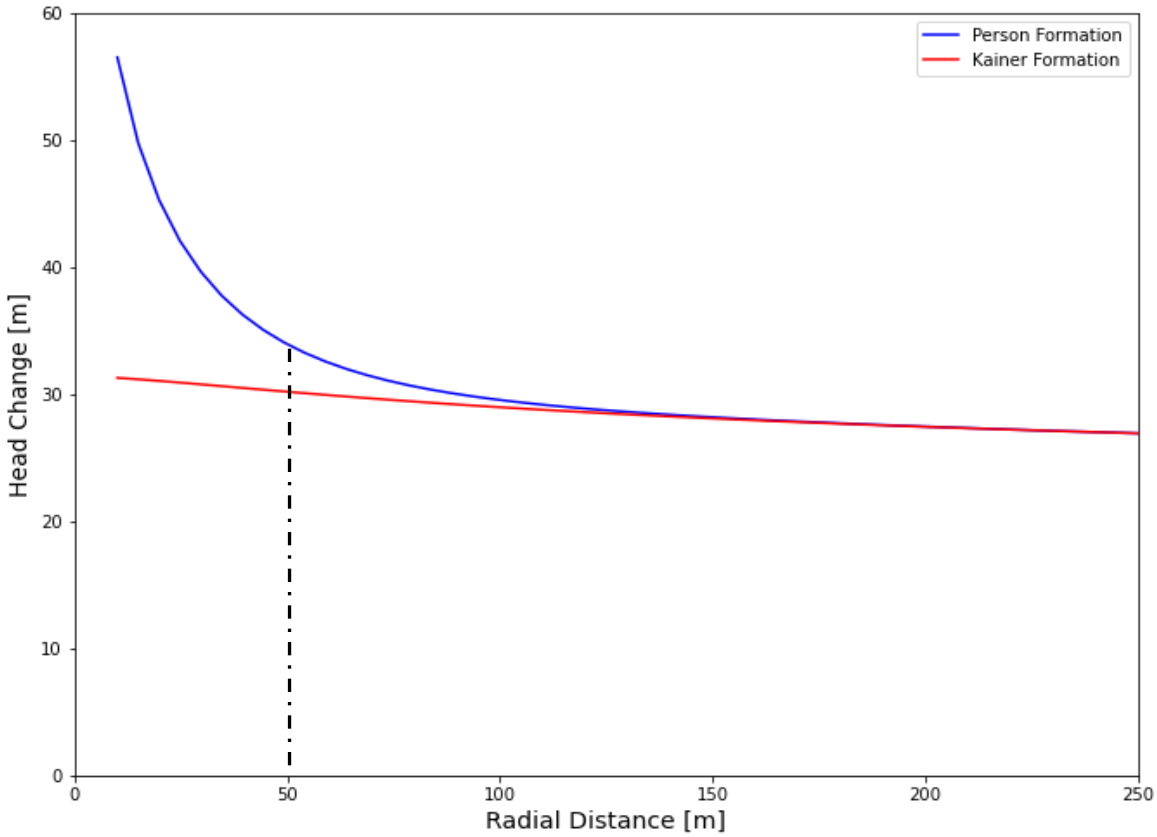

Supplemental Figure 3.5. The evolution of the groundwater head changes with the radial distance. Note both monitoring wells are located at circa 50 m from the ASR well.

Using the Hemker analytical solution developed in python and considering that both monitoring wells are roughly 50 meters from the ASR well (i.e., at r = 50 m), supplemental **Table 3.4** below provides the results of the groundwater head change (m), the gradient, the flux (m^3/sec), and the horizontal travel time (days) in both aquifer zones:

	Person Fm.	Kainer Fm.
Head change	33.9	30.2
Gradient	-0.18	-0.03
Flux	0.008	0.009
Horizontal travel time	37	177

The analysis of the results yields the following observations:

(a) the modeled values of the groundwater head changes in the Person Formation (33.9 m), and Kainer Formation (30.2 m) are roughly similar to the observed groundwater head changes in supplemental Figure 3.2, considering the apparent non-uniform recharge rates in the steady state model that assumes averages.

(b) The fluxes from both zones add up to the overall time-weighted average injection rate of about 0.017 m^3/sec, indicating that flow is conserved properly.

(c) The horizontal travel times (calculated by numerical integration of the gradient as a function of radius) offer an explanation for the observed evolution of chloride concentrations in both monitoring wells: travel time for the advective front to travel from the ASR well to the Person Formation monitoring well (MW-1) is 37 m, which is considerably shorter than that in the Kainer Formation (MW-2) which is of 177 m. Uncertainty in the calculation of these travel times includes assumptions of uniform injection rate, uniform porosity value, the role of mixing and dispersion, fractures and heterogeneities, etc. However, the model results substantiate the slower chloride tracer signal arrival in the Kainer Formation.

References

Haitjema, H., 2006. The role of hand calculations in ground water flow modeling. *Groundwater 44, no.* 6, 786-791.

Hemker, C. J., 1984. Steady groundwater flow in leaky multiple-aquifer systems. *Journal of Hydrology* 72, no. 3-4, 355–37

Appendix C: Supplemental information for Chapter 4: Managing arsenic mobilization during aquifer storage and recovery in carbonate aquifers (Floridan aquifer, Florida, USA).

Supplemental Table 4.1. Fifth cycle ASR data in all five Tampa ASR fields.

ASR Field	Sample Date	Recharge [MG]	Storage [days]	Recovery [MG] (% recovery)	DO mg/L	pH std.units	ORP mV	Arsenic µg/L
ASR-4	08/02/05	119.7			5.6	8.0		<.001
	08/09/05				20.6	7.9		<.001
	08/16/05				0.5	8.1		<.001
	08/23/05				<0.1	8.0		<.001
	08/30/05				18.7	8.2		<.001
	09/06/05				0.6			<.001
	09/13/05				17.6	8.0		<.001
	09/20/05				15.8	8.0		<.001
	09/27/05					8.0		<.001
	10/04/05				17.5	8.0		<.001
	10/11/05				17.1	7.2		<.001
	10/18/05				5.5	7.7		<.001
	10/25/05				30.7	7.7		<.001
	11/01/05				14.7	7.5		<.001
	11/08/05				12.9	7.6		<.001
	11/15/05				9.5	7.8		<.001
	11/22/05				37.5	8.0		<.001
	12/06/05		63		35.4	7.6		<.001
	01/03/06				22.2	7.4		<.001
	02/07/06					7.6		<.001
	03/21/06			127.23 (106%)	3.5	7.5	-14	5
	03/23/06				7.4	7.3	115	9

ASR Field	Sample Date	Recharge [MG]	Storage [days]	Recovery [MG] (% recovery)	DO mg/L	pH std.units	ORP mV	Arsenic µg/L
	03/28/06				0.5	7.2	-24	12
	03/30/06				4.5	7.6	8	14
	04/04/06				2.4	7.6	5	18
	04/06/06				1.5	7.5	-132	20
	04/11/06				2.0	7.4	-11	22
	04/13/06				<0.1	7.5	-103	20
	04/18/06				0.1	7.5	24	21
	04/20/06				3.8	7.7	-78	22
	04/25/06				2.7	7.5	-40	27
	04/27/06				0.1	7.5	-203	26
	05/02/06				0.4	7.3	-111	26
	05/04/06				6.8	7.6	-55	25
	05/09/06				0.2	7.3	-24	27
	05/11/06				0.5	6.9	13	31
	05/16/06				6.6	7.5	53	31
	05/18/06				5.0	8.2	37	27
	05/23/06				1.9	7.4	98	27
	05/25/06				1.9	7.7	79	26
	05/30/06							30
	06/01/06				2.2	7.4	65	30
	06/06/06				0.9	7.5	20	31
	06/13/06				0.1	7.5	-1	28
	06/15/06				1.3	7.6	15	31
	06/20/06				0.4	7.4	22	30
	06/22/06				0.2	7.4	2	26
ASR-5	08/02/05	**79.86**			5.6	8.0	216	<.001

ASR Field	Sample Date	Recharge [MG]	Storage [days]	Recovery [MG] (% recovery)	DO mg/L	pH std.units	ORP mV	Arsenic µg/L
	08/09/05				20.6	7.9	315	<.001
	08/16/05				0.5	8.1	199	<.001
	08/23/05				<0.1	8.0	183	<.001
	08/30/05				18.7	8.2	292	<.001
	09/06/05				0.6		196.8	<.001
	09/13/05				17.6	8.0	231.4	<.001
	09/20/05				15.8	8.0	235.6	<.001
	09/27/05					8.0	261.8	<.001
	10/04/05				17.5	8.0	351.9	<.001
	10/11/05				17.1	7.2	297.5	<.001
	10/18/05				5.5	7.7	344.9	<.001
	10/25/05				30.7	7.7	371.8	<.001
	11/01/05				14.7	7.5	367	<.001
	11/08/05				12.9	7.6	461	<.001
	11/15/05				9.5	7.8	368	<.001
	11/22/05				37.5	8.0	400	<.001
	12/06/05		**63.00**		35.4	7.6	385.6	<.001
	01/03/06				22.2	7.4	325	<.001
	02/07/06					7.6	398.2	<.001
	03/21/06			**126.66 (158.6%)**	2.1	7.4	-34	6
	03/23/06				7.9	7.4	45	10
	03/28/06				0.8	7.3	-47	12
	03/30/06				1.5	7.5	5	15
	04/04/06				1.5	7.6	-89	20
	04/06/06				3.1	7.5	-101	16
	04/11/06				2.0	7.5	-18	21

ASR Field	Sample Date	Recharge [MG]	Storage [days]	Recovery [MG] (% recovery)	DO mg/L	pH std.units	ORP mV	Arsenic µg/L
	04/13/06				<0.1	7.5	-113	21
	04/18/06				0.4	7.6	-81	14
	04/20/06				1.3	7.6	-82	20
	04/25/06				1.2	7.5	-31	23
	04/27/06				0.1	7.6	-201	24
	05/02/06				0.2	7.6	-65	24
	05/04/06				2.8	7.5	-61	25
	05/09/06				0.3	7.3	-26	28
	05/11/06				0.2	7.0	-50	23
	05/16/06				1.0	7.4	54	30
	05/18/06				5.2	8.0	45	29
	05/23/06				1.7	7.3	109	33
	05/25/06				1.7	7.4	61	24
	05/30/06							32
	06/01/06				2.5	7.4	78	35
	06/06/06				1.3	7.5	110	37
	06/08/06				0.3	7.2	39	38
	06/13/06				0.9	7.1	18	36
	06/15/06				1.2	7.7	17	38
	06/20/06				<0.1	7.5	34	36
	06/22/06				1.4	7.4	9	36
	06/27/06				1.2	7.4	83	37
ASR-6	08/02/05	**121.65**			5.6	8.0	216	<.001
	08/09/05				20.6	7.9	315	<.001
	08/16/05				0.5	8.1	199	<.001
	08/23/05				<0.1	8.0	183	<.001

ASR Field	Sample Date	Recharge [MG]	Storage [days]	Recovery [MG] (% recovery)	DO mg/L	pH std.units	ORP mV	Arsenic µg/L
	08/30/05				18.7	8.2	292	<.001
	09/06/05				0.6		197	<.001
	09/13/05				17.6	8.0	231	<.001
	09/20/05				15.8	8.0	236	<.001
	09/27/05					8.0	262	<.001
	10/04/05				17.5	8.0	352	<.001
	10/11/05				17.1	7.2	298	<.001
	10/18/05				5.5	7.7	345	<.001
	10/25/05				30.7	7.7	372	<.001
	11/01/05				14.7	7.5	367	<.001
	11/08/05				12.9	7.6	461	<.001
	11/15/05				9.5	7.8	368	<.001
	11/22/05				37.5	8.0	400	<.001
	12/06/05		**63.00**		35.4	7.6	386	<.001
	01/03/06				22.2	7.4	325	<.001
	02/07/06					7.6	398	<.001
	03/21/06			**120.41 (99%)**	4.1	7.6	-64	3
	03/28/06				0.9	7.4	-31	1
	03/30/06				3.9	7.6	-6	2
	04/04/06				6.3	8.0	-10	6
	04/06/06				2.4	7.6	-67	7
	04/11/06				2.0	7.5	-11	8
	04/13/06				<0.1	7.5	-93	7
	04/18/06				<0.1	7.5	3	6
	04/20/06				5.0	7.8	-76	11
	04/25/06				2.6	7.5	-42	15

ASR Field	Sample Date	Recharge [MG]	Storage [days]	Recovery [MG] (% recovery)	DO mg/L	pH std.units	ORP mV	Arsenic µg/L
	04/27/06				<0.1	7.6	-208	15
	05/02/06				<0.1	7.5	-78	16
	05/04/06				8.1	7.7	-55	15
	05/09/06				0.2	7.3	-53	16
	05/11/06				0.3	7.0	-47	16
	05/16/06				5.2	7.5	38	16
	05/18/06				5.8	8.2	21	16
	05/23/06				2.3	7.4	88	15
	05/25/06				2.2	7.6	84	15
	05/30/06							15
	06/01/06				2.0	7.4	25	16
	06/06/06				0.4	7.4	44	18
	06/08/06				<0.1	7.2	24	16
	06/13/06				<0.1	7.1	-35	26
	06/15/06				2.8	7.7	7	17
	06/20/06				<0.1	7.4	5	17
	06/22/06				<0.1	7.3	-1	19
	06/27/06				3.0	7.5	102	19
ASR-7	08/02/05	**110.13**			5.6	8.0	216	<.001
	08/09/05				20.6	7.9	315	<.001
	08/16/05				0.5	8.1	199	<.001
	08/23/05				<0.1	8.0	183	<.001
	08/30/05				18.7	8.2	292	<.001
	09/06/05				0.6		197	<.001
	09/13/05				17.6	8.0	231	<.001
	09/20/05				15.8	8.0	236	<.001

ASR Field	Sample Date	Recharge [MG]	Storage [days]	Recovery [MG] (% recovery)	DO mg/L	pH std.units	ORP mV	Arsenic µg/L
	10/04/05				17.5	8.0	352	<.001
	10/11/05				17.1	7.2	298	<.001
	10/18/05				5.5	7.7	345	<.001
	10/25/05				30.7	7.7	372	<.001
	11/01/05				14.7	7.5	367	<.001
	11/08/05				12.9	7.6	461	<.001
	11/15/05				9.5	7.8	368	<.001
	11/22/05				37.5	8.0	400	<.001
	12/06/05		**63.00**		35.4	7.6	386	<.001
	01/03/06				22.2	7.4	325	<.001
	02/07/06					7.6	398	<.001
	03/21/06			**127.44 (116%)**	7.2	7.9	7	7
	03/23/06				7.8	7.4	47	9
	03/28/06				1.7	7.5	-51	8
	03/30/06				5.2	7.7	-38	5
	04/04/06				4.8	7.5	-88	12
	04/06/06				1.0	7.8	-95	15
	04/11/06				5.2	7.6	-32	19
	04/13/06				<0.1	7.4	-123	20
	04/18/06				0.1	7.4	19	27
	04/20/06				4.8	7.8	-101	29
	04/25/06				4.5	7.5	-40	33
	04/27/06				<0.1	7.5	-208	33
	05/02/06				0.1	7.6	-117	30
	05/04/06				7.1	7.8	-51	30
	05/09/06				0.3	7.3	-42	29

ASR Field	Sample Date	Recharge [MG]	Storage [days]	Recovery [MG] (% recovery)	DO mg/L	pH std.units	ORP mV	Arsenic µg/L
	05/11/06				<0.1	6.9	-41	31
	05/16/06				3.6	7.5	43	29
	05/18/06				3.3	8.0	17	31
	05/23/06				2.1	7.4	93	32
	05/25/06				2.1	7.7	100	33
	05/30/06							31
	06/01/06				2.6	7.4	53	32
	06/06/06				0.6	7.4	75	37
	06/08/06				<0.1	7.3	169	33
	06/13/06				<0.1	7.4	18	37
	06/15/06				4.7	7.7	4	36
	06/20/06				0.5	7.5	28	36
	06/22/06				0.2	7.4	24	35
	06/29/06				3.2	7.6	118	37
ASR-8	08/01/05	**155.46**						0
	08/02/05				5.6	8.0	216	<.001
	08/09/05				20.6	7.9	315	<.001
	08/16/05				0.5	8.1	199	<.001
	08/23/05				<0.1	8.0	183	<.001
	08/30/05				18.7	8.2	292	<.001
	09/06/05				0.6		197	<.001
	09/13/05				17.6	8.0	231	<.001
	09/20/05				15.8	8.0	236	<.001
	09/27/05					8.0	262	<.001
	10/04/05				17.5	8.0	352	<.001
	10/11/05				17.1	7.2	298	<.001

ASR Field	Sample Date	Recharge [MG]	Storage [days]	Recovery [MG] (% recovery)	DO mg/L	pH std.units	ORP mV	Arsenic µg/L
	10/18/05				5.5	7.7	345	<.001
	10/25/05				30.7	7.7	372	<.001
	11/01/05				14.7	7.5	367	<.001
	11/08/05				12.9	7.6	461	<.001
	11/15/05				9.5	7.8	368	<.001
	11/22/05				37.5	8.0	400	<.001
	12/06/05				35.4	7.6	386	<.001
	01/03/06		**63.00**		22.2	7.4	325	<.001
	02/07/06					7.6	398	<.001
	03/21/06				3.0	7.2	-75	16
	03/23/06				6.7	7.3	-80	10
	03/28/06				5.4	7.5	-137	17
	03/30/06				1.8	7.5	-46	17
	04/04/06				2.2	7.5	-150	15
	04/06/06				2.0	7.5	-229	13
	04/11/06				2.5	7.2	-36	15
	04/13/06				<0.1	7.5	-190	16
	04/18/06			**124.34 (80%)**	0.1	7.5	-138	14
	04/20/06				1.5	7.3	-140	14
	04/25/06				1.4	7.4	-102	17
	04/27/06				<0.1	7.5	-223	17
	05/02/06				0.2	7.5	134	16
	05/04/06				2.7	7.4	-112	16
	05/09/06				0.2	7.3	-115	14
	05/11/06				0.3	6.9	-94	14
	05/16/06				2.8	7.3	9	16

ASR Field	Sample Date	Recharge [MG]	Storage [days]	Recovery [MG] (% recovery)	DO mg/L	pH std.units	ORP mV	Arsenic µg/L
	05/18/06				4.0	8.0	-18	15
	05/23/06				1.4	7.4	28	13
	05/25/06				1.4	7.0	58	17
	05/30/06							12
	06/01/06				1.8	7.4	-7	13
	06/06/06				0.3	7.4	-31	13
	06/08/06				<0.1	6.8	-23	13
	06/13/06				<0.1	7.3	-43	15
	06/15/06				1.7	7.5	9	13
	06/20/06				0.1	7.5	-38	12
	06/22/06				<0.1	7.3	-26	11

Supplemental Table 4.2. Results of arsenic species, oxygen and Fe oxyhydroxide concentrations yielded from the GWB reactive transport model considering the buffer zone model scenario for a modeled flow path of 1,000 m.

X position	H_3AsO_3	$As(OH)_4^-$	AsO_4^{3-}	$H_2AsO_4^-$	H_3AsO_4	$HAsO_4^{2-}$	$O_2(aq)$	>(w)FeH_2AsO_4	>(w)FeHAsO4$^-$	>(w)$FeOHAsO_4^{3-}$	$Fe(OH)_3$	Pyrite
m	ug/l	ug/l	ug/l	ug/l	ug/l	ug/l	ug/l	ug/l	ug/l	ug/l	mg/kg	mg/kg
5	2.7E-29	9.5E-31	6.8E-05	3.7E-02	1.3E-07	3.9E-01	4.2E+03	5.6E-02	8.4E+00	9.8E+03	4.9E+02	
15	1.6E-29	5.6E-31	3.6E-05	2.1E-02	7.1E-08	2.1E-01	3.7E+03	3.6E-02	6.1E+00	8.7E+03	5.6E+02	
25	1.5E-29	5.1E-31	3.0E-05	1.8E-02	6.2E-08	1.8E-01	3.2E+03	3.2E-02	5.4E+00	8.1E+03	5.5E+02	
35	1.6E-29	5.4E-31	2.9E-05	1.7E-02	6.1E-08	1.7E-01	2.8E+03	3.1E-02	5.4E+00	8.0E+03	5.5E+02	
45	1.8E-29	5.9E-31	2.8E-05	1.7E-02	6.2E-08	1.7E-01	2.3E+03	3.2E-02	5.4E+00	8.0E+03	5.5E+02	
55	2.1E-29	6.6E-31	2.7E-05	1.7E-02	6.3E-08	1.7E-01	1.8E+03	3.2E-02	5.5E+00	8.0E+03	5.5E+02	
65	2.4E-29	7.7E-31	2.6E-05	1.7E-02	6.5E-08	1.6E-01	1.4E+03	3.3E-02	5.6E+00	8.0E+03	5.5E+02	
75	3.0E-29	9.4E-31	2.5E-05	1.7E-02	6.6E-08	1.6E-01	9.4E+02	3.4E-02	5.7E+00	8.0E+03	5.5E+02	
85	4.3E-29	1.3E-30	2.7E-05	1.9E-02	7.2E-08	1.7E-01	5.3E+02	3.7E-02	6.1E+00	8.3E+03	5.6E+02	

X position	H_3AsO_3	$As(OH)_4^-$	AsO_4^{3-}	$H_2AsO_4^-$	H_3AsO_4	$HAsO_4^{2-}$	$O_2(aq)$	$>(w)FeH_2AsO_4$	$>(w)FeHAsO4^-$	$>(w)FeOHAsO_4^{3-}$	$Fe(OH)_3$	Pyrite
m	ug/l	ug/l	ug/l	ug/l	ug/l	ug/l	ug/l	ug/l	ug/l	ug/l	mg/kg	mg/kg
95	1.4E-28	4.1E-30	4.8E-05	3.5E-02	1.4E-07	3.2E-01	1.9E+02	9.4E-02	1.4E+01	1.5E+04	7.7E+02	
105	3.8E+00	1.2E-01	3.8E-09	2.7E-06	1.1E-11	2.5E-05	1.5E-63	0.0E+00	0.0E+00	0.0E+00		9.4E+01
115	7.3E+00	2.2E-01	7.4E-09	5.2E-06	2.0E-11	4.8E-05	1.5E-63	0.0E+00	0.0E+00	0.0E+00		6.2E+02
125	1.1E+01	3.3E-01	1.1E-08	7.7E-06	3.0E-11	7.1E-05	1.5E-63	0.0E+00	0.0E+00	0.0E+00		6.2E+02
135	1.4E+01	4.4E-01	1.4E-08	1.0E-05	4.0E-11	9.4E-05	1.5E-63	0.0E+00	0.0E+00	0.0E+00		6.2E+02
145	1.8E+01	5.4E-01	1.8E-08	1.3E-05	5.0E-11	1.2E-04	1.5E-63	0.0E+00	0.0E+00	0.0E+00		6.2E+02
155	2.1E+01	6.5E-01	2.2E-08	1.5E-05	6.0E-11	1.4E-04	1.5E-63	0.0E+00	0.0E+00	0.0E+00		6.2E+02
165	2.5E+01	7.6E-01	2.5E-08	1.8E-05	7.0E-11	1.6E-04	1.5E-63	0.0E+00	0.0E+00	0.0E+00		6.2E+02
175	2.8E+01	8.7E-01	2.9E-08	2.0E-05	7.9E-11	1.9E-04	1.5E-63	0.0E+00	0.0E+00	0.0E+00		6.2E+02
185	3.2E+01	9.7E-01	3.2E-08	2.3E-05	8.9E-11	2.1E-04	1.5E-63	0.0E+00	0.0E+00	0.0E+00		6.2E+02
195	3.5E+01	1.1E+00	3.6E-08	2.5E-05	9.9E-11	2.3E-04	1.5E-63	0.0E+00	0.0E+00	0.0E+00		6.2E+02
205	3.9E+01	1.2E+00	3.9E-08	2.8E-05	1.1E-10	2.6E-04	1.5E-63	0.0E+00	0.0E+00	0.0E+00		6.2E+02
215	4.2E+01	1.3E+00	4.3E-08	3.0E-05	1.2E-10	2.8E-04	1.5E-63	0.0E+00	0.0E+00	0.0E+00		6.2E+02
225	4.6E+01	1.4E+00	4.6E-08	3.3E-05	1.3E-10	3.0E-04	1.5E-63	0.0E+00	0.0E+00	0.0E+00		6.2E+02
235	4.9E+01	1.5E+00	5.0E-08	3.5E-05	1.4E-10	3.2E-04	1.5E-63	0.0E+00	0.0E+00	0.0E+00		6.2E+02
245	5.3E+01	1.6E+00	5.4E-08	3.8E-05	1.5E-10	3.5E-04	1.5E-63	0.0E+00	0.0E+00	0.0E+00		6.2E+02
255	5.6E+01	1.7E+00	5.7E-08	4.0E-05	1.6E-10	3.7E-04	1.5E-63	0.0E+00	0.0E+00	0.0E+00		6.2E+02
265	6.0E+01	1.8E+00	6.1E-08	4.3E-05	1.7E-10	3.9E-04	1.5E-63	0.0E+00	0.0E+00	0.0E+00		6.2E+02
275	6.3E+01	1.9E+00	6.4E-08	4.5E-05	1.8E-10	4.2E-04	1.5E-63	0.0E+00	0.0E+00	0.0E+00		6.2E+02
285	6.7E+01	2.0E+00	6.8E-08	4.8E-05	1.9E-10	4.4E-04	1.5E-63	0.0E+00	0.0E+00	0.0E+00		6.2E+02
295	7.0E+01	2.1E+00	7.1E-08	5.1E-05	2.0E-10	4.6E-04	1.5E-63	0.0E+00	0.0E+00	0.0E+00		6.2E+02
305	7.4E+01	2.2E+00	7.5E-08	5.3E-05	2.1E-10	4.9E-04	1.5E-63	0.0E+00	0.0E+00	0.0E+00		6.2E+02
315	7.7E+01	2.4E+00	7.8E-08	5.6E-05	2.2E-10	5.1E-04	1.5E-63	0.0E+00	0.0E+00	0.0E+00		6.2E+02
325	8.1E+01	2.5E+00	8.2E-08	5.8E-05	2.3E-10	5.3E-04	1.5E-63	0.0E+00	0.0E+00	0.0E+00		6.2E+02
335	8.4E+01	2.6E+00	8.6E-08	6.1E-05	2.4E-10	5.6E-04	1.5E-63	0.0E+00	0.0E+00	0.0E+00		6.2E+02
345	8.8E+01	2.7E+00	8.9E-08	6.3E-05	2.5E-10	5.8E-04	1.5E-63	0.0E+00	0.0E+00	0.0E+00		6.2E+02
355	9.1E+01	2.8E+00	9.3E-08	6.6E-05	2.6E-10	6.0E-04	1.5E-63	0.0E+00	0.0E+00	0.0E+00		6.2E+02

X position	H_3AsO_3	$As(OH)_4^-$	AsO_4^{3-}	$H_2AsO_4^-$	H_3AsO_4	$HAsO_4^{2-}$	$O_2(aq)$	$>(w)FeH_2AsO_4$	$>(w)FeHAsO4^-$	$>(w)FeOHAsO_4^{3-}$	$Fe(OH)_3$	Pyrite
m	ug/l	ug/l	ug/l	ug/l	ug/l	ug/l	ug/l	ug/l	ug/l	ug/l	mg/kg	mg/kg
365	9.4E+01	2.9E+00	9.6E-08	6.8E-05	2.7E-10	6.3E-04	1.5E-63	0.0E+00	0.0E+00	0.0E+00		6.2E+02
375	9.8E+01	3.0E+00	1.0E-07	7.1E-05	2.8E-10	6.5E-04	1.5E-63	0.0E+00	0.0E+00	0.0E+00		6.2E+02
385	1.0E+02	3.1E+00	1.0E-07	7.3E-05	2.9E-10	6.7E-04	1.5E-63	0.0E+00	0.0E+00	0.0E+00		6.2E+02
395	1.0E+02	3.2E+00	1.1E-07	7.6E-05	3.0E-10	7.0E-04	1.5E-63	0.0E+00	0.0E+00	0.0E+00		6.2E+02
405	1.1E+02	3.3E+00	1.1E-07	7.8E-05	3.1E-10	7.2E-04	1.5E-63	0.0E+00	0.0E+00	0.0E+00		6.2E+02
415	1.1E+02	3.4E+00	1.1E-07	8.1E-05	3.2E-10	7.4E-04	1.5E-63	0.0E+00	0.0E+00	0.0E+00		6.2E+02
425	1.2E+02	3.5E+00	1.2E-07	8.3E-05	3.3E-10	7.7E-04	1.5E-63	0.0E+00	0.0E+00	0.0E+00		6.2E+02
435	1.2E+02	3.6E+00	1.2E-07	8.6E-05	3.3E-10	7.9E-04	1.5E-63	0.0E+00	0.0E+00	0.0E+00		6.2E+02
445	1.2E+02	3.7E+00	1.2E-07	8.8E-05	3.4E-10	8.1E-04	1.5E-63	0.0E+00	0.0E+00	0.0E+00		6.2E+02
455	1.3E+02	3.8E+00	1.3E-07	9.1E-05	3.5E-10	8.4E-04	1.5E-63	0.0E+00	0.0E+00	0.0E+00		6.2E+02
465	1.3E+02	3.9E+00	1.3E-07	9.3E-05	3.6E-10	8.6E-04	1.5E-63	0.0E+00	0.0E+00	0.0E+00		6.2E+02
475	1.3E+02	4.0E+00	1.4E-07	9.6E-05	3.7E-10	8.8E-04	1.5E-63	0.0E+00	0.0E+00	0.0E+00		6.2E+02
485	1.4E+02	4.1E+00	1.4E-07	9.9E-05	3.8E-10	9.0E-04	1.5E-63	0.0E+00	0.0E+00	0.0E+00		6.2E+02
495	1.4E+02	4.2E+00	1.4E-07	1.0E-04	3.9E-10	9.3E-04	1.5E-63	0.0E+00	0.0E+00	0.0E+00		6.2E+02
505	1.4E+02	4.4E+00	1.5E-07	1.0E-04	4.0E-10	9.5E-04	1.6E-63	0.0E+00	0.0E+00	0.0E+00		6.2E+02
515	1.5E+02	4.5E+00	1.5E-07	1.1E-04	4.1E-10	9.7E-04	1.6E-63	0.0E+00	0.0E+00	0.0E+00		6.2E+02
525	1.5E+02	4.6E+00	1.5E-07	1.1E-04	4.2E-10	1.0E-03	1.6E-63	0.0E+00	0.0E+00	0.0E+00		6.2E+02
535	1.5E+02	4.7E+00	1.6E-07	1.1E-04	4.3E-10	1.0E-03	1.6E-63	0.0E+00	0.0E+00	0.0E+00		6.2E+02
545	1.6E+02	4.8E+00	1.6E-07	1.1E-04	4.4E-10	1.0E-03	1.6E-63	0.0E+00	0.0E+00	0.0E+00		6.2E+02
555	1.6E+02	4.9E+00	1.6E-07	1.2E-04	4.5E-10	1.1E-03	1.6E-63	0.0E+00	0.0E+00	0.0E+00		6.2E+02
565	1.6E+02	5.0E+00	1.7E-07	1.2E-04	4.6E-10	1.1E-03	1.6E-63	0.0E+00	0.0E+00	0.0E+00		6.2E+02
575	1.7E+02	5.1E+00	1.7E-07	1.2E-04	4.7E-10	1.1E-03	1.6E-63	0.0E+00	0.0E+00	0.0E+00		6.2E+02
585	1.7E+02	5.2E+00	1.8E-07	1.2E-04	4.8E-10	1.1E-03	1.6E-63	0.0E+00	0.0E+00	0.0E+00		6.2E+02
595	1.7E+02	5.3E+00	1.8E-07	1.3E-04	4.9E-10	1.2E-03	1.6E-63	0.0E+00	0.0E+00	0.0E+00		6.2E+02
605	1.8E+02	5.4E+00	1.8E-07	1.3E-04	5.0E-10	1.2E-03	1.6E-63	0.0E+00	0.0E+00	0.0E+00		6.2E+02
615	1.8E+02	5.5E+00	1.9E-07	1.3E-04	5.1E-10	1.2E-03	1.6E-63	0.0E+00	0.0E+00	0.0E+00		6.2E+02
625	1.8E+02	5.6E+00	1.9E-07	1.3E-04	5.2E-10	1.2E-03	1.6E-63	0.0E+00	0.0E+00	0.0E+00		6.2E+02

X position	H_3AsO_3	$As(OH)_4^-$	AsO_4^{3-}	$H_2AsO_4^-$	H_3AsO_4	$HAsO_4^{2-}$	$O_2(aq)$	$>(w)FeH_2AsO_4$	$>(w)FeHAsO4^-$	$>(w)FeOHAsO_4^{3-}$	$Fe(OH)_3$	Pyrite
m	ug/l	ug/l	ug/l	ug/l	ug/l	ug/l	ug/l	ug/l	ug/l	ug/l	mg/kg	mg/kg
635	1.9E+02	5.7E+00	1.9E-07	1.4E-04	5.3E-10	1.3E-03	1.6E-63	0.0E+00	0.0E+00	0.0E+00		6.2E+02
645	1.9E+02	5.8E+00	2.0E-07	1.4E-04	5.4E-10	1.3E-03	1.6E-63	0.0E+00	0.0E+00	0.0E+00		6.2E+02
655	1.9E+02	5.9E+00	2.0E-07	1.4E-04	5.5E-10	1.3E-03	1.6E-63	0.0E+00	0.0E+00	0.0E+00		6.2E+02
665	2.0E+02	6.0E+00	2.0E-07	1.4E-04	5.6E-10	1.3E-03	1.6E-63	0.0E+00	0.0E+00	0.0E+00		6.2E+02
675	2.0E+02	6.1E+00	2.1E-07	1.5E-04	5.7E-10	1.3E-03	1.6E-63	0.0E+00	0.0E+00	0.0E+00		6.2E+02
685	2.0E+02	6.2E+00	2.1E-07	1.5E-04	5.8E-10	1.4E-03	1.6E-63	0.0E+00	0.0E+00	0.0E+00		6.2E+02
695	2.1E+02	6.3E+00	2.1E-07	1.5E-04	5.9E-10	1.4E-03	1.6E-63	0.0E+00	0.0E+00	0.0E+00		6.2E+02
705	2.1E+02	6.4E+00	2.2E-07	1.5E-04	6.0E-10	1.4E-03	1.6E-63	0.0E+00	0.0E+00	0.0E+00		6.2E+02
715	2.1E+02	6.5E+00	2.2E-07	1.6E-04	6.1E-10	1.4E-03	1.6E-63	0.0E+00	0.0E+00	0.0E+00		6.2E+02
725	2.2E+02	6.6E+00	2.3E-07	1.6E-04	6.2E-10	1.5E-03	1.6E-63	0.0E+00	0.0E+00	0.0E+00		6.2E+02
735	2.2E+02	6.7E+00	2.3E-07	1.6E-04	6.3E-10	1.5E-03	1.6E-63	0.0E+00	0.0E+00	0.0E+00		6.2E+02
745	2.2E+02	6.8E+00	2.3E-07	1.6E-04	6.4E-10	1.5E-03	1.6E-63	0.0E+00	0.0E+00	0.0E+00		6.2E+02
755	2.3E+02	7.0E+00	2.4E-07	1.7E-04	6.5E-10	1.5E-03	1.6E-63	0.0E+00	0.0E+00	0.0E+00		6.2E+02
765	2.3E+02	7.1E+00	2.4E-07	1.7E-04	6.6E-10	1.6E-03	1.6E-63	0.0E+00	0.0E+00	0.0E+00		6.2E+02
775	2.3E+02	7.2E+00	2.4E-07	1.7E-04	6.7E-10	1.6E-03	1.6E-63	0.0E+00	0.0E+00	0.0E+00		6.2E+02
785	2.4E+02	7.3E+00	2.5E-07	1.7E-04	6.8E-10	1.6E-03	1.6E-63	0.0E+00	0.0E+00	0.0E+00		6.2E+02
795	2.4E+02	7.4E+00	2.5E-07	1.8E-04	6.9E-10	1.6E-03	1.6E-63	0.0E+00	0.0E+00	0.0E+00		6.2E+02
805	2.4E+02	7.5E+00	2.5E-07	1.8E-04	7.0E-10	1.7E-03	1.6E-63	0.0E+00	0.0E+00	0.0E+00		6.2E+02
815	2.5E+02	7.6E+00	2.6E-07	1.8E-04	7.1E-10	1.7E-03	1.6E-63	0.0E+00	0.0E+00	0.0E+00		6.2E+02
825	2.5E+02	7.7E+00	2.6E-07	1.8E-04	7.2E-10	1.7E-03	1.6E-63	0.0E+00	0.0E+00	0.0E+00		6.2E+02
835	2.5E+02	7.8E+00	2.7E-07	1.9E-04	7.3E-10	1.7E-03	1.6E-63	0.0E+00	0.0E+00	0.0E+00		6.2E+02
845	2.6E+02	7.9E+00	2.7E-07	1.9E-04	7.4E-10	1.7E-03	1.6E-63	0.0E+00	0.0E+00	0.0E+00		6.2E+02
855	2.6E+02	8.0E+00	2.7E-07	1.9E-04	7.5E-10	1.8E-03	1.6E-63	0.0E+00	0.0E+00	0.0E+00		6.2E+02
865	2.6E+02	8.1E+00	2.8E-07	1.9E-04	7.6E-10	1.8E-03	1.6E-63	0.0E+00	0.0E+00	0.0E+00		6.2E+02
875	2.7E+02	8.2E+00	2.8E-07	2.0E-04	7.7E-10	1.8E-03	1.6E-63	0.0E+00	0.0E+00	0.0E+00		6.2E+02
885	2.7E+02	8.3E+00	2.8E-07	2.0E-04	7.8E-10	1.8E-03	1.6E-63	0.0E+00	0.0E+00	0.0E+00		6.2E+02
895	2.7E+02	8.4E+00	2.9E-07	2.0E-04	7.9E-10	1.9E-03	1.6E-63	0.0E+00	0.0E+00	0.0E+00		6.2E+02

X position	H_3AsO_3	$As(OH)_4^-$	AsO_4^{3-}	$H_2AsO_4^-$	H_3AsO_4	$HAsO_4^{2-}$	$O_2(aq)$	$>(w)FeH_2AsO_4$	$>(w)FeHAsO4^-$	$>(w)FeOHAsO_4^{3-}$	$Fe(OH)_3$	Pyrite
m	ug/l	ug/l	ug/l	ug/l	ug/l	ug/l	ug/l	ug/l	ug/l	ug/l	mg/kg	mg/kg
905	2.8E+02	8.5E+00	2.9E-07	2.0E-04	8.0E-10	1.9E-03	1.6E-63	0.0E+00	0.0E+00	0.0E+00		6.2E+02
915	2.8E+02	8.6E+00	2.9E-07	2.1E-04	8.1E-10	1.9E-03	1.6E-63	0.0E+00	0.0E+00	0.0E+00		6.2E+02
925	2.8E+02	8.7E+00	3.0E-07	2.1E-04	8.2E-10	1.9E-03	1.6E-63	0.0E+00	0.0E+00	0.0E+00		6.2E+02
935	2.9E+02	8.8E+00	3.0E-07	2.1E-04	8.3E-10	2.0E-03	1.6E-63	0.0E+00	0.0E+00	0.0E+00		6.2E+02
945	2.9E+02	8.9E+00	3.1E-07	2.1E-04	8.4E-10	2.0E-03	1.6E-63	0.0E+00	0.0E+00	0.0E+00		6.2E+02
955	2.9E+02	9.0E+00	3.1E-07	2.2E-04	8.5E-10	2.0E-03	1.6E-63	0.0E+00	0.0E+00	0.0E+00		6.2E+02
965	3.0E+02	9.1E+00	3.1E-07	2.2E-04	8.6E-10	2.0E-03	1.6E-63	0.0E+00	0.0E+00	0.0E+00		6.2E+02
975	3.0E+02	9.2E+00	3.2E-07	2.2E-04	8.6E-10	2.0E-03	1.6E-63	0.0E+00	0.0E+00	0.0E+00		6.2E+02
985	3.0E+02	9.3E+00	3.2E-07	2.2E-04	8.7E-10	2.1E-03	1.6E-63	0.0E+00	0.0E+00	0.0E+00		6.2E+02
995	3.0E+02	9.3E+00	3.2E-07	2.3E-04	8.8E-10	2.1E-03	1.6E-63	0.0E+00	0.0E+00	0.0E+00		6.2E+02

Supplemental Table 4.3. Results of arsenic species, oxygen and Fe oxyhydroxide concentrations yielded from the GWB reactive transport model considering the model scenario with no buffer zone for a modeled flow path of 1,000 m.

X position	H_3AsO_3	$As(OH)_4^-$	AsO_4^{3-}	$H_2AsO_4^-$	H_3AsO_4	$HAsO_4^{2-}$	$O_2(aq)$	$>(w)FeH_2AsO_4$	$>(w)FeHAsO4^-$	$>(w)FeOHAsO_4^{3-}$	Fe(OH)3	Pyrite
m	ug/l	ug/l	ug/l	ug/l	ug/l	ug/l	ug/l	ug/l	ug/l	ug/l	mg/kg	mg/kg
5	1.9E-29	6.6E-31	4.1E-05	2.4E-02	8.2E-08	2.4E-01	3.5E+03	0.04	6.56	8913.39	536.43	
15	1.9E-29	6.3E-31	2.8E-05	1.8E-02	6.4E-08	1.7E-01	2.1E+03	0.03	5.57	8112.53	554.93	
25	3.4E-29	1.1E-30	2.9E-05	2.0E-02	7.5E-08	1.8E-01	9.2E+02	0.04	6.39	8692.10	568.34	
35	5.1E-28	1.6E-29	1.2E-04	8.6E-02	3.4E-07	7.9E-01	8.5E+01	0.16	19.53	14432.61	558.08	
45	1.2E+01	3.8E-01	1.1E-08	8.0E-06	3.1E-11	7.3E-05	1.2E-63	0	0	0		553.27
55	2.4E+01	7.3E-01	2.2E-08	1.5E-05	6.1E-11	1.4E-04	1.2E-63	0	0	0		621.63
65	3.6E+01	1.1E+00	3.2E-08	2.3E-05	9.0E-11	2.1E-04	1.2E-63	0	0	0		621.63
75	4.7E+01	1.4E+00	4.3E-08	3.1E-05	1.2E-10	2.8E-04	1.2E-63	0	0	0		621.63
85	5.9E+01	1.8E+00	5.4E-08	3.8E-05	1.5E-10	3.5E-04	1.2E-63	0	0	0		621.63
95	7.1E+01	2.1E+00	6.5E-08	4.6E-05	1.8E-10	4.2E-04	1.2E-63	0	0	0		621.63
105	8.2E+01	2.5E+00	7.5E-08	5.4E-05	2.1E-10	4.9E-04	1.3E-63	0	0	0		621.63

X position	H_3AsO_3	$As(OH)_4^-$	AsO_4^{3-}	$H_2AsO_4^-$	H_3AsO_4	$HAsO_4^{2-}$	$O_2(aq)$	>(w)FeH_2AsO_4	>(w)FeHAsO4$^-$	>(w)$FeOHAsO_4^{3-}$	Fe(OH)3	Pyrite
m	ug/l	ug/l	ug/l	ug/l	ug/l	ug/l	ug/l	ug/l	ug/l	ug/l	mg/kg	mg/kg
115	9.4E+01	2.9E+00	8.6E-08	6.1E-05	2.4E-10	5.6E-04	1.3E-63	0	0	0		621.63
125	1.1E+02	3.2E+00	9.7E-08	6.9E-05	2.7E-10	6.3E-04	1.3E-63	0	0	0		621.63
135	1.2E+02	3.6E+00	1.1E-07	7.7E-05	3.0E-10	7.0E-04	1.3E-63	0	0	0		621.63
145	1.3E+02	3.9E+00	1.2E-07	8.4E-05	3.3E-10	7.7E-04	1.3E-63	0	0	0		621.63
155	1.4E+02	4.2E+00	1.3E-07	9.2E-05	3.6E-10	8.5E-04	1.3E-63	0	0	0		621.63
165	1.5E+02	4.6E+00	1.4E-07	1.0E-04	3.9E-10	9.2E-04	1.3E-63	0	0	0		621.63
175	1.6E+02	4.9E+00	1.5E-07	1.1E-04	4.2E-10	9.9E-04	1.3E-63	0	0	0		621.63
185	1.7E+02	5.3E+00	1.6E-07	1.2E-04	4.5E-10	1.1E-03	1.3E-63	0	0	0		621.63
195	1.8E+02	5.6E+00	1.7E-07	1.2E-04	4.8E-10	1.1E-03	1.3E-63	0	0	0		621.63
205	2.0E+02	6.0E+00	1.9E-07	1.3E-04	5.1E-10	1.2E-03	1.3E-63	0	0	0		621.63
215	2.1E+02	6.3E+00	2.0E-07	1.4E-04	5.4E-10	1.3E-03	1.3E-63	0	0	0		621.63
225	2.2E+02	6.7E+00	2.1E-07	1.5E-04	5.7E-10	1.3E-03	1.3E-63	0	0	0		621.63
235	2.3E+02	7.0E+00	2.2E-07	1.5E-04	6.0E-10	1.4E-03	1.3E-63	0	0	0		621.63
245	2.4E+02	7.4E+00	2.3E-07	1.6E-04	6.4E-10	1.5E-03	1.3E-63	0	0	0		621.63
255	2.5E+02	7.7E+00	2.4E-07	1.7E-04	6.7E-10	1.6E-03	1.4E-63	0	0	0		621.63
265	2.6E+02	8.0E+00	2.5E-07	1.8E-04	7.0E-10	1.6E-03	1.4E-63	0	0	0		621.63
275	2.7E+02	8.4E+00	2.6E-07	1.9E-04	7.3E-10	1.7E-03	1.4E-63	0	0	0		621.63
285	2.9E+02	8.7E+00	2.8E-07	1.9E-04	7.6E-10	1.8E-03	1.4E-63	0	0	0		621.63
295	3.0E+02	9.1E+00	2.9E-07	2.0E-04	7.9E-10	1.9E-03	1.4E-63	0	0	0		621.63
305	3.1E+02	9.4E+00	3.0E-07	2.1E-04	8.2E-10	1.9E-03	1.4E-63	0	0	0		621.63
315	3.2E+02	9.7E+00	3.1E-07	2.2E-04	8.5E-10	2.0E-03	1.4E-63	0	0	0		621.63
325	3.3E+02	1.0E+01	3.2E-07	2.3E-04	8.8E-10	2.1E-03	1.4E-63	0	0	0		621.63
335	3.4E+02	1.0E+01	3.3E-07	2.3E-04	9.1E-10	2.2E-03	1.4E-63	0	0	0		621.63
345	3.5E+02	1.1E+01	3.4E-07	2.4E-04	9.4E-10	2.2E-03	1.4E-63	0	0	0		621.63
355	3.6E+02	1.1E+01	3.5E-07	2.5E-04	9.8E-10	2.3E-03	1.4E-63	0	0	0		621.63
365	3.7E+02	1.1E+01	3.7E-07	2.6E-04	1.0E-09	2.4E-03	1.4E-63	0	0	0		621.63
375	3.8E+02	1.2E+01	3.8E-07	2.7E-04	1.0E-09	2.5E-03	1.4E-63	0	0	0		621.63

X position	H_3AsO_3	$As(OH)_4^-$	AsO_4^{3-}	$H_2AsO_4^-$	H_3AsO_4	$HAsO_4^{2-}$	$O_2(aq)$	$>(w)FeH_2AsO_4$	$>(w)FeHAsO4^-$	$>(w)FeOHAsO_4^{3-}$	Fe(OH)3	Pyrite
m	ug/l	ug/l	ug/l	ug/l	ug/l	ug/l	ug/l	ug/l	ug/l	ug/l	mg/kg	mg/kg
385	3.9E+02	1.2E+01	3.9E-07	2.7E-04	1.1E-09	2.5E-03	1.4E-63	0	0	0		621.63
395	4.1E+02	1.2E+01	4.0E-07	2.8E-04	1.1E-09	2.6E-03	1.4E-63	0	0	0		621.63
405	4.2E+02	1.3E+01	4.1E-07	2.9E-04	1.1E-09	2.7E-03	1.4E-63	0	0	0		621.63
415	4.3E+02	1.3E+01	4.2E-07	3.0E-04	1.2E-09	2.7E-03	1.4E-63	0	0	0		621.63
425	4.4E+02	1.3E+01	4.4E-07	3.1E-04	1.2E-09	2.8E-03	1.4E-63	0	0	0		621.63
435	4.5E+02	1.4E+01	4.5E-07	3.1E-04	1.2E-09	2.9E-03	1.4E-63	0	0	0		621.63
445	4.6E+02	1.4E+01	4.6E-07	3.2E-04	1.3E-09	3.0E-03	1.4E-63	0	0	0		621.63
455	4.7E+02	1.4E+01	4.7E-07	3.3E-04	1.3E-09	3.0E-03	1.4E-63	0	0	0		621.63
465	4.8E+02	1.5E+01	4.8E-07	3.4E-04	1.3E-09	3.1E-03	1.5E-63	0	0	0		621.63
475	4.9E+02	1.5E+01	4.9E-07	3.5E-04	1.3E-09	3.2E-03	1.5E-63	0	0	0		621.63
485	5.0E+02	1.5E+01	5.0E-07	3.5E-04	1.4E-09	3.3E-03	1.5E-63	0	0	0		621.63
495	5.1E+02	1.6E+01	5.2E-07	3.6E-04	1.4E-09	3.3E-03	1.5E-63	0	0	0		621.63
505	5.2E+02	1.6E+01	5.3E-07	3.7E-04	1.4E-09	3.4E-03	1.5E-63	0	0	0		621.63
515	5.3E+02	1.6E+01	5.4E-07	3.8E-04	1.5E-09	3.5E-03	1.5E-63	0	0	0		621.63
525	5.4E+02	1.7E+01	5.5E-07	3.9E-04	1.5E-09	3.6E-03	1.5E-63	0	0	0		621.63
535	5.5E+02	1.7E+01	5.6E-07	4.0E-04	1.5E-09	3.6E-03	1.5E-63	0	0	0		621.63
545	5.7E+02	1.7E+01	5.7E-07	4.0E-04	1.6E-09	3.7E-03	1.5E-63	0	0	0		621.63
555	5.8E+02	1.8E+01	5.9E-07	4.1E-04	1.6E-09	3.8E-03	1.5E-63	0	0	0		621.63
565	5.9E+02	1.8E+01	6.0E-07	4.2E-04	1.6E-09	3.9E-03	1.5E-63	0	0	0		621.63
575	6.0E+02	1.8E+01	6.1E-07	4.3E-04	1.7E-09	3.9E-03	1.5E-63	0	0	0		621.63
585	6.1E+02	1.9E+01	6.2E-07	4.4E-04	1.7E-09	4.0E-03	1.5E-63	0	0	0		621.63
595	6.2E+02	1.9E+01	6.3E-07	4.4E-04	1.7E-09	4.1E-03	1.5E-63	0	0	0		621.63
605	6.3E+02	1.9E+01	6.4E-07	4.5E-04	1.8E-09	4.2E-03	1.5E-63	0	0	0		621.63
615	6.4E+02	2.0E+01	6.6E-07	4.6E-04	1.8E-09	4.2E-03	1.5E-63	0	0	0		621.63
625	6.5E+02	2.0E+01	6.7E-07	4.7E-04	1.8E-09	4.3E-03	1.5E-63	0	0	0		621.63
635	6.6E+02	2.0E+01	6.8E-07	4.8E-04	1.8E-09	4.4E-03	1.5E-63	0	0	0		621.63
645	6.7E+02	2.1E+01	6.9E-07	4.8E-04	1.9E-09	4.5E-03	1.5E-63	0	0	0		621.63

X position	H_3AsO_3	$As(OH)_4^-$	AsO_4^{3-}	$H_2AsO_4^-$	H_3AsO_4	$HAsO_4^{2-}$	$O_2(aq)$	>(w)FeH_2AsO_4	>(w)FeHAsO4$^-$	>(w)$FeOHAsO_4^{3-}$	Fe(OH)3	Pyrite
m	ug/l	ug/l	ug/l	ug/l	ug/l	ug/l	ug/l	ug/l	ug/l	ug/l	mg/kg	mg/kg
655	6.8E+02	2.1E+01	7.0E-07	4.9E-04	1.9E-09	4.5E-03	1.5E-63	0	0	0		621.63
665	6.9E+02	2.1E+01	7.1E-07	5.0E-04	1.9E-09	4.6E-03	1.5E-63	0	0	0		621.63
675	7.0E+02	2.1E+01	7.3E-07	5.1E-04	2.0E-09	4.7E-03	1.5E-63	0	0	0		621.63
685	7.1E+02	2.2E+01	7.4E-07	5.2E-04	2.0E-09	4.8E-03	1.5E-63	0	0	0		621.63
695	7.2E+02	2.2E+01	7.5E-07	5.2E-04	2.0E-09	4.8E-03	1.5E-63	0	0	0		621.63
705	7.3E+02	2.2E+01	7.6E-07	5.3E-04	2.1E-09	4.9E-03	1.5E-63	0	0	0		621.63
715	7.4E+02	2.3E+01	7.7E-07	5.4E-04	2.1E-09	5.0E-03	1.5E-63	0	0	0		621.63
725	7.5E+02	2.3E+01	7.8E-07	5.5E-04	2.1E-09	5.1E-03	1.6E-63	0	0	0		621.63
735	7.6E+02	2.3E+01	8.0E-07	5.6E-04	2.2E-09	5.1E-03	1.6E-63	0	0	0		621.63
745	7.7E+02	2.4E+01	8.1E-07	5.6E-04	2.2E-09	5.2E-03	1.6E-63	0	0	0		621.63
755	7.8E+02	2.4E+01	8.2E-07	5.7E-04	2.2E-09	5.3E-03	1.6E-63	0	0	0		621.63
765	7.9E+02	2.4E+01	8.3E-07	5.8E-04	2.2E-09	5.4E-03	1.6E-63	0	0	0		621.63
775	8.0E+02	2.5E+01	8.4E-07	5.9E-04	2.3E-09	5.4E-03	1.6E-63	0	0	0		621.63
785	8.1E+02	2.5E+01	8.5E-07	6.0E-04	2.3E-09	5.5E-03	1.6E-63	0	0	0		621.63
795	8.2E+02	2.5E+01	8.7E-07	6.0E-04	2.3E-09	5.6E-03	1.6E-63	0	0	0		621.63
805	8.3E+02	2.6E+01	8.8E-07	6.1E-04	2.4E-09	5.7E-03	1.6E-63	0	0	0		621.63
815	8.4E+02	2.6E+01	8.9E-07	6.2E-04	2.4E-09	5.7E-03	1.6E-63	0	0	0		621.63
825	8.5E+02	2.6E+01	9.0E-07	6.3E-04	2.4E-09	5.8E-03	1.6E-63	0	0	0		621.63
835	8.6E+02	2.6E+01	9.1E-07	6.4E-04	2.5E-09	5.9E-03	1.6E-63	0	0	0		621.63
845	8.7E+02	2.7E+01	9.2E-07	6.4E-04	2.5E-09	6.0E-03	1.6E-63	0	0	0		621.63
855	8.8E+02	2.7E+01	9.4E-07	6.5E-04	2.5E-09	6.0E-03	1.6E-63	0	0	0		621.63
865	8.9E+02	2.7E+01	9.5E-07	6.6E-04	2.6E-09	6.1E-03	1.6E-63	0	0	0		621.63
875	9.0E+02	2.8E+01	9.6E-07	6.7E-04	2.6E-09	6.2E-03	1.6E-63	0	0	0		621.63
885	9.1E+02	2.8E+01	9.7E-07	6.8E-04	2.6E-09	6.3E-03	1.6E-63	0	0	0		621.63
895	9.2E+02	2.8E+01	9.8E-07	6.8E-04	2.6E-09	6.3E-03	1.6E-63	0	0	0		621.63
905	9.3E+02	2.9E+01	9.9E-07	6.9E-04	2.7E-09	6.4E-03	1.6E-63	0	0	0		621.63
915	9.4E+02	2.9E+01	1.0E-06	7.0E-04	2.7E-09	6.5E-03	1.6E-63	0	0	0		621.63

X position	H_3AsO_3	$As(OH)_4^-$	AsO_4^{3-}	$H_2AsO_4^-$	H_3AsO_4	$HAsO_4^{2-}$	$O_2(aq)$	$>(w)FeH_2AsO_4$	$>(w)FeHAsO4^-$	$>(w)FeOHAsO_4^{3-}$	Fe(OH)3	Pyrite
m	ug/l	ug/l	ug/l	ug/l	ug/l	ug/l	ug/l	ug/l	ug/l	ug/l	mg/kg	mg/kg
925	9.5E+02	2.9E+01	1.0E-06	7.1E-04	2.7E-09	6.6E-03	1.6E-63	0	0	0		621.63
935	9.6E+02	2.9E+01	1.0E-06	7.2E-04	2.8E-09	6.6E-03	1.6E-63	0	0	0		621.63
945	9.7E+02	3.0E+01	1.0E-06	7.2E-04	2.8E-09	6.7E-03	1.6E-63	0	0	0		621.63
955	9.8E+02	3.0E+01	1.1E-06	7.3E-04	2.8E-09	6.8E-03	1.6E-63	0	0	0		621.63
965	9.9E+02	3.0E+01	1.1E-06	7.4E-04	2.9E-09	6.9E-03	1.6E-63	0	0	0		621.63
975	9.9E+02	3.1E+01	1.1E-06	7.5E-04	2.9E-09	6.9E-03	1.6E-63	0	0	0		621.63
985	1.0E+03	3.1E+01	1.1E-06	7.5E-04	2.9E-09	7.0E-03	1.6E-63	0	0	0		621.63
995	1.0E+03	3.1E+01	1.1E-06	7.6E-04	2.9E-09	7.0E-03	1.6E-63	0	0	0		621.63